

UNIVERSITÉ DU QUÉBEC À MONTRÉAL

LES EFFETS DES CHANGEMENTS CLIMATIQUES SUR LA ZONE LITTORALE DU SUD-EST DE LA MER
DE BEAUFORT, BASSIN HERSCHEL, CANADA, À PARTIR D'ENREGISTREMENTS
MICROPALÉONTOLOGIQUES

THÈSE

PRÉSENTÉE

COMME EXIGENCE PARTIELLE

DU DOCTORAT EN SCIENCES DE LA TERRE ET DE L'ATMOSPHÈRE

PAR

JADE FALARDEAU

SEPTEMBRE 2023

UNIVERSITÉ DU QUÉBEC À MONTRÉAL
Service des bibliothèques

Avertissement

La diffusion de cette thèse se fait dans le respect des droits de son auteur, qui a signé le formulaire *Autorisation de reproduire et de diffuser un travail de recherche de cycles supérieurs* (SDU-522 – Rév.04-2020). Cette autorisation stipule que «conformément à l'article 11 du Règlement no 8 des études de cycles supérieurs, [l'auteur] concède à l'Université du Québec à Montréal une licence non exclusive d'utilisation et de publication de la totalité ou d'une partie importante de [son] travail de recherche pour des fins pédagogiques et non commerciales. Plus précisément, [l'auteur] autorise l'Université du Québec à Montréal à reproduire, diffuser, prêter, distribuer ou vendre des copies de [son] travail de recherche à des fins non commerciales sur quelque support que ce soit, y compris l'Internet. Cette licence et cette autorisation n'entraînent pas une renonciation de [la] part [de l'auteur] à [ses] droits moraux ni à [ses] droits de propriété intellectuelle. Sauf entente contraire, [l'auteur] conserve la liberté de diffuser et de commercialiser ou non ce travail dont [il] possède un exemplaire.»

REMERCIEMENTS

Pour moi, ce doctorat peut se comparer à un grand voyage. Et dans les deux cas, même si l'on tente de notre mieux de s'y préparer, on finit toujours par s'enchevêtrer dans des détours, rencontrer des obstacles, oublier sa brosse à dents, et alouette. Mais surtout, on fait le plein de moments incroyables, on se surprend à accomplir des choses dont on ne se croyait pas capable, et on grandit. Et pour un voyage, comme un doctorat, on part avec un bagage. Dans le mien, il y avait ma famille (ma mère Johanne, mon père Régis, ma sœur Maude, mon beau-frère Mathieu, et les petits Louis et Raphaël qui y ont été ajoutés plus tard!), mes ami.e.s adoré.e.s (Agata, Alice, Anthony, Camille, Carmelle, Catherine, Claudie, Dom, Elliot, Geneviève, Mathieu, Myriam et Sarah), ainsi que ma superviseure, Anne de Vernal. Il y avait de ces ami.e.s qui ont joué aussi un rôle de guide, c'est-à-dire qui m'ont accompagnée dans les méandres du doctorat, car elles.ils avaient déjà fait le voyage avant moi. Je pense bien sûr à Dame Estelle, Natasha petit pois, Marie-Michèle et Williams. Tout au long de l'aventure, je savais que je pouvais fouiller dans ce bagage pour y trouver les outils ou le soutien dont j'avais besoin. Tous ces gens constituent ma base, mon pilier, grâce auquel j'ai été en mesure d'avancer. Ils sont la clé de l'achèvement de cette thèse aujourd'hui.

Mon voyage a débuté en janvier 2018. Et je me suis rapidement mise à arpenter de nouveaux sentiers, à dévaler des pentes ou à conduire dans la brousse, et tout ça sans jamais m'égarer, car à travers toutes mes péripéties des cinq dernières années, j'ai croisé sur mon chemin des guides, des cartes et des balises pour m'aider. Pour cela, j'aimerais remercier Anne de Vernal et Colin P. Gallagher d'avoir cru en moi et en mon projet dès le début. Merci à mes co-superviseurs Michael Fritz et Philippe Archambault d'avoir eu mon succès à cœur. Merci à Laura Gemery, Marit-Solveig Seidenkrantz, Claude Hillaire-Marcel et Thomas M. Cronin d'avoir partagé vos connaissances avec moi. Je tiens également à remercier les membres du Géotop pour leur soutien technique et humain, que ce soit un simple échange à l'heure du lunch ou dans le corridor, ou encore leur disponibilité à m'offrir un coup de main. Je pense à Sandrine, JF, Bianca, Dolores, Julien, Agnieszka et André. De plus, merci Tiffany, Anna, Vlad, Philippe et Léo pour leur aide au laboratoire, sur le terrain ou pour les analyses des échantillons. Enfin, je remercie Adina, Rocío et Lucille, celles qui ont fait le voyage en même temps que moi.

Au cours de l'aventure, je n'ai jamais cessé de remplir mon bagage. Je le remplissais de connaissances, de nouvelles compétences, de moments emplis de fierté, de persévérance, de beaux paysages et de magnifiques rencontres. Certains de ces moments marquants ne sont pas vraiment catégorisés comme un

écart dans mon itinéraire, mais plutôt des efforts supplémentaires qui en ont valu la peine, car ils m'ont conduite aux plus beaux points de vue. Ici, je parle notamment de ma famille ArcTrain, que j'ai coordonnée quelques années avec beaucoup d'amour; grâce à elle, j'ai rencontré des personnes fantastiques (Lera, Laura, Charles, Damien et Kelsey) et je me suis outillée dans un tout autre domaine. Je remercie aussi ma famille Nunataryuk, qui m'a donné l'opportunité d'aller sur le terrain et une bonne raison de visiter Venise. Merci en particulier à Rachele et Susanna pour votre présence. Je n'oublie pas non plus le projet sur le climat du passé avec Marie-Michèle. Nous avons toutes les deux essayé quelque chose de nouveau et je suis très fière de ce que nous avons accompli. Finalement, je suis reconnaissante d'avoir pu faire mon petit bout de chemin jusqu'à Aklavik et Inuvik à plusieurs reprises. J'ai pu établir une connexion avec cette région incroyable, mais surtout avec les gens qui y habitent. Je les remercie d'avoir donné un sens et une motivation à mon voyage!

J'en ressors avec un bagage deux fois plus lourd et le cœur deux fois plus léger, fière de moi et prête à relever d'autres défis!

Merci à toutes ces personnes qui ont fait partie de mon cheminement de près ou de loin, que je n'ai pas nommées.

À une prochaine aventure!

DÉDICACE

Je dédie cette thèse à Claire Harvey et Lucille Linteau, des femmes de tête et de cœur. Je vous aime.

AVANT-PROPOS

Cette thèse est née d'un désir d'utiliser des outils que je maîtrisais, la micropaléontologie et la paléocéanographie, et de les utiliser dans un contexte plus tangible qui répondrait à des enjeux environnementaux concrets tels que la gestion de la faune et de la flore. Ma motivation était donc de faire un saut de la géologie marine à l'écologie, afin d'agrandir mes horizons de recherche. Ma quête m'a conduite au parc national d'Ivvavik sur la côte nord du Yukon, Canada, directement au sud de l'île Herschel – Qikiqtaruk. Grâce au soutien financier du Programme de formation scientifique dans le Nord de Savoir polaire Canada, du Programme de suppléments aux subventions à la découverte en recherche nordique du CRSNG (à Anne de Vernal et Claude Hillaire-Marcel) et au projet Horizon 2020 Nunataryuk, j'ai pu me rendre dans les communautés les plus concernées, Aklavik et Inuvik, Territoires du Nord-Ouest, à maintes reprises, en plus d'accéder au parc territorial de l'île Herschel – Qikiqtaruk en 2018 pour une campagne d'échantillonnage. Mes visites dans les communautés ont été possibles grâce à la collaboration de Colin Gallgagher, biologiste au ministère des Pêches et Océans Canada, qui m'a invitée à participer aux rencontres annuelles de co-gestion du Dolly Varden (*Arctic char ou Ikalukpik*), le *West Side Working Group*, et avec qui nous avons dessiné les questions initiales du projet de recherche. Nous espérions développer des séries temporelles décrivant les conditions marines de la zone littorale, afin de les mettre en contexte avec les changements de stocks et de conditions physiques des populations de Dolly Varden. Toutefois, la théorie et la pratique ne se rencontrent pas toujours et des contraintes se sont tracées principalement dans les échelles, autant spatiales que temporelles.

La motivation initiale pour entreprendre cette thèse a été malgré tout grandement utile, mais d'un point de vue différent que je l'avais imaginé au départ. De fil en aiguille, toutes les collaborations créées avec des agents gouvernementaux de Parcs Canada, de Pêches et Océans Canada et tout spécialement avec des actrices et acteurs locaux. Les m'ont permis d'avoir une compréhension holistique de la dynamique environnementale de la région d'étude et de mieux discerner les enjeux des pêcheurs et pêcheuses face à un territoire qui se transforme à vue d'œil. Leurs perspectives et leur connaissance de la problématique environnementale étaient une information précieuse que j'ai toujours gardée en tête au fil du projet de recherche. Malgré certaines contraintes matérielles, cette thèse m'a permis d'identifier des effets importants du réchauffement climatique sur la zone littorale du sud-est de la mer de Beaufort et de traiter de liens entre les changements environnementaux, la biodiversité et la qualité de l'habitat côtier,

particulièrement dans le deuxième chapitre. La thèse répond donc à la motivation initiale, mais dans un cadre plus global.

Cette thèse se présente en trois chapitres écrits en anglais et dont le texte a été adapté pour fin de publication dans des revues scientifiques. Le premier chapitre s'intitule *Microfaunal recording of recent environmental changes in the Herschel Basin, western Arctic Ocean* et a paru dans la revue *Journal of Foraminiferal Research* en janvier 2023. Une version révisée du deuxième chapitre intitulé *Impacts of stronger winds and longer ice-free summers on the Canadian Beaufort Sea shelf ecosystems since the late 1900s* a été soumis à la revue *Estuarine, Coastal and Shelf Science* le 21 août 2023 à la suite de corrections mineures. Le chapitre trois se nomme *A 1300-year microfaunal record from the Beaufort Sea shelf indicates exceptional climate-related environmental changes over the last two centuries* et a été accepté pour publication à la revue *Palaeogeography, Palaeoclimatology, Palaeoecology* le 5 juin 2023 et paraîtra dans le numéro de septembre 2023. Une introduction et une conclusion écrites en français accompagnent les trois chapitres.

TABLE DES MATIÈRES

REMERCIEMENTS	ii
DÉDICACE	iv
AVANT-PROPOS.....	v
TABLE DES MATIÈRES	vii
LISTE DES FIGURES.....	xii
LISTE DES TABLEAUX	xix
LISTE DES ABRÉVIATIONS, DES SIGLES ET DES ACRONYMES.....	xx
RÉSUMÉ	xxiii
ABSTRACT	xxv
INTRODUCTION	1
0.1 La dynamique climatique terrestre.....	1
0.2 L'Arctique en plein changement	1
0.3 Motivation de la thèse	4
0.4 Compilation des enregistrements paléoclimatiques dans le nord-ouest américain	5
0.4.1 Enregistrements marins.....	6
0.4.2 Enregistrements terrestres	7
0.4.3 Le bassin Herschel.....	7
0.5 Objectifs et hypothèses.....	9
0.6 Le plateau continental de la mer de Beaufort : physiographie et hydrographie.....	11
0.6.1 Les courants marins	13
0.6.2 Les changements récents.....	14
0.7 Les approches méthodologiques	14
0.7.1 Les foraminifères benthiques	14
0.7.2 Les isotopes stables des tests de foraminifères	15
0.7.3 Les ostracodes.....	16
0.8 Carottes marines.....	18
0.9 La structure de la thèse.....	18
CHAPITRE 1 MICROFAUNAL RECORDING OF RECENT ENVIRONMENTAL CHANGES IN THE HERSCHEL BASIN, WESTERN ARCTIC OCEAN	21
Abstract	22

1.1	Introduction	23
1.2	Regional settings	24
1.2.1	The Herschel Basin.....	24
1.2.2	Hydrography	25
1.2.3	Winds and sea ice	27
1.3	Material and methods.....	28
1.3.1	Sea ice	28
1.3.2	Sediment cores	28
1.3.2.1	Acoustic survey	29
1.3.2.2	Core description.....	29
1.3.2.3	Chronology and sedimentation rates	30
1.3.3	Micropaleontological analyses	31
1.3.4	Community diversity and statistical analyses.....	40
1.4	Results.....	41
1.4.1	Core HBGC01, basin margin	41
1.4.1.1	Lithology and grain size	41
1.4.1.2	Radiogenic isotope activity and age model	41
1.4.1.3	Ecological zonation	42
1.4.1.4	Microfossil concentrations and fluxes.....	42
1.4.1.5	Foraminiferal assemblages	44
1.4.1.6	Ostracod assemblages	47
1.4.2	Core PG2303-1, deep basin	47
1.4.2.1	Lithology and grain size	47
1.4.2.2	Radiogenic isotope activity and age model	49
1.4.2.3	Ecological zonation	50
1.4.2.4	Microfossil concentrations	50
1.4.2.5	Foraminiferal assemblages	51
1.4.2.6	Ostracod assemblages	54
1.5	Discussion.....	55
1.5.1	Basin margin vs. deep basin.....	55
1.5.1.1	Bottom water masses	55
1.5.1.2	Microfaunal assemblages	56
1.5.2	The ~2000 CE shift	58
1.5.2.1	Sea ice and salinity.....	58
1.5.2.2	<i>Eoeponidella pulchella</i> and productivity.....	59
1.5.2.3	<i>Tintinnopsis fimbriata</i> and suspended particulate matter-rich freshwater	60
1.5.2.4	Ecological considerations about <i>Eoeponidella pulchella</i> , <i>Haynesina nivea</i> , <i>Tintinnopsis fimbriata</i> , and ostracod abundance.....	61
1.6	Conclusions	62
1.7	Acknowledgements.....	63
1.8	References.....	64
1.9	Supplementary material	77

CHAPITRE 2 IMPACTS OF STRONGER WINDS AND LONGER ICE-FREE SUMMERS ON CANADIAN BEAUFORT SEA SHELF ECOSYSTEMS SINCE THE LATE 1990S	80
Abstract	81
2.1 Introduction	82
2.2 Study area	83
2.3 Material and methods.....	84
2.3.1 Microfaunal analyses	84
2.3.2 Geochemistry.....	85
2.3.2.1 Carbonate shells	85
2.3.2.2 Bulk sediment	85
2.3.3 Environmental parameters	86
2.3.3.1 Sea-ice cover and seasonality.....	86
2.3.3.2 Wind data.....	88
2.3.3.3 River discharge.....	89
2.3.3.4 Air temperatures.....	89
2.3.3.5 Atmospheric oscillation indices	89
2.3.4 Cluster analyses and rate of change	90
2.4 Results and discussion.....	91
2.4.1 Environmental changes.....	91
2.4.2 Changes in the marine habitat.....	92
2.4.2.1 Microfaunal community	92
2.4.2.2 Geochemistry and lithology.....	93
2.4.3 Consequences of climate change on the coastal ecosystem.....	95
2.4.3.1 Easterly winds, sea ice, and unstable marine conditions	95
2.4.3.2 Food sources and turbidity	96
2.5 Conclusions	98
2.6 Acknowledgements.....	99
2.7 References.....	99
2.8 Supplementary material	107
CHAPITRE 3 A 1300-YEAR MICROFAUNAL RECORD FROM THE BEAUFORT SEA SHELF INDICATES EXCEPTIONAL CLIMATE-RELATED ENVIRONMENTAL CHANGES OVER THE LAST TWO CENTURIES	110
Abstract	112
3.1 Introduction	113
3.2 Regional setting.....	114
3.3 Methods	115
3.3.1 Sediment cores	115
3.3.2 Grain size.....	115
3.3.3 Radiometric chronology.....	117
3.3.4 Micropaleontological preparations	119
3.3.5 PCA analyses and community diversity	122
3.3.6 Stable isotopes.....	123

3.4 Results	124
3.4.1 PG2303 grain size and age model.....	124
3.4.2 PG2303 Microfossil abundances.....	124
3.4.3 Benthic foraminiferal assemblages.....	126
3.4.4 Stable isotopes.....	129
3.4.5 Ostracod assemblages	130
3.4.6 Ecozones and ecological shifts.....	133
3.5 Discussion.....	133
3.5.1 Identification of environmental conditions from micropaleontological proxies.....	133
3.5.1.1 Variable salinities and turbidity on Arctic shelves.....	133
3.5.1.2 Relationships to sea ice and food requirements	134
3.5.1.3 The shelf-break waters	135
3.5.2 History of environmental conditions prior to ~1800 CE.....	136
3.5.2.1 Influence of oceanic waters in the Herschel Basin from ~700 to 1150 CE	136
3.5.2.2 The culmination of a regional cooling between ~1150 and 1650 CE	137
3.5.2.3 The early decline of harsh climate conditions near the coast, ~1650-1800 CE	137
3.5.3 The modern warming after ~1800 CE.....	138
3.5.3.1 The environmental impact of the gradual warming from ca 1800 to 2000 CE	138
3.5.3.2 The post-2000 CE environmental conditions.....	139
3.6 Conclusion.....	140
3.7 Acknowledgements.....	142
3.8 References.....	143
3.9 Supplementary material	155
3.9.1 Appendix 3-A.1 – Interpretations of $^{210}\text{Pb}_{\text{tot}}$, ^{226}Ra , ^{137}Cs activity profiles of cores PG2303 and PG2303-1.....	155
3.9.2 References	161
CONCLUSION	162
4.1 La capacité d'analyse	162
4.2 Les différences entre la marge et le fond du bassin – Carottes HBGC01 et PG2303-1	163
4.3 La transition de 1998 CE.....	164
4.4 Les 1300 dernières années.....	165
4.5 Les traceurs écologiques et les questions qu'ils soulèvent	166
4.6 Contributions et travaux futurs.....	167
ANNEXE A COMPTAGES BRUTS DES FORAMINIFÈRES BENTHIQUES CALCAIRES DANS LA CAROTTE YC18-HB-GC01	174
ANNEXE B COMPTAGES BRUTS DES FORAMINIFÈRES BENTHIQUES AGGLUTINANTS ET AUTRES TYPES DE MICROFOSSILES DANS LA CAROTTE YC18-HB-GC01	176
ANNEXE C COMPTAGES BRUTS DES OSTRACODES DANS LA CAROTTE YC18-HB-GC01.....	178

ANNEXE D COMPTAGES BRUTS DE FORAMINIFÈRES BENTHIQUES CALCAIRES DANS LA CAROTTE PG2303-1180	
ANNEXE E COMPTAGES BRUTS DE FORAMINIFÈRES BENTHIQUES AGGLUTINANTS ET AUTRES TYPES DE MICROFOSSILES DANS LA CAROTTE PG2303-1	181
ANNEXE F COMPTAGES BRUTS DES OSTRACODES DANS LA CAROTTE PG2303-1.....	182
ANNEXE G COMPTAGES BRUTS DES FORAMINIFÈRES BENTHIQUES CALCAIRES DANS LA CAROTTE PG2303	183
ANNEXE H COMPTAGES BRUTS DES FORAMINIFÈRES BENTHIQUES AGGLUTINANTS ET AUTRES TYPES DE MICROFOSSILES DANS LA CAROTTE PG2303	185
ANNEXE I COMPTAGES BRUTS DES OSTRACODES DANS LA CAROTTE PG2303	187
ANNEXE J COMPTAGES DES PALYNOMORPHES DANS LA CAROTTE PG2303	189
RÉFÉRENCES	191

LISTE DES FIGURES

- Figure 0.1 Schéma des anomalies de température de l'air (Jouzel *et al.*, 2007) et de concentrations de CO₂ atmosphérique (Bereiter *et al.*, 2015) en Antarctique au cours des 800 000 dernières années et au cours de l'intervalle 1980-2000 CE basé sur des données instrumentales (Global Climate Change: Evidence, 2021; Global Monitoring Laboratory, 2021), ainsi que les prévisions pour les 100 prochaines années (RCP6.5; IPCC, 2014). Gracieuseté d'Alison McCreesh. 2
- Figure 0.2: Carte des sites d'enregistrements paléoclimatiques et paléocéanographiques de la région d'étude avec un gros plan sur le bassin Herschel au bas à gauche. 6
- Figure 0.3 Carte des courants marins et de la localisation des sites d'étude. Les stations hydrométriques et météorologiques sont représentées par des losanges blancs et noirs, respectivement. Un gros plan du bassin Herschel et des sites est illustré au bas à gauche et la direction des vents dominants est présentée au bas à droite de la figure par les flèches grises..... 13
- Figure 0.4 Schéma représentant le bassin Herschel et les sites d'étude dans leur cadre environnemental. Gracieuseté de Mark-Antoine Thibodeau Breault. 17
- Figure 0.5 Représentation schématique (a) des effets de vents d'est forts et dominants et (b) des effets de vents d'est modérés. Pour les indicateurs écologiques, le code de couleur réfère aux couleurs utilisées dans le schéma (p. ex., vert pâle pour les remontées d'eaux riches en nutriments et bleu foncé pour les eaux profondes salées). Gracieuseté de Mark-Antoine Thibodeau Breault. 19
- Figure 1.1 (A) Regional map of northwestern North America with the main currents in the Bering Strait and the western Arctic Ocean (based on Grebmeier *et al.*, 2006). (B) Study area [white box in (A)] and surface ocean currents (based on Lin *et al.*, 2020). The black dots represent the grid used for the mean summer sea-ice concentrations. The gray arrows in the lower left corner indicate the two dominant wind directions at Herschel Island – Qikiqtaruk (based on Radosavljevic *et al.*, 2016). The a–b transect marks the section used for the (C) salinity profile with data from the World Ocean Database 2018 (Boyer *et al.*, 2018) using Ocean Data View (Schlitzer, 2018). The thin vertical black lines are the locations of all the CTD measurements (mostly summer to fall measurements) used for the reconstruction of the water mass transect. The dotted lines delimitate approximately the Pacific (31.5–33.5 psu) and Atlantic (>33.5 psu) water masses. (D) Location of core sites in the Herschel Basin and location of two CTD measurements taken in August 2015 (red dot) and April 2016 (blue dot; see Fig. 1.2). The black lines indicate the northwest–southeast (Fig. 1-A.1) and west–east (Fig. 1-A.2) seismic transects. The main currents are illustrated in (A) and (B) as follows: pink arrow for the Alaskan coastal water, blue arrows for the other Pacific water masses (winter/summer), red dotted arrow for the subsurface Atlantic waters, yellow arrows for the Beaufort Gyre, purple arrow for the coastal flow, and green arrow for the shelf current. 26
- Figure 1.2 Salinity and temperature profiles in the Herschel Basin in August 2015 (A) and April 2016 (B) from CTD data measured with a hand-held CastAway-CTD device. Yellow and purple diamonds mark the water depth of cores YC18-HB-GC01 and PG2303-1, respectively. The brackish summer surface waters (<28 psu) are indicated by the light gray zone. The darker gray zones illustrate waters composed of a mix of brines and upwelled water from the shelf break (mostly Pacific waters). The red and blue dots refer to the location of the CTD measurements shown in Figure 1.1D. 27

Figure 1.3 Summer (JJAS) mean sea-ice concentrations (%) calculated from 18-grid points of 25 km x 25 km covering the study area (see Fig. 1.1B; data compiled from NOAA/NSIDC climate data record of passive microwave sea-ice concentration; cf. Meier et al., 2017). The horizontal black lines mark the mean of the 1979–2006 CE and of the 2007–2017 CE intervals.....	28
Figure 1.4 (A) The CT-scan of core HBGC01 with (B) the $^{210}\text{Pb}_{\text{tot}}$ (yellow), ^{226}Ra (orange), and ^{137}Cs (gray) activity profiles in core HBGC01. The dark orange line marks the mean ^{226}Ra used to estimate $^{210}\text{Pb}_{\text{sup}}$ (see text) and the pink dashed line marks the depth of the 1963 maximum ^{137}Cs activity (cf. Aoyama et al., 2006). (C) Natural logarithm of $^{210}\text{Pb}_{\text{ex}}$ (blue dots). The gray line marks the linear regression of the $\ln^{210}\text{Pb}_{\text{ex}}$ below 10 cm. (D) HBGC01 core age models obtained with Plum (mean ages = red line; minimum and maximum ages = gray dotted lines), with the CFCS model (black line) and with the CRS-piecewise model (green line; see Fig. 1-A.4 for the original age model graph produced by Plum). The gray shaded areas in (C) and (D) represent the proposed mixed layer.....	30
Figure 1.5 Calcareous benthic foraminifera from the Herschel Basin. 1 <i>Nonionellina labradorica</i> . 2 <i>Quinqueloculina seminulum</i> . 3 <i>Triloculina trihedra</i> . 4 <i>Stainforthia loeblichii</i> . 5, 9 <i>Elphidium clavatum</i> . 6 <i>Haynesina nivea</i> . 7 <i>Cassidulina reniforme</i> . 8 <i>Elphidium hallandense</i> . 10 <i>Buccella frigida</i> . 11 <i>Eoepionidella pulchella</i> . 12 <i>Elphidium asklundi</i> . 13 <i>Pyrgo williamsoni</i>	35
Figure 1.6 Calcareous benthic foraminifera from the Herschel Basin. 1 <i>Elphidium bartletti</i> . 2 <i>Elphidiella groenlandica</i> . 3 <i>Islandiella helena</i> . 4 <i>Islandiella norcrossi</i> . 5 <i>Quinqueloculina stalker</i> . 6 <i>Stainforthia feylingi</i> . 7 <i>Valvularia</i> sp. 8 <i>Parafissurina himatiostoma</i> . 9 <i>Bolivinellina pseudopunctata</i> . 10 <i>Cornuspira involvens</i> . 11 <i>Stetsonia horvathi</i> . 12 <i>Haynesina orbicularis</i>	36
Figure 1.7 Agglutinated benthic foraminifera from the Herschel Basin. 1 <i>Ammotium cassis</i> . 2 <i>Lagenammina diffugiformis</i> . 3 <i>Textularia earlandi</i> . 4 <i>Spiroplectammina biforis</i> . 5 <i>Eggerelloides advenus</i> . 6 <i>Portetrochammina karica</i> . 7 <i>Textularia torquata</i> . 8 <i>Cribrostomoides crassimargo</i> . 9 <i>Recurvoides turbinatus</i>	37
Figure 1.8 Ostracods from the Herschel Basin. 1, 2 <i>Paracyprideis pseudopunctillata</i> . 3, 4 <i>Eucythere</i> sp. 5 <i>Sarsicytheridea bradii</i> . 6 <i>Heterocyprideis sorbyana</i> . 7 <i>Loxoconcha venepidermoidea</i> (juvenile).	38
Figure 1.9 Ostracods from the Herschel Basin. 1 <i>Rabilimis mirabilis</i> (juvenile). 2 <i>Cytheropteron sulense</i> . 3 <i>Cluthia cluthae</i> . 4 <i>Cytheropteron elaeni</i> . 5 <i>Eucytherura delineata</i> . 6 <i>Semicytherura complanata</i> . 7 <i>Cytheropteron brastadensis/discoveria</i> . 8 <i>Cytheropteron suzdalskyi</i>	39
Figure 1.10 Other microfossils from the Herschel Basin. 1 <i>Picea</i> sp. 2 <i>Spongotorchus glacialis</i> . 3 <i>Coccolithus pelagicus</i> . 4, 5, 6 <i>Tintinnopsis fimbriata</i> . 7 <i>Coscinodiscus</i> sp.	40
Figure 1.11 Microfossil content (concentrations in black and fluxes in gray), summary grain size data (black = sand; gray = silt; white = clay) and mass accumulation rates in core HBGC01 reported versus depth (cm) and age (year CE). The light gray dotted lines represent the error in accumulation rates and fluxes. The RDA results were used to define the two ecozones.	43
Figure 1.12 Redundancy analysis of the foraminiferal assemblages (red arrows) and the microfossil fluxes and percentage of sand (blue arrows) in core HBGC01. The black dots represent the sample scores on each axis. Indicators of saline waters are circled in dark blue, and indicators of low salinity or high productivity are circled in green. See Table 1.4 for the abbreviation corresponding names.	44

Figure 1.13 Percentages of benthic foraminiferal taxa in core HBGC01 expressed versus depth (cm) and age (year CE). The proportion of agglutinated foraminifera is the percentage of agglutinated foraminifera over the total number of benthic foraminifera (calcareous and agglutinated included). The RDA results were used to define the two ecozones.....	45
Figure 1.14 Ostracod assemblages versus depth (cm) and age (year CE) in core HBGC01. Low salinity tolerant taxa (LST) and the euhaline taxa (>30 psu) are indicated. <i>Sarsicytheridea bradii</i> does tolerate low salinities (<30 psu), but it is not associated with other LST because it is cosmopolitan, living in a wide range of salinity, temperature and oxygen-level conditions (Stepanova et al., 2019; Gemery et al., 2021). Note that assemblages in the upper 19 cm should be considered with caution, as counts are low; <10 valves per sample. The two ecozones were defined from the RDA of the benthic foraminiferal assemblages and are reported as in Figures 1.11 and 1.13.	46
Figure 1.15 (A) $^{210}\text{Pb}_{\text{tot}}$ (purple), ^{226}Ra (orange) and ^{137}Cs (gray) activity profiles in core PG2303-1 and the $^{210}\text{Pb}_{\text{tot}}$ in core HBGC01 (yellow). The dark orange line marks the ^{226}Ra average ($^{210}\text{Pb}_{\text{sup}}$) of core PG2303-1. (B) PG2303-1 core age model obtained with Plum including the mean ages (red line) and the minimum and maximum ages (gray dotted lines). See Figure 1-A.5 for the original age model graph produced by Plum.	48
Figure 1.16 Microfossil content and grain size data (black = sand; gray = silt; white = clay) in core PG2303-1 reported versus of depth (cm). The RDA results were used to define the three ecozones.....	51
Figure 1.17 Redundancy analysis of the foraminiferal assemblage (red arrows) and the microfossil concentrations and percentage of sand (blue arrows) in samples from core PG2303-1. The black dots represent the sample scores on each axis. Indicators of high productivity are circled in green and of low productivity are circled in brown. See Table 1.4 for the abbreviation corresponding names.	52
Figure 1.18 Percentages of benthic foraminiferal taxa in core PG2303-1 expressed versus depth (cm). The proportion of agglutinated foraminifera is the percentage of agglutinated foraminifera over the total number of benthic foraminifera (calcareous and agglutinated included). The RDA results were used to define the three ecozones.	53
Figure 1.19 Ostracod assemblages versus depth (cm) in core PG2303-1. The low salinity tolerant taxa (LST) and the euhaline taxa (>30 psu) are indicated. Note that occurrences in assemblages with less than 10 valves should be considered with caution. The three ecozones were defined from the RDA of the benthic foraminiferal assemblages and are reported as in Figures 1.16 and 1.18.	55
Figure 1-A.1 A northwest–southeast seismic profile that crosses the Herschel Island – Qikiqtaruk shore to the middle of the Herschel Basin. The red arrow marks the location of the UWITEC gravity core YC18-HB-GC01.....	77
Figure 1-A.2 A near west–east seismic profile across the Herschel Basin showing the location of the PG2303 coring site. The red arrow marks the location of the UWITEC gravity core PG2303-1.	77
Figure 1-A.3 Photograph, CT-scan and density data of core YC18-HB-GC01.....	78
Figure 1-A.4 Original graph of the YC18-HB-GC01 age model produced by Plum.....	78
Figure 1-A.5 Original graph of the PG2303-1 age model produced by Plum.....	79

Figure 2.1 a) Study area in the southern Canadian Beaufort Sea and b) close-up of the core site location. White and black diamonds represent the location of the hydrometric and weather stations, respectively. The black dots correspond to the grid used to calculate the mean summer sea-ice concentration. The purple arrow corresponds to the longshore current carrying low saline waters derived from the coastal river outflows and the extension of the Alaskan coastal waters; the blue arrow corresponds to the nutrient-rich and saline (>31.5) Pacific waters flowing through the “Beaufort Sea shelfbreak jet” (Pickart, 2004); the yellow arrows show the Beaufort Gyre and the associated recirculation currents and finally, the green arrow in (b) indicates the cold (<-1°C) and low salinity (<31) surface waters (<30 m) flowing through the shelf current (based on Lin et al., 2020). Maps were made in Ocean Data View (Schlitzer, 2018) 83

Figure 2.2 Heat maps and time-constrained hierachal clusters are illustrated as dendograms of the (a) foraminiferal relative abundances, including the selected ecological indicators, and the (b) environmental parameters reordered based on their weighted average from the cluster score. See Tables 2.1 and 2.2 for the ecological affinity references and the abbreviation corresponding names. 91

Figure 2.3 Summary figure of regional changes from the 1970s to 2018 as recorded in the study core, and the environmental and climatic archives. Rate of change of the a) benthic foraminiferal assemblages and the b) environmental parameters (see section 2.3.4). c), d), e), and f) Selected environmental indicators. g), h) and i) Geochemical measurements performed in the HBGC01 core together with the atomic C/N ratio (black line). j) Accumulation rates ($\text{g}\cdot\text{cm}^{-2}$) and k) concentration of sand (%). l) $\delta^{13}\text{C}$ and m) $\delta^{18}\text{O}$ of *Elphidium clavatum* (gray) and *Cassidulina reniforme* (black). n) Fluxes ($\#\cdot\text{cm}^{-2}\cdot\text{a}^{-1}$) of *Tintinnopsis fimbriata* (black shaded area) and ostracod valves (gray shaded area) and o) fluxes of calcareous (black line) and agglutinated (gray line) benthic foraminifera. p) Relative abundance (%) of *Eoepionidella pulchella* (green shaded area) and the cumulative abundance (%) purple shaded area) of *Islandiella norcrossi* and *Stainforthia feylingi* from 1970 to 2018 (see Falardeau et al., 2023a). The solid purple line delineates the abundance of *S. feylingi* (below) and *I. norcrossi* (above). The gray shaded areas highlight the 1999-2017 and the 1994-2017 subsets of the foraminiferal taxa and the environmental parameters, respectively. 93

Figure 2-A.1 Radiogenic isotope data and age model of core HBGC01 slightly modified from Falardeau et al. (2023a). (a) CT-scan of core HBGC01 in which laminations can be observed in the core top 10 cm. (b) Total ^{210}Pb (yellow), ^{226}Ra (orange), and ^{137}Cs (gray) activity profiles in core HBGC01. The mean ^{226}Ra activity at $1.60 \pm 0.05 \text{ dpm}\cdot\text{g}^{-1}$ would represent the value of the supported ^{210}Pb , which was subtracted from the total ^{210}Pb activity to obtain the ^{210}Pb in excess. The pink dotted line marks the peak in ^{137}Cs at 38-37 cm. (c) Natural logarithm of excess ^{210}Pb (blue dots). The gray line marks the linear regression of the $\ln^{210}\text{Pb}$ in excess below 10 cm. (d) HBGC01 core age model obtained with *Plum* (mean ages = red line; minimum and maximum ages = gray dotted lines). The pink arrow marks the age of the nuclear weapon test in 1963 (Aoyama et al., 2006). The gray shaded areas in (c) and (d) represent the interval of the proposed mixed layer. 107

Figure 2-A.2 The direction of strong winds ($>10\text{m}\cdot\text{s}^{-1}$) during the open water season over the years at a) Herschel Island and b) Komakuk Beach weather stations..... 108

Figure 2-A.3 The hydrography of the Firth (blue), Babbage (red), and Mackenzie (black) rivers. The freshet discharge value and the mean summer discharge of the Mackenzie River were divided by 100. .. 109

Figure 3.1 a) Regional map showing the location of the study area (dotted white square) and the Hanna Shoal (black square). The pink and orange arrows indicate the flow of the Alaskan Coastal Waters (ACW) and other Pacific water branches (winter/summer water masses), respectively; the dotted red arrow shows the path of the subsurface Atlantic Water along the continental margin, and the yellow arrows represent the Beaufort Gyre based on Grebmeier et al. (2006). b) Map of the study area showing the coastal flow (purple arrow), the Beaufort shelfbreak jet (dark blue arrow), and the waters recirculating in the Mackenzie Trough under the Beaufort Gyre influence (yellow arrows) based on Lin et al. (2020). The gray arrows in the lower right corner mark the dominant wind directions (Radosavljevic et al., 2016), the black diamonds show the location of cores mentioned in the text, and the white diamond shows the location of the Komakuk Beach weather station. In the lower-left corner is a close-up of the study area with the core site location (pink diamond) and bathymetry of the Herschel Basin (EBA Engineering Consultants Ltd., 1992). c) Salinity (purple) and temperature (green) profiles in the Herschel Basin in August 2015 (solid line) and April 2016 (dotted lines) from CTD data (Falardeau et al., 2023). The blue and yellow dots refer to the location of the CTD measurements shown in the close-up of Fig. 3.1b, while the gray shading area separates the local surface waters from the bottom waters..... 116

Figure 3.2 Core PG2303 age model based on OxCal (version 4.4; Bronk Ramsey, 2008, 2009). The vertical gray bar indicates the length of the core section used for this study. The blue shading indicates the 2-sigma probability range of the age depth model. Details on the two constrained ages based on ^{210}Pb and ^{137}Cs activity profiles at the top of the core can be found in the methods Section 3.3.3 and Appendix 3-A.1. The age model of core PG2303–1 (20–0 cm) from Falardeau et al. (2023) is illustrated in the gray rectangle in the top right corner..... 125

Figure 3.3 Microfossil concentrations (black lines), fluxes (green lines), grain size (black = sand; gray = silt; green = clay), and mass accumulation rates of the composite sequence of cores PG2303–1/PG2303 as a function of depth (cm). Dashed lines represent the flux and mass accumulation rate errors. 126

Figure 3.4 Percentages of benthic foraminiferal taxa in the composite sediment sequence of cores PG2303–1/PG2303 as a function of depth (cm). The assemblages calculated with <300 foraminiferal tests are represented in gray. The principal component analysis (PCA) scores are represented by thick black bars (PC1) and thin gray bars (PC2). The ecozones were defined based on the PCA of the foraminiferal assemblages (see Fig. 3.5) and a shift in the dominant taxa..... 127

Figure 3.5 PCA plot of foraminiferal assemblages in the composite sediment sequence of cores PG2303–1/PG2303 (black dots for piston core PG2303 samples and orange dots for the short gravity PG2303–1 core samples). Agglutinated foraminifera are shown in blue, the low-oxygen tolerant calcareous species *Bolivinellina pseudopunctata* (B_pseu) is in green, while the remaining calcareous species are shown in red. See Table 3.3 for the full names of the abbreviations used. 128

Figure 3.6 a) Stable isotope ratios ($\delta^{18}\text{O}$ and $\delta^{13}\text{C}$) of *Elphidium clavatum* and *Cassidulina reniforme* in the composite sediment sequence of cores PG2303–1/PG2303 as a function of depth (cm). The thin lines surrounding the main curves illustrate the analytical uncertainty. b) The equilibrium calcite $\delta^{18}\text{O}$ as a function of salinity (black dots; Table 3-A.7) calculated from $\delta^{18}\text{O}$ in the water column measured in the Herschel Basin at different depths in summer 2015 (gray dots; Table 3-A.8). A negative offset of 1.0 ‰ for *Elphidium clavatum* is depicted. 129

Figure 3.7 Relative abundances of ostracod taxa in the composite sediment sequence of cores PG2303–1/PG2303 as a function of depth (cm). The assemblages calculated with <10 ostracod valves are

represented in gray. The principal component analysis scores are represented by thick black bars (PC1) and thin gray bars (PC2). The ecozones were defined based on the PCA of the ostracod assemblages (see Fig. 3.8).	130
Figure 3.8 PCA plot of the ostracod assemblages in the composite sediment sequence of cores PG2303–1/PG2303 (black dots for piston core PG2303 samples and orange dots for the short gravity PG2303–1 core samples). The LST taxa are in blue and the euhaline taxa are in red. See Table 3.3 for the full names of the abbreviations used.	131
Figure 3.9 Summary figure of paleoecological data from the Herschel Basin site PG2303 in function of depth (cm) compared with existing data of temperature anomalies in Alaska (Nicolle et al., 2018) and summer sea-ice extent in the Arctic Ocean from 600 to 2000 CE (Kinnard et al., 2011; black line) with a close-up from 2000 to 2022 CE (Fetterer et al., 2017; yellow line) in function of age (year CE). Three important shifts are identified: at 1160 ± 130 CE, a transition to particularly cold conditions, and at 1790 ± 30 CE and at 1955 ± 10 CE to mark the early onset and the acceleration of the modern warming, respectively. For the ostracod indicators (cumulative percentages): Pacific waters (orange) = <i>Kotoracythere arctoborealis</i> ; Productivity (light green) = <i>Normanicysthere leioderma</i> ; Low salinity tolerant (light blue) = <i>Heterocyprideis sorbyana</i> , <i>Loxoconcha venepidermoidea</i> and <i>Eucythere</i> spp.; Persistent frigid waters (dark blue) = <i>Paracyprideis pseudopunctillata</i> , <i>Cluthia cluthae</i> and <i>Semicytherura complanata</i> . For the benthic foraminiferal indicators (cumulative percentages): Variable salinity (light blue) = <i>Haynesina nivea</i> ; Bacterial/complex organic carbon feeders (brown) = <i>Textularia earlandi</i> , <i>Stetsonia horvathi</i> and <i>Quinqueloculina stalkerii</i> ; Productivity (light green) = <i>Eoeponidella pulchella</i> and <i>Epistominella takayanagii</i> ; Sea-ice margin productivity (dark green) = <i>Stainforthia feylingi</i> . <i>Triloculina trihedra</i> refers to cool and stable saline waters (red).	140
Figure 3-A.1 Photograph of PG2303 core sampling in April 2016 during the Yukon Coast spring expedition led by the Alfred Wegener Institute in Potsdam. Photo credit: Michael Fritz	157
Figure 3-A.2 $^{210}\text{Pb}_{\text{tot}}$, ^{226}Ra , and ^{137}Cs of cores PG2303 and PG2303-1 activity profiles. The red vertical dotted lines indicate the mean of the measured ^{226}Ra in both cores, separately, with their respective error represented at the top and bottom of the dotted line. b) The natural logarithm of the $^{210}\text{Pb}_{\text{ex}}$ natural logarithm using a $^{210}\text{Pb}_{\text{sup}}$ of 1.72 dpm g^{-1} . By dividing the disintegration constant (Sanchez-Cabeza & Ruiz-Fernández, 2012) with the rate of the linear trend between 44.5 cm and 9.5 cm, we obtain a mean sedimentation rate of 0.41 cm a^{-1}	158
Figure 3-A.3 Assemblages of calcareous benthic foraminifera (black bars) and agglutinated benthic foraminifera (gray bars) calculated separately together with the total benthic foraminifera (calcareous and agglutinated included) concentrations (black line) and fluxes (green line) with its associated errors in dotted green lines as a function of depth (cm).	159
Figure 3-A.4 Distribution maps of selected ostracod taxa relative abundances using the Arctic Ostracode Database 2020 (AOD2020; Cronin et al., 2021). Prior to the relative abundance calculations, we did a preliminary validation of the coordinates using GEBCO 2014 and IBCAO 2012 combined to ensure the points yielded below water level values. 47 points were discarded. Furthermore, we only kept the samples that comprised 10 counted ostracod shells or more to allow a minimum significance of the calculated assemblages. Out of the 1574 points, 1137 were left. The maps were developed using Ocean Data View (Schlitzer, 2018).	160
Figure 4.1 Modèle résumant la structure de la thèse	171

Figure 4.2 Extrait de la bande dessinée créée dans le cadre du projet *Stories about Climate* (Falardeau, J. et Ouellet-Bernier, en prép.). On y voit le personnage principal échantillonner une carotte de sédiment accompagné de nul autre que moi-même et d'autres membres de l'équipe. Gracieuseté de Mark-Antoine Thibodeau Breault..... 173

LISTE DES TABLEAUX

Tableau 0.1 Compilation des enregistrements paléoclimatiques et paléocénographiques du nord-ouest américain. AP signifie « avant le présent ».	8
Table 1.1 List of benthic foraminiferal species and genera. *=miliolids; **=polymorphinids.....	32
Table 1.2 List of ostracod species and genera. References: 1 Olausson (1982), 2 McDougall et al. (1986), 3 Stepanova et al. (2003), 4 Gemery et al. (2017), 5 Stepanova et al. (2019), 6 Tian et al. (2020), 7 Gemery et al. (2021).....	33
Table 1.3 List of other microfossils.....	34
Table 1.4 List of abbreviations used in the Figures 1.12 and 1.17.....	49
Table 2.1 List of the microfaunal taxa, the corresponding abbreviation names, and their ecological affinities when applicable. *Selected ecological indicators	86
Table 2.2 List of the environmental parameters and their corresponding abbreviation names.....	88
Table 3.1 ^{14}C ages on core PG2303 calibrated according to Marine20 with the CALIB 8.20 calibration program (Stuiver and Reimer, 1993) in consideration of a ΔR of 330 ± 41 years. The ^{14}C age in gray was not considered in the model. The ^{14}C ages with a laboratory sample ID starting with AWI and COL were measured at AWI MICADAS and at the University of Cologne, respectively.	117
Table 3.2 a) List of benthic foraminiferal and tintinnid taxa identified in the cores (x =present). b) List of ostracod taxa identified in the cores (x = present).....	120
Table 3.3 List of abreviations for foraminiferal and ostracod taxa in the Figs. 3.5 and 3.8.....	132

LISTE DES ABRÉVIATIONS, DES SIGLES ET DES ACRONYMES

	Français	Anglais ou expression latine
ACW	Eaux côtières de l'Alaska	<i>Alaskan Coastal Waters</i>
ALBSA	Dépression des Aléoutiennes – Anticyclone de la mer de Beaufort	<i>Aleutian Low – Beaufort Sea Anticyclone</i>
AMS	Accélérateur par spectrométrie de masse	<i>Accelerator Mass Spectrometry</i>
AO	Oscillation arctique	<i>Arctic Oscillation</i>
AOO	Oscillation de l'océan Arctique	<i>Arctic Ocean Oscillation</i>
AP	Avant le présent	
BP	Avant le présent	<i>Before present</i>
C	Carbone	<i>Carbon</i>
cal. year	Année calibrée	<i>Calibrated year</i>
C ₂ Cl ₄	Tétrachloroéthylène	<i>Tetrachlorethylene</i>
CE	Ère commune	<i>Common era</i>
cf.	Se reporter à	<i>Confer</i>
CFCS	Flux constant et sédimentation constante	<i>Constant Flux Constant Sedimentation</i>
CID	Carbone inorganique dissous	
CO ₂	Dioxyde de carbone	<i>Carbon dioxide</i>
C _{org}	Carbone organique	<i>Organic carbon</i>

CRS	Taux d'apport constant	<i>Constant Rate of Supply</i>
Cs	Césium	<i>Cesium</i>
CTD	Conductivité, température, profondeur	<i>Conductivity, Temperature, Depth</i>
E	Est	<i>East</i>
e.g.	Par exemple	<i>Exempli gratia</i>
<i>et al.</i>	Et autres	<i>Et alli</i>
Fe	Fer	<i>Iron</i>
H	Hydrogène	<i>Hydrogen</i>
HCl	Acide chlorydrique	<i>Hydrochloric acid</i>
HF	Acide fluorhydrique	<i>Hydrofluoric acid</i>
HNO ₃	Acide nitrique	<i>Nitric acid</i>
H ₂ O ₂	Peroxyde d'hydrogène	<i>Hydrogen peroxide</i>
i.e.	C'est-à-dire	<i>Id est</i>
IPCC	Groupe d'experts intergouvernemental sur l'évolution du climat	<i>Intergovernmental Panel on Climate Change</i>
LST	Tolérant à de faibles salinités	<i>Low Salinity Tolerant</i>
N	Nord ou Azote	<i>North or Nitrogen</i>
NPI	Indice du Pacifique Nord	<i>North Pacific Index</i>
O	Oxygène	<i>Oxygen</i>

p. ex.	Par exemple	
PC	Composante principale	<i>Principal Component</i>
PCA	Analyse des composantes principales	<i>Principal Component Analysis</i>
Pb	Plomb	<i>Lead</i>
Pb _{ex}	Plomb en excès	<i>Lead in excess</i>
Pb _{sup}	Plomb supporté	<i>Supported lead</i>
Pb _{tot}	Plomb total	<i>Total lead</i>
PDO	Oscillation décennale du Pacifique	<i>Pacific Decadal Oscillation</i>
Po	Polonium	
Ra	Radium	
RDA	Analyse de redondance	<i>Redundancy Analysis</i>
S	Sud	<i>South</i>
TOC	Carbone organique total	<i>Total organic carbon</i>
VPDB		<i>Vienna Pee Dee Belemnite</i>
vs.	Versus	
VSMOW		<i>Vienna Standard Mean Ocean Water</i>
W	Ouest	<i>West</i>

RÉSUMÉ

Le sud-est de la mer de Beaufort est marqué par des changements environnementaux importants dus au réchauffement atmosphérique récent. Les changements incluent la diminution de la couverture de glace de mer, une augmentation de l'intensité et de la durée des tempêtes, ainsi qu'une augmentation de l'érosion côtière. Leurs répercussions sur les écosystèmes de la zone littorale sont toutefois difficiles à évaluer, car les enregistrements des conditions marines (température, salinité, turbulence, etc.) et du biote (population, diversité et productivité) sont rares et souvent épisodiques. Des enregistrements continus et couvrant plusieurs décennies sont nécessaires pour évaluer la contribution du réchauffement anthropique sur les changements climatiques récents, *a fortiori* pour la zone littorale qui est sensible vis-à-vis des vents locaux et se caractérise par une grande variabilité. Par ailleurs, les effets des changements climatiques sur la zone littorale du sud-est de la mer de Beaufort peuvent influencer les membres des communautés locales qui y chassent et pêchent pour leur subsistance et pour préserver des traditions culturelles.

Dans ce contexte, cette thèse vise à reconstituer les conditions environnementales du milieu marin de la zone littorale du sud-est de la mer de Beaufort à partir d'une approche micropaléontologique. Des analyses sur les assemblages de foraminifères benthiques, d'ostracodes et de tintinnides, en plus de mesures des isotopes stables ($\delta^{18}\text{O}$ et $\delta^{13}\text{C}$) sur les tests des foraminifères benthiques *Elphidium clavatum* et *Cassidulina reniforme* ont été réalisées. Les microfossiles ont été analysés à partir de carottes de sédiment prélevées dans le bassin Herschel. Le bassin Herschel se situe à moins de 10 km au large de la côte nord du Yukon, Canada, dans un milieu où les apports de matériaux biogéniques et détritiques sont continus et leur taux d'accumulation rapide. Les carottes sédimentaires proviennent des sites YC18-HB-GC01 (69.544°N; 138.970°O; 18 m de profondeur) et PG2303 (69.513°N; 138.895°O; 32 m de profondeur).

Les carottes par gravité YC18-HB-GC01 (40 cm) et PG2303-1 (20 cm) couvrent de 1970 à 2018 CE et de 1998 à 2016 CE, respectivement, avec des vitesses de sédimentation de 0,7 à 1,7 cm·a⁻¹. Ces carottes courtes livrent ainsi des séries chronologiques avec une résolution temporelle quasi annuelle correspondant à la période de données environnementales, permettant ainsi une évaluation de la signification des indicateurs microfossiles. Les assemblages de foraminifères benthiques et d'ostracodes de la marge et du fond du bassin suggèrent que les assemblages répondent principalement aux variations de salinité et des courants profonds. Dans la carotte YC18-HB-GC01, les indicateurs d'une salinité faible et variable, d'eaux de fond turbulentes, d'apports terrigènes et de productivité marine augmentent vers la surface soit depuis 1994 ± 5 CE. Dans l'environnement, cette transition coïncide avec des vents d'est plus forts et des tempêtes plus fréquentes, une diminution de la concentration moyenne de glace de mer en été de 16% et une circulation anticyclonique dominante dans l'océan Arctique. De telles conditions peuvent accentuer le mélange vertical dans la colonne d'eau, accélérer la remise en suspension des particules, le taux d'érosion côtière, et entraîner la dispersion du panache de la rivière Mackenzie vers l'ouest jusqu'aux sites d'étude. Il s'agit de facteurs jouant un rôle important sur les apports terrigènes et l'instabilité du milieu. Les changements environnementaux des deux dernières décennies ont ainsi eu des conséquences directes sur l'habitat et la biodiversité de la zone littorale.

Les analyses micropaléontologiques des 324 premiers centimètres de la carotte à piston PG2303 qui couvrent de ~710 à 1998 CE révèlent que le réchauffement climatique en cours aurait débuté dès ~1800 CE, que ses effets se sont amplifiés à partir de 1950 CE et qu'ils atteignent des maximums après 1998 CE,

probablement en réponse au forçage anthropique. Les changements associés au 21^e siècle sont sans précédent à l'échelle des 1300 dernières années et se situent donc en dehors de la variabilité naturelle de l'environnement régional. Ces « nouvelles conditions climatiques » soulèvent des questions importantes notamment au sujet de l'augmentation de la turbidité des eaux côtières, qui obstrue la pénétration des rayons solaires et peut entraver la production primaire. De plus, la dégradation du carbone organique terrigène par les bactéries conduit à une désoxygénation des eaux qui affecte potentiellement déjà la productivité des ostracodes et pourrait toucher d'autres organismes vulnérables dans les milieux pauvres en oxygène dissous.

Mots-clés : Foraminifères benthiques, ostracodes, Arctique, glace de mer, salinité

ABSTRACT

Large scale environmental changes are occurring in the southeastern Beaufort Sea in response to recent atmospheric warming. They include reduced sea-ice cover, increased storm frequency and intensity, and increased coastal erosion. However, their impacts on nearshore ecosystems are difficult to evaluate because the records of variations in water mass conditions (temperature, salinity, turbulence, etc.) and biota (population, diversity, and productivity) are sparse and often cover too short observation intervals. Continuous and long-term records are essential to assess the contribution of anthropogenic warming on recent climate changes, especially for nearshore areas that are submitted to wind influence and are characterized by variable sea-surface conditions. Furthermore, the effects of climate change on the southeastern Beaufort Sea nearshore areas may influence the local community members who hunt and fish for subsistence and to preserve cultural traditions.

This thesis aims to reconstruct the marine conditions of the southeastern Beaufort Sea nearshore areas based on a micropaleontological approach. Analyses of benthic foraminiferal, ostracod, and tintinnid assemblages were combined with measurements of stable isotope ($\delta^{18}\text{O}$ and $\delta^{13}\text{C}$) in the tests of *Elphidium clavatum* and *Cassidulina reniforme* from sediment cores collected in the Herschel Basin. The Herschel Basin is located less than 10 km offshore the northern Yukon coastal plain, Canada, where the input of biogenic and detrital particles is continuous and results in high accumulation rates. Sediment cores are from sites YC18-HB-GC01 (69.544°N; 138.970°W; 18 m depth) and PG2303 (69.513°N; 138.895°W; 32 m depth).

The gravity cores YC18-HB-GC01 (40 cm) and PG2303-1 (20 cm) span 1970 to 2018 CE and 1998 to 2016 CE, respectively, with sedimentation rates ranging from 0.7 to 1.7 cm·a⁻¹. These two short cores permitted analyses with a nearly annual resolution over the instrumental period, making the comparison of micropaleontological indicators and environmental parameters possible. The benthic foraminiferal and ostracod assemblages at the margin and at the bottom of the basin suggest a response mainly driven by salinity variations and deep current dynamics. The data from core YC18-HB-GC01 indicate more variable and lower salinity, more turbulent bottom waters, high terrestrial inputs, and productivity increase since 1994 ± 5 CE. This transition coincides with stronger easterly winds and frequent storms, a 16% decrease in mean summer sea-ice concentration, and a strong anticyclonic circulation in the Arctic Ocean. Together, these parameters may contribute to enhancing vertical mixing and resuspension, to an acceleration of coastal erosion, and to triggering the westward spreading of the Mackenzie River plume to the study sites. Hence, they play an important role in terrestrial inputs and environmental instability, with consequences on the nearshore habitat and biodiversity.

Micropaleontological analyses of the upper 324 cm in the piston core PG2303 that span ~710 to 1998 CE reveal that the impacts of the ongoing climate warming started as early as ~1800 CE, with an increase after 1950 CE to reach maximum values after 1998 CE, likely in response to anthropogenic forcing. The impacts recorded in the microfauna in sediments of the 21st century are unprecedented at the scale of the last 1300 years and therefore exceed those of the natural variability. These "new climatic conditions" raise important questions about the impacts of increased turbidity in coastal waters, as turbidity impedes the penetration of solar radiation and reduces primary production. In addition, the microbial degradation of terrestrial organic carbon leads to high oxygen consumption that has potentially diminished already the ostracod productivity and may affect other organisms vulnerable in oxygen-poor environments.

Keywords: Benthic foraminifera, ostracods, Arctic, sea ice, salinity

INTRODUCTION

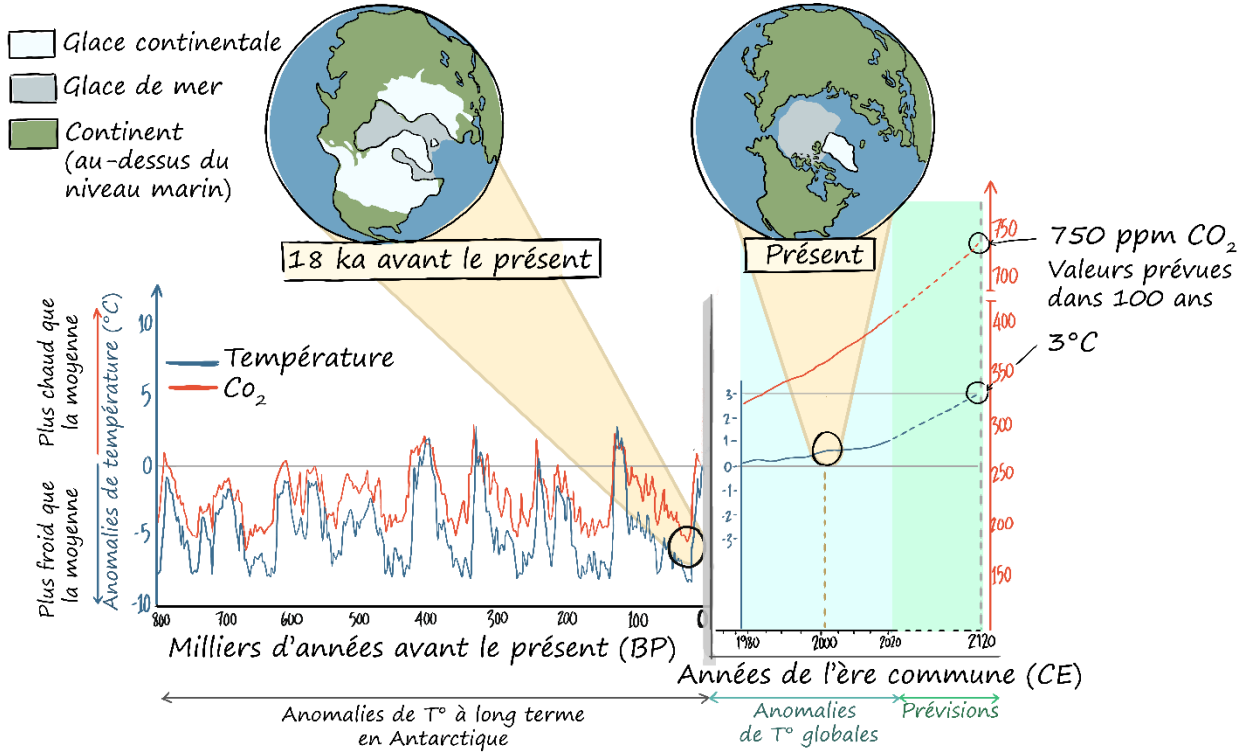
0.1 La dynamique climatique terrestre

Les océans, l'atmosphère et le couvert de glace font partie des variables déterminantes qui régulent la dynamique complexe du climat terrestre global. En effet, chacune des variables qui le composent dépend de forçages, d'interactions et de rétroactions. La paléoclimatologie aide à analyser le climat terrestre en documentant l'effet de certaines de ses composantes à travers le temps. Les reconstitutions des conditions climatiques passées, sur de plus ou moins longues échelles temporelles, permettent de mieux discerner les causes et effets des variations climatiques. Il a été mis en évidence qu'au cours des 800 000 dernières années, le climat a varié selon des cycles d'environ 100 000 ans, passant d'intervalles glaciaires à interglaciaires (Figure 0.1; Clark *et al.*, 1999; Jouzel *et al.*, 2007). L'alternance de périodes froides et chaudes serait liée aux changements des paramètres de l'orbite terrestre (Jouzel *et al.*, 2007; Lisiecki, 2010), soit aux cycles de Milankovitch (Milankovitch, 1941), car ils déterminent la quantité et la répartition de rayonnement solaire. Le rayonnement solaire est un forçage dont l'effet est amplifié par des mécanismes telles l'émission et l'absorption de dioxyde de carbone (CO_2) atmosphérique (Shackleton, 2000). En effet, le CO_2 atmosphérique est un gaz à effet de serre jouant un rôle majeur sur le climat (Figure 0.1; Royer, 2006; Tripati *et al.*, 2009) dont l'augmentation récente liée aux activités anthropiques rend compte d'un réchauffement notable (IPCC, 2021; Notz et Stroeve, 2016). Le CO_2 a atteint des concentrations qui n'ont jamais été égalées dans les dernières centaines de milliers d'années, voire de millions d'années (Figure 0.1; Bereiter *et al.*, 2015) et l'augmentation de la concentration du CO_2 atmosphérique anthropique déroute la planète de la trajectoire de son cycle climatique naturel (Figure 0.1).

0.2 L'Arctique en plein changement

L'Arctique s'est réchauffé quatre fois plus vite que la moyenne globale au cours des deux dernières décennies (Rantanen *et al.*, 2022) en raison du phénomène d'amplification polaire qui résulte de rétroactions positives liées à la réduction de la glace de mer. De 1979 à 2018 CE, le couvert de glace de mer en septembre a diminué de 12.8% par décennie dans l'océan Arctique (IPCC, 2021; Meier et Stroeve, 2022) contribuant de façon notable au phénomène d'amplification, car la diminution d'albédo causée par la fonte de la glace augmente l'accumulation de chaleur à la surface de l'océan (Serreze et Barry, 2011).

Figure 0.1 Schéma des anomalies de température de l'air (Jouzel *et al.*, 2007) et de concentrations de CO₂ atmosphérique (Bereiter *et al.*, 2015) en Antarctique au cours des 800 000 dernières années et au cours de l'intervalle 1980-2000 CE basé sur des données instrumentales (Global Climate Change: Evidence, 2021; Global Monitoring Laboratory, 2021), ainsi que les prévisions pour les 100 prochaines années (RCP6.5; IPCC, 2014). Gracieuseté d'Alison McCreesh.



0.2.1 Les écosystèmes des marges continentales arctiques

Les effets du réchauffement atmosphérique et de la diminution de la glace de mer qui s'en suit engendrent des modifications rapides dans les habitats marins de l'Arctique. Les modifications sont notamment perceptibles sur la zone littorale en raison de l'érosion accrue des côtes. En effet, les rivages de l'océan Arctique consistent principalement de pergélisol (Lantuit *et al.*, 2012) qui peut être riche en glace atteignant jusqu'à ~47% dans la plaine côtière nordique du Yukon, Canada, par exemple (Couture et Pollard, 2017). Les rivages sont donc très sensibles non seulement à la hausse de la température, mais aussi à l'action des vagues et des marées lorsqu'elles ne sont pas protégées par la glace de mer (Günther *et al.*, 2015; Overeem *et al.*, 2011). L'érosion côtière génère une augmentation des émissions de CO₂ par dégradation du sol organique (Tanski *et al.*, 2021), des apports terrigènes et de carbone organique (C_{org}; Jong *et al.*, 2020), ainsi que des eaux côtières troubles (Klein *et al.*, 2019) et leurs conséquences sur les écosystèmes littoraux arctiques restent peu connues jusqu'à présent (Fritz *et al.*, 2017). De plus, avec des

saisons libres de glace de mer de plus en plus longues, la durée et la fréquence des tempêtes s'intensifient (Mioduszewski *et al.*, 2018), ce qui exacerbe le phénomène d'érosion. La sensibilité des côtes à l'érosion pourrait doubler d'ici la fin de ce siècle (Nielsen *et al.*, 2022).

Lorsque les eaux sont libres de glace de mer, les vents exercent également un rôle plus important sur la vitesse de dispersion des panaches de rivières (Mulligan *et al.*, 2010) et sur les mélanges verticaux dans les zones peu profondes (Hill et Nadeau, 1989; Klein *et al.*, 2019; Rainville et Woodgate, 2009). Par conséquent, le transport vertical et horizontal d'eau douce, de nutriments et de particules en suspension devient de plus en plus variable dans le temps et l'espace (Ehn *et al.*, 2019; Klein *et al.*, 2019; Mulligan et Perrie, 2019). Le C_{org} terrigène libéré par une augmentation de l'érosion côtière, de la remise en suspension des particules et des panaches de rivières serait une source de nourriture suffisante pour soutenir le réseau trophique marin (Bell *et al.*, 2016; Dunton *et al.*, 2006; Terhaar *et al.*, 2021). Toutefois, une augmentation de l'érosion peut être à l'origine d'eaux turbides. Des eaux turbides peuvent obstruer la pénétration des rayons solaires dans la colonne d'eau et ainsi nuire à la production primaire (Bonsell et Dunton, 2016; Lewis *et al.*, 2020; Retamal *et al.*, 2008), en plus de causer l'acidification et la désoxygénéation des eaux par la dégradation microbienne du C_{org} terrigène qu'elles contiennent (Mathis *et al.*, 2007; Semiletov *et al.*, 2016). Une transition vers une diète basée sur le C_{org} terrigène peut également modifier la population de zooplanctons et donc affecter les niveaux trophiques supérieurs (Bell *et al.*, 2016; Comeau *et al.*, 2011).

Un autre effet du réchauffement climatique est l'adoucissement de la couche d'eaux superficielles par la fonte de glace de mer et les apports d'eau fluviale qui accentuent la stratification dans la colonne d'eau. Une couche superficielle dessalée et peu dense peut entraver la remontée (*upwelling*) de masses d'eaux de subsurface riches en nutriments vers la surface ou entraîner les nutriments sous la zone photique (Blais *et al.*, 2017; McLaughlin et Carmack, 2010; Retamal *et al.*, 2008). Jusqu'à présent, une diminution de la glace de mer a entraîné un bilan positif pour la productivité primaire, la base de la chaîne alimentaire, à l'échelle de l'océan Arctique, grâce à une saison libre de glace plus longue et plus étendue. Cependant, l'accès aux nutriments est fondamental pour le développement du phytoplancton (Bélanger *et al.*, 2013; Arrigo et van Dijken, 2015; Lewis *et al.*, 2020).

En bref, une gamme de modifications sur l'habitat du littoral arctique est possible en réponse au réchauffement climatique. Ces effets touchent aussi le réseau trophique marin et donc peuvent influer sur

les communautés locales qui pratiquent la chasse et la pêche pour leur subsistance et pour préserver les traditions culturelles (Brewster *et al.*, 2016; Falardeau, M. *et al.*, 2022; Fechhelm *et al.*, 2007). Les effets des changements climatiques sur ceux et celles qui occupent les zones côtières arctiques englobent également la perte de territoires traditionnels et d'héritages (Irrgang *et al.*, 2019) due à l'érosion côtière et la perte de mobilité avec la diminution du couvert neigeux et de glace de mer (Ford *et al.*, 2019).

0.3 Motivation de la thèse

Les membres des communautés du nord-ouest du Canada, dans la région désignée des Inuvialuit, pêchent dans la zone littorale du sud-est de la mer de Beaufort depuis des centaines d'années (Usher, 2002). Pêcheurs et pêcheuses ont remarqué des changements dans les populations de poissons (Brewster *et al.*, 2016; Papik *et al.*, 2003), ainsi qu'une dénaturation de la couleur et de la consistance de la chair des ressources halieutiques (Andrachuk et Pearce, 2010; Brewster *et al.*, 2016). Les populations de poisson d'une des espèces favorites, le Dolly Varden (*Salvelinus malma malma*), diminuent depuis 2018, atteignant des niveaux sous la moyenne de 2007-2014 CE. Pourtant, des stocks relativement élevés avaient été dénombrés au cours de la période 2015-2017 CE (Colin Gallagher, conversation personnelle) et la surpêche ne peut expliquer de telles variations. L'augmentation de la turbidité de l'eau le long du littoral et dans les rivières diminue également le succès des pêches, en plus d'abîmer et de souiller les filets (Choudhury et Dick, 1997; Scharffenberg *et al.*, 2019; West Side Working Group, conversation personnelle).

Selon des pêcheur.euse.s de Shingle Point (Figure 0.2), les changements observés dans les ressources halieutiques sont en partie associés à l'habitat marin, en particulier en raison d'eaux de surface plus chaudes et douces (Brewster *et al.*, 2016; Scharffenberg *et al.*, 2020). Quelques études récentes soulignent d'ailleurs l'importance des conditions de l'habitat marin sur la distribution, l'abondance et la qualité des ressources halieutiques. La direction et la puissance des vents dominants, la couverture de glace de mer et la température et la salinité des eaux de fond seraient des facteurs déterminants (Gallagher *et al.*, 2021; George *et al.*, 2015; Lin *et al.*, 2016; Logerwell *et al.*, 2018; Scharffenberg *et al.*, 2020). Des enregistrements des conditions biotiques et abiotiques de la zone littorale du nord du Yukon restent toutefois assez fragmentaires et très ponctuels dans le temps et l'espace. Ils ne permettent guère de dissocier les effets qui découlent du réchauffement climatique récent de ceux liés aux variations naturelles de l'environnement. Pour ce faire, des enregistrements continus et couvrant de longs intervalles de temps sont nécessaires. Qui plus est, peu d'approches méthodologiques permettent de retracer les paramètres telles la température et la salinité en surface et en profondeur dans les masses d'eau.

La majorité des enregistrements environnementaux sont basés sur des données instrumentales et satellitaires ou sur des mesures *in situ*. Les données instrumentales, comme le vent, la température de l'air ou les débits de rivières s'étendent au mieux de 1973 à 2018 CE dans les stations météorologiques et hydrométriques environnantes (Figure 0.3; Environnement et changement climatique Canada, 2020). De façon similaire, les données satellitaires sont disponibles depuis environ 1978 CE pour la glace de mer (p. ex., Meier et al., 2017), et plus récemment depuis ~2000 CE pour d'autres paramètres tels que l'indice de chl-*a* (aqua/MODIS), indicateur de productivité primaire. Les données de vitesse et direction des courants marins, ainsi que de température et de salinité sont issues de mouillages, mais ils couvrent quelques années tout au plus (p. ex., Lin et al., 2020; Lin et al., 2016; Rainville et Woodgate, 2009; Schulze et Pickart, 2012).

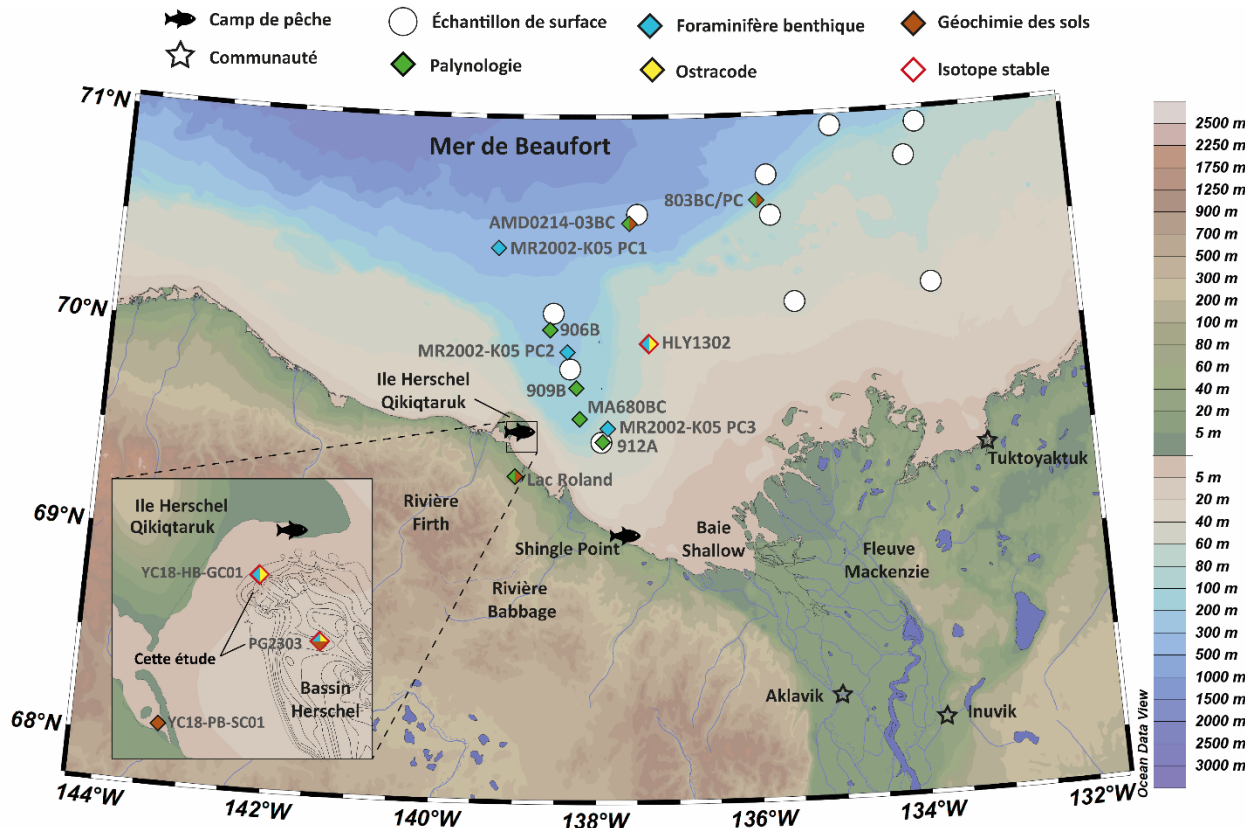
Au même titre que la paléoclimatologie, la paléocéanographie peut s'avérer un outil pertinent pour produire des enregistrements environnementaux continus de longue durée, permettant ainsi de combler des lacunes. Des approches telles que la sclérochronologie sur les otolithes de poisson (Hart et al., 2015, Morrison, 2017), le varech (Bonsell et Dunton, 2018) et les dents de phoques (Nguyen et al., 2017) dans la mer de Beaufort ou encore sur les bivalves (Olivier et al., 2020; Poitevin et al., 2019) et les coraux (Davin, 2019) dans d'autres régions marines polaires, peuvent s'avérer utiles, mais elles ne sont pas univoques et ne permettent pas de couvrir plus de quelques décennies. Cette thèse se base plutôt sur une approche micropaléontologique. L'analyse du contenu en microfossiles des archives sédimentaires le long des marges continentales arctiques permet de reconstituer les conditions marines de centaines à des milliers d'années. Parmi les paramètres que les traceurs micropaléontologiques permettent de reconstituer, on compte la couverture de glace de mer, la température, la salinité et les apports nutritifs, en plus de la diversité des espèces, et la productivité primaire ou hétérotrophe (p. ex., Allan et al., 2021; Gemery et al., 2013; Heikkilä et al., 2022; Seidenkrantz et al., 2013;).

0.4 Compilation des enregistrements paléoclimatiques dans le nord-ouest américain

Plusieurs carottes sédimentaires ont été récoltées et analysées dans la zone d'intérêt (Tableau 0.1; Figure 0.2), afin de reconstituer les conditions marines du sud-est de la mer de Beaufort. Les reconstitutions se concentrent surtout dans la dépression du Mackenzie et le talus continental (Figure 0.2), car les carottes proviennent de sites plus profonds et donc plus faciles d'accès pour les navires de recherche où il est par ailleurs possible de récupérer des sédiments anciens, couvrant de longues périodes (> 3 ka; Tableau 0.1). Plusieurs échantillons de sédiments de surface ont été prélevés pour documenter la diversité des

foraminifères benthiques (Figure 0.2; Scott *et al.*, 2008; voir la section 0.7.1), mais il n'y a que trois sites qui présentent une reconstitution temporelle à partir de l'analyse des microfossiles sur le plateau continental (Tableau 0.1; Gemery *et al.*, 2023, Richerol *et al.*, 2008; Schell *et al.*, 2008; Seidenstein *et al.*, 2018). Les enregistrements paléoécologiques sont rares près des côtes à l'échelle de l'Arctique (Heikkilä *et al.*, 2022).

Figure 0.2: Carte des sites d'enregistrements paléoclimatiques et paléocéanographiques de la région d'étude avec un gros plan sur le bassin Herschel au bas à gauche.



0.4.1 Enregistrements marins

Des intervalles marqués par des climats différents ont été identifiés au cours des mille dernières années à partir d'enregistrements paléocéanographiques. L'intervalle de 800 à 1200-1500 CE serait marqué par un climat doux, principalement caractérisé par une longue saison libre de glace, favorisant la dispersion du panache de la rivière Mackenzie et favorisant la productivité primaire en marge de la glace de mer (Gemery *et al.*, 2023; Kutos *et al.*, 2021; Seidenstein *et al.*, 2018). Il est suivi d'un refroidissement entre 1500 et

1850 CE associé à des eaux de surface et subsurface plus froides, une augmentation de la couverture de glace de mer et par une augmentation des eaux de fonte en été (Bringué et Rochon, 2012; Gemery *et al.*, 2023; Kutos *et al.*, 2021; Seidenstein *et al.*, 2018). La majorité des auteurs associent cet intervalle au petit âge glaciaire (1400-1700 CE; Mann *et al.*, 2009). Finalement, une tendance vers un réchauffement climatique s'amorce vers 1850-1900 CE (Bringué et Rochon, 2012; Gemery *et al.*, 2023), bien que certaines études proposent une augmentation de la couverture de glace de mer (Bringué et Rochon, 2012; Schell *et al.*, 2008; Scott *et al.*, 2009). Il est important d'ajouter qu'il existe potentiellement un décalage du signal de la côte vers le large et un réchauffement « moderne » pourrait avoir eu lieu aussi tôt que 1630 CE dans la carotte 912A, alors qu'enregistré à 1920 CE dans la carotte 906B (Fig. 0.2; Richerol *et al.*, 2008). Les changements reconstitués des dernières décennies ne se distinguent toutefois pas ou peu de l'amplitude des variations du dernier millénaire et donc de la variabilité naturelle du milieu (Durantou *et al.*, 2012; Gemery *et al.*, 2023; Richerol *et al.*, 2008). Une faible résolution temporelle des analyses ou des problèmes de préservation peuvent limiter l'identification de changements récents (> 2000 CE; Tableau 0.1; p. ex., Kutos *et al.*, 2021; Schell *et al.*, 2008; Scott *et al.*, 2009; Seidenstein *et al.*, 2018).

0.4.2 Enregistrements terrestres

Une compilation d'enregistrements terrestres d'Alaska est disponible pour les 2 derniers milliers d'années (Nicolle *et al.*, 2018). Elle illustre des oscillations climatiques en milieu terrestre qui s'apparentent à celles du milieu marin, c'est-à-dire une période avec un climat plus doux de 600 à 1250 CE, une période froide de 1250 à 1800 CE et un réchauffement de ~1800 CE jusqu'à l'actuel (Nicolle *et al.*, 2018). Un réchauffement récent est identifié à partir de 1900 CE dans des enregistrements dendrochronologiques et limnologiques (Anchukaitis *et al.*, 2013; Bird *et al.*, 2009; Porter *et al.*, 2013; Wolter *et al.*, 2017). Abram *et al.* (2016) notent également un réchauffement à partir de 1820 CE qui s'amplifie après 1930 CE pour toute la région arctique. Dans les dernières décennies, l'accélération continue du réchauffement en raison des effets anthropiques a mené à des reconstitutions des températures de l'air en milieu terrestre plus élevées que celles des derniers siècles (Abram *et al.*, 2016; Anchukaitis *et al.*, 2013; Nicolle *et al.*, 2018; Porter *et al.*, 2013).

0.4.3 Le bassin Herschel

Dans la zone littorale, à quelques kilomètres de la côte et du site de pêche de l'île Herschel – Qikiqtaruk, se trouve le bassin Herschel (Figures 0.2 et 0.3; Mackay, 1959). Une carotte de 12 m de longueur prélevée

dans le bassin permet d'estimer des vitesses de sédimentation moyennes de 0.33 cm an⁻¹ sur les 4000 dernières années (Grotheer *et al.*, 2020), ce qui équivaut à une capacité d'analyse pluriannuelle pour un sous-échantillonnage de la carotte aux centimètres. Les analyses de sédiments dans le bassin Herschel se concentrent jusqu'à présent surtout sur le cycle du carbone (Grotheer *et al.*, 2020; Jong *et al.*, 2021 Tanski *et al.*, en prép.), mais aucune reconstitution climatique n'a été présentée à ce jour.

Tableau 0.1 Compilation des enregistrements paléoclimatiques et paléocénographiques du nord-ouest américain. AP signifie « avant le présent ».

Zone	Référence	Méthodes	Site	Profon-deur	Latitude	Longitude	Couverture temporelle approximative	Résolution temporelle approximative	Note
Talus continental	Kutos <i>et al.</i> , 2021	Palyntologie Géochimie des sédiments	AMD0214-03BC	1048 m	70.550°N	137.533°O	3 ka AP	Décennale à séculaire	Préservation altérée dans les derniers 50 ans
	Bringué et Rochon, 2012	Palyntologie Géochimie des sédiments	803 BC	218 m	70.636°N	135.917°O	1750 à 2000 CE	Décennale	
	Bringué et Rochon, 2012	Palyntologie Géochimie des sédiments	803 PC	218 m	70.632°N	135.880°O	4.5 à 0.5 ka AP	Multidécennale	
	Durantou <i>et al.</i> , 2012	Palyntologie	MA680BC	125 m	69.604°N	138.226°O	1850 à 2000 CE	Pluriannuelle	
	Richerol <i>et al.</i> , 2008	Palyntologie	2004-804-912A	54 m	69.487°N	137.940°O	1400 à 2000 CE	Pluriannuelle	
	Richerol <i>et al.</i> , 2008	Palyntologie	2004-804-909B	169 m	69.752°N	138.2716°O	1800-2000 CE	Pluriannuelle à multidécennale	Peu d'âges ¹⁴ C
	Richerol <i>et al.</i> , 2008	Palyntologie	2004-804-906B	272 m	70.019°N	138.596°O	1900-2000 CE	Multidécennale	Peu d'âges ¹⁴ C
	Scott <i>et al.</i> , 2009	Foraminifère benthique	BC750	1087 m	71.20°N	134.08°O	~1.5 ka AP	Décennale à multidécennale	
	Scott <i>et al.</i> , 2009	Foraminifère benthique	PC750	1087 m	71.20°N	134.06°O	4.5 ka AP	Multidécennale à milléniale	
	Schell <i>et al.</i> , 2008	Foraminifère benthique	MR2002-K05 PC1	671 m	70.401°N	139.307°O	11.5 ka AP	Pluriannuelle à séculaire	
	Schell <i>et al.</i> , 2008	Foraminifère benthique	MR2002-K05 PC2	223 m	69.925°N	138.384°O	8 ka AP	Multidécennale à pluriséculaire	
Terrestre	Wolter <i>et al.</i> , 2017	Palyntologie (grains de pollen) Géochimie des sédiments	Lac Roland	3 m	69.328°N	139.027°O	1730 à 2010 CE	Pluriannuelle à décennale	
	Bird <i>et al.</i> , 2009	Varve	Lac Blue	4 m	68.086°N	150.465°O	2 ka AP	Annuelle	

Plateau continental/zones littorale	Gemery et al., 2023; Seidenstein et al., 2018	Foraminifère benthique Ostracode	HLY1302-JPC-32	60 m	69.974°N	137.239°O	3 à 1.5 ka AP	Multidécennale
	Gemery et al., 2023	Isotope stable						
	Gemery et al., 2023; Seidenstein et al., 2018	Foraminifère benthique Ostracode	HLY1302-GGC-30	60 m	69.974°N	137.242°O	550 -1945 CE	Multidécennale
	Gemery et al., 2023	Isotope stable						
	Gemery et al., 2023; Seidenstein et al., 2018	Foraminifère benthique Ostracode	HLY1302-MC-29	60 m	69.975°N	137.242°O	1600-2000 CE	Décennale à multidécennale
	Gemery et al., 2023	Isotope stable						
	Schell et al., 2008	Foraminifère benthique	MR2002-K05 PC3	57.5 m	69.561°N	137.8721°O	7 ka AP	Multidécennal à pluricentennale
	Richerol et al., 2008	Palynologie	2004-804-912A	54 m	69.487°N	137.9405°O	1400-2000 CE	Pluriannuelle à multidécennale
	Tanski et al., en prép.	Géochimie des sédiments	YC18-PB-SC01	3 m	69.482°N	139.085°O	1943-2018 CE	Annuelle à pluriannuelle
	Grotheer et al., 2020	Géochimie des sédiments	PG2303-1	32 m	69.513°N	138.895°O	4 ka AP	Multidécennale à pluricentennale
Cette étude	Foraminifère benthique (Chap. 1)	Ostracode (Chap. 1)	YC18-HB-GC01	18 m	69.544°N	138.970°O	1970-2018 CE	Annuelle à pluriannuelle
	Isotope stable (Chap. 2)							
Cette étude	Foraminifère benthique (Chap. 1)	Ostracode (Chap. 1)	PG2303-1	32 m	69.513°N	138.895°O	2000-2016 CE	Annuelle
	Isotope stable (Chap. 3)							
Cette étude	Foraminifère benthique (Chap. 3)	Ostracode (Chap. 3)	PG2303	32 m	69.513°N	138.895°O	700-1998 CE	Décennale à multidécennale
	Isotope stable (Chap. 3)							

0.5 Objectifs et hypothèses

À partir des enregistrements marins et terrestres disponibles dans la littérature, il est intéressant de noter que la région a subi des changements climatiques avec des intervalles plus chauds à plus froids, au cours des mille dernières années (voir la section précédente). Ces changements, d'amplitude et de durée

différentes, ont probablement eu des répercussions sur l'habitat littoral du sud-est de la mer de Beaufort, et donc potentiellement sur les ressources halieutiques. Toutefois, tous les sites étudiés jusqu'à présent sont relativement loin des côtes (> 30 km) et à l'extérieur des zones de pêche. Ces sites se retrouvent donc non seulement à distance des enjeux physiques spécifiques aux zones littorales comme la dynamique de la banquise, l'érosion côtière et les apports fluviatiles et terrestres, mais aussi à distance des enjeux sociaux. Il est d'autant plus urgent de se pencher sur la question, car les zones côtières répondent potentiellement de façons différentes aux forçages climatiques (par ex., Richerol *et al.*, 2008). Finalement, le réchauffement anthropique des dernières décennies a des répercussions indéniables sur la glace de mer (Fetterer *et al.*, 2017; Kinnard *et al.*, 2011) et la température de l'air (IPCC, 2021; Mann, 2007). Bien que visibles dans les reconstitutions dendrochronologiques (Anchukaitis *et al.*, 2013; Porter *et al.*, 2013), les effets du réchauffement récent dans le milieu marin ne semblent pas univoques (p. ex., Durandou *et al.*, 2012; Gemery *et al.*, 2023). Ceci peut s'expliquer par la distance des sites étudiés par rapport à la côte, une résolution temporelle d'analyse insuffisante, ou encore à des lacunes sédimentologiques ou des traceurs peu sensibles.

Dans ce contexte, l'objectif principal de cette thèse est de mieux circonscrire les effets des changements climatiques dans la zone littorale du sud-est de la mer de Beaufort à partir d'une approche micropaléontologique. Dans l'optique où le bassin Herschel peut offrir des enregistrements sédimentaires adéquats, c'est-à-dire continus, avec une résolution temporelle suffisante pour capter les variations des dernières décennies et de les distinguer de celles des derniers millénaires, les objectifs spécifiques de cette étude sont :

- 1) D'évaluer la portée de l'utilisation de l'approche micropaléontologique dans le bassin Herschel et de développer/valider des indicateurs écologiques;
- 2) D'identifier les principaux effets des changements climatiques récents sur l'écosystème de la zone littorale du sud-est de la mer de Beaufort;
- 3) De déterminer l'amplitude des effets des changements climatiques récents par rapport à la variabilité naturelle du milieu.

Comme le couvert de glace de mer des deux dernières décennies est le plus faible jamais enregistré et mesuré des mille dernières années (Fetterer *et al.*, 2017; Kinnard *et al.*, 2011), nous pouvons supposer que

les conséquences sur les microorganismes de l'écosystème littoral seront d'une ampleur équivalente, surtout dans la mesure où la glace de mer joue un rôle primordial sur l'impact des tempêtes et l'érosion des côtes (Günther *et al.*, 2015; Mioduszewski *et al.*, 2018), et donc sur les apports terrigènes et la perturbation dans ce milieu peu profond (Hill et Nadeau, 1989; Klein *et al.*, 2019). La débâcle précoce et une diminution de la glace de mer favorisent la productivité primaire (Arrigo et van Dijken, 2015), les apports nutritifs vers le benthos (Grebmeier et Barry, 2007), ainsi que la reproduction et la condition physique des ressources halieutiques (Falardeau, M. *et al.*, 2022; George *et al.*, 2015; Nguyen *et al.*, 2017). Des effets positifs similaires sur la productivité des microorganismes sont donc envisageables.

Toutefois, si l'on tient compte de l'augmentation des particules en suspension dans les eaux littorales et de la dégradation du C_{org} qui découlent de l'augmentation des tempêtes, de l'érosion des côtes, et de la dispersion des eaux fluviales, une diminution de la production primaire (Bonsell et Dunton, 2018; Retamal *et al.*, 2008) et de la concentration en oxygène dissout (Mathis *et al.*, 2007) sont à prévoir. De plus, une diminution de la glace de mer implique l'altération du couplage entre le benthos et la glace de mer et donc une altération de l'approvisionnement des organismes benthiques en carbone sympathique, une source de nourriture de haute qualité dont ils dépendent (Kohlbach *et al.*, 2019; Yunda-Guarin *et al.*, 2020). Une diminution de la taille moyenne du phytoplancton due à l'adoucissement des eaux de surface arctiques (Li, W. K. W. *et al.*, 2009) et une augmentation de la consommation phytoplanctonique par le zooplancton en réponse au réchauffement des eaux de surface et à la migration d'espèces de zooplancton vers le nord (Grebmeier, 2012) minimisent également les apports nutritifs en profondeur. Pour ces raisons, nous anticipons que le bilan des effets du réchauffement anthropique sera globalement négatif sur la productivité des microorganismes benthiques étudiés et que, par ailleurs, les enregistrements paléooceanographiques s'avéreront un outil utile pour retracer les effets du changement climatique sans précédent des dernières décennies.

0.6 Le plateau continental de la mer de Beaufort : physiographie et hydrographie

Le plateau continental de la mer de Beaufort est bordé par l'île Herschel – Qikiqtaruk à l'est et par la baie Shallow, l'une des deux embouchures de la rivière Mackenzie, à l'ouest (Figure 0.3). Le plateau s'étend donc sur ~530 km et a une largeur d'environ 120 km. Le bassin Herschel se situe à moins de 10 km de l'est de l'île Herschel – Qikiqtaruk et du nord de la côte nord du Yukon, Canada (Figure 0.3). L'île et le bassin Herschel se seraient formés lors de l'emplacement d'une faille géologique datant d'il y a environ 30 000

ans (Mackay, 1959). Le bassin a une grandeur de 40 par 15 km et une profondeur maximale de 70 m (EBA Engineering Consultants Ltd, 1992).

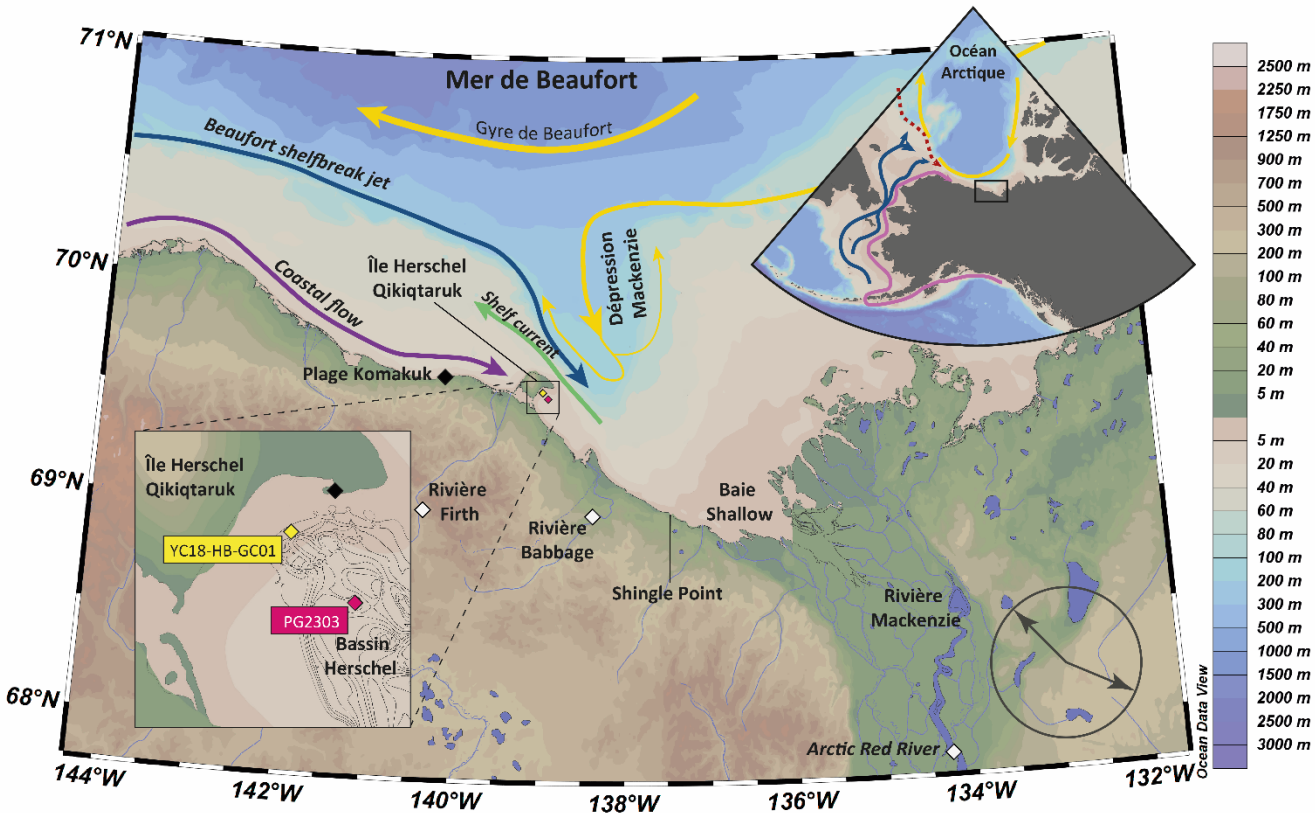
Les sédiments qui s'accumulent dans le bassin Herschel sont principalement d'origine terrigène, résultant en grande partie de l'érosion des côtes environnantes et sans doute d'apports de la rivière Mackenzie (Grotheer *et al.*, 2020). La rivière Mackenzie décharge le plus grand volume d'eau fluviale dans la région (Données hydrométriques historiques d'Environnement et ressources naturelles Canada, 2020) et détient la quatrième position de l'océan Arctique ($316 \text{ km}^3 \cdot \text{a}^{-1}$ pour 1999-2008 CE; Holmes *et al.*, 2012). Son panache se déploie à des centaines de kilomètres, particulièrement lors de la crue survenant en mai-juin, mais aussi sous l'effet des vents en été (Juhls, 2021; Wood *et al.*, 2015). Les rivières Firth et Babbage (Figure 0.3), et autres tributaires peuvent contribuer aux apports terrigènes à échelle plus locale (p. ex., Speetjens *et al.*, 2022; Tanski *et al.*, en prép.).

Les eaux sont stratifiées en été en raison d'apports d'eau douce issus de la fonte de la glace de mer et des rivières qui forment une couche de surface de faible salinité (21-22 psu), et donc de faible densité, qui se réchauffe en été pour atteindre des températures de 8-9°C (Figure 0.4). La halocline sépare la couche de surface de la couche profonde constituée d'eaux plus froides ($< 0^\circ\text{C}$) et plus salées (31-32 psu) et se situe environ entre 7 et 12 m de profondeur (Figure 0.4; Carmack et Macdonald, 2002; Mulligan *et al.*, 2010). La couche profonde est formée d'un mélange entre les eaux de subsurface qui circulent le long du talus continental et remontent sur le plateau continental par des remontées d'eau de fond et les eaux très froides et salées des saumures qui sont expulsées lors de la formation de la glace de mer (Williams et Carmack, 2012). À l'approche de l'hiver, les eaux s'homogénéisent verticalement et atteignent des valeurs uniformes de la couche profonde à la surface. Le bassin Herschel est couvert de glace de mer, soit d'une banquise, d'octobre jusqu'à la débâcle en juin (Carmack et Macdonald, 2002).

Les vents dominants proviennent soit de l'est ou du nord-ouest (Radosavljevic *et al.*, 2016; Figure 0.3) donnant lieu à des conditions environnementales distinctes. En effet, sous vents d'est, le panache de la rivière Mackenzie est étendu, la glace de mer diverge de la côte vers le large, et s'amincit (Frey *et al.*, 2015; Wood *et al.*, 2013) et les remontées d'eaux profondes et riches en nutriments sont favorisées (Pickart, 2004; Pickart *et al.*, 2011), pouvant mener à des floraisons phytoplanctoniques (Pickart *et al.*, 2013; Tremblay *et al.*, 2011). Inversement, les vents d'ouest restreignent le panache et maintiennent la glace de mer près de la côte. Ces deux scénarios sont illustrés à la Figure 0.5. Les conditions de la marge

continentale de la mer de Beaufort, incluant les courants marins (Kulikov *et al.*, 1998; Lin *et al.*, 2020), sont donc très variables au cours d'une même saison et d'une année à l'autre, en grande partie en raison de ses liens étroits avec la direction et l'intensité des vents.

Figure 0.3 Carte des courants marins et de la localisation des sites d'étude. Les stations hydrométriques et météorologiques sont représentées par des losanges blancs et noirs, respectivement. Un gros plan du bassin Herschel et des sites est illustré au bas à gauche et la direction des vents dominants est présentée au bas à droite de la figure par les flèches grises.



0.6.1 Les courants marins

Les masses d'eaux provenant de l'océan Pacifique, légèrement salées (~ 31 psu) et riches en nutriments, circulent généralement vers l'est le long du talus continental via le *Beaufort Sea shelfbreak current* (flèche bleue; Figure 0.3; Pickart, 2004). Elles se superposent aux eaux plus chaudes et plus salées d'origine atlantique (flèche pointillée rouge; Figure 0.3; Lin *et al.*, 2020). Circulant également vers l'est, des eaux relativement chaudes et peu salées, formées d'un mélange entre les eaux météoritiques et les eaux côtières de l'Alaska (flèche rose), baignent les rives nord de l'Alaska et du Yukon (flèche mauve; *Coastal Flow*; Figure 0.3). À la limite nord du plateau continental, le *Shelf current* qui transporte des eaux de salinité

relativement faible (< 31 psu), froides et peu profondes (< 30 m) circule vers l'ouest (flèche verte; Figure 0.3; Lin *et al.*, 2020). Finalement, le gyre de Beaufort, qui circule dans un sens anticyclonique, transporte les eaux du large vers l'ouest, une partie se propageant et recirculant dans la dépression du Mackenzie (flèches jaunes; Figure 0.3).

0.6.2 Les changements récents

Lorsqu'on se focalise sur les effets du réchauffement du climat récent, on remarque que l'étendue de la glace de mer a diminué dix fois plus rapidement entre 2000 et 2012 CE, comparativement à la moyenne de 1979 à 2000 CE (Frey *et al.*, 2015). Le taux d'érosion côtière de la rive de la mer de Beaufort est le plus élevé de l'océan Arctique (Lantuit *et al.*, 2012). Localement, l'érosion de l'île Herschel enregistre des taux 50% plus rapides depuis 2000 CE que de 1970 à 2000 CE (Obu *et al.*, 2016). La rivière Mackenzie décharge des eaux de plus en plus riches en particules en suspension, leur concentration ayant augmenté de 50% en dix ans (2003-2013 CE; Doxaran *et al.*, 2015).

0.7 Les approches méthodologiques

0.7.1 Les foraminifères benthiques

Notre approche micropaléontologique s'appuie principalement sur l'étude des assemblages de foraminifères benthiques. Les foraminifères benthiques sont des organismes eucaryotes hétérotrophes et leur coquille, ou test, se préserve dans le sédiment. Selon que leur test est composé de carbonate de calcium ou de particules minérales, les foraminifères benthiques sont qualifiés de calcaires ou d'agglutinants, respectivement. Certains foraminifères, épibenthiques, vivent à la surface du sédiment et d'autres, endobenthiques, vivent dans le sédiment souvent dans les quelques premiers centimètres sous la surface. Pour certaines espèces, ces deux modes de vie sont interchangeables et dépendent surtout des conditions ambiantes ou de stress environnementaux comme une augmentation des flux sédimentaires ou une diminution de l'oxygène (Murray, 2006). Certaines espèces sont sessiles, alors que d'autres peuvent se mouvoir. La mobilité de ces dernières sert surtout à la recherche de nourriture. Elle est toutefois lente ($<50 \mu\text{m}\cdot\text{min}^{-1}$) et limitée (Murray, 2006). Les habitudes alimentaires des foraminifères sont très diversifiées, basées sur la consommation d'algues, de bactéries, de matière en suspension ou de débris organiques. Peu d'information existe sur le type d'alimentation propre à chaque espèce.

Les foraminifères benthiques sont abondants et ont une diversité taxonomique élevée sur les plateaux continentaux de l'océan Arctique. Plusieurs études de leur distribution ont permis de déterminer les conditions préférentielles de certains assemblages. Les assemblages sont associés à des conditions données de température et salinité, à certains types de substrat, au couvert de glace de mer et aux apports de matière organique (Polyak *et al.*, 2002; Polyak *et al.*, 2003; Scott *et al.*, 2008; Wollenburg et kuhnt, 2000). Les assemblages de foraminifères sont donc de bons traceurs pour reconstituer les conditions marines passées dans les archives sédimentaires. Dans les zones côtières, les foraminifères sont aussi utilisés comme traceurs d'hypoxie et de polluants (p. ex., Alve, 2003; Cearreta *et al.*, 2000). Les interprétations écologiques à partir des assemblages de foraminifères benthiques ne sont toutefois pas univoques, car les facteurs environnementaux qui régulent les communautés de foraminifères varient d'une région à l'autre (Murray, 2006). Une compréhension exhaustive de la zone d'étude est donc primordiale.

0.7.2 Les isotopes stables des tests de foraminifères

En plus des assemblages de foraminifères benthiques, notre approche inclut l'analyse de la composition isotopique de l'oxygène et du carbone de leurs tests ($\delta^{18}\text{O}$ et $\delta^{13}\text{C}$). Comme le carbonate du test des foraminifères se précipite en fonction de la composition isotopique de l'oxygène de l'eau ambiante, sa géochimie peut être utilisée comme marqueur de salinité dans les zones estuariennes arctiques (Bauch *et al.*, 2004; Polyak *et al.*, 2003). En effet, dans ce type de milieu, la couche d'eau de surface, peu salée et relativement chaude, formée des apports d'eau fluviale et de la fonte de la glace est appauvrie en isotopes lourds (^{18}O), alors que les eaux plus profondes et hauturières, salées et froides, sont enrichies en ^{18}O . Il se développe alors une relation linéaire entre la salinité et le $\delta^{18}\text{O}$ de l'eau en été (Lansard *et al.*, 2012; Polyak *et al.*, 2003). Toutefois, la présence de saumures, très salées, mais appauvries en ^{18}O , peut altérer la relation $\delta^{18}\text{O}$ -salinité. De plus, la vitesse et la température de calcification, l'âge du foraminifère (juvénile ou mature), ainsi que l'effet vital de chaque espèce peuvent modifier la signature isotopique du test par rapport à celle de l'eau (Ravelo et Hillaire-Marcel, 2007).

Le $\delta^{13}\text{C}$ des tests de foraminifères reflète la composition du carbone inorganique dissous de l'eau (CID). Dans les eaux du plateau continental de la mer de Beaufort, le $\delta^{13}\text{C-CID}$ a tendance à être élevé (valeurs autour de 1.0-1.5‰) dans les eaux de surface/subsurface, là où la productivité primaire a lieu, car les isotopes légers sont préférentiellement utilisés lors de la photosynthèse. En revanche, le $\delta^{13}\text{C-CID}$ est plus

faible (0-0.5 ‰) lorsque la respiration du carbone est maximale (Mol *et al.*, 2018). Le CID de l'eau est alors généralement appauvri près des rivières, à l'interface avec le sédiment et sous la pycnocline, aux endroits où la matière organique s'accumule et se décompose. Dans un enregistrement continu d'une même espèce, une diminution du $\delta^{13}\text{C}$ peut être liée à une augmentation des apports en C_{org} dans la colonne d'eau (Ravelo et Hillaire-Marcel, 2007; Mackensen, 2008). Toutefois, la signature isotopique du carbone dans les tests de foraminifères peut s'avérer complexe à interpréter. En effet, si les foraminifères sont endobenthiques, le $\delta^{13}\text{C}$ ne reflète pas la composition isotopique de la masse d'eau profonde, mais plutôt celle de l'eau porale et livre ainsi des valeurs $\delta^{13}\text{C}$ plus faibles, voire négatives (Bauch *et al.*, 2004; Polyak *et al.*, 2003). Le $\delta^{13}\text{C}$ diminue davantage plus l'espèce vit en profondeur dans le sédiment (McCorkle *et al.*, 1997; Polyak *et al.*, 2003), car la matière organique y est de plus en plus décomposée causant une augmentation du CO₂ partiel appauvri en ¹³C. Le $\delta^{13}\text{C}$ des eaux porales peut aussi être modifié par le taux de respiration spécifique au foraminifère lors de la calcification de son test (Ravelo et Hillaire-Marcel, 2007; Cesbron *et al.*, 2016).

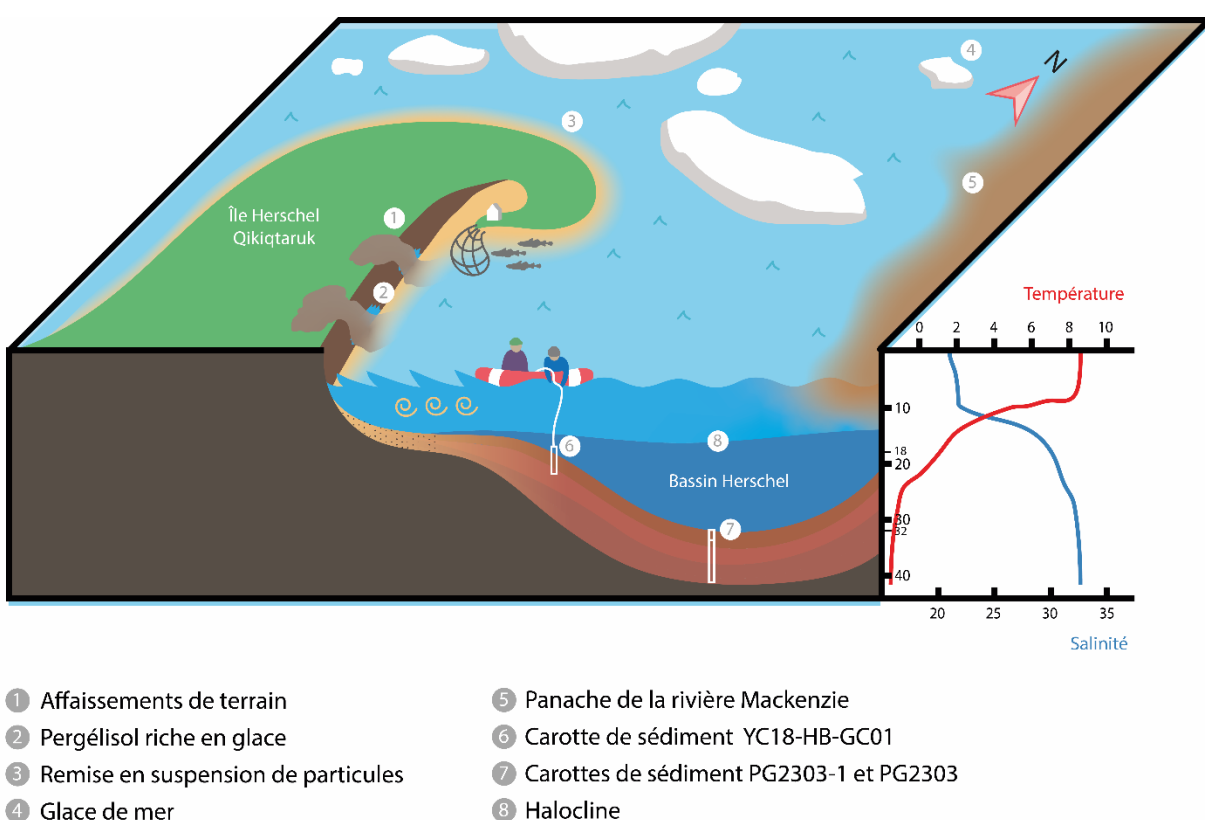
Les analyses de la composition isotopique ($\delta^{18}\text{O}$ et $\delta^{13}\text{C}$) des tests de foraminifères benthiques sont effectuées sur deux espèces : *Elphidium clavatum* et *Cassidulina reniforme*. *E. clavatum* est l'espèce la plus commune des marges de l'océan Arctique et la composition isotopique de son test a déjà été documentée (Bauch *et al.*, 2004; Erlenkeuser et von Grafenstein, 1999; Polyak *et al.*, 2003). *Elphidium clavatum* tolère des taux de sédimentation élevés et peut facilement circuler dans le sédiment (Ullrich *et al.*, 2009), ce qui concorde avec un $\delta^{13}\text{C}$ négatif (Bauch *et al.*, 2004; Polyak *et al.*, 2003). De plus, *E. clavatum* se reproduit en été (Korsun et Hald, 2000; Ullrich *et al.*, 2009) et serait donc un marqueur des conditions estivales. Des informations sur la composition isotopique de *C. reniforme* sont plus rares dans la documentation scientifique, mais il a été démontré que *C. reniforme* se calcifie normalement près de l'équilibre en raison de son faible effet vital (Austin et Kroon, 1996) .

0.7.3 Les ostracodes

L'analyse des assemblages d'ostracodes fait également partie de l'approche micropaléontologique. Les ostracodes sont des crustacés méiobenthiques protégés par deux valves de carbonate de calcium. Les ostracodes se nourrissent de différents débris organiques et ils ne se déplacent pas activement dans l'eau, se laissant plutôt transporter par les courants. Comme les foraminifères benthiques, plusieurs espèces d'ostracodes occupent les marges continentales de l'océan Arctique (Gemery *et al.*, 2017). La composition

des assemblages d'ostracodes varie en fonction de la salinité, de la température, de la vitesse des courants marins profonds, du substrat, de la formation de glace de mer et des apports nutritifs (Gemery *et al.*, 2013; Gemery *et al.*, 2017; Gemery *et al.*, 2021; McDougall *et al.*, 1986; Reimnitz *et al.*, 1993; Stepanova *et al.*, 2003; Stepanova *et al.*, 2007). Comme les assemblages d'ostracodes diffèrent en fonction de la profondeur de la colonne d'eau, ils marqueraient également des changements dans le niveau marin et donc dans le volume de glace continentale (p. ex., Cronin *et al.*, 2022). L'étude des variations de leur population dans les carottes sédimentaires est donc un outil pour reconstituer le milieu marin des eaux de fond.

Figure 0.4 Schéma représentant le bassin Herschel et les sites d'étude dans leur cadre environnemental. Gracieuseté de Mark-Antoine Thibodeau Breault.



0.7.4 Les tintinnides

Outre les foraminifères benthiques et les ostracodes, d'autres types de microfossiles peuvent être identifiés. Le long de la marge continentale de la mer de Beaufort, Schell *et al.* (2008) et Scott *et al.* (2008) ont identifié des tintinnides qui sont des eucaryotes hétérotrophes appartenant aux ciliés. Plus

précisément, l'espèce *Tintinnopsis rioplatensis* (Souto, 1979) a été identifiée, ou plutôt identifiée à l'espèce *Tintinnopsis fimbriata* (Agatha, 2008; Meunier, 1919) dans cette thèse, que les auteur.rice.s associent avec le panache de la rivière Mackenzie. En effet, *T. fimbriata* préfère les milieux près des côtes et aux embouchures de rivières (Burkovsky, 1976; Echols et Fowler, 1973; Rogers *et al.*, 1981), donc des apports d'eaux peu salées et turbides. *T. fimbriata* est une espèce agglutinante et doit construire sa coquille dite lorica à partir de particules détritiques (Pierce et Turner, 1993). Cette espèce vit entre 0 et 40 m de profondeur (Paranjape, 1987) et fournit ainsi des indications sur les conditions des masses d'eau de surface et subsurface, complémentaires de celles livrées par les ostracodes et foraminifères qui sont des marqueurs des eaux de fond.

0.8 Carottes marines

Cette étude se base sur trois carottes sédimentaires provenant de deux sites distincts du bassin Herschel. La carotte YC18-HB-GC01 (69.544°N; 138.970°O; HBGC01 ci-après) a été prélevée lors de l'expédition *Nunataryuk Yukon coast* en août 2018 avec un carottier par gravité déployé manuellement d'un zodiac. Cette carotte a été prélevée spécifiquement pour cette étude. Un total de 40 cm de matériel a été récupéré. Le site HBGC01 se trouve en bordure ouest du bassin à 18 m de profondeur et à seulement 3 km de la rive de l'île Herschel – Qikiqtaruk (Figures 0.3 et 0.4). Le deuxième site, PG2303 (69.513°N; 138.895°O), se trouve plus en profondeur dans le bassin, à 32 m (Figures 0.3 et 0.4). La carotte courte PG2303-1 (20 cm) et la carotte longue PG2303-1 (12 m) ont été prélevées avec l'aide d'un trépied sur la glace lors d'une expédition hivernale de la *Alfred Wegener Institute* à Potsdam en avril 2016. Afin de préserver l'interface eau-sédiment, la carotte PG2303-1 a été récupérée par un carottier par gravité, alors qu'un carottier à piston a été utilisé pour la carotte longue PG2303. Seulement les 324 premiers centimètres de cette dernière ont été analysés pour répondre aux objectifs de cette étude (Chapitre 3).

0.9 La structure de la thèse

Le premier chapitre prépare le terrain pour les deux autres qui suivront. Il vise à valider l'utilisation des assemblages de foraminifères benthiques, d'ostracodes et de tintinnides comme traceurs de leur environnement dans les carottes par gravité HBGC01 et PG2303-1. Ce chapitre, sous forme d'article scientifique, présente la complexité de la zone d'étude et l'ensemble des espèces de foraminifères benthiques, d'ostracodes et autres microfossiles observés accompagnés de planches photographiques. De plus, comme cette étude comprend deux sites de profondeurs différentes (Figure 0.4), elle permet de faire une revue comparative de la biodiversité dans le bassin. Ce chapitre explore aussi le rôle de la glace de

mer sur les changements observés au cours des 50 dernières années. Il s'intitule *Microfaunal recording of recent environmental changes in the Herschel Basin, western Arctic Ocean* et il a été publié dans la revue *Journal of Foraminiferal Research* en janvier 2023 dans un numéro spécial soulignant les travaux de feu David B. Scott.

Figure 0.5 Représentation schématique (a) des effets de vents d'est forts et dominants et (b) des effets de vents d'est modérés. Pour les indicateurs écologiques, le code de couleur réfère aux couleurs utilisées dans le schéma (p. ex., vert pâle pour les remontées d'eaux riches en nutriments et bleu foncé pour les eaux profondes salées). Gracieuseté de Mark-Antoine Thibodeau Breault.

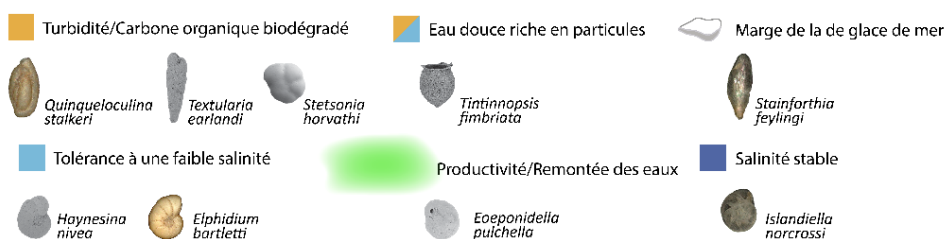
a) 1998-2017 CE



b) 1979-1998 CE



Indicateurs Écologiques



Le deuxième chapitre fait la démonstration de l'utilité des microfossiles comme traceurs écologiques dans un contexte de changements climatiques récents. Il explore en détail les relations entre les changements dans l'habitat littoral, à partir des traceurs écologiques utilisés, et les changements environnementaux au cours des 40 dernières années. Cette étude contribue à l'identification des principaux effets des activités anthropiques sur cet écosystème côtier. Ce chapitre tente de répondre à la motivation initiale de cette thèse et il est également un exercice d'adaptation de l'usage de la micropaléontologie pour un public non expert. Un résumé graphique a été développé pour ce chapitre qui est présenté dans la Figure 0.5. Le deuxième chapitre a été soumis le 21 avril 2023 à la revue *Estuarine, Coastal and Shelf Science*. Suite aux commentaires d'évaluateurs externes, il a fait l'objet de modifications mineures et le manuscrit révisé a été transmis le 21 août 2023.

Finalement, le dernier chapitre est une reconstitution des conditions des masses d'eau dans le bassin Herschel au cours des 1300 dernières années, avec comme points de mire la salinité, la température et les apports terrigènes. Ce chapitre permet de situer l'amplitude et la portée des changements récents en parallèle avec la variabilité naturelle du milieu, un atout caractéristique de la paléocéanographie. La reconstitution couvrant les 1300 dernières années est également mise en contexte avec les variations climatiques déjà rapportées dans la région (p. ex., Bringué et Rochon, 2012; Gemery *et al.*, 2023; Nicolle *et al.*, 2018; Richerol *et al.*, 2008). Ce troisième chapitre intitulé *A 1300-year microfaunal record from the Beaufort Sea shelf indicates exceptional climate-related environmental changes over the last two centuries* a été accepté pour publication à la revue *Palaeogeography, Palaeoclimatology, Palaeoecology* et paraîtra dans le numéro de septembre 2023.

CHAPITRE 1

MICROFAUNAL RECORDING OF RECENT ENVIRONMENTAL CHANGES IN THE HERSCHEL BASIN, WESTERN ARCTIC OCEAN

Jade Falardeau^a, Anne de Vernal^a, Marit-Solveig Seidenkrantz^b, Thomas M. Cronin^c, Laura Gemery^c, Léopold Chassiot^d, Michael Fritz^e, Vladislav Carnero-Bravo^{a,f}, Claude Hillaire-Marcel^a, and Philippe Archambault^g

- a. Geotop Research Center in Earth System Dynamics and Département des sciences de la Terre et de l'atmosphère, Université du Québec à Montréal, Montréal, Canada
- b. Paleoceanography and Paleoclimate Group, Arctic Research Centre, and iClimate centre, Department of Geoscience, Aarhus University, Aarhus, Denmark
- c. Geological Survey, Florence Bascom Geoscience Center, National Center, Reston, VA, USA
- d. Département de Géographie, Faculté de foresterie, de géographie et de géomatique, Université Laval, Centre d'Étude Nordique and INRS-ETE, Québec, Canada
- e. Permafrost Research Unit, Alfred Wegener Institute, Helmholtz Centre for Polar and Marine Research, Potsdam, Germany
- f. Instituto de Ecología, Universidad del Mar, Campus Puerto Ángel, Puerto Ángel, Oaxaca, México
- g. Québec Océan, ArcticNet, Takuviq, Département de biologie, Université Laval, Québec, Canada

Cet article est paru dans la revue *Journal of Foraminiferal Research* en janvier 2023 :

Falardeau, J., de Vernal, A., Seidenkrantz, M.-S., Cronin, T.M., Gemery, L., Chassiot, L., Fritz, M., Carnero-Bravo, V., Hillaire-Marcel, C. et Archambault, P. (2023). Microfaunal recording of recent environmental changes in the Herschel Basin, western Arctic Ocean. *Journal of Foraminiferal Research*, 53(1), 20-48.

Les figures en matériel supplémentaire se retrouvent après les références de ce chapitre. Les tableaux supplémentaires ne seront accessibles qu'en ligne; voir les Annexes A à F pour les comptages micropaléontologiques bruts des carottes YC18-HB-GC01 et PG2303-1.

Abstract

Microfaunal assemblages of benthic foraminifera, ostracods, and tintinnids from two marine sediment cores retrieved from the Herschel Basin of the Canadian Beaufort Sea shelf document relationships with environmental parameters such as salinity, sea-ice cover, and turbulence. Cores YC18-HB-GC01 and PG2303-1 were collected at 18 and 32 m water depth, respectively. At these sites, sediment accumulation rates range between 0.6 and 1.7 cm yr⁻¹ allowing a near-annual temporal resolution over the last 50 years. Multivariate analyses indicate that benthic foraminiferal assemblages respond primarily to food supply. Dissimilarities between the microfaunal assemblages of the two cores are mainly the result of bottom water salinity levels linked to water depth. High abundance of the benthic foraminiferal species *Elphidium clavatum* and occurrences of *Elphidium bartletti* point to varying, but relatively low, salinities at the shallow core site YC18-HB-GC01, which may be affected by variations in the summer halocline depth. Higher species diversity and more abundant *Cassidulina reniforme* and *Stainforthia feylingi* characterize the deeper core PG2303-1, which might reflect more stable conditions and higher bottom-water salinities throughout the studied time interval. The most important microfaunal shift of the last 50 years, observed in the shallower longer core YC18-HB-GC01, occurred at the turn of the 21st century. Prior to ~2000 CE, the presence of *Islandiella norcrossi* indicates more stable and saline conditions. Since ~2000 CE, increased abundances of *Haynesina nivea* and of the ciliate *Tintinnopsis fimbriata* suggest decreased salinity and increased turbidity. An increased abundance of *Eoepionidella pulchella* after ~2000 CE suggests a concurrent increase in productivity in the last two decades. This shift is nearly synchronous with a decrease in mean summer sea-ice concentration, which can play an important role in bottom water stability on the shelf. Easterly winds can induce a reduction in the sea-ice cover, but also foster a westward spreading of the Mackenzie River plume and the upwelling of nutrient-rich Pacific waters onto the shelf. Both factors would explain the increased freshening and productivity of the Herschel Basin. The last two decades were also marked by a decrease in ostracod abundance that may relate to higher water turbidity. This study shows that combining information from benthic foraminifera, ostracods, and tintinnids provides a comprehensive insight into recent hydrographic/climatic changes in nearshore Arctic habitats, where productivity is critical for the food security of local communities.

Keywords: Benthic foraminifera, Ostracods, Tintinnids, Beaufort Sea, Arctic coast, Salinity

1.1 Introduction

The 21st century marks the lowest level of sea-ice extent in the Arctic Ocean of the last 1400 years (Kinnard et al., 2011; IPCC, 2019). This decrease has led to increased net primary production, essentially due to both a longer open water season and an increased area of open water (Arrigo et al., 2008; Barber et al., 2012; Arrigo & van Dijken, 2015), at least until ca. 2008 CE. However, since then, new nutrients imported to the Arctic Ocean from the Pacific and the Atlantic oceans have become a major contributor to the increase in net primary production (Lewis et al., 2020). Partial ice cover also fosters upwelling of nutrient-rich waters onto the Arctic shelves (Barber et al., 2012; Schulze & Pickart, 2012) that act as a hotspot for phytoplankton blooms (Tremblay et al., 2011, 2012; Walkusz et al., 2012). However, the transition to a seasonally ice-free Arctic Ocean raises questions about the long-term effects of changes in the plankton community (Li et al., 2009; Comeau et al., 2011; Dolan et al., 2014; Lefebvre et al., 2016) and in the stratification and vertical mixing of the water masses (McLaughlin & Carmack, 2010; Blais et al., 2017) on the Arctic marine food web. Open waters also modify the exchange of heat with the atmosphere and lead to a generally more unstable climate due to increased wind speed and storm events (Simmonds & Keay, 2009; Mioduszewski et al., 2018). Along Arctic coastlines, higher air temperatures and reduced sea-ice cover enhance coastal erosion, which increases the flux of carbon and sediment to continental shelves, also affecting the food web (Fritz et al., 2017). The role of terrigenous nutrients linked to coastal erosion is rarely considered (Ardyna & Arrigo, 2020; Lewis et al., 2020), but they could contribute up to 21% to the primary production in the Arctic Ocean (Terhaar et al., 2021). However, coastal erosion also leads to increased turbidity in the nearshore areas (Klein et al., 2019, Jong et al., 2020), with a documented negative impact on primary production (Anthony et al., 2004; Retamal et al., 2008; Bonsell & Dunton, 2018; Lewis et al., 2020). It may also contribute to ocean acidification through the degradation of terrestrial organic matter (Semiletov et al., 2016; Fritz et al., 2017).

In coastal Arctic environments, it is often difficult to disentangle the impacts of the recent climate change from interannual and local variations because direct measurements over several decades are rare, especially when it comes to the biota. Micropaleontological tracers can be used to develop such biological time series and to reconstruct longer-term changes in environmental conditions. Among microfossils, benthic foraminiferal assemblages are largely controlled by water depth, salinity, temperature (e.g., Polyak et al., 2002, 2003), and food availability (carbon fluxes; e.g., Wollenburg & Kuhnt, 2000). Moreover, some species thrive under sea-ice marginal conditions (Scott et al., 2008a; Seidenkrantz, 2013; Seidenstein et al., 2018), while others may tolerate reduced dissolved oxygen availability (Seidenkrantz, 2013; Moffitt

et al., 2014). In shallow benthic environments, ostracods are also abundant and represented by numerous species (Gemery et al., 2017). Their assemblages relate to salinity and temperature, sea level, and river inputs (McDougall et al., 1986; Reimnitz et al., 1993; Stepanova et al., 2003, 2007; Gemery et al., 2013, 2017, 2021; Cronin et al., 2017), in addition to sea-ice cover (Cronin et al., 2010). Tintinnid microfossils may also occur in marine sediment of the Arctic. They belong to ciliates, which are important grazers in the western Arctic Ocean microzooplankton community (Sherr et al., 2009). Previous studies of tintinnids have highlighted their potential use as tracers of salinity and sea level (Echols & Fowler, 1973; Burkovsky, 1976; Rogers et al., 1981; Pierce & Turner, 1993).

Several studies have documented the spatial distribution and ecological affinities of benthic foraminifera on Arctic continental shelves (e.g., Hald & Steinsund, 1996; Wollenburg & Mackensen, 1998; Wollenburg & Kuhnt, 2000; Polyak et al., 2002; Lloyd, 2006; Scott et al., 2008a, 2008b; Husum et al., 2015). However, high-resolution temporal reconstructions of past nearshore environments of the Arctic using benthic foraminifera are rare due to the lack of continuous sedimentological records. In this study, the Herschel Basin provides us with the opportunity to establish multiannual time series (Grotheer et al., 2020) of microfaunal changes in a nearshore Arctic area that is presently influenced by sea-ice loss (Frey et al., 2015) and increased terrestrial supply from coastal erosion and rivers (Doxaran et al., 2015; Ehn et al., 2019; Klein et al., 2019; Jong et al., 2020). The Herschel Basin is located off northern Yukon, Canada (Fig. 1.1), where benthic foraminiferal and ostracod assemblages have not hitherto been documented. Thus, our first objective is to describe the microfaunal assemblages that characterize the last decades at two different depths in the basin, which may be used as a baseline for future paleo studies on the Beaufort Sea continental shelf. The second objective is to document interannual variations of the microfaunal records and eventually, to relate these to recent environmental changes and develop their use as tracers of biogenic productivity and diversity in nearshore Arctic areas.

1.2 Regional settings

1.2.1 The Herschel Basin

The Herschel Basin is located on the continental shelf of the Beaufort Sea offshore the northern Yukon coastal plain, around 10 km east of Herschel Island – Qikiqtaruk and 135 km west of Shallow Bay (Fig. 1.1B, D). This 40-km long, 15-km wide, and up to 70-m deep basin (EBA Engineering Consultants Ltd., 1992; Fig. 1.1D) allows continuous sediment accumulation (Grotheer et al., 2020). A shallow sill with a water depth of 13 m forms the northern limit of the basin (EBA Engineering Consultants Ltd., 1992). The sill prevents

large stamukhi, or sea-ice rubble, and other floating ice from reaching the basin. The land-fast ice is generally 2 m thick on the shelf (Carmack & MacDonald, 2002), which also limits ice scouring at depth in the basin.

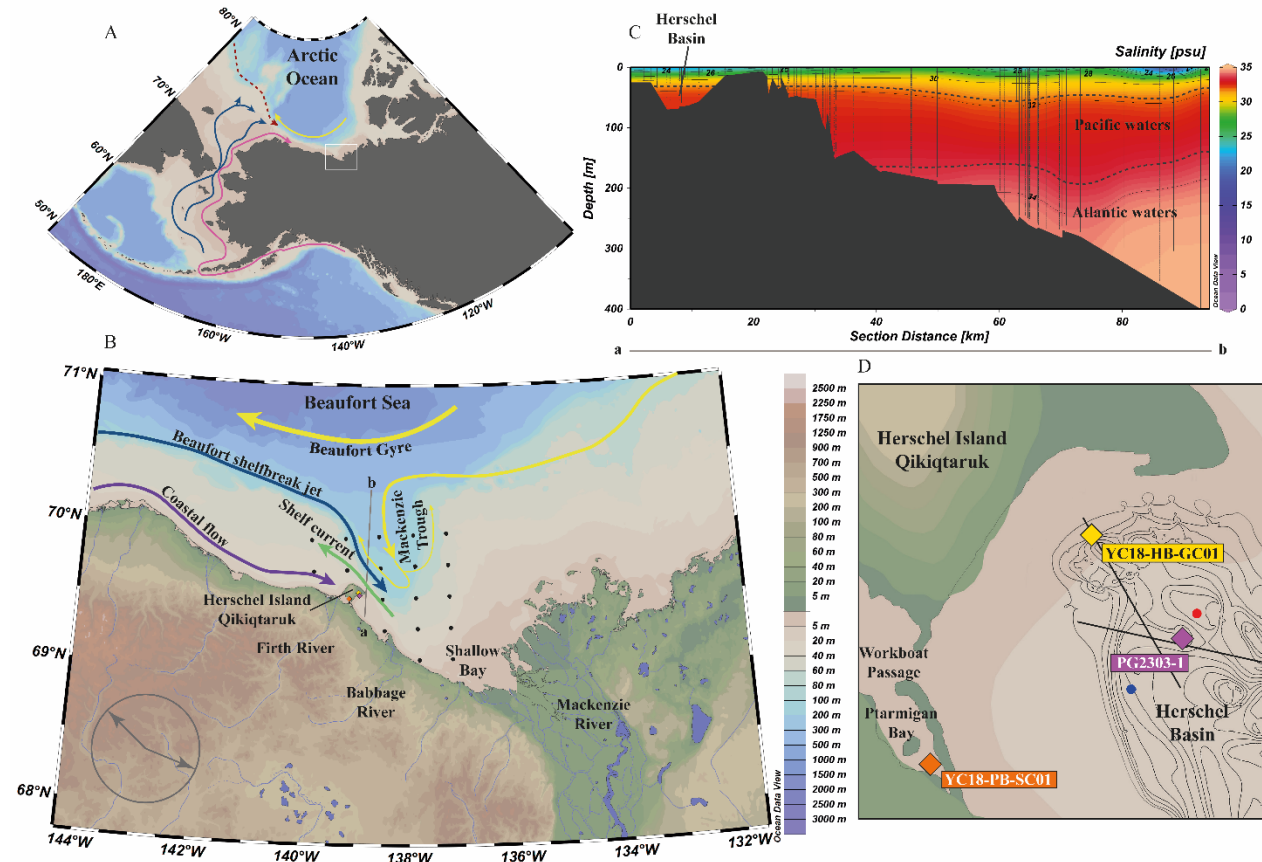
1.2.2 Hydrography

The regional hydrography of the Herschel Basin area is complex and unstable as it is controlled by winds that vary in direction and strength (see below; Kulikov et al., 1998; Lin et al., 2020). In summer, the predominantly eastward coastal flow (Fig. 1.1B, purple) carries relatively warm and low salinity waters alongshore ($>0^{\circ}\text{C}$ and $<31 \text{ psu}$, respectively) that derive from the Bering summer waters (Lin et al., 2020). The shelf current (Fig. 1.1B, green arrow) flows predominantly westward and carries cold ($<-1^{\circ}\text{C}$) and relatively fresh ($<31 \text{ psu}$) surface waters ($<30 \text{ m}$) mainly formed from sea-ice melt and meteoric waters (Kulikov et al., 1998; Weingartner et al., 2017; Lin et al., 2020). In contrast, at the shelf break, the waters flow eastward as the “Beaufort shelfbreak jet” (Fig. 1.1A, B, blue arrow) transporting predominantly the relatively saline ($>31.5 \text{ psu}$) and nitrate-rich Pacific winter water mass known as the remnant winter waters (hereafter referred to as Pacific waters; Pickart, 2004; Lin et al., 2016, 2020). These waters sit on top of dense and saline subsurface Atlantic waters ($>33.5 \text{ psu}$; Lin et al., 2016, 2020; Ardyna et al., 2017; Fig. 1.1C). Further to the north, the Beaufort Gyre circulates clockwise (Fig. 1.1A, B, yellow arrow) under the influence of the Beaufort Sea High (Serreze & Barrett, 2011). Part of the southern gyre recirculates into the Mackenzie Trough (Lin et al., 2020; Fig. 1.1B, thin yellow arrows). A strong anticyclonic regime generates dominant easterly winds in the marginal seas that induce sea-ice drift to the central Arctic Ocean usually resulting in a reduced sea-ice cover (Ogi & Wallace, 2007; Ogi et al., 2008). Increased easterly winds in the Beaufort Sea continental slope area under a strong Beaufort Sea High would also reduce the entry of Pacific waters through the Beaufort shelfbreak jet (Brugler et al., 2014).

The Mackenzie River is the most important freshwater source in the area (Carmack et al., 2006), and it has the fourth largest discharge of freshwater into the Arctic Ocean (Holmes et al., 2011). Its main flux usually occurs at the beginning of June during the spring freshet (Carmack & MacDonald, 2002). The Mackenzie River plume is very rich in dissolved organic carbon (Holmes et al., 2011; Juhls, 2021) and terrestrial suspended particles (Doxaran et al., 2015), both of which are dispersed up to hundreds of kilometres westward during the freshet and depending on the winds during summer (Wood et al., 2015; Juhls, 2021). The Firth and Babbage estuaries are located approximately 20 km and 40 km, respectively, from our study site (Fig. 1.1B). However, their impact on the hydrography of the study area is low as their mean summer

flow is significantly less than that of the Mackenzie River (Environment and Climate Change Canada Historical Hydrometric Database, 2020).

Figure 1.1 (A) Regional map of northwestern North America with the main currents in the Bering Strait and the western Arctic Ocean (based on Grebmeier et al., 2006). (B) Study area [white box in (A)] and surface ocean currents (based on Lin et al., 2020). The black dots represent the grid used for the mean summer sea-ice concentrations. The gray arrows in the lower left corner indicate the two dominant wind directions at Herschel Island – Qikiqtaruk (based on Radosavljevic et al., 2016). The a–b transect marks the section used for the (C) salinity profile with data from the World Ocean Database 2018 (Boyer et al., 2018) using Ocean Data View (Schlitzer, 2018). The thin vertical black lines are the locations of all the CTD measurements (mostly summer to fall measurements) used for the reconstruction of the water mass transect. The dotted lines delimitate approximately the Pacific (31.5–33.5 psu) and Atlantic (>33.5 psu) water masses. (D) Location of core sites in the Herschel Basin and location of two CTD measurements taken in August 2015 (red dot) and April 2016 (blue dot; see Fig. 1.2). The black lines indicate the northwest–southeast (Fig. 1-A.1) and west–east (Fig. 1-A.2) seismic transects. The main currents are illustrated in (A) and (B) as follows: pink arrow for the Alaskan coastal water, blue arrows for the other Pacific water masses (winter/summer), red dotted arrow for the subsurface Atlantic waters, yellow arrows for the Beaufort Gyre, purple arrow for the coastal flow, and green arrow for the shelf current.

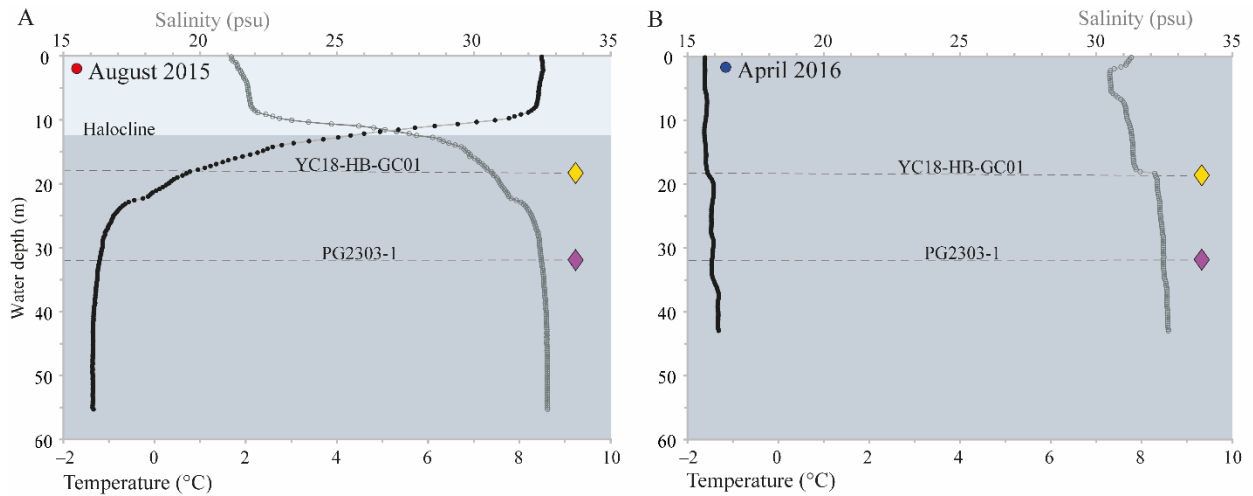


The water masses in summer are strongly stratified on the Beaufort Sea shelf due to the low salinity of the surface waters (Figs. 1.1C, 1.2A, light gray zone). The halocline depth ranges between 5 and 10 m depth in summer (Carmack & MacDonald, 2002), and could reach deeper levels according to the summer 2016

Conductivity Temperature Depth (CTD) measurements (Fig. 1.2A). The temperature and salinity of the surface water layer in summer are 8–9°C and 21–22 psu, respectively, while they are close to the freezing point and 32–33 psu below the halocline (Fig. 1.2A).

The cold and saline bottom waters of the Herschel Basin originate from upwelling of waters at the shelf break (Fig. 1.1C) via the Mackenzie Trough (Fig. 1.1B) and brine rejections from sea-ice formation (Williams & Carmack, 2012; Fig. 1.2, dark gray zones). As the land-fast ice forms in October up to the freshet season in June, the stratification breaks down and the water column homogenizes (Fig. 1.2B).

Figure 1.2 Salinity and temperature profiles in the Herschel Basin in August 2015 (A) and April 2016 (B) from CTD data measured with a hand-held CastAway-CTD device. Yellow and purple diamonds mark the water depth of cores YC18-HB-GC01 and PG2303-1, respectively. The brackish summer surface waters (<28 psu) are indicated by the light gray zone. The darker gray zones illustrate waters composed of a mix of brines and upwelled water from the shelf break (mostly Pacific waters). The red and blue dots refer to the location of the CTD measurements shown in Figure 1.1D.

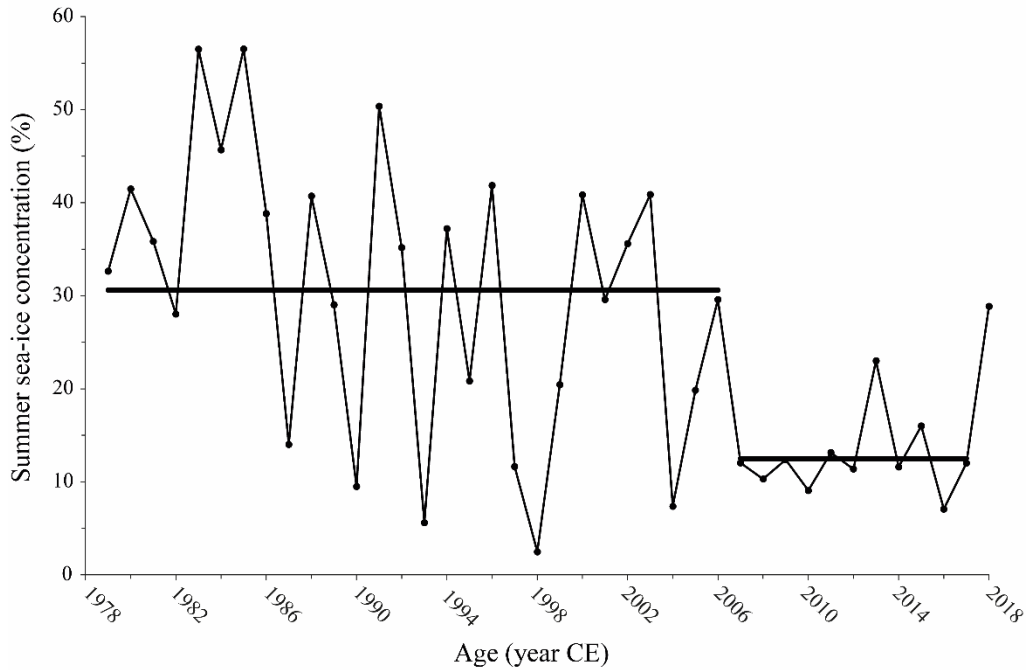


1.2.3 Winds and sea ice

Local winds are an important parameter in nearshore ecosystems, as they act as the main drivers of water and sea-ice transport (Kulikov et al., 1998; Frey et al., 2015; Lin et al., 2020), thus controlling sediment and nutrient transport. The important intra- and inter-annual environmental variability in our study area reflects this close relationship to local winds. Around Herschel Island – Qikiqtaruk, strong winds originate either from the northwest or from the east-southeast (Radosavljevic et al., 2016; Fig. 1.1B). During periods of dominant westerly winds, the Mackenzie River plume and the sea ice remain nearshore. In contrast, dominant easterly winds lead to offshore spreading of the Mackenzie River plume and foster sea-ice spreading and upwelling (Carmack & MacDonald, 2002; Pickart et al., 2011; Wood et al., 2015), thus

enhancing regional primary productivity (Tremblay et al., 2011, 2012; Pickart et al., 2013). The sea ice that interacts with marine currents, upwelling, and vertical mixing (Barber et al., 2012; Schulze & Pickart, 2012; Williams & Carmack, 2015) also plays a protective role along the coastline (Günther et al., 2015).

Figure 1.3 Summer (JJAS) mean sea-ice concentrations (%) calculated from 18-grid points of 25 km x 25 km covering the study area (see Fig. 1.1B; data compiled from NOAA/NSIDC climate data record of passive microwave sea-ice concentration; cf. Meier et al., 2017). The horizontal black lines mark the mean of the 1979–2006 CE and of the 2007–2017 CE intervals.



1.3 Material and methods

1.3.1 Sea ice

We calculated the mean summer sea-ice concentration in the study area as the average of daily sea-ice concentrations in June through September of each year. A breakpoint analysis on the 1979–2017 data highlights a shift in the mean in 2006 CE. Between 1979 and 2006 CE, summer sea-ice concentrations varied from 55% down to 5% with a mean of 31%. After 2006 CE, it stabilized around 7–16% with a mean of 13% (Fig. 1.3).

1.3.2 Sediment cores

This study is based on the analysis of two sediment cores collected in the Herschel Basin: core YC18-HB-GC01 (hereafter HBGC01) and core PG2303-1. The HBGC01 core is from the western part of the Herschel

Basin (69.544°N , 138.970°W ; 18 m water depth), while core PG2303-1 was retrieved from the deeper part of the basin (69.513°N , 138.895°W ; 32 m water depth; Fig. 1.1D).

1.3.2.1 Acoustic survey

Hydro-acoustic data were acquired using a Knudsen sub-bottom profiler (12 kHz; Figs. 1.1D, 1-A.1, 1-A.2). The acoustic image crossing the shelf (NW–SE transect; Fig. 1.1D) displays faintly laminated to chaotic reflections above 16 m water depth that evolve downslope into finely laminated reflections below the slope break. This lateral variation of acoustic facies suggests a transition from littoral coarse sediments to fine sediments (Fig. 1-A.1). Thus, the HBGC01 core was collected at the slope below the littoral platform. For the PG2303-1 core site (E–W transect; Fig. 1.1D), acoustic data show high-amplitude and parallel reflections interpreted as clastic mud (Fig. 1-A.2).

1.3.2.2 Core description

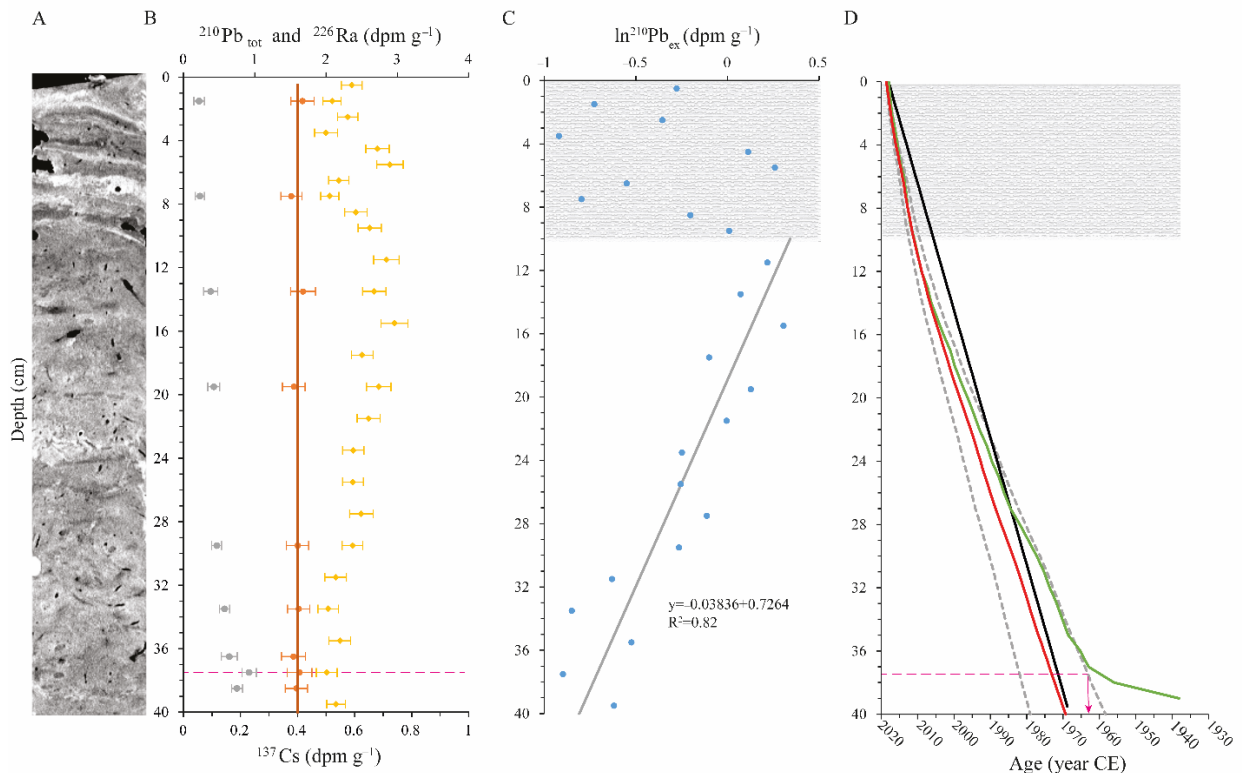
The 40-cm long HBGC01 core was retrieved using a UWITEC gravity corer deployed from a zodiac during the 2018 Nunataryuk Yukon Coast expedition on August 9th. The core was stored at 3°C and cut lengthwise in halves at Université Laval, Canada, where the lithological analyses were performed. One half-core was subsampled at 1-cm intervals for micropaleontology and dating (this study). The 20-cm long PG2303-1 core was retrieved on April 20th, 2016, with a UWITEC gravity corer from a tripod on the sea ice during a winter expedition led by the Alfred Wegener Institute. The core was stored cool in a refrigerator and subsampled at 1-cm intervals with a vertical extrusion system. Thus, the short core PG2303-1 was not cut lengthwise, and no descriptive lithology is available.

The HBGC01 core was photographed and scanned for 3D imagery and density by X-rays Computed-Tomography Scanner (CT-scan) at INRS-ETE facilities using a SIEMENS Somatom Definition AS128 (e.g., Fortin et al., 2013, Figs. 1.4A, 1-A.3) with the settings adjusted to 165–175 kV and 250–300 mA s⁻¹. We used the ImageJ software (Rasband, 2018) to export and process the raw DICOM format images.

The samples of core HBGC01 were analyzed for grain size at the Laboratoire de géomorphologie et sédimentologie of the Université Laval using a Spectrex Particle counter paired with a Horiba laser diffraction particle size analyzer allowing for grain-size measurements between 0.01 and 3000 µm. The samples of core PG2303-1 were processed at the Université du Québec à Montréal (UQAM) using a Microtrac MRB Bluewave laser diffraction instrument, which can detect grain sizes from 0.01 to 2000 µm.

Prior to the measurement, the samples were treated with hydrogen peroxide (30%) to dissolve organic matter. Data were processed in GRADISTAT (Blott, 2010), which defines sand as particles between 2 mm and 63 μ m, silt between 63 μ m and 2 μ m, and clays <2 μ m.

Figure 1.4 (A) The CT-scan of core HBGC01 with (B) the $^{210}\text{Pb}_{\text{tot}}$ (yellow), ^{226}Ra (orange), and ^{137}Cs (gray) activity profiles in core HBGC01. The dark orange line marks the mean ^{226}Ra used to estimate $^{210}\text{Pb}_{\text{sup}}$ (see text) and the pink dashed line marks the depth of the 1963 maximum ^{137}Cs activity (cf. Aoyama et al., 2006). (C) Natural logarithm of $^{210}\text{Pb}_{\text{ex}}$ (blue dots). The gray line marks the linear regression of the $\ln^{210}\text{Pb}_{\text{ex}}$ below 10 cm. (D) HBGC01 core age models obtained with Plum (mean ages = red line; minimum and maximum ages = gray dotted lines), with the CFCS model (black line) and with the CRS-piecewise model (green line; see Fig. 1-A.4 for the original age model graph produced by Plum). The gray shaded areas in (C) and (D) represent the proposed mixed layer.



1.3.2.3 Chronology and sedimentation rates

The age models are primarily based on ^{210}Pb analyses (raw data in Carnero-Bravo et al., 2021). The measurements procedure of ^{210}Pb followed Baskaran & Naidu (1995), assuming its secular equilibrium with ^{210}Po and using a spike of ^{209}Po . Sediment samples were digested with three acid solutions, successively (HNO_3 ; HCl , HF , and HNO_3 ; H_2O_2 and HNO_3). Residues were dissolved in a solution of HCl 0.5 N with ascorbic acid as a reducing agent for Fe, then spiked. Both ^{210}Po and ^{209}Po were finally deposited (plating) on a silver

disk. The measurement was performed by alpha spectrometry using ORTEC™ detectors and the Maestro™ data acquisition software.

We obtained ^{226}Ra and ^{137}Cs activity (γ -emitters) by high-resolution gamma spectrometry using a germanium detector (ORTEC). The efficiency calibration was calculated based on the Columbia River Basalt reference material (BCR-2; USGS). ^{226}Ra was used to estimate the supported ^{210}Pb fraction ($^{210}\text{Pb}_{\text{sup}}$), in which $^{210}\text{Pb}_{\text{sup}}$ is the average of all measurements of ^{226}Ra . The unsupported ^{210}Pb ($^{210}\text{Pb}_{\text{ex}}$) is the result of the total ^{210}Pb ($^{210}\text{Pb}_{\text{tot}}$) minus the $^{210}\text{Pb}_{\text{sup}}$.

The age models were made using the Plum software (Aquino-López et al., 2018) under R (R Core Team, 2021) and compared with the Constant Flux Constant Sedimentation (CFCS) and the Constant Rate of Supply (CRS) model using the serac package (Bruel & Sabatier, 2020). A first order estimate of the accumulation rate (in a cm^{-1} in Plum) of each core was specified prior to running the software. Plum takes into consideration the $^{210}\text{Pb}_{\text{tot}}$ activity and density (g cm^{-3}) of each sample, the $^{210}\text{Pb}_{\text{sup}}$ value, and the dates of coring. Ultimately, the mass accumulation rate ($\text{g cm}^{-2}\text{a}^{-1}$) of each sample was calculated by multiplying the sedimentation rates (cm a^{-1}) derived from the Plum runs and the densities (g cm^{-3}) of the sample section (Table 1-A.1). Sedimentation rate uncertainties were obtained by calculating the sedimentation rates of the highest and lowest ages given by the model (Table 1-A.1). Then, the uncertainties of mass accumulation rate were obtained by following error propagation principles.

1.3.3 Micropaleontological analyses

Sixty samples, 40 from core HBGC01 and 20 from core PG2303-1, were analyzed for their microfossil content, with special attention paid to benthic foraminifera, ostracods, and tintinnids. For each sample, 6–7 g of dry sediment were wet-sieved at 63 μm at Geotop-UQAM and dried again. Then, the microfossils were observed and picked with a fine brush under a stereo microscope at 40 \times to 115 \times magnification. Each sample was scanned in its entirety, but to ease the work process, the 63–106 μm and $>106 \mu\text{m}$ fractions were counted separately. In samples containing high concentrations of fine sand, we used a solution of tetrachlorethylene (C_2Cl_4) with a specific gravity of 1.6 g cm^{-3} to separate mineral particles from biogenic remains (Table 1-A.2).

Benthic foraminifera, including calcareous and agglutinated taxa, were identified based on Feyling-Hanssen et al. (1971), Polyak et al. (2002), and Scott et al. (2008b). Identification was made at species level

(Table 1.1; Figs. 1.5–7), except for the Polymorphinoidea superfamily (hereafter polymorphinids), which has a high diversity of species with poorly known ecology.

Table 1.1 List of benthic foraminiferal species and genera. *=miliolids; **=polymorphinids

Benthic foraminifera	HBGC01	PG2303-1	Figure
Calcareous foraminifera			
<i>Bolivinellina pseudopunctata</i> (Höglund, 1947)	x	x	Fig. 1.6-9
<i>Buccella frigida</i> (Cushman, 1922)	x	x	Fig. 1.5-10
<i>Cassidulina reniforme</i> Nørvang, 1945	x	x	Fig. 1.5-7
<i>Cornuspira involvens</i> (Reuss, 1850)	x	x	Fig. 1.6-10
<i>Elphidiella groenlandica</i> (Cushman, 1933)	x	-	Fig. 1.6-2
<i>Elphidium albumbilicatum</i> (Weiss, 1954)	x	x	-
<i>Elphidium asklundi</i> Brotzen, 1943	x	x	Fig. 1.5-12
<i>Elphidium bartletti</i> Cushman, 1933	x	x	Fig. 1.6.1
<i>Elphidium clavatum</i> Cushman, 1930	x	x	Figs. 1.5-5, 1.5-9
<i>Elphidium hallandense</i> Brotzen, 1943	x	x	Fig. 1.5-8
<i>Eoeponidella pulchella</i> (Parker, 1952a)	x	x	Fig. 1.5-11
<i>Epistominella takayanagii</i> Iwasa, 1955	x	x	-
<i>Haynesina nivea</i> (Lafrenz, 1963)	x	x	Fig. 1.5-6
<i>Haynesina orbicularis</i> (Brady, 1881a)	x	x	Fig. 1.6-12
<i>Islandiella helena</i> Feyling-Hanssen & Buzas, 1976	x	x	Fig. 1.6-3
<i>Islandiella norcrossi</i> (Cushman, 1933)	x	x	Fig. 1.6-4
<i>Nonionellina labradorica</i> (Dawson, 1860)	x	x	Fig. 1.5-1
<i>Parafissurina himatiostoma</i> Loeblich & Tappan, 1953**	x	x	Fig. 1.6-8
Polymorphinoidea			
<i>Pyrgo williamsoni</i> (Sylvestri, 1923)*	x	x	Fig. 1.5-13
<i>Quinqueloculina stalker</i> Loeblich & Tappan, 1953*	x	x	Fig. 1.6-5
<i>Quinqueloculina seminulum</i> (Linnaeus, 1758)*	x	x	Fig. 1.5-2
<i>Quinqueloculina lata</i> Terquem, 1876*	x	-	-
<i>Stainforthia feylingi</i> Knudsen & Seidenkrantz, 1994	x	x	Fig. 1.6-6
<i>Stainforthia loeblichi</i> (Feyling-Hanssen, 1954)	x	x	Fig. 1.5-4
<i>Stetsonia horvathi</i> Green, 1960	x	x	Fig. 1.6-11
<i>Triloculina trihedra</i> Loeblich & Tappan, 1953*	x	x	Fig. 1.5-3
<i>Vaginulina trondheimensis</i> (Feyling-Hanssen, 1964)	x	-	-
<i>Valvularineria</i> spp. Cushman (1926)	x	x	Fig. 1.6-7
Agglutinated foraminifera			
<i>Ammotium cassis</i> (Parker, 1870)	-	x	Fig. 1.7-1
<i>Cribrostomoides crassimargo</i> (Norman, 1892)	-	x	Fig. 1.7-8
<i>Eggerelloides advenus</i> (Cushman, 1922)	-	x	Fig. 1.7-5
<i>Lagenammina diffugiformis</i> (Brady, 1876)	x	x	Fig. 1.7-2
<i>Portatrochammina karica</i> Shchedrina, 1946	x	x	Fig. 1.7-6

<i>Recurvooides turbinatus</i> (Brady, 1881b)	x	x	Fig. 1.7-9
<i>Sigmoiopsis schlumbergeri</i> (Silvestri, 1904)	x	-	-
<i>Spiroplectammina biformis</i> (Parker & Jones, 1865)	x	x	Fig. 1.7-4
<i>Textularia earlandi</i> Parker, 1952b	x	x	Fig. 1.7-3
<i>Textularia torquata</i> Parker, 1952a	x	x	Fig. 1.7-7

Table 1.2 List of ostracod species and genera. References: 1 Olausson (1982), 2 McDougall et al. (1986), 3 Stepanova et al. (2003), 4 Gemery et al. (2017), 5 Stepanova et al. (2019), 6 Tian et al. (2020), 7 Gemery et al. (2021).

Ostracods	Low Salinity			Euhaline	References	Figure
	HBGC01	PG2303-1	Tolerant			
<i>Isthmia cluthae</i> (Brady, Crosskey & Robertson, 1874)	x	-		x	1, 5, 6	Fig. 1.9-3
<i>Cytheropteron brastadensis</i> Lord, 1981/ <i>Cytheropteron discoveria</i> Brouwers, 1994	-	x		x	1, 2, 6	Fig. 1.9-7
<i>Cytheropteron elaeeni</i> Cronin, 1989	x	x		x	2, 4, 5	Fig. 1.9-4
<i>Cytheropteron sulense</i> Lev, 1972	-	x		x	5	Fig. 1.9-2
<i>Cytheropteron suzdalskyi</i> Lev, 1972	x	x		x	2	Fig. 1.9-8
<i>Eucythere</i> spp.: <i>Eucythere argus</i> (Sars, 1866); <i>Eucythere declivis</i> (Norman, 1865)	x	x	x		5	Figs. 1.8-3, 1.8-4
<i>Eucytherura delineata</i> Whatley & Eynon, 1996	x	x		x	4	Fig. 1.9-5
<i>Heterocyprideis sorbyana</i> (Jones, 1857)	x	x	x		3, 5, 6	Fig. 1.8-6
<i>Loxoconcha venepidermoidea</i> (Swain, 1963)	x	x	x		2	Fig. 1.8-7
<i>Paracyprideis pseudopunctillata</i> Swain, 1963	x	x	x		2, 3, 4, 5	Figs. 1.8-1, 1.8-2
<i>Rabilimis mirabilis</i> (Brady, 1868)	x	x		x	1, 2, 5	Fig. 1.9-1
<i>Sarsicytheridea bradii</i> (Norman, 1865)	x	-	x	x	2, 5, 6, 7	Fig. 1.8-5
<i>Semicytherura complanata</i> (Brady, Crosskey & Robertson, 1874)	x	x		x	6	Fig. 1.9-6

Ostracods were identified to genus or species level (Table 1.2; Figs. 1.8, 1.9) based on Gemery et al. (2017) and Stepanova et al. (2003). Specimens identified only to genus level were mainly early instars (molts on juvenile specimens). The ostracod taxa that can tolerate low salinity (<30 psu) and the taxa that prefer salinity >30 psu (euhaline) were distinguished based on Olausson (1982), McDougall et al. (1986), Stepanova et al. (2003, 2019), Tian et al. (2020), and Gemery et al. (2017, 2021; see Table 1.2).

The agglutinated loricas of tintinnid were all identified as belonging to *Tintinnopsis fimbriata* (Meunier, 1919), which was re-described by Agatha (2008; Table 1.3). It is important to mention that the loria of *T.*

fimbriata, usually 48–74 µm in length (Agatha, 2008), can be smaller than the sieving mesh size used here (63 µm). Hence, our *T. fimbriata* counts probably provide an underestimation of the population.

Other microfossils recovered in lower numbers in the >63 µm fraction include bisaccate pollen grains (*Picea* spp.), diatoms (*Coscinodiscus* spp.), radiolarians, and planktic foraminifera (Table 1.3; Fig. 1.10). The radiolarians were identified as *Spongotrochus glacialis* (Itaki et al., 2003). Being part of the zooplankton dwelling in the open ocean, the radiolarians might be reworked here. Finally, we encountered coccoliths in radiolarian alveoli in one sample (35–34 cm, core HBGC01). The detailed counts of all microfossils are reported in the appendix (Table 1-A.3).

Table 1.3 List of other microfossils.

Other microfossils	HBGC01	PG2303-1	Figure
<i>Picea</i> spp.	x	x	Fig. 1.10-1
<i>Coccolithus pelagicus</i> (Wallich, 1877)	x	-	Fig. 1.10-3
<i>Coscinodiscus</i> spp.	x	x	Fig. 1.10-7
<i>Tintinnopsis fimbriata</i> Meunier, 1919	x	x	Figs. 1.10-4 to 1.10-6
<i>Spogontrochus glacialis</i> Popofsky, 1908	x	-	Fig. 1.10-2

We calculated the concentrations (number of microfossils per gram of sediment; # g⁻¹) for the calcareous and agglutinated benthic foraminifera, ostracods, and tintinnids. Since the size of the observed pollen grains was close to the minimum mesh size (63 µm), if not smaller, we do not report their abundance. The other identified microfossils (diatoms, radiolarians, and planktic foraminifera) were too sparse to calculate concentrations. Fluxes (# cm⁻²a⁻¹) were obtained by multiplying the mass accumulation rates (g cm⁻²a⁻¹) with the microfossil concentrations (# g⁻¹). Minimum and maximum fluxes were calculated, taking into consideration the accumulation rate uncertainties.

The assemblages of benthic foraminifera and ostracods are presented in terms of relative abundance (%). Fatela & Taborda (2002) concluded that a minimum of 100 foraminiferal shells are satisfactory for assemblage assessments of dominant taxa (>5%), but that minimum counts should be 300 specimens for the non-dominant taxa. In all samples, the total counts of foraminifera including calcareous and agglutinated is >100 specimens, except for two samples of core HBGC01 (62 and 94 counted specimens in samples 5–4 cm and 4–3 cm, respectively). The required minimum number for ostracod valves was set at 10.

Figure 1.5 Calcareous benthic foraminifera from the Herschel Basin. **1** *Nonionellina labradorica*. **2** *Quinqueloculina seminulum*. **3** *Triloculina trihedra*. **4** *Stainforthia loeblichii*. **5, 9** *Elphidium clavatum*. **6** *Haynesina nivea*. **7** *Cassidulina reniforme*. **8** *Elphidium hallandense*. **10** *Buccella frigida*. **11** *Eoepnidella pulchella*. **12** *Elphidium asklundi*. **13** *Pyrgo williamsoni*.

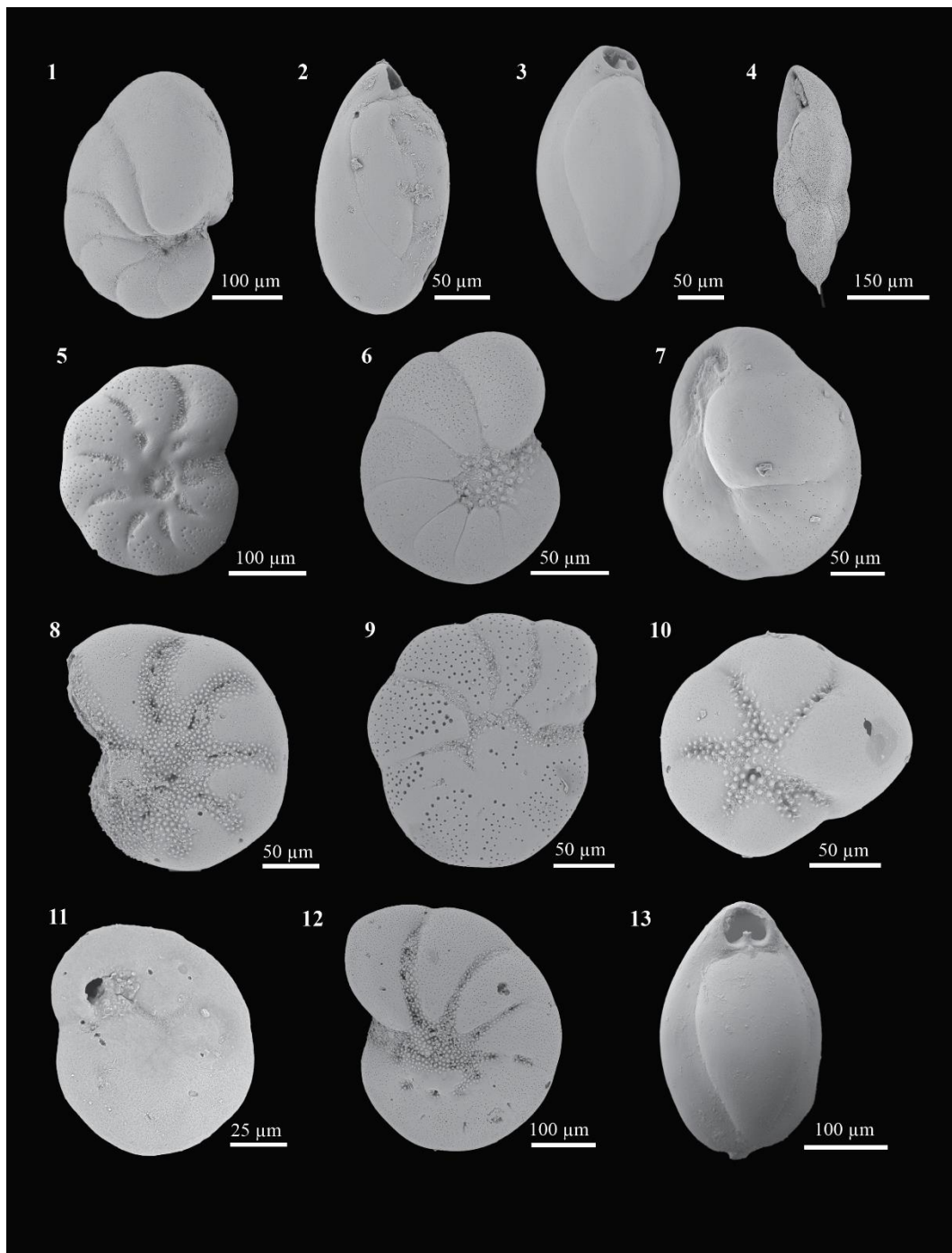


Figure 1.6 Calcareous benthic foraminifera from the Herschel Basin. **1** *Elphidium bartletti*. **2** *Elphidiella groenlandica*. **3** *Islandiella helena*e. **4** *Islandiella norcrossi*. **5** *Quinqueloculina stalkeri*. **6** *Stainforthia feylingi*. **7** *Valvulinaria* sp. **8** *Parafissurina himatiostoma*. **9** *Bolivinellina pseudopunctata*. **10** *Cornuspira involvens*. **11** *Stetsonia horvathi*. **12** *Haynesina orbicularis*.

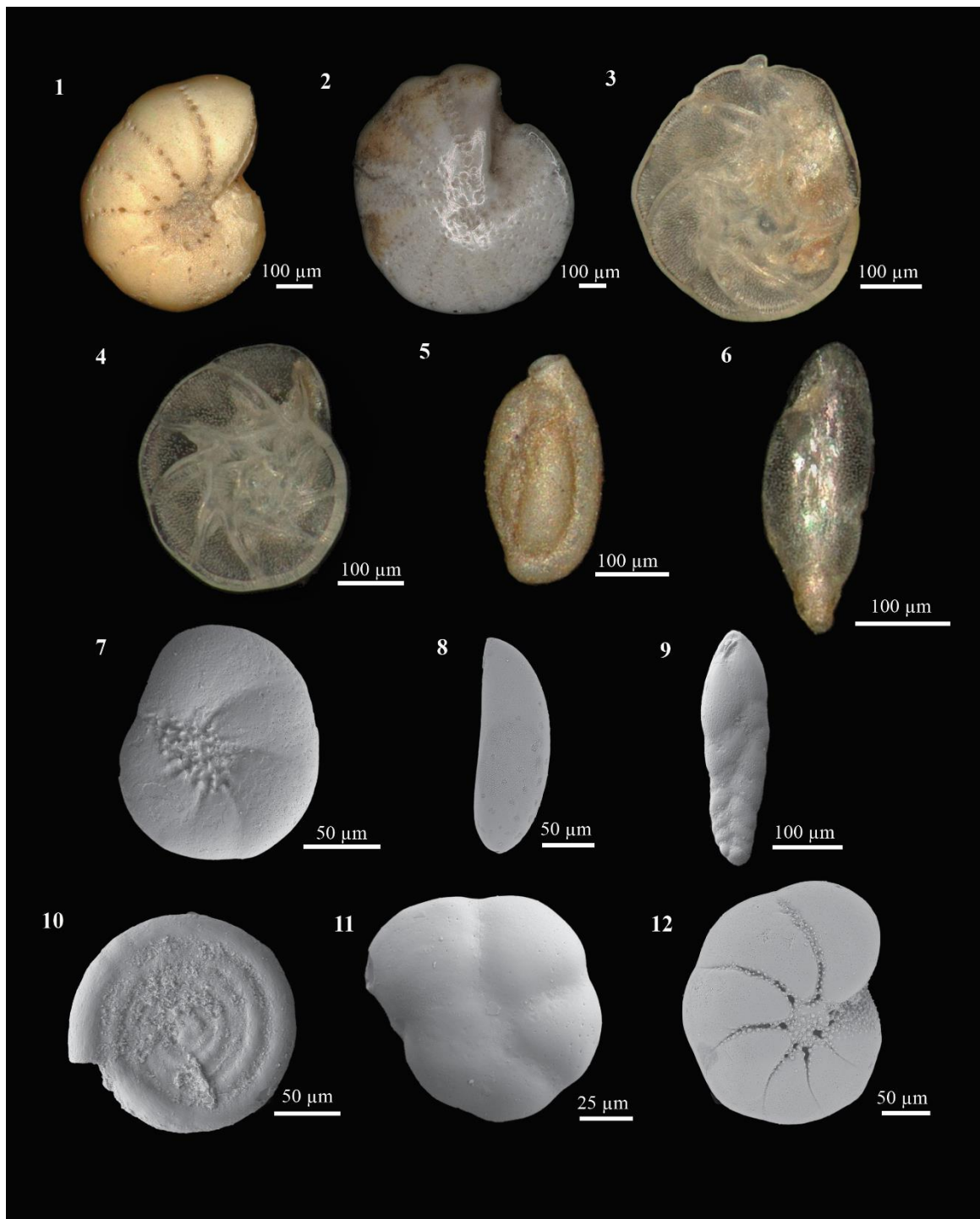


Figure 1.7 Agglutinated benthic foraminifera from the Herschel Basin. **1** *Ammotium cassis*. **2** *Lagenammina difflugiformis*. **3** *Textularia earlandi*. **4** *Spiroplectammina biformis*. **5** *Eggerelloides advenus*. **6** *Portatrochammina karica*. **7** *Textularia torquata*. **8** *Cribrostomoides crassimargo*. **9** *Recurvoides turbinatus*.

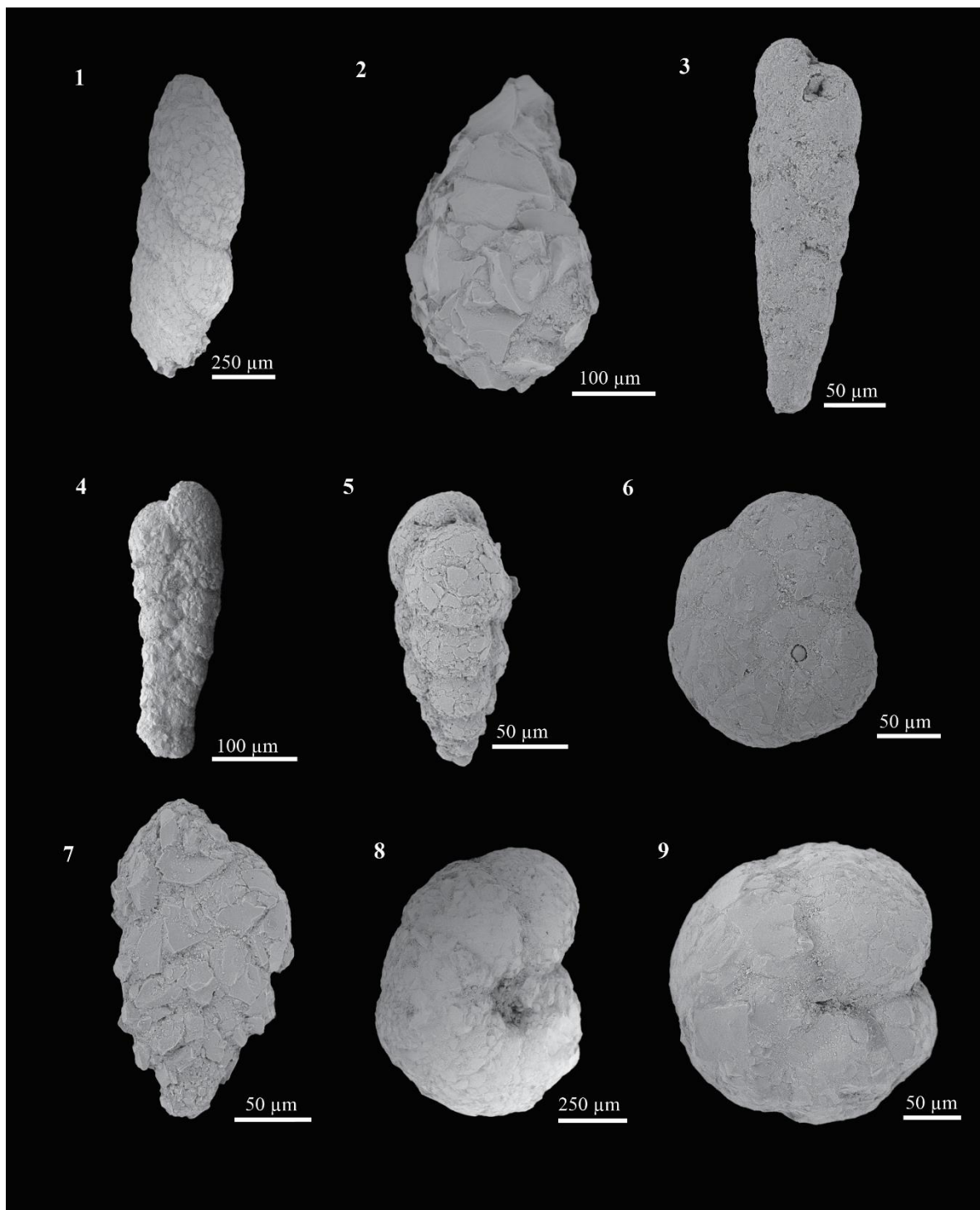


Figure 1.8 Ostracods from the Herschel Basin. **1, 2** *Paracyprideis pseudopunctillata*. **3, 4** *Eucythere* sp. **5** *Sarsicytheridea bradii*. **6** *Heterocyprideis sorbyana*. **7** *Loxoconcha venepidermoidea* (juvenile).

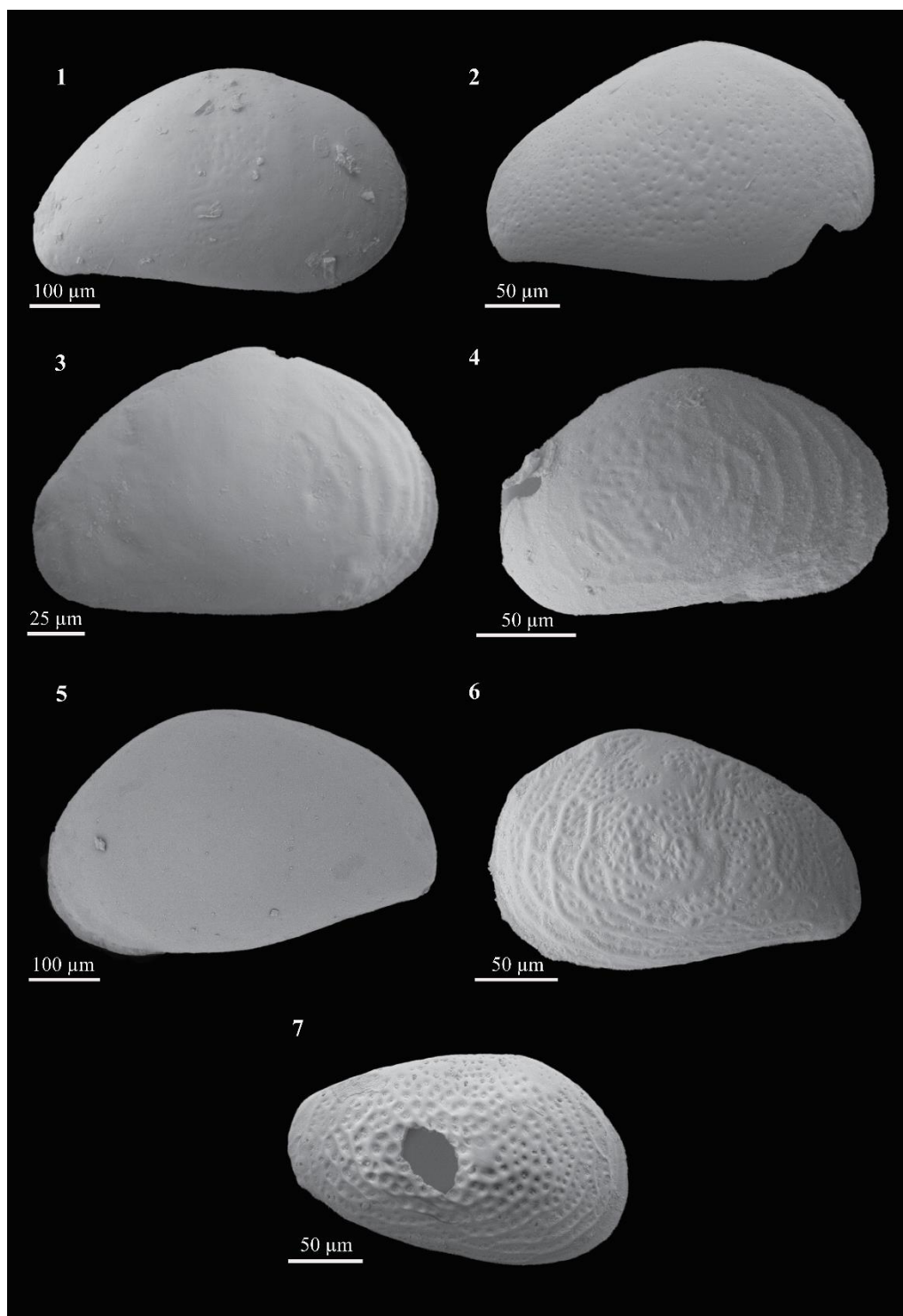


Figure 1.9 Ostracods from the Herschel Basin. **1** *Rabilimis mirabilis* (juvenile). **2** *Cytheropteron sulense*. **3** *Cluthia clutchae*. **4** *Cytheropteron elaeeni*. **5** *Eucytherura delineata*. **6** *Semicytherura complanata*. **7** *Cytheropteron brastadensis/discoveria*. **8** *Cytheropteron suzdalskyi*.

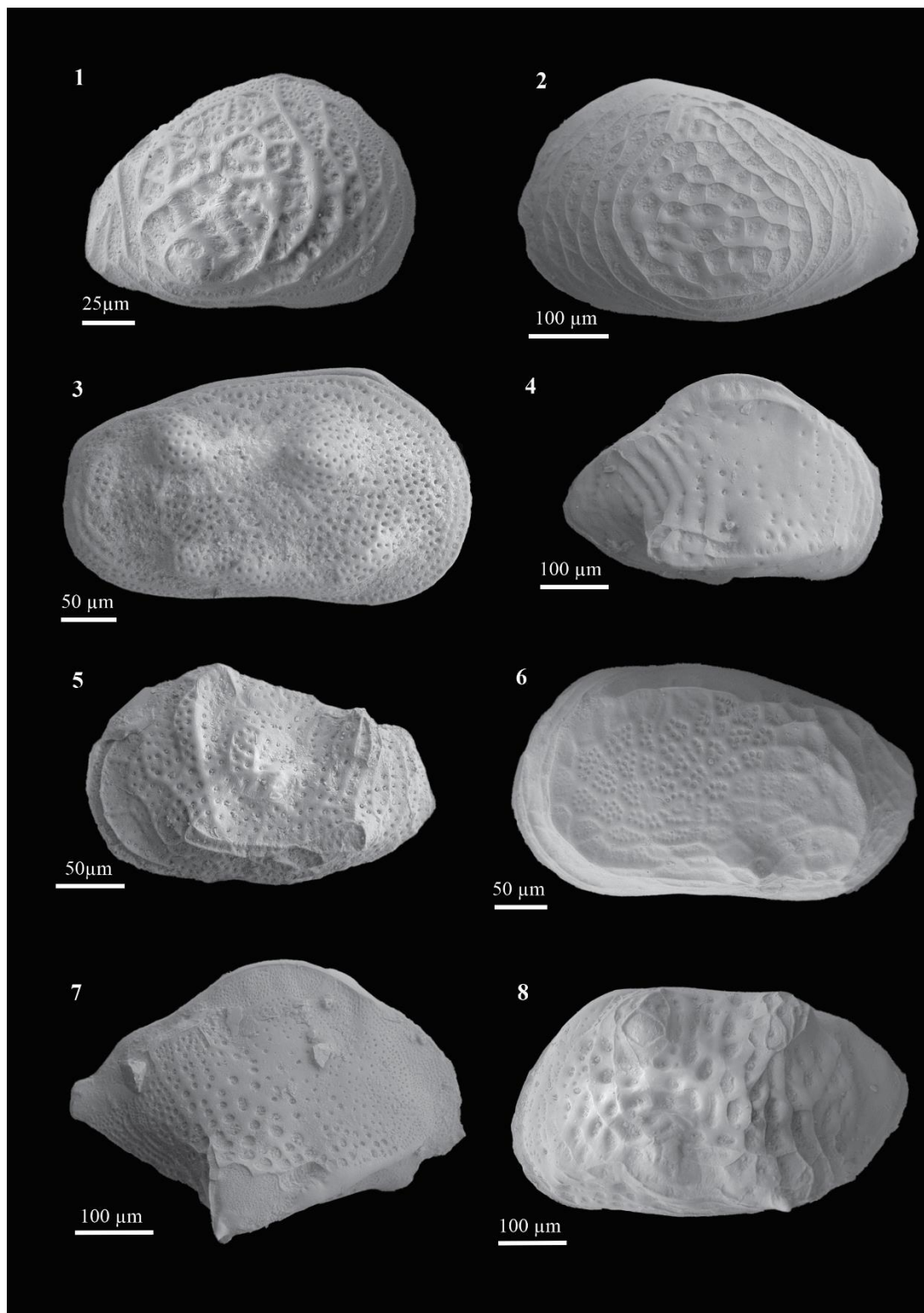
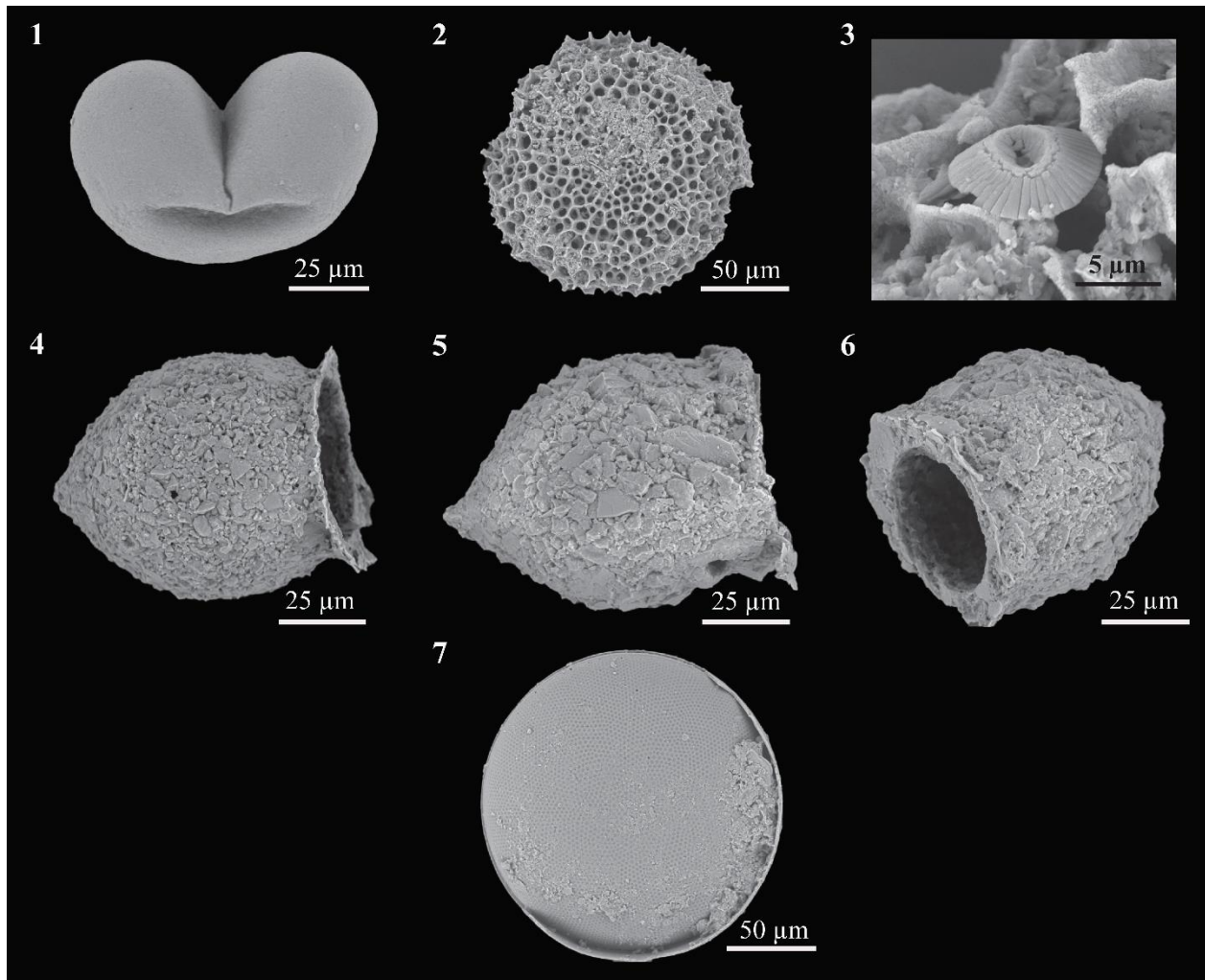


Figure 1.10 Other microfossils from the Herschel Basin. **1** *Picea* sp. **2** *Spongotrochus glacialis*. **3** *Coccolithus pelagicus*. **4, 5, 6** *Tintinnopsis fimbriata*. **7** *Coscinodiscus* sp.



1.3.4 Community diversity and statistical analyses

We calculated the Shannon entropy on the benthic foraminifera and ostracods *Hellinger*-transformed raw counts in the vegan package (Oksanen et al., 2013) under R. The exponential of the Shannon entropy is then used to obtain the Shannon diversity. This diversity considers the abundance and evenness of the species in one sample and is thus less sensitive to rare species, which seemed appropriate for an Arctic Ocean shelf, where transported allochthonous microfossils from nearshore currents or ice rafting may occur (Wollenburg & Kuhnt, 2000). Among the foraminifera, the polymorphinids remained grouped together for the analysis. Benthic foraminifera not identified to species level were removed from the diversity index calculation but included in the percentage and flux calculations. For ostracods, the Shannon diversity was calculated using identification at the genus level.

Redundancy Analyses (RDAs) were performed using the vegan package under R with the Hellinger-transformed raw counts of foraminifera as the response matrix and standardized concentration of sand (%) and microfossil fluxes (for core HBGC01) or microfossil concentrations (for core PG2303-1) as the explanatory variables. For both cores, the RDAs were used to help discriminate ecozones and major shifts in the assemblages. RDAs were not performed on the ostracods due to their low counts especially in core HBGC01 (see section on the Microfossil concentrations and fluxes of core HBGC01).

1.4 Results

1.4.1 Core HBGC01, basin margin

1.4.1.1 Lithology and grain size

The sediments in core HBGC01 are brownish gray with sparse presence of millimetric dark laminations. The CT-scan reveals homogenous sediment from the bottom of the core to 10 cm with signs of bioturbation marked by pale mottles and holes (Figs. 1.4A, 1-A.3). The upper 10 cm show faintly laminated sediments that are discontinuous and of unequal thickness. The content of sand, silt, and clay is almost uniform throughout the record with a mean of $10\pm5\%$, $81\pm4\%$ and $9\pm4\%$, respectively (Fig. 1.11). Sand content increases to a mean of $17\pm7\%$ in the upper 7 cm with a peak of 31% in the surface sample. The samples mean sediment density is $1.06\pm0.20 \text{ g cm}^{-3}$ (Table 1-A.1).

1.4.1.2 Radiogenic isotope activity and age model

The $^{210}\text{Pb}_{\text{sup}}$ (^{226}Ra average) in core HBGC01 is $1.60\pm0.05 \text{ dpm g}^{-1}$ (disintegrations per minute per gram, Fig. 1.4B). A log-decrease of $^{210}\text{Pb}_{\text{ex}}$ can be evidenced between 40 and 10 cm depth (Fig. 1.4C). Such a behavior supports continuous accumulation of sediments. The $^{210}\text{Pb}_{\text{tot}}$ in the upper 10 cm shows oscillations of large amplitude (Fig. 1.4B). Laminations in this layer (Figs. 1.4A, 1-A.3) suggest pulses of reworked sediments with variable $^{210}\text{Pb}_{\text{ex}}$ through coastal erosion and nearshore processes (tides, waves, storms, currents, etc.) of shallow-water environments (<20 m; Hill & Nadeau, 1989; Corbett et al., 2006; Hanna et al., 2014). The ^{137}Cs data record a minimum of $0.05\pm0.02 \text{ dpm g}^{-1}$ near the surface and an increasing trend downcore to a maximum of $0.23\pm0.03 \text{ dpm g}^{-1}$ at 38–37 cm. For the Plum model, we considered a mean accumulation (acc. mean) of 1.23 a cm^{-1} by dividing the ^{210}Pb disintegration constant with the slope of the linear regression of $\log^{210}\text{Pb}_{\text{ex}}$ observed between 40 and 10 cm depth (Sanchez-Cabeza & Ruiz-Fernández, 2012; Fig. 1.4C).

Based on these data, the Plum model provides an age of \sim 1969 CE at the bottom of the core up to the year of coring (2018 CE) at the surface (Fig. 1.4D). The mean sediment accumulation rates average 0.8 ± 0.1 g cm $^{-2}$ a $^{-1}$ below 10 cm and are higher but variable above (Fig. 1.11). The mean estimated age at 38–37 cm is 1973 ± 9 CE (minimum is 1963 CE; Fig. 1.4D), which coincides with increased ^{137}Cs activity (Fig. 1.4B) assigned to the maximum nuclear fallout (Aoyama et al., 2006). Although this ^{137}Cs peak is weakly recorded in core HBGC01, it is clearly recorded in a well-dated core collected in the nearby Ptarmigan Bay (Carnero-Bravo et al., 2021; YC18-PB-SC01; Fig. 1.1D). The Plum output is represented in Figure 1.4D with the CFCS and the CRS models for which a mixed layer of 10 cm was included. The CRS model was also forced to fit with the 1963 CE ^{137}Cs peak (CRS-piecewise). All three models yield comparable results. Hence, the age model presented here is as robust as possible given all the available radiogenic and lithological data.

1.4.1.3 Ecological zonation

Two ecozones are defined in core HBGC01 based on the redundancy analyses of the benthic foraminiferal assemblage, specifically the scores of the first RDA axis (Figs. 1.12, 1.13). They are named Ecozone HBGC01-B (1969–2000 CE) and Ecozone HBGC01-A (2000–2018 CE). Details on the two ecozones can be found below.

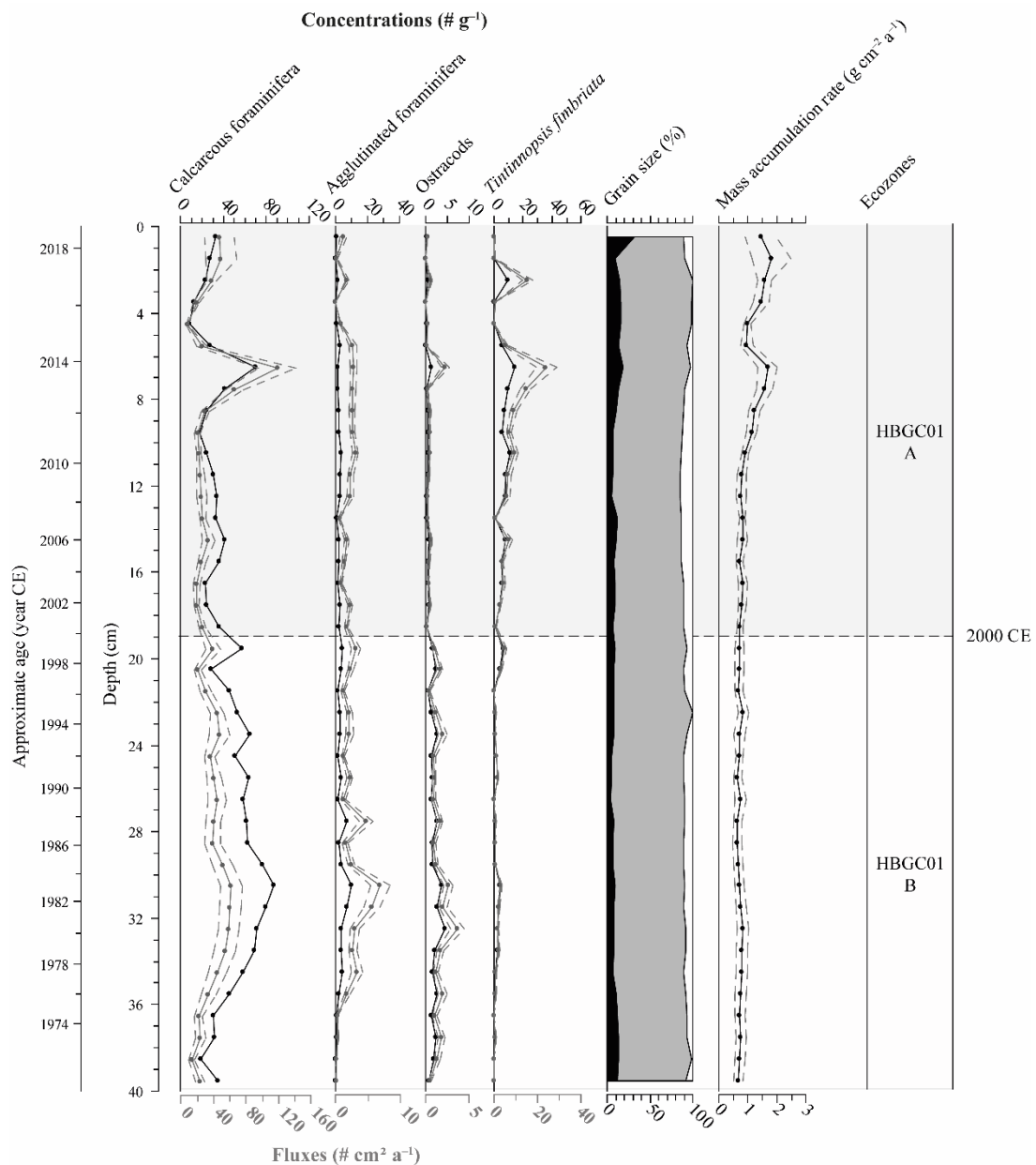
1.4.1.4 Microfossil concentrations and fluxes

Counts of calcareous benthic foraminifera were >100 in most samples of core HBGC01 (288 ± 134 ; Table 1-A.3). This corresponds to concentrations of calcareous benthic foraminifera ranging between 8 and 87 foraminifera g $^{-1}$ throughout the record. Agglutinated foraminifera were found in lower numbers (17 ± 14 ; Table 1-A.3) with concentrations between 0 and 10 g $^{-1}$. The quasi-continuous presence of agglutinated and calcareous foraminifera suggests generally good preservation.

From 1969 to 2000 CE (Ecozone HBGC01-B), the calcareous foraminiferal concentration averaged to 55 ± 17 g $^{-1}$. After 2000 CE (Ecozone HBGC01-A), this average decreased to 30 ± 13 g $^{-1}$. Estimated foraminiferal fluxes are about 37 ± 19 cm $^{-2}$ a $^{-1}$ throughout the record (Fig. 1.11). Agglutinated foraminifera record a mean concentration of 3 ± 2 g $^{-1}$, which corresponds to fluxes between 0 and 7 cm $^{-2}$ a $^{-1}$ (Fig. 1.11). Ostracod concentrations range between 0 and 5 g $^{-1}$ in Ecozone HBGC01-B. Ostracod fluxes are low throughout the record (<3 cm $^{-2}$ a $^{-1}$), particularly in the upper section (2000–2018 CE), where they number <1 g $^{-1}$ of sediment. The mean concentration of *Tintinnopsis fimbriata* is 3 ± 4 g $^{-1}$. From the bottom of the core to 1996 CE, *T. fimbriata* is five times less abundant (1 ± 1 g $^{-1}$) than in the 1996 CE to present interval (5 ± 4 g $^{-1}$).

This corresponds to low fluxes until \sim 1991 CE ($<3 \text{ cm}^{-2} \text{ a}^{-1}$) and a mean of $6 \pm 6 \text{ cm}^{-2} \text{ a}^{-1}$ afterwards (Fig. 1.11), with maxima between 2008 and 2014 ($11 \pm 6 \text{ cm}^{-2} \text{ a}^{-1}$).

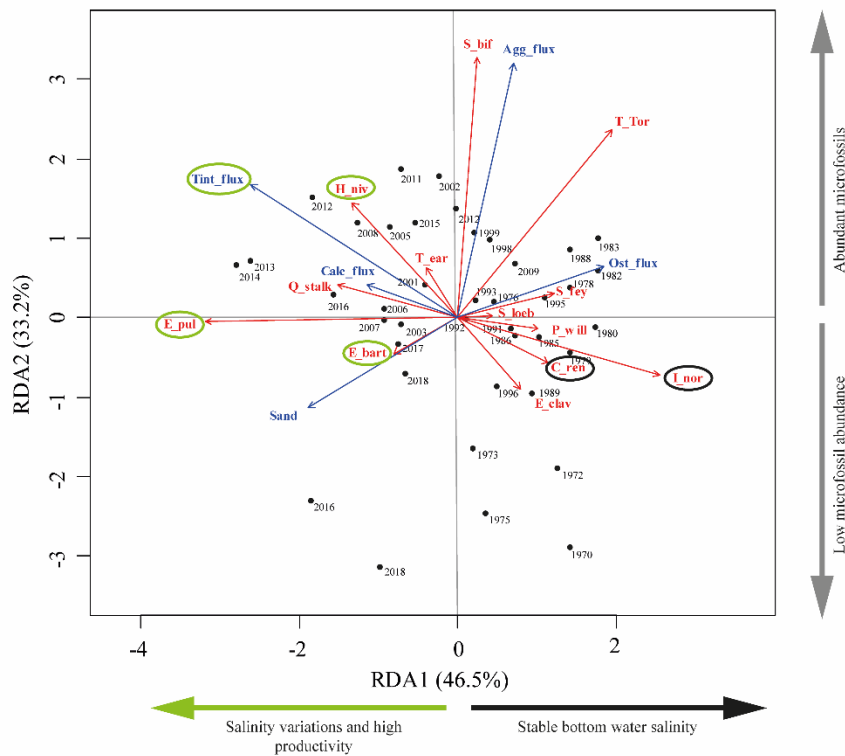
Figure 1.11 Microfossil content (concentrations in black and fluxes in gray), summary grain size data (black = sand; gray = silt; white = clay) and mass accumulation rates in core HBGC01 reported versus depth (cm) and age (year CE). The light gray dotted lines represent the error in accumulation rates and fluxes. The RDA results were used to define the two ecozones.



The most important feature in the microfaunal record of core HBGC01 is the opposite shifts in *T. fimbriata* and ostracod concentrations at ca. 2000 CE (at the boundary between ecozones HBGC01-B and HBGC01-

A; see the last section of the Discussion). We also note that the 2013–2015 CE sediment layer is characterized by maximum calcareous benthic foraminiferal, ostracod, and *T. fimbriata* occurrences, with fluxes reaching up to $119 \pm 23 \text{ cm}^{-2}\text{a}^{-1}$, $2 \text{ cm}^{-2}\text{a}^{-1}$, and $24 \pm 5 \text{ cm}^{-2}\text{a}^{-1}$, respectively (Fig. 1.11).

Figure 1.12 Redundancy analysis of the foraminiferal assemblages (red arrows) and the microfossil fluxes and percentage of sand (blue arrows) in core HBGCO1. The black dots represent the sample scores on each axis. Indicators of saline waters are circled in dark blue, and indicators of low salinity or high productivity are circled in green. See Table 1.4 for the abbreviation corresponding names.



1.4.1.5 Foraminiferal assemblages

Twenty-six (26) species of calcareous benthic foraminifera were identified in core HBGCO1 (Table 1.1; Figs. 1.5, 1.6). In addition, some specimens were identified to the genus level only (i.e., *Valvularia* spp.) or grouped as polymorphinids. The dominant species are *Elphidium clavatum* and *Cassidulina reniforme*, with *Eoepionidella pulchella* and *Haynesina nivea* as occasional accompanying species (Fig. 1.13). A total of seven agglutinated foraminiferal taxa were identified: *Spiroplectammina biformis* and *Textularia torquata* were dominant, while *Textularia earlandi* and *Recurvoides turbinatus* were found occasionally. Rare occurrences of *Lagenammina difflugiformis*, *Portatrochammina karica* (also called *P. bipolaris*), and *Sigmoilopsis schlumbergeri* were noted (Tables 1.1, 1-A.3; Fig. 1.7).

Figure 1.13 Percentages of benthic foraminiferal taxa in core HBGC01 expressed versus depth (cm) and age (year CE). The proportion of agglutinated foraminifera is the percentage of agglutinated foraminifera over the total number of benthic foraminifera (calcareous and agglutinated included). The RDA results were used to define the two ecozones.

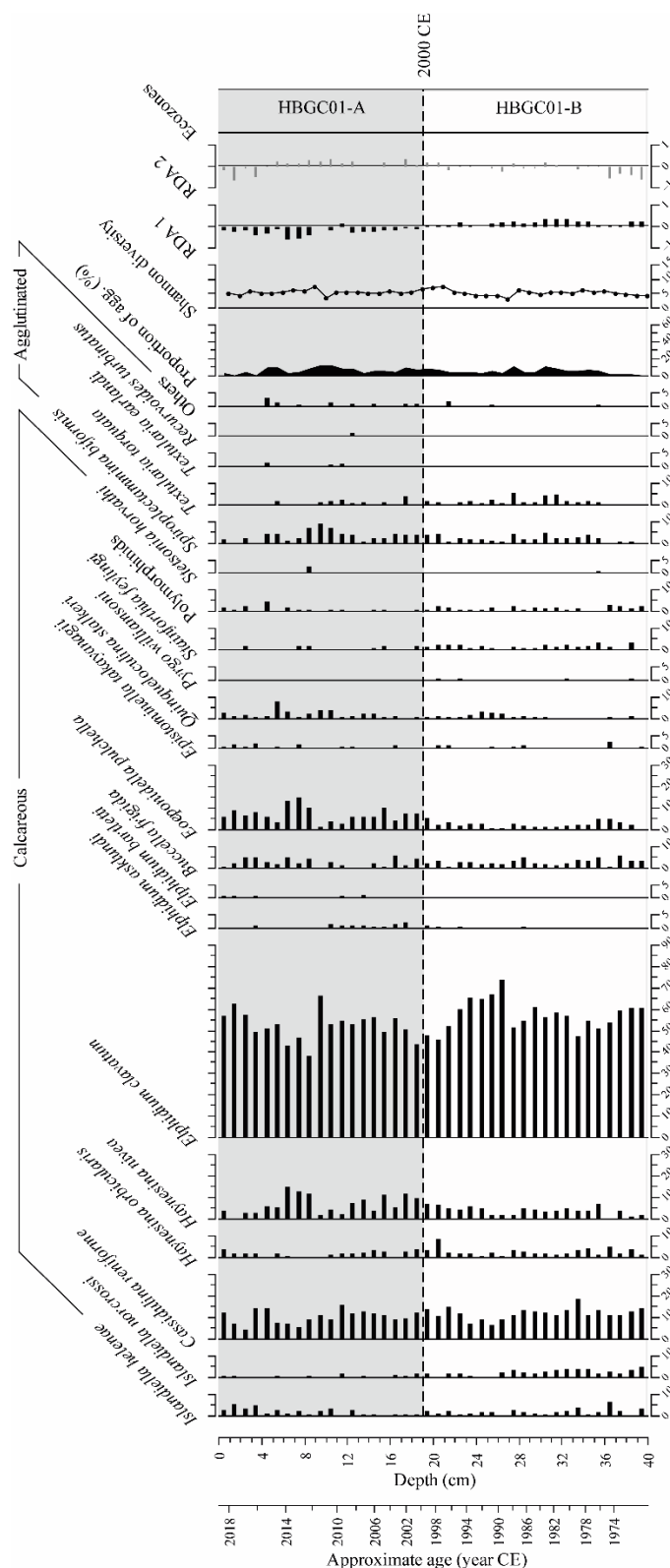
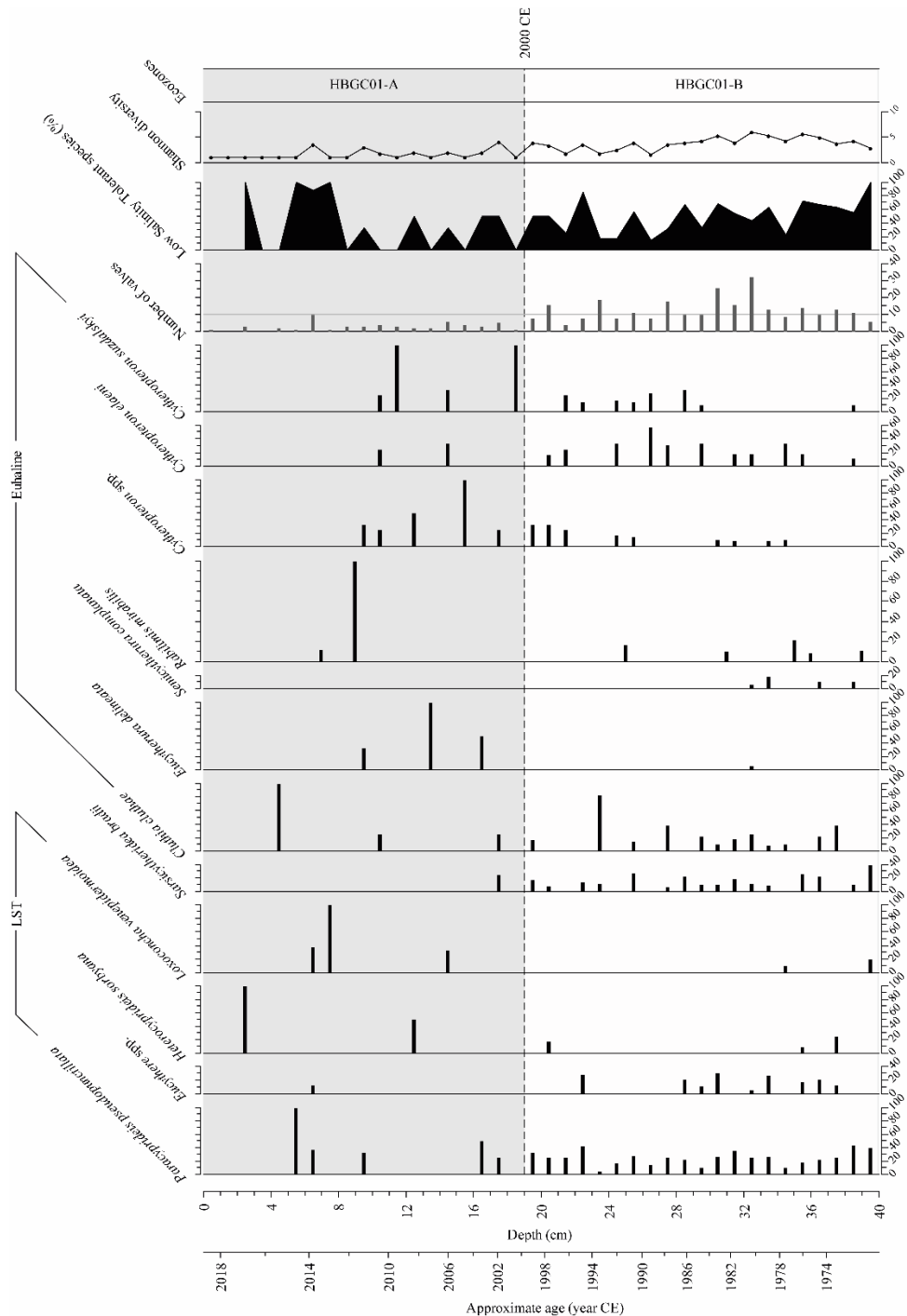


Figure 1.14 Ostracod assemblages versus depth (cm) and age (year CE) in core HBGC01. Low salinity tolerant taxa (LST) and the euhaline taxa (>30 psu) are indicated. *Sarsicytheridea bradii* does tolerate low salinities (<30 psu), but it is not associated with other LST because it is cosmopolitan, living in a wide range of salinity, temperature and oxygen-level conditions (Stepanova et al., 2019; Gemery et al., 2021). Note that assemblages in the upper 19 cm should be considered with caution, as counts are low; <10 valves per sample. The two ecozones were defined from the RDA of the benthic foraminiferal assemblages and are reported as in Figures 1.11 and 1.13.



The first RDA axis explains 46.5% of the variance. It shows an opposite direction of *Eoepionidella pulchella*, *Haynesina nivea*, and *Quinqueloculina stalker* that record negative scores and *Islandiella norcrossi*, *Textularia torquata*, *Stainforthia feylingi*, and *Pyrgo williamsoni* that record positive scores (Fig. 1.12; see Table 1.4 for abbreviation corresponding names). Axis 1 also shows an opposite direction of *Tintinnopsis fimbriata* fluxes and percentage of sand on the negative side and ostracod abundance on the positive side. The second RDA axis explains 33.2% of the variance and shows an opposition between most of agglutinated benthic foraminiferal taxa, which have positive scores, and *Elphidium clavatum*, *Islandiella norcrossi*, and *Cassidulina reniforme*, which have negative scores. Axis 2 is possibly related to microfossil abundances since all microfossil fluxes record positive scores, unlike the sand content.

The species diversity of benthic foraminiferal assemblages is relatively high (Shannon index of 5±1, on average) in core HBGC01 (Fig. 1.13). *Elphidium clavatum* remains dominant throughout the record (40–65%; Fig. 1.13). However, the relative abundance of accompanying species records a significant change around 2000 CE when the RDA axis 1 shifts from positive to negative values (Figs. 1.12, 1.13) at the ecozone HBGC01-B/A boundary. *Haynesina nivea* and *Eoepionidella pulchella* percentages peak synchronously at ~2013 CE, when they together reached 28% of the assemblage (Fig. 1.13).

1.4.1.6 Ostracod assemblages

A total of 11 taxa of ostracods were identified in core HBGC01 (Table 1.2; Figs. 1.8, 1.9). Among those, *Paracyprideis pseudopunctillata* is a recurrent low salinity tolerant (<30 psu) taxon, while *Cluthia cluthae* and *Cytheropteron elaeni* are the dominant euhaline species. In Ecozone HBGC01-B, from the bottom of the core to ~ 2000 CE, *Sarsicytheridea bradii*, *Paracyprideis pseudopunctillata*, and *Cluthia cluthae* are frequent (Fig. 1.14) and *Rabilimis mirabilis*, *Eucythere* spp., and *Semicytherura complanata* occur occasionally. This interval is characterized by relatively high diversity with a Shannon index of 4±1. After 2000 CE (Ecozone HBGC01-A), the occurrence of *Eucytherura delineata* increased (Fig. 1.14), but the general low counts of ostracod valves do not permit statistical assessments.

1.4.2 Core PG2303-1, deep basin

1.4.2.1 Lithology and grain size

Although the sediment of core PG2303-1 was not described, the visual description of a long piston core collected at the same location (core PG2303; Fig. 1-A.2) revealed homogenous gray-brownish sediment (Pfalz, 2017). Sediment density measured on core PG2303-1 revealed almost uniform values with a mean

of 1.1 ± 0.2 g cm $^{-3}$ (Table 1-A.1), suggesting even water content and low sediment compaction. The core is composed of coarser sediments from 20 to 12 cm, corresponding to \sim 1998–2005 CE (Fig. 1.15B), where the sand content reaches a mean of $15 \pm 9\%$, but the average grain size distribution is $9 \pm 8\%$ of sand, $72 \pm 3\%$ of silt, and $18 \pm 5\%$ of clay (Fig. 1.16).

Figure 1.15 (A) $^{210}\text{Pb}_{\text{tot}}$ (purple), ^{226}Ra (orange) and ^{137}Cs (gray) activity profiles in core PG2303-1 and the $^{210}\text{Pb}_{\text{tot}}$ in core HBGC01 (yellow). The dark orange line marks the ^{226}Ra average ($^{210}\text{Pb}_{\text{sup}}$) of core PG2303-1. (B) PG2303-1 core age model obtained with Plum including the mean ages (red line) and the minimum and maximum ages (gray dotted lines). See Figure 1-A.5 for the original age model graph produced by Plum.

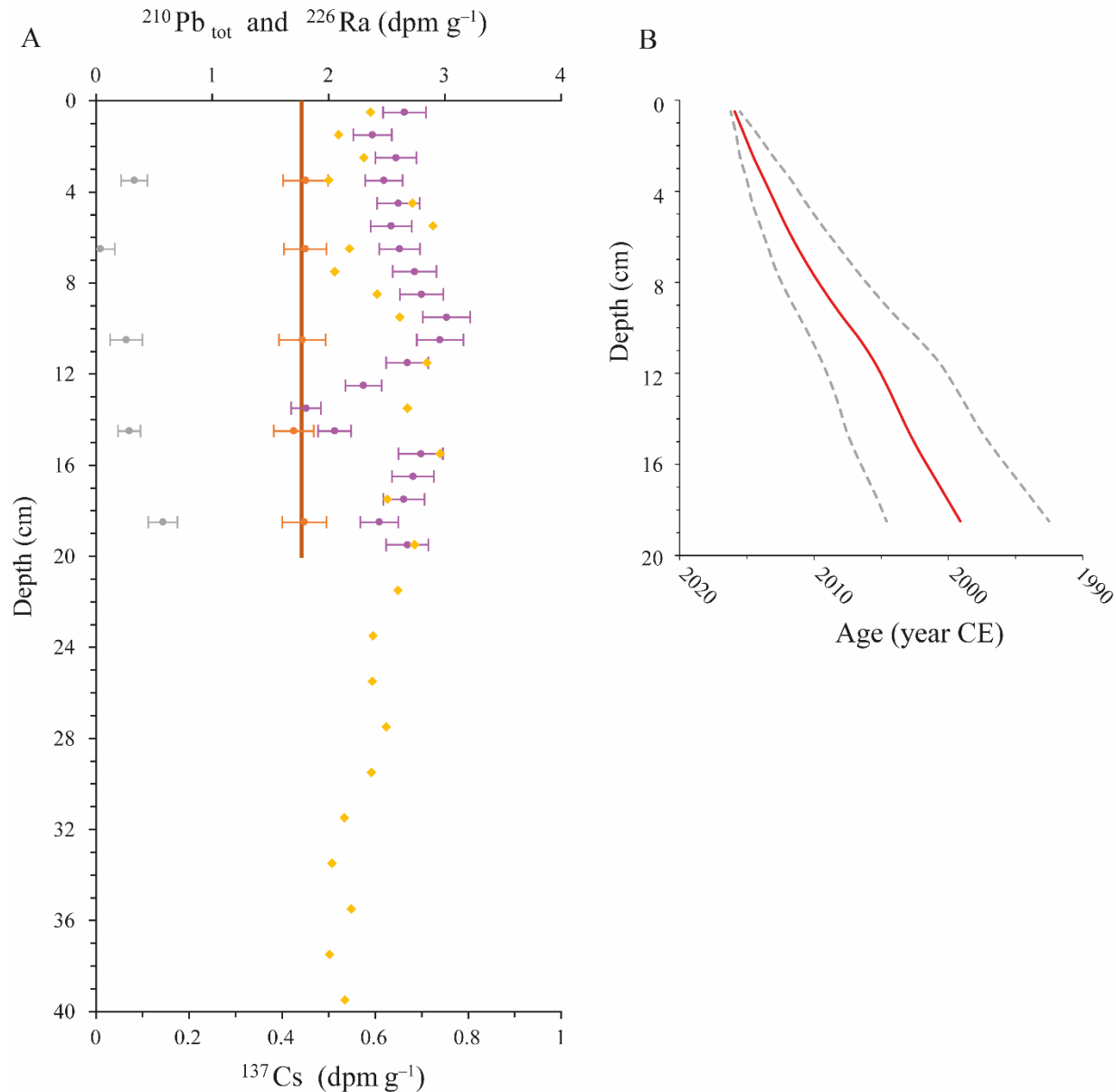


Table 1.4 List of abbreviations used in the Figures 1.12 and 1.17.

<u>B_frig</u>	<i>Buccella frigida</i>
<u>B_pseu</u>	<i>Bolinivellina pseudopunctata</i>
<u>C_inv</u>	<i>Cornuspira involvens</i>
<u>C_ren</u>	<i>Cassidulina reniforme</i>
<u>E_bart</u>	<i>Elphidium bartletti</i>
<u>E_clav</u>	<i>Elphidium clavatum</i>
<u>E_pul</u>	<i>Eoeponidella pulchella</i>
<u>H_niv</u>	<i>Haynesina nivea</i>
<u>H_orb</u>	<i>Haynesina orbicularis</i>
<u>I_hel</u>	<i>Islandiella helena</i>
<u>I_nor</u>	<i>Islandiella norcossi</i>
<u>P_will</u>	<i>Pyrgo williamsoni</i>
<u>Q_stalk</u>	<i>Quinqueloculina stalkeri</i>
<u>R_turb</u>	<i>Recurvoides turbinatus</i>
<u>S_bif</u>	<i>Spiroplectammina biformis</i>
<u>S_fey</u>	<i>Stainforthia feylingi</i>
<u>S_hor</u>	<i>Stetsonia horvathi</i>
<u>S_loeb</u>	<i>Stainforthia loeblichii</i>
<u>T_ear</u>	<i>Textularia earlandi</i>
<u>T_tor</u>	<i>Textularia torquata</i>
<u>Agg_conc</u>	Agglutinated benthic foraminiferal concentrations
<u>Agg_flux</u>	Agglutinated benthic foraminiferal fluxes
<u>Calc_conc</u>	Calcareous benthic foraminiferal concentrations
<u>Calc_flux</u>	Calcareous benthic foraminiferal fluxes
<u>Ost_conc</u>	Ostracod concentrations
<u>Ost_flux</u>	Ostracod fluxes
<u>Sand</u>	Sand concentration (%)
<u>Tint_conc</u>	<i>Tintinnopsis fimbriata</i> concentrations
<u>Tint_flux</u>	<i>Tintinnopsis fimbriata</i> fluxes

1.4.2.2 Radiogenic isotope activity and age model

In core PG2303-1, the $^{210}\text{Pb}_{\text{tot}}$ activity ranges between 1.8 to 3.0 dpm g^{-1} with an average of 2.6 ± 0.3 dpm g^{-1} (Fig. 1.15A). $^{210}\text{Pb}_{\text{tot}}$ decreases down to 1.8 ± 0.1 dpm g^{-1} at 14–13 cm, coinciding with a maximum of sand (31%; Fig. 1.16). The average ^{226}Ra ($^{210}\text{Pb}_{\text{sup}}$) is 1.77 ± 0.03 dpm g^{-1} . The ^{137}Cs activity is <0.14 dpm g^{-1} and all measurements overlap taking in consideration uncertainties.

For the calculation of a Plum age model in core PG2303-1, we used the average age at which the incomplete inventory of $^{210}\text{Pb}_{\text{ex}}$ at 20 cm in core PG2303-1 (17.5 dpm cm^{-2}) was reached in cores HBGC01 and YC18-PB-SC01 (Fig. 1.1D; Sanchez-Cabeza & Ruiz-Fernández, 2012; Carnero-Bravo et al., 2021) and estimated a mean accumulation rate of 0.83 a cm^{-1} . The Plum model suggests that core PG2303-1 is younger than ~ 1998 CE (Fig. 1.15B), indicating that the entire core corresponds in age only to Ecozone HBGC01-A. However, due to the high apparent sediment mixing, the uncertainty in mean accumulation rate, and the short length of the record, we did not interpret the record in terms of age and thus report all results against depth. For the same reason, the mass accumulation rate and microfossil fluxes were not calculated.

1.4.2.3 Ecological zonation

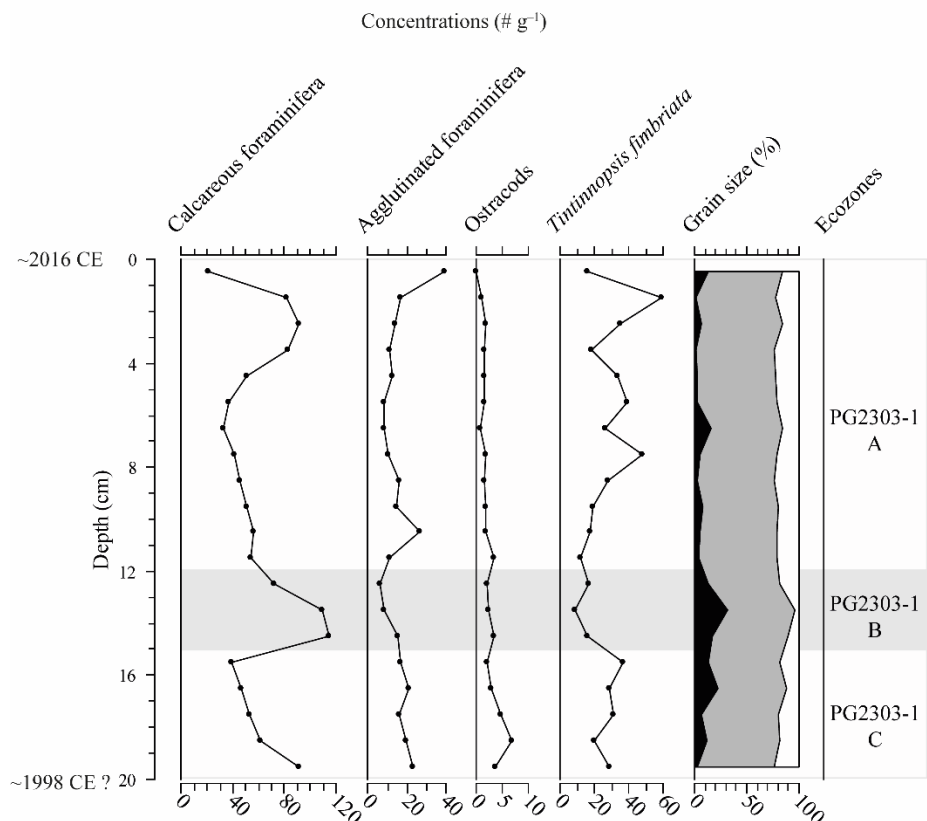
Despite the short time span covered by the core, the high sample resolution permitted the definition of three ecozones based on the RDA (Figs. 1.17, 1.18). Ecozone PG2303-1-C corresponds to the 15–20 cm core depth interval, Ecozone PG2303-1-B covers from 12 to 15 cm, and Ecozone PG2303-1-A encompasses the upper 12 cm.

1.4.2.4 Microfossil concentrations

Counts of calcareous foraminifera range between 208 and 646 specimens per sample ($\sim 6\text{--}7 \text{ g}$ of dry sediment; mean of 330 ± 149 specimens; Table 1-A.3). More than 50 agglutinated foraminifera were counted in each sample (mean of 80 ± 28 ; Table 1-A.3). A mean of 11 ± 7 ostracod valves was identified per sample with a maximum of 34. *Tintinnopsis fimbriata* was abundant with >49 specimens counted in each sample. These counts produce mean concentrations of 62 ± 26 calcareous foraminifera g^{-1} and 16 ± 8 agglutinated foraminifera g^{-1} , which suggest good microfossil preservation with depth in the Herschel Basin. Mean ostracod and *Tintinnopsis fimbriata* concentrations are $2\pm 2 \text{ g}^{-1}$ and $27\pm 13 \text{ g}^{-1}$, respectively.

There are three abundance peaks of calcareous foraminifera ($>80 \text{ g}^{-1}$): at the bottom of the core, at 15–13 cm (approximately corresponding to Ecozone PG2303-1-B), and at 3–1 cm. The agglutinated foraminiferal concentrations do not vary, but the ostracod abundance seems to diminish towards the top of the core, while *Tintinnopsis fimbriata* records maximum concentrations in the upper part of the core (Fig. 1.16).

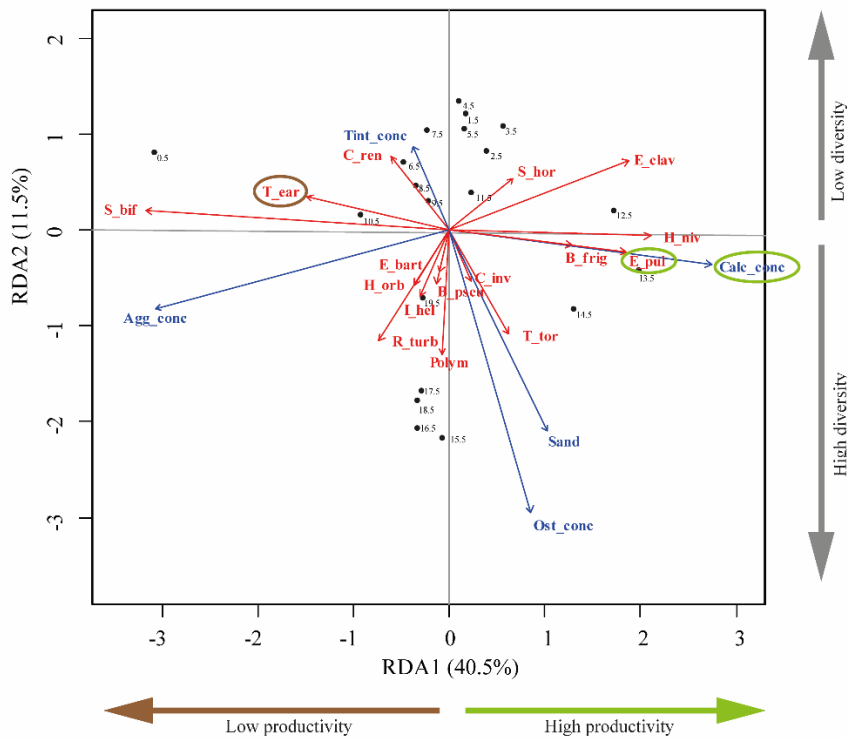
Figure 1.16 Microfossil content and grain size data (black = sand; gray = silt; white = clay) in core PG2303-1 reported versus of depth (cm). The RDA results were used to define the three ecozones.



1.4.2.5 Foraminiferal assemblages

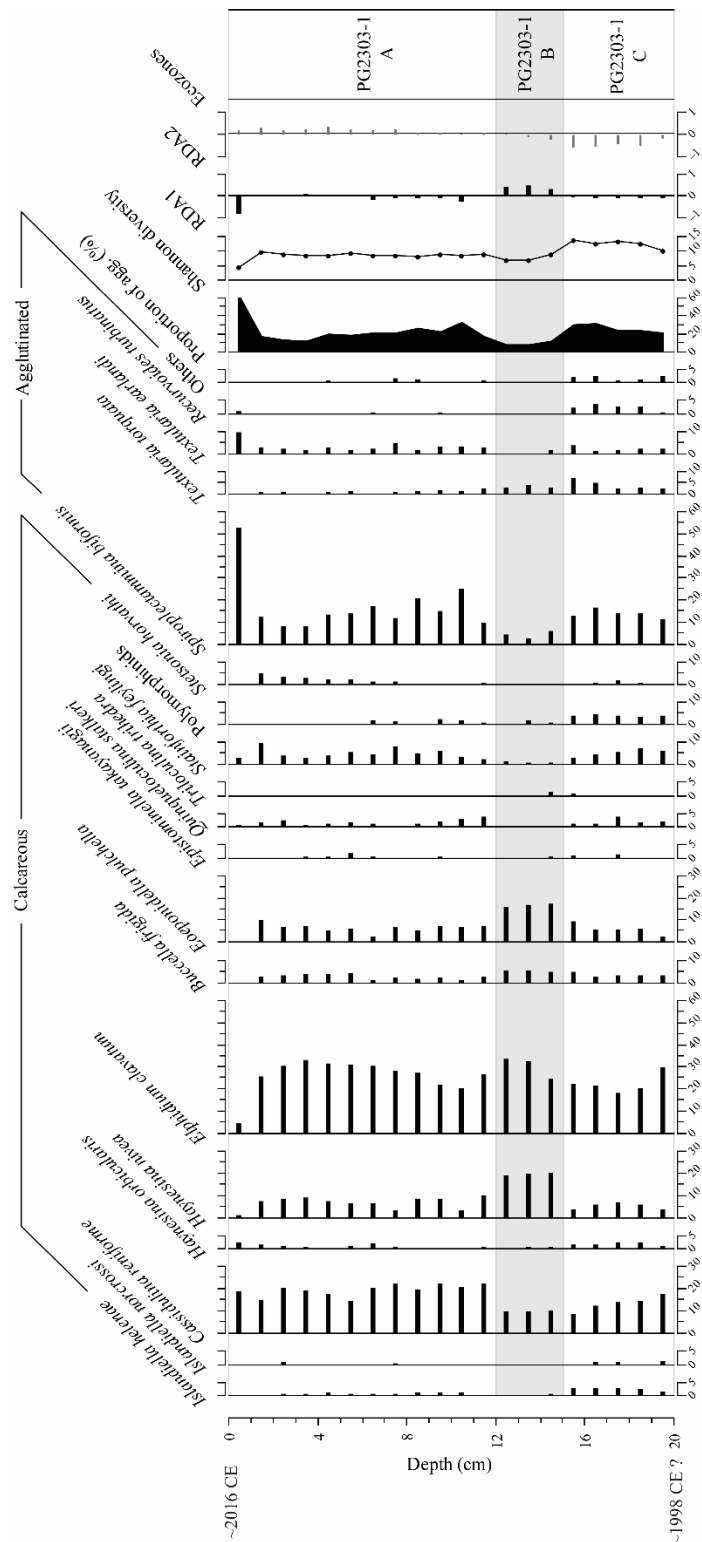
All calcareous benthic foraminiferal taxa observed in core PG2303-1 also occur in core HBGC01 (Table 1.1; Figs. 1.5, 1.6), with 24 taxa in total. As in core HBGC01, *Elphidium clavatum* and *Cassidulina reniforme* are the dominant species throughout the record, comprising 20–35% and 10–20% of the assemblages, respectively (Fig. 1.18). Accompanying species are *Haynesina nivea* (5–20%) and *Eoepionidella pulchella* (5–20%) and to a lesser extent *Stainforthia feylingi* (1–10%) and *Buccella frigida* (0–5%). There are nine species of agglutinated foraminifera, including *Spiroplectammina biformis* that dominate, together with *Textularia earlandi*, *Textularia torquata* and *Recurvooides turbinatus*, which are the main accompanying species. The occurrence of other species including *Cribrostomoides crassimargo* and *Eggerelloides advenus* is occasional (Tables 1.1, 1-A.3; Fig. 1.7). The Shannon diversity index is higher than in core HBGC01 with a mean of 9±2 (Fig. 1.18).

Figure 1.17 Redundancy analysis of the foraminiferal assemblage (red arrows) and the microfossil concentrations and percentage of sand (blue arrows) in samples from core PG2303-1. The black dots represent the sample scores on each axis. Indicators of high productivity are circled in green and of low productivity are circled in brown. See Table 1.4 for the abbreviation corresponding names.



The RDA reveals an inverse relationship of the abundance of the agglutinated taxa *Spiroplectammina biformis* and *Textularia earlandi* and the calcareous taxa *Elphidium clavatum*, *Haynesina nivea*, *Eoepionidella pulchella*, and *Buccella frigida* on the first axis (40.5% of the variance; Fig. 1.17; see Table 1.4 for the abbreviation corresponding names). Accordingly, the concentrations of agglutinated foraminifera have a negative score, while calcareous foraminiferal concentrations score positively. The second axis, which explains 11.5% of the variance, shows an opposite direction of ostracod concentrations, sand (%) and the abundance of numerous foraminiferal taxa on the negative side with *Tintinnopsis fimbriata* concentrations, *Cassidulina reniforme* and *Elphidium clavatum* on the positive side (Fig. 1.17).

Figure 1.18 Percentages of benthic foraminiferal taxa in core PG2303-1 expressed versus depth (cm). The proportion of agglutinated foraminifera is the percentage of agglutinated foraminifera over the total number of benthic foraminifera (calcareous and agglutinated included). The RDA results were used to define the three ecozones.

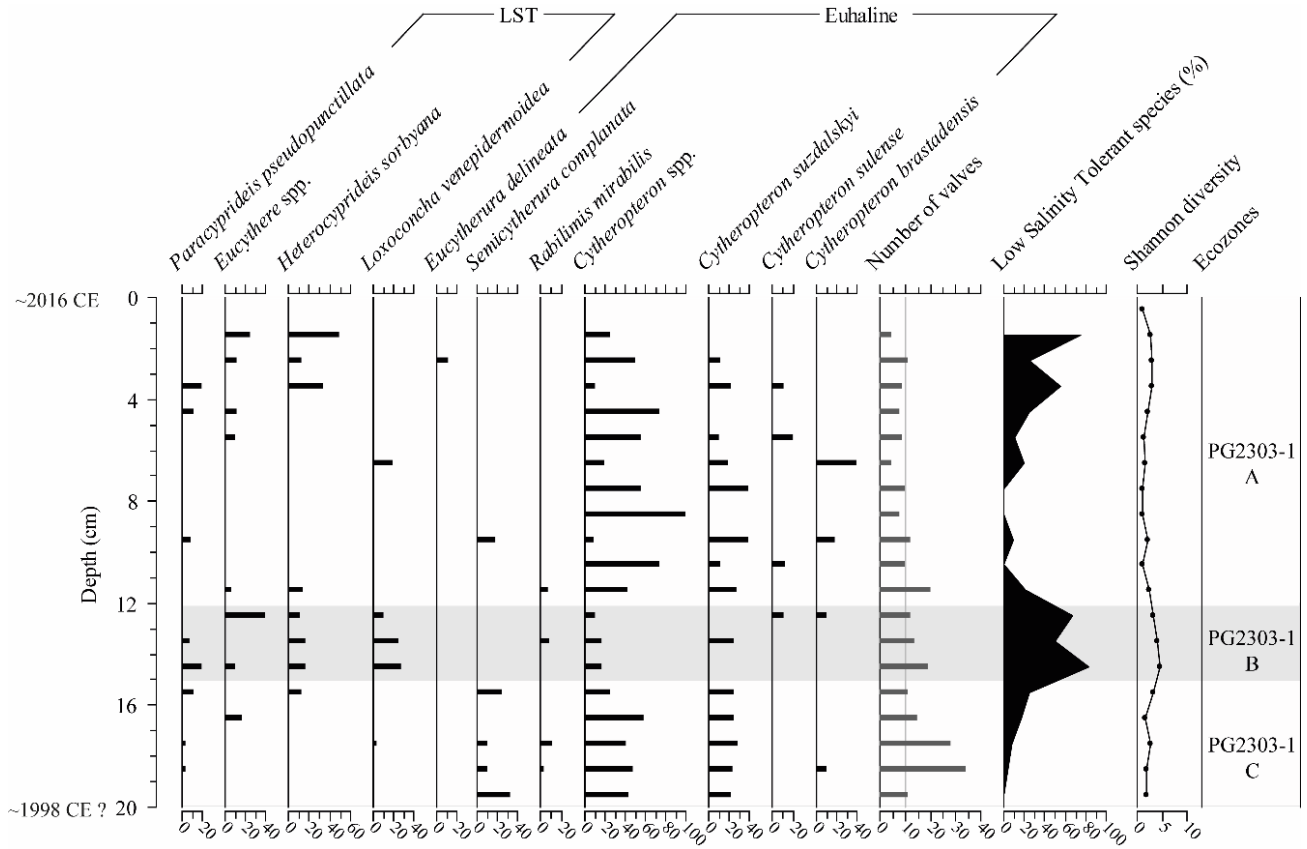


In Ecozone PG2303-1-C, from 20 to 15 cm, the diversity is the highest of the core (Shannon diversity index >10; Fig. 1.18). Thus, the RDA Axis 2 scores negatively as several taxa reach maximum percentages, including *Islandiella norcrossi*, *Islandiella helenae*, polymorphinids, and *Recurvooides turbinatus* (Figs. 1.17, 1.18). In Ecozone PG2303-1-B, from 15 to 12 cm, the RDA axis 1 is positive due to abundant *Haynesina nivea*, *Eoepionidella pulchella*, and *Buccella frigida* (Figs. 1.17, 1.18). Finally, in Ecozone PG2303-1-A, from 12 cm to the top of the core, the RDA axis 1 is close to nil, while there is a slight increase of *Cassidulina reniforme* and *Spiroplectammina biformis*, *Quinqueloculina stalker*, *Stainforthia feylingi*, and *Textularia earlandi* are also present. In the 8 to 1 cm section, the continuous occurrence of *Stetsonia horvathi* is notable (mean of 3±1%; Fig. 1.18). The uppermost sample differs from all others with negative RDA axis 1 score, abundant agglutinated taxa and low percentages of *Elphidium clavatum*, together with the disappearance of *Buccella frigida* and *Eoepionidella pulchella*. This atypical assemblage recorded in the upper cm of the core might relate to the winter season rather than mean annual conditions, taking into consideration the very high sedimentation rates and the date of coring (April 2016).

1.4.2.6 Ostracod assemblages

The ostracod assemblages in core PG2303-1 contain 11 taxa (Table 1.2; Figs. 1.8, 1.9). Among those, *Cytheropteron brastadensis (discoveria)* and *Cytheropteron sulense* are restricted to this core, while *Cluthia cluthae* and *Sarsicytheridea bradii* are exclusive to the HBGC01 core. The most common species in core PG2303-1 are *Cytheropteron* spp. and *Cytheropteron suzdalskyi*. The mean Shannon diversity index is 2±1. The three ecozones as defined by the RDA of the foraminiferal assemblages (Figs. 1.17, 1.18) also reflect changes in the ostracod assemblages. The 20–15 cm interval, Ecozone PG2303-1-C, is dominated by euhaline taxa (Fig. 1.19), notably *Semicytherura complanata*, *Cytheropteron suzdalskyi*, and *Cytheropteron* spp., and ostracod concentrations reach maximum values (Figs. 1.16, 1.17). From 15 to 12 cm, in Ecozone PG2303-1-B, low-salinity tolerant taxa, including *Heterocyprideis sorbyana* and *Loxoconcha venepidermoidea*, constitute most of the assemblages (Fig. 1.19). The species diversity is maximum in this interval, as the samples contain both low-salinity tolerant and euhaline taxa. In the first part of Ecozone PG2303-1-A, from 12 to 6 cm, the assemblages are dominated by euhaline taxa, but with low occurrence of *Semicytherura complanata*. Finally, in the upper seven centimetres of Ecozone PG2303-1-A, corresponding to the level where *Stetsonia horvathi* increases in the foraminiferal assemblage (Fig. 1.18), the ratio between low-salinity tolerant and euhaline ostracods is approximately even.

Figure 1.19 Ostracod assemblages versus depth (cm) in core PG2303-1. The low salinity tolerant taxa (LST) and the euhaline taxa (>30 psu) are indicated. Note that occurrences in assemblages with less than 10 valves should be considered with caution. The three ecozones were defined from the RDA of the benthic foraminiferal assemblages and are reported as in Figures 1.16 and 1.18.



1.5 Discussion

1.5.1 Basin margin vs. deep basin

1.5.1.1 Bottom water masses

With a water depth of 18 m, site HBGC01 is located close to the depth of the summer halocline (Fig. 1.2A). Vertical mixing in response to storm events and tidal dynamics may cause the upper layer (~22–24 psu and >0°C) to mix with the subsurface waters (30 psu and ~0°C; Hill & Nadeau, 1989; Rainville & Woodgate, 2009; Fig. 1.2A). Hence, the bottom waters at this site may be influenced by the low salinity surface waters that also carry a high concentration of suspended particles either from the Mackenzie River (Doxaran et al., 2015; Ehn et al., 2019; Juhls, 2021) or from terrestrial sources in relation with coastal erosion and resuspension (Klein et al., 2019; Jong et al., 2020). In contrast, core PG2303-1 was retrieved from 32 m water depth, which is significantly deeper than the summer halocline. Consequently, this deep and more offshore site is less likely to be affected by turbidity than the nearshore shallower core HBGC01 (Fig. 1.1D).

see the last section of the Discussion). Turbidity in surface waters could have negative impacts on primary production (Anthony et al., 2004; Retamal et al., 2008; Bonsell & Dunton, 2018; Lewis et al., 2020). In winter, however, below the two-meter-thick land-fast ice, subsurface waters return to saline (32–33 psu) and frigid (<0°C) conditions and sites HBGC01 and PG2303-1 are both bathed by the same water mass, recording values close to the annual mean of the 32 m deep site PG2303-1 (Figs. 1.2A, B).

In addition to bottom water salinity and turbidity in summer, the two study sites are subject to different bottom current speeds and dynamics. The higher clay content in core PG2303-1 compared to core HBGC01 suggests a higher proportion of suspended sediments deposited by settling in the deeper part of the Herschel Basin, and thus a quieter depositional environment than at the basin margin (Figs. 1.11, 1.16). Moreover, the thin laminations in the top 10 cm of the shallow core HBGC01 (Figs. 1.4A, 1-A.3) could suggest a more dynamic depositional environment, possibly linked to events of resuspension and reworking (Hill & Nadeau, 1984; Corbett et al., 2006; Hanna et al., 2014) during the last decade. Laminations in sediment cores may also refer to oxygen depletion, but supplementary information would be needed to address this assumption.

1.5.1.2 Microfaunal assemblages

In general, the benthic foraminiferal and ostracod assemblages of the two studied cores compare well with assemblages described from other Arctic shelf settings (McDougall et al., 1986; Reimnitz et al., 1993; Wollenburg & Mackensen, 1998; Wollenburg & Kuhnt, 2000; Polyak et al., 2002; Scott et al., 2008b, Husum et al., 2015; Gemery et al., 2017). The dominance of *Elphidium clavatum*, the abundance of agglutinated taxa such as *Spiroplectammina biformis* and *Textularia* spp., and the presence of taxa tolerant to low salinity such as *Haynesina orbicularis*, *Buccella frigida*, and polymorphinids, are typical of Arctic shelf environments (Polyak et al., 2002; Scott et al., 2008a; Figs. 1.13, 1.18). However, in our study, we report for the first time the occurrence of the accompanying taxon *Haynesina nivea* on the Beaufort Sea shelf. This species has been associated with shallow and low salinity environments (Madsen & Knudsen, 1994; Luoto et al., 2011; Voltski et al., 2015; see section below on sea ice and salinity).

The two sites also show some important differences in the microfossil assemblages. The shallow core HBGC01 holds high relative abundance of taxa tolerant to river proximal and low salinity environment such as *Elphidium clavatum* (cf. Hald & Steinsund, 1996; Hald & Korsun, 1997; Polyak et al., 2002; Knudsen et al., 2008), *Islandiella helena* (cf. Cage et al., 2021), and *Elphidium bartletti* (cf. Polyak et al., 2002). The

occurrence of *Elphidium asklundi* in core HBGC01 probably also suggests a tolerance to low salinities. In contrast, *Cassidulina reniforme*, related to cold and saline conditions (Hald & Korsun, 1997; Polyak et al., 2002), is more abundant at the deeper site of core PG2303-1 (Fig. 1.18), where euhaline ostracods also dominate (Fig. 1.19). *Stainforthia feylingi* is also more abundant in core PG2303-1 than in core HBGC01, which might be due to the higher salinities and closer proximity to productive sea-ice margins (cf. Seidenkrantz, 2013) evident for the central Herschel Basin compared to the near-coastal area. The differences in microfaunal assemblages at the two study sites probably reflect the water depth, with increased seasonal salinity gradient and bottom water instability at the shallower site HBGC01, proximal to the summer halocline and wave action. Salinity variations at site HBGC01 may partly control the changes in foraminiferal assemblages, which is illustrated by the low-salinity tolerant taxa *Haynesina nivea* and *Elphidium bartletti* that vary in opposite to *Islandiella norcrossi* and *Cassidulina reniforme* (Fig. 1.12). However, changes in foraminiferal assemblages in the Herschel Basin would primarily be linked with food supply as shown by the occurrence of *Eoepionidella pulchella*, a foraminiferal taxon indicative of high primary productivity (Knudsen et al., 2008; Wollenburg & Kuhnt, 2000) highly weighted on the first axis of both cores (Figs. 1.12, 1.17). This relationship is especially clear in core PG2303-1, as *E. pulchella* is inversely related to *Textularia earlandi*, a low trophic requirement taxon (Jennings et al., 2020; Fig. 1.17).

The sediment substrate and bottom currents may also affect the assemblages. The coarser-grained sediments of the shallow core HBGC01 go together with abundant *Elphidium bartletti* (Polyak et al., 2002). The ostracod *Sarsicytheridea bradii*, which is only observed in core HBGC01 (Fig. 1.14), may also prefer coarser substrates (Gemery et al., 2021). Moreover, *Sarsicytheridea bradii* can tolerate a wide range of salinity, temperature, and oxygen levels (Stepanova et al., 2019; Gemery et al., 2021), which better corresponds to the more variable conditions that likely characterize the shallow HBGC01 core site. Early instars of ostracods are less abundant in core HBGC01 than core PG2303-1 (mainly *Cytheropteron* spp.; Figs. 1.14, 1.19), which also suggest a higher-energy environment in the basin margin (Whatley, 1983).

High sand content could potentially point to preservation issues and/or unfavorable enhanced bottom currents at the shallow site HBGC01, as it is opposed to microfossil abundances, especially agglutinated foraminifera (Fig. 1.12). This relationship is expressed in a few samples at the core top and in the 1969–1975 CE interval (Figs. 1.11–1.13). Similarly, particularly abundant sand in Ecozone PG2303-1-B (>~10%; Fig. 1.16) may have negatively affected the preservation condition or productivity of the agglutinated foraminifera (Figs. 1.16, 1.18). However, the sand content at the deeper site PG2303-1 seems to be

associated to a certain extent with increased primary productivity, as it reaches maximum values in Ecozone PG2303-1-B concurrently with high calcareous foraminiferal concentrations and *E. pulchella* abundances (Figs. 1.16–1.18). The sand content is also relatively high in Ecozone PG2303-1-C, accompanied by high ostracod concentrations (Fig. 1.16) and abundant *Semicytherura complanata* (Fig. 1.19). Because *Semicytherura complanata* has been associated with polynyas (Stepanova et al., 2003), we hypothesize the presence of a polynya-type environment in Ecozone PG2303-1-C with enhanced brine rejections that lead to vertical mixing (Smith & Morison, 1998) and oxygenated bottom waters, in addition to high salinity. Accordingly, *Islandiella norcrossi*, which prefers saline stable bottom waters (Cage et al., 2021), reaches its maximum occurrence (Fig. 1.18). Such conditions might have contributed to maximum foraminiferal species diversity at the bottom of the Herschel Basin (Fig. 1.18).

1.5.2 The ~2000 CE shift

1.5.2.1 Sea ice and salinity

An important shift is recorded in the shallow core HBGC01 at the transition between ecozones HBGC01-B and HBGC01-A (~2000 CE). It is marked by a transition from abundant *Islandiella norcrossi* and *Cassidulina reniforme* that have preference for salinity >30 psu (Polyak et al., 2002; Cage et al., 2021) to assemblages characterized by *Elphidium bartletti* and *Haynesina nivea* that are both tolerant to low salinity (Fig. 1.13; Madsen & Knudsen, 1994; Polyak et al., 2002; Luoto et al., 2011; Voltski et al., 2015). Hence, the shift at ~2000 CE seems to correspond to a transition from a relatively stable and saline environment to an environment marked by lower salinity and unstable conditions. The occurrence of *H. nivea* seems particularly significant to explain this transition. Hence, in modern assemblages of the Scoresby Sound and the White Sea, *H. nivea* was retrieved in very shallow environments (<10 m), where high seasonal fluctuations occur with warm and low saline summer surface waters and currents fostering high sand content (Madsen & Knudsen, 1994; Voltski et al., 2015). In paleoceanographic studies, this species was often related to shallow marine environments (Feyling-Hanssen & Ulleberg, 1984; Hansen & Knudsen, 1995; Luoto et al. 2011). In Ecozone PG2303-1-B, *H. nivea* reaches maximum values concomitantly with low salinity tolerant ostracod taxa such as *Loxoconcha venepidermoidea* and *Heterocyprideis sorbyana* (Figs. 1.18, 1.19).

At the shallow site HBGC01, sea ice may foster stable conditions in the bottom water, as it is a natural barrier for waves and winds (Overeem et al., 2011; Schulze & Pickart, 2012). The transition towards lower mean summer sea-ice concentrations after 2006 CE (Fig. 1.3) follows slightly the shift in microfaunal

assemblages dated at 2000±4 CE and appears closely synchronous with the near-disappearance of *Islandiella norcrossi* (Fig. 1.13). The benthic foraminifera *I. norcrossi* in the lower part of core HBGC01 could thus be an indirect indicator of sea ice-induced stratification and increased bottom-water stability at this site prior to 2006 CE. In contrast, the high sand fraction may indicate increased bottom water instability from wind-induced nearshore currents and wave action in longer ice-free seasons towards the present (Fig. 1.11), which could have generated reworking and resuspension in the surface sediment (10–0 cm; Figs. 1.4A, 1-A.3; see the Radiogenic isotope and age model section of core HBGC01).

1.5.2.2 *Eoeponidella pulchella* and productivity

A significant microfaunal change in Ecozone HBGC01-A is indicated by the high percentages of *Eoeponidella pulchella* in this zone (Fig. 1.13). In modern assemblages, *E. pulchella* is common on Arctic shelves and shelf breaks (Wollenburg & Mackensen, 1998; Wollenburg & Kuhnt, 2000; Scott et al., 2008b; Griffiths, 2010), but was also found in the Gulf of Mexico (Poag & Tresslar, 1981), and is often linked to high primary productivity. In surface sediments of the Canadian Arctic Ocean, *E. pulchella* constitutes ~9% of the benthic foraminiferal assemblage off Cape Bathurst (59 m; Scott et al., 2008b), known for the advection of saline nutrient-rich upwelled waters (Tremblay et al., 2011; Walkusz et al., 2012). *Eoeponidella pulchella* was also noted as an important species (20% of the living fauna) in the surface sample of core PS2480 in Vilkitsky Strait, Laptev Sea (51 m; Fütterer, 1994; Wollenburg & Kuhnt, 2000), which is characterized by high biogenic silica content (Nürnberg, 1996), chlorophyll-*a* concentrations (Boetius et al., 1996) and marine organic carbon (Boucsein & Stein, 2000). Furthermore, in 1993 CE, the year that core PS2480 was collected, the wind conditions favored upwelling in the Laptev Sea (Janout et al., 2015; Osadchiev et al., 2020). The distribution of *E. pulchella* in surface sediment samples of the eastern Arctic Ocean documented by Wollenburg & Kuhnt (2000) also supports a strong link to high primary productivity.

In our study, the maximum foraminiferal concentrations occurred concurrently with peaks in *E. pulchella* at ~2013 CE in core HBGC01 (Figs. 1.11–1.13) and in Ecozone PG2303-1-B (Figs. 1.16–1.18), which suggests high benthic foraminiferal fluxes linked to high primary productivity. Wollenburg & Kuhnt (2000) argued that assemblages of benthic foraminifera provide a better indication of trophic level than foraminiferal concentrations due to preservation issues. Still, in our study, the good preservation of foraminiferal shells throughout the sequences allows us to consider the total concentrations and fluxes of benthic foraminifera as a valuable productivity indicator in the Herschel Basin. We also conclude that *E. pulchella* is an excellent

indicator of productivity in the Herschel Basin. However, at present it is not clear if the high productivity is due to longer sea ice-free seasons (Fig. 1.3), the replenishment of nutrient-rich Pacific waters, increased organic carbon from rivers and coasts, or a mix of all the above (more specifications in the last section of the Discussion).

1.5.2.3 *Tintinnopsis fimbriata* and suspended particulate matter-rich freshwater

A special feature in the micropaleontological records of the shallow core HBGC01 is the high *Tintinnopsis fimbriata* fluxes, particularly pronounced after 2008 CE. This coincides with enhanced *T. fimbriata* concentrations at the end of Ecozone PG2303-1-A (<9 cm; Figs. 1.11, 1.16). Concentrations of *T. fimbriata* can be underestimated due to their small size. However, specimens tend to be bigger when they are abundant (Rogers et al., 1981), as observed for several tintinnid species (Dolan et al., 2014). The lower abundance of *T. fimbriata* before 1996 CE is likely not due to poor preservation as it occurs downcore together with abundant agglutinated foraminifera (Fig. 1.11). Hence, the increase in *T. fimbriata* fluxes after 1996 CE at the basin margin presumably reflects a real increase in tintinnid abundance.

According to previous studies, *T. fimbriata* occurs in nearshore areas near river mouths (Echols & Fowler, 1973; Burkovsky, 1976; Rogers et al., 1981). It was probably observed in sediments from the Beaufort Sea shelf by Scott al. (2008a, b), who reported it as *Tintinnopsis rioplatensis* (Souto, 1973). Tintinnid abundances in the water column have shown positive correlations with chlorophyll-a concentrations (Dolan et al., 2007). Additionally, maximum abundance of *T. fimbriata* occurred in relation to maximum chlorophyll-a concentration in a Hudson Bay inlet (Rogers et al., 1981) and early spring bloom in the Bedford Basin (Paranjape, 1987; Li, 2014). However, *T. fimbriata* also reaches peak occurrence during winter in the White Sea (Burkovsky, 1976), when primary production is limited (Chernov et al., 2018), which suggests it could be a low-temperature tolerant opportunistic species. It has also been proposed that the abundance of tintinnids might depend more upon the nature of the prey than the quantity of the food (Dolan et al., 2014).

Preferential occurrence of *T. fimbriata* in river proximal areas could be related to the availability of small mineral particles to build agglutinated lorica (Pierce & Turner, 1993). Scott et al. (2008b) associated the agglutinated tintinnids with the Mackenzie River water discharges, thus to freshwaters rich in suspended particulate matter. Its association with suspended particles is consistent with the concomitant increase of *Quinqueloculina stalker*, which is known to tolerate turbidity and to be a bacterial-feeder rather than an

algal-feeder (Guilbault et al., 2003; Figs. 1.11, 1.13). Hence, *T. fimbriata* might be an indicator of turbid freshwater discharge, but a relationship to primary productivity remains equivocal. The significant increase of *T. fimbriata* after 2008 CE may reflect a western spreading of the Mackenzie River plume to the study site, which could also be related to reduced sea-ice concentration (Fig. 1.3). The detrital particles used to build their agglutinated lorica might also originate from a more local source related to coastal erosion that has increased since ~2000 CE (Jones et al., 2009; Obu et al., 2016; Radosavljevic et al., 2016).

1.5.2.4 Ecological considerations about *Eoeponidella pulchella*, *Haynesina nivea*, *Tintinnopsis fimbriata*, and ostracod abundance

The occurrences of *E. pulchella* and *H. nivea* are closely correlated ($r = 0.68$ and $r = 0.78$ in cores HBGC01 and PG2303-1, respectively). Both species show increased occurrences in ecozones HBGC01-A and PG2303-1-B, which leads us to suggest a change towards increased productivity concurrently with low salinity excursions. Kutos et al. (2021) already proposed a relationship between benthic productivity and freshwater discharge in the Mackenzie Trough. In our study, the influence of low salinity waters from river discharge is further supported by the abundance of *Tintinnopsis fimbriata* fluxes over the last two decades in the shallow HBGC01 core (Fig. 1.11).

The main source of freshwater is the Mackenzie River. However, the Mackenzie River is not particularly rich in nutrients compared to other Arctic rivers (Holmes et al., 2011), especially at distal locations from the plume (Emmerton et al., 2008; Tremblay et al., 2014). Nevertheless, the terrigenous organic carbon and/or the microbial activity therein, either from the more distal Mackenzie River or the proximal permafrost thaw, may provide large food sources (Bell et al., 2016; Terhaar et al., 2021). Another source of nutrients originates from the upwelling of nutrient-rich Pacific waters onto the shelf during easterly winds (Tremblay et al., 2011, 2012; Pickart et al., 2013). The Mackenzie River plume reaching the study site and upwelling of deeper waters may both occur during periods of strong easterly winds, which could explain the duality between freshwater and productivity and the co-occurrence of *H. nivea* and *T. fimbriata* with *E. pulchella*.

The rapidly changing environment of the 21st century may also have negative impacts on the microfauna, as suggested by the decrease in ostracod fluxes at the shallow site of core HBGC01 (Fig. 1.11). From the inverse relationship between ostracod and *T. fimbriata* concentrations (Figs. 1.11, 1.16), we suggest that an increased supply of low salinity waters rich in suspended particulate matter at the HBGC01 site is unfavorable for ostracods. Because low salinity is not a limitation for ostracods, as several taxa can tolerate

extreme salinity variations (for ex., from 6.5 to >30 psu for *Sarsicytheridea bradii*; Stepanova et al., 2019), the turbidity is a more likely limiting factor. Vertical mixing of the surface waters rich in suspended particulate matter may lead to turbid bottom waters, especially at the shallow site of core HBGC01 (Hill & Nadeau, 1989; Rainville & Woodgate, 2009; see Bottom water masses section). However, turbidity might not be the direct cause. Various physico-chemical effects derived from increased suspended particulate matter supply, like acidification (Semiletov et al., 2016), could also affect ostracod abundance.

1.6 Conclusions

This study presents micropaleontological data of benthic foraminifera, ostracods, and tintinnids that provide time series with annual to multiannual time resolution in an Arctic nearshore environment. The three groups of microfossils provide complementary information on pelagic and bottom water conditions at two sites in the Herschel Basin, one near the summer halocline (HBGC01, 18 m depth) and the other below the halocline (PG2303-1, 32 m depth). The microfaunal communities of the two cores illustrate the sensitivity of micropaleontological tracers to water conditions at local scales, especially with regards to salinity and productivity. The 40-cm-long core HBGC01 covers the period ca. 1969–2018 CE, while an age model could not be established for the short 20-cm long core PG2303-1. A redundancy analysis performed on the foraminiferal assemblages in both cores permitted us to identify ecozones that were also consistent with the ostracod assemblage data and *Tintinnopsis fimbriata* abundance. Thus, the three studied microfossil groups responded simultaneously to decadal environmental changes and can be used as complementary paleo-tracers to distinguish the impacts of recent climate changes over long-scale environmental variations in Arctic nearshore areas.

Among the most important microfaunal changes is an increase in the benthic foraminifera *Eoepionidella pulchella*, which indicates enhanced primary productivity since ~2000 CE. The last two decades are also marked by the high occurrence of the shallow, low-salinity species *Haynesina nivea*, while *Islandiella norcrossi*, which requires more stable saline conditions, decreased in abundance. The microfaunal record of the shallow core HBGC01 thus suggests a transition from stable saline bottom waters to more unstable bottom water salinity. The decrease in summer sea-ice concentration that occurred after 2003 CE and more clearly after 2006 CE might best explain this transition at the basin margin, as the loss in summer sea-ice cover may have led to increased vertical mixing and thus to lower and varying bottom-water salinity. Moreover, the high fluxes of the tintinnid *T. fimbriata* combined with increased sand content, the abundance of *Quinqueloculina stalkerii*, and a reduction in ostracod concentrations during the most recent

decade points to enhanced turbidity of the water. Turbid waters could derive from increased inputs of particulate matter-rich freshwaters related to Mackenzie River discharge, local rivers and/or coastal erosion, which could be facilitated in the context of reduced sea-ice cover. We suggest that increased productivity might be caused by enhanced terrigenous organic fluxes and/or upwelling during easterly wind events, which would be amplified under reduced summer sea-ice concentration.

1.7 Acknowledgements

We wish to thank the *Fonds de recherche du Québec Nature et technologies* (FRQNT) for their financial support to JF through scholarships. Additional thanks are due for technical support provided by the Geotop Research Center. This study has been supported by the Natural Sciences and Engineering Research Council (NSERC) of Canada through a Discovery grant to AdV, a CREATE grant to ArcTrain [grant no. 432295] and a National Council of Science and Technology (CONACYT) postdoc grants from Mexico [CVU no. 174856] to VCB. Fieldwork was also supported by Polar Knowledge Canada through the Northern Scientific Training Program. M.-S. Seidenkrantz is funded by the Danish Council for Independent Research [grant no. 7014-00113B G-Ice project, and 0135-00165B GreenShelf] and through the European Union's Horizon 2020 research and innovation program under Grant Agreement [grant no. 869383; ECOTIP]. We want to thank the EU Horizon 2020 project Nunataryuk [BG-2017-1] and the Aurora Research Institute for making the fieldwork possible and the Qikiqtaruk Territorial Park, chief ranger Richard Gordon and the other park rangers, who have welcomed our team on Herschel Island – Qikiqtaruk. We want to thank all the colleagues who helped in the coring and mapping activities, mostly George Tanski and Konstantin Klein. We acknowledge many other colleagues and collaborators who participated in this study: Charles Brunette for the sea-ice data, Diogo Barnetche for the rental of equipment, Anna To for lab work, Tiffany Audet for managing the laboratory, Pierre Francus and Patrick Lajeunesse for providing access to CT-scan and laser granulometer facilities, Nicole Sanderson for her support with the *Plum* software and Pierre Poitevin for the photographs with the Keyence. TMC and LG were funded by the U.S. Geological Survey Climate Change Research Program. Any use of trade firm, or product names is for descriptive purposes only and does not imply endorsement by the U.S. Government. Finally, we are grateful to the anonymous reviewers of the *Journal* for their thorough examination of the manuscript and constructive comments. Appendices can be found linked to the online version of this article.

1.8 References

- Agatha, S., 2008, Redescription of the tintinnid ciliate *Tintinnopsis fimbriata* Meunier, 1919 (Spirotricha, Choretrichida) from coastal waters of Northern Germany: Denisia, v. 23, p. 261–272.
- Anthony, K. R., Ridd, P. V., Orpin, A. R., Larcombe, P., and Lough, J., 2004, Temporal variation of light availability in coastal benthic habitats: Effects of clouds, turbidity, and tides: Limnology and Oceanography, v. 49, p. 2201–2211.
- Aoyama, M., Hirose, K., and Igarashi, Y., 2006, Re-construction and updating our understanding on the global weapons tests ^{137}Cs fallout: Journal of Environmental Monitoring, v. 8, p. 431–438.
- Aquino-López, M. A., Blaauw, M., Christen, J. A., and Sanderson, N. K., 2018, Bayesian analysis of ^{210}Pb dating: Journal of Agricultural, Biological and Environmental Statistics, v. 23, p. 317–333.
- Ardyna, M., and Arrigo, K. R., 2020, Phytoplankton dynamics in a changing Arctic Ocean: Nature Climate Change, v. 10, p. 892–903.
- Ardyna, M., Babin, M., Devred, E., Forest, A., Gosselin, M., Raimbault, P., and Tremblay, J.-É., 2017, Shelf-basin gradients shape ecological phytoplankton niches and community composition in the coastal Arctic Ocean (Beaufort Sea): Limnology and Oceanography, v. 62, p. 2113–2132.
- Arrigo, K. R., and van Dijken, G. L., 2015, Continued increases in Arctic Ocean primary production: Progress in Oceanography, v. 136, p. 60–70.
- Arrigo, K. R., van Dijken, G., and Pabi, S., 2008, Impact of a shrinking Arctic ice cover on marine primary production: Geophysical Research Letters, v. 35, DOI: 10.1029/2008GL035028.
- Barber, D. G., Asplin, M. G., Papakyriakou, T. N., Miller, L., Else, B. G., Iacozza, J., Mundy, C., Gosselin, M., Asselin, N. C., and Ferguson, S., 2012, Consequences of change and variability in sea ice on marine ecosystem and biogeochemical processes during the 2007–2008 Canadian International Polar Year program: Climatic Change, v. 115, p. 135–159.
- Baskaran, M., and Naidu, A. S., 1995, ^{210}Pb -derived chronology and the fluxes of ^{210}Pb and ^{137}Cs isotopes into continental shelf sediments, East Chukchi Sea, Alaskan Arctic: Geochimica et Cosmochimica Acta, v. 59, p. 4435–4448.

Bell, L. E., Bluhm, B. A., and Iken, K., 2016, Influence of terrestrial organic matter in marine food webs of the Beaufort Sea shelf and slope: *Marine Ecology Progress Series*, v. 550, p. 1–24.

Blais, M., Ardyna, M., Gosselin, M., Dumont, D., Bélanger, S., Tremblay, J.-É., Gratton, Y., Marchese, C., and Poulin, M., 2017, Contrasting interannual changes in phytoplankton productivity and community structure in the coastal Canadian Arctic Ocean: *Limnology and Oceanography*, v. 62, p. 2480–2497.

Blott, S., 2010, GRADISTAT ver. 8.0: A grain size distribution and statistics package for the analysis of unconsolidated sediments by sieving or laser granulometer: Kenneth Pye Associates, Solihull, UK.

Boetius, A., Grahl, C., Kröncke, I., Liebezeit, G., and Nöthig, E., 1996, Distribution of plant pigments in surface sediments of the Eastern Arctic, in Stein, R., et al. (eds.), *Surface-sediment Composition and Sedimentary Processes in the Central Arctic Ocean and Along the Eurasian Continental Margin: Berichte zur Polarforschung* 212, Bremerhaven, Alfred Wegener Institute, p. 213–218.

Bonsell, C., and Dunton, K. H., 2018, Long-term patterns of benthic irradiance and kelp production in the central Beaufort Sea reveal implications of warming for Arctic inner shelves: *Progress in Oceanography*, v. 162, p. 160–170.

Boucsein, B., and Stein, R., 2000, Particulate organic matter in surface sediments of the Laptev Sea (Arctic Ocean): Application of maceral analysis as organic-carbon-source indicator: *Marine Geology*, v. 162, p. 573–586.

Boyer, T. P., Baranova, O. K., Coleman, C., Garcia, H. E., Grodsky, A., Locarnini, R. A., Mishonov, A.V., Paver C. R., Reagan, J. R., Seidov, D., Smolyar, I. V., Weathers, K., and Zweng, M. M., 2018, World Ocean Database 2018: Mishonov, A.V. Technical Ed., NOAA Atlas NESDIS 87, Retrieved from https://www.ncei.noaa.gov/sites/default/files/2020-04/wod_intro_0.pdf.

Bruel, R., and Sabatier, P., 2020, *serac*: An R package for ShortlivEd RAdionuclide chronology of recent sediment cores: *Journal of Environmental Radioactivity*, v. 225, DOI: 10.1016/j.jenvrad.2020.106449.

Brugler, E. T., Pickart, R. S., Moore, G., Roberts, S., Weingartner, T. J., and Statscewich, H., 2014, Seasonal to interannual variability of the Pacific water boundary current in the Beaufort Sea: *Progress in Oceanography*, v. 127, p. 1–20.

Burkovsky, I., 1976, Ecology of Tintinnida (Ciliata) of the White Sea: *Zoologicheskii Zhurnal*, v. 55, p. 497–507.

- Cage, A. G., Pieńkowski, A. J., Jennings, A., Knudsen, K. L., and Seidenkrantz, M.-S., 2021, Comparative analysis of six common foraminiferal species of the genera *Cassidulina*, *Paracassidulina*, and *Islandiella* from the Arctic–North Atlantic domain: Journal of Micropalaeontology, v. 40, p. 37–60.
- Carmack, E. C., and Macdonald, R. W., 2002, Oceanography of the Canadian Shelf of the Beaufort Sea: A setting for marine life: Arctic, v. 55, p. 29–45.
- Carmack, E. C., Barber, D., Christensen, J., Macdonald, R., Rudels, B., and Sakshaug, E., 2006, Climate variability and physical forcing of the food webs and the carbon budget on panarctic shelves: Progress in Oceanography, v. 71, p. 145–181.
- Carnero-Bravo, V., Falardeau, J., Chassiot, L., Tanski, G., Hillaire-Marcel, C., Ghaleb, B., de Vernal, A., Vonk, J. E., Lantuit, H., Fritz, M., and Preda, M., 2021, Sediment structure and deposition rates in the Yukon coast: PANGAEA, DOI: 10.1594/PANGAEA.937387.
- Chernov, I., Lazzari, P., Tolstikov, A., Kravchishina, M., and Iakovlev, N., 2018, Hydrodynamical and biogeochemical spatiotemporal variability in the White Sea: A modeling study: Journal of Marine Systems, v. 187, p. 23–35.
- Comeau, A. M., Li, W. K., Tremblay, J.-É., Carmack, E. C., and Lovejoy, C., 2011, Arctic Ocean microbial community structure before and after the 2007 record sea ice minimum: Plos One, v. 6, DOI: 10.1371/journal.pone.0027492.
- Corbett, D. R., McKee, B., and Allison, M., 2006, Nature of decadal-scale sediment accumulation on the western shelf of the Mississippi River delta: Continental Shelf Research, v. 26, p. 2125–2140.
- Cronin, T. M., Gemery, L., Briggs, W., Jr., Jakobsson, M., Polyak, L., and Brouwers, E., 2010, Quaternary Sea-ice history in the Arctic Ocean based on a new Ostracod sea-ice proxy: Quaternary Science Reviews, v. 29, p. 3415–3429.
- Cronin, T. M., O'Regan, M., Pearce, C., Gemery, L., Toomey, M., Semiletov, I., and Jakobsson, M., 2017, Deglacial sea level history of the East Siberian Sea and Chukchi Sea margins: Climate of the Past, v. 13, p. 1097–1110.
- Dolan, J., Ritchie, M., and Ras, J., 2007, The "neutral" community structure of planktonic herbivores, tintinnid ciliates of the microzooplankton, across the SE Tropical Pacific Ocean: Biogeosciences, v. 4, p. 297–310.
- Dolan, J. R., Yang, E. J., Kim, T. W., and Kang, S.-H., 2014, Microzooplankton in a warming Arctic: A comparison of tintinnids and radiolarians from summer 2011 and 2012 in the Chukchi Sea: Acta Protozoologica, v. 53, p. 101–113.

Doxaran, D., Devred, E., and Babin, M., 2015, A 50% increase in the mass of terrestrial particles delivered by the Mackenzie River into the Beaufort Sea (Canadian Arctic Ocean) over the last 10 years: *Biogeosciences*, v. 12, p. 3551–3565.

EBA Engineering Consultants Ltd., 1992, Proceedings of the Beaufort Sea granular resources workshop, Part 1: Reports on NOGAP regional studies, 11 p.

Echols, R. J., and Fowler, G. A., 1973, Agglutinated tintinnid loricae from some Recent and Late Pleistocene shelf sediments: *Micropaleontology*, v. 19, p. 431–443.

Ehn, J. K., Reynolds, R. A., Stramski, D., Doxaran, D., Lansard, B., and Babin, M., 2019, Patterns of suspended particulate matter across the continental margin in the Canadian Beaufort Sea during summer: *Biogeosciences*, v. 16, p. 1583–1605.

Emmerton, C. A., Lesack, L. F., and Vincent, W. F., 2008, Nutrient and organic matter patterns across the Mackenzie River, estuary and shelf during the seasonal recession of sea-ice: *Journal of Marine Systems*, v. 74, p. 741–755.

Fatela, F., and Taborda, R., 2002, Confidence limits of species proportions in microfossil assemblages: *Marine Micropaleontology*, v. 45, p. 169–174.

Feyling-Hanssen, R. W., Jørgensen, J. A., Knudsen, K. L., Lykke-Andersen, A.-L., 1971, Late Quaternary Foraminifera from Vendsyssel, Denmark and Sandnes, Norway: *Bulletin of the Geological Society of Denmark*, v. 21, p. 67–317.

Feyling-Hanssen, R. W., and Ulleberg, K., 1984, A Tertiary-Quaternary section at Sarsbukta, Spitsbergen, Svalbard, and its foraminifera: *Polar Research*, v. 2, p. 77–106.

Fortin, D., Francus, P., Gebhardt, A. C., Hahn, A., Kliem, P., Lisé-Pronovost, A., Roychowdhury, R., Labrie, J., and St-Onge, G., The PASADO Science Team, 2013, Destructive and non-destructive density determination: method comparison and evaluation from the Laguna Potrok Aike sedimentary record: *Quaternary Science Reviews*, v. 71, p. 147–153.

Frey, K. E., Moore, G., Cooper, L. W., and Grebmeier, J. M., 2015, Divergent patterns of recent sea ice cover across the Bering, Chukchi, and Beaufort seas of the Pacific Arctic Region: *Progress in Oceanography*, v. 136, p. 32–49.

Fritz, M., Vonk, J. E., and Lantuit, H., 2017, Collapsing Arctic coastlines: *Nature Climate Change*, v. 7, p. 6–7.

Fütterer, D., 1994, Die Expedition ARCTIC'93: der Fahrtabschnitt ARK-IX/4 mit FS "Polarstern" 1993: *Berichte zur Polarforschung* 149, Bremerhaven, Alfred Wegener Institute, 244 p.

Gemery, L., Cronin, T., Cooper, L., and Grebmeier, J., 2013, Temporal changes in benthic ostracod assemblages in the Northern Bering and Chukchi Seas from 1976 to 2010: Deep Sea Research Part II: Topical Studies in Oceanography, v. 94, p. 68–79.

Gemery, L., Cronin, T. M., Briggs, W. M., Brouwers, E. M., Schornikov, E. I., Stepanova, A., Wood, A. M., and Yasuhara, M., 2017, An Arctic and Subarctic ostracod database: Biogeographic and paleoceanographic applications: *Hydrobiologia*, v. 786, p. 59–95.

Gemery, L., Cronin, T. M., Cooper, L. W., Dowsett, H. J., and Grebmeier, J. M., 2021, Biogeography and ecology of Ostracoda in the US northern Bering, Chukchi, and Beaufort Seas: *Plos One*, v. 16, DOI: 10.1371/journal.pone.0251164.

Environment and Climate Change Canada, Historical Hydrometric Data, Retrieved April, 2020 from https://wateroffice.ec.gc.ca/mainmenu/historical_data_index_e.html.

Grebmeier, J. M., Cooper, L. W., Feder, H. M., and Sirenko, B. I., 2006, Ecosystem dynamics of the Pacific-influenced northern Bering and Chukchi Seas in the Amerasian Arctic: *Progress in Oceanography*, v. 71, p. 331–361.

Griffiths, J., 2010, Microfossil Evidence for Recent and Past Changes to Hudson Bay Oceanography: Dalhousie University, Halifax, 115 p.

Grotheer, H., Meyer, V., Riedel, T., Pfalz, G., Mathieu, L., Hefter, J., Gentz, T., Lantuit, H., Mollenhauer, G., and Fritz, M., 2020, Burial and origin of permafrost-derived carbon in the nearshore zone of the southern Canadian Beaufort Sea: *Geophysical Research Letters*, v. 47, DOI: 10.1029/2019GL085897.

Guilbault, J.-P., Barrie, J.V., Conway, K., Lapointe, M., and Radi, T., 2003, Paleoenvironments of the Strait of Georgia, British Columbia during the last deglaciation: Microfaunal and microfloral evidence: *Quaternary Science Reviews*, v. 22, p. 839–857.

Günther, F., Overduin, P. P., Yakshina, I. A., Opel, T., Baranskaya, A. V., and Grigoriev, M. N., 2015, Observing Muostakh disappear: Permafrost thaw subsidence and erosion of a ground-ice-rich island in response to arctic summer warming and sea ice reduction: *The Cryosphere*, v. 9, p. 151–178.

Hald, M., and Korsun, S., 1997, Distribution of modern benthic foraminifera from fjords of Svalbard, European Arctic: *Journal of Foraminiferal Research*, v. 27, p. 101–122.

Hald, M., and Steinsund, P., 1996, Benthic foraminifera and carbonate dissolution in the surface sediments of the Barents and Kara Sea in Stein, R., et al. (eds.), *Surface-sediment Composition and Sedimentary Processes in the Central Arctic Ocean and Along the Eurasian Continental Margin: Berichte zur Polarforschung* 212, Bremerhaven, Alfred Wegener Institute, p. 285–307.

- Hanna, A. J., Allison, M. A., Bianchi, T. S., Marcantonio, F., and Goff, J. A., 2014, Late Holocene sedimentation in a high Arctic coastal setting: Simpson Lagoon and Colville Delta, Alaska: *Continental Shelf Research*, v. 74, p. 11–24.
- Hansen, A., and Knudsen, K. L., 1995, Recent foraminiferal distribution in Freemansundet and Early Holocene stratigraphy on Edgeøya, Svalbard: *Polar Research*, v. 14, p. 215–238.
- Hill, P. R., and Nadeau, O. C., 1989, Storm-dominated sedimentation on the inner shelf of the Canadian Beaufort Sea: *Journal of Sedimentary Research*, v. 59, p. 455–468.
- Holmes, R. M., McClelland, J. W., Peterson, B. J., Tank, S. E., Bulygina, E., Eglinton, T. I., Gordeev, V. V., Gurtovaya, T. Y., Raymond, P. A., and Repeta, D. J., 2011, Seasonal and annual fluxes of nutrients and organic matter from large rivers to the Arctic Ocean and surrounding seas: *Estuaries and Coasts*, v. 35, p. 369–382.
- Husum, K., Hald, M., Stein, R., and Weißschnur, M., 2015, Recent benthic foraminifera in the Arctic Ocean and Kara Sea continental margin: *Arktos*, v. 1, DOI: 10.1007/s41063-015-0005-9.
- IPCC, 2019, *IPCC Special Report on the Ocean and Cryosphere in a Changing Climate*: Cambridge University Press, Cambridge, 755 p.
- Itaki, T., Ito, M., Narita, H., Ahagon, N., and Sakai, H., 2003, Depth distribution of radiolarians from the Chukchi and Beaufort Seas, western Arctic: *Deep Sea Research Part I: Oceanographic Research Papers*, v. 50, p. 1507–1522.
- Janout, M. A., Aksenov, Y., Hölemann, J. A., Rabe, B., Schauer, U., Polyakov, I. V., Bacon, S., Coward, A. C., Karcher, M., and Lenn, Y. D., 2015, Kara Sea freshwater transport through Vilkitsky Strait: Variability, forcing, and further pathways toward the western Arctic Ocean from a model and observations: *Journal of Geophysical Research: Oceans*, v. 120, p. 4925–4944.
- Jennings, A., Andrews, J., Reilly, B., Walczak, M., Jakobsson, M., Mix, A., Stoner, J., Nicholls, K. W., and Cheseby, M., 2020, Modern foraminiferal assemblages in northern Nares Strait, Petermann Fjord, and beneath Petermann ice tongue, NW Greenland: *Arctic, Antarctic, and Alpine Research*, v. 52, p. 491–511.
- Jones, B. M., Arp, C. D., Jorgenson, M. T., Hinkel, K. M., Schmutz, J. A., and Flint, P. L., 2009, Increase in the rate and uniformity of coastline erosion in Arctic Alaska: *Geophysical Research Letters*, v. 36, DOI: 10.1029/2008GL036205.
- Jong, D., Bröder, L., Tanski, G., Fritz, M., Lantuit, H., Tesi, T., Haghipour, N., Eglinton, T. I., and Vonk, J. E., 2020, Nearshore zone dynamics determine pathway of organic carbon from eroding permafrost coasts: *Geophysical Research Letters*, v. 47, DOI: 10.1029/2020GL088561.

Juhls, B., 2021, Land-Ocean Interactions in Arctic Coastal Waters: Ocean Colour Remote Sensing and Current Carbon Fluxes to the Arctic Ocean: Freie Universität Berlin, Berlin, 165 p.

Kinnard, C., Zdanowicz, C. M., Fisher, D. A., Isaksson, E., de Vernal, A., and Thompson, L. G., 2011, Reconstructed changes in Arctic sea ice over the past 1,450 years: *Nature*, v. 479, p. 509–512.

Klein, K. P., Lantuit, H., Heim, B., Fell, F., Doxaran, D., and Irrgang, A. M., 2019, Long-term high-resolution sediment and sea surface temperature spatial patterns in Arctic nearshore waters retrieved using 30-year landsat archive imagery: *Remote Sensing*, v. 11, DOI: 10.3390/rs11232791.

Knudsen, K. L., Stabell, B., Seidankrantz, M.-S., Eriksson, J., and Blake, W., Jr., 2008, Deglacial and Holocene conditions in northernmost Baffin Bay: Sediments, foraminifera, diatoms and stable isotopes: *Boreas*, v. 37, p. 346–376.

Kulikov, E., Carmack, E. C., and Macdonald, R., 1998, Flow variability at the continental shelf break of the Mackenzie Shelf in the Beaufort Sea: *Journal of Geophysical Research: Oceans*, v. 103, p. 12725–12741.

Kutos, O., Rochon, A., and Montero-Serrano, J.-C., 2021, Evolution of palaeo-sea-surface conditions and sediment dynamics over the last 2700 years on the Mackenzie Slope, Beaufort Sea (Canadian Arctic): *Boreas*, v. 50, p. 893–914.

Lefebvre, K. A., Quakenbush, L., Frame, E., Huntington, K. B., Sheffield, G., Stimmelmayr, R., Bryan, A., Kendrick, P., Ziel, H., and Goldstein, T., 2016, Prevalence of algal toxins in Alaskan marine mammals foraging in a changing arctic and subarctic environment: *Harmful Algae*, v. 55, p. 13–24.

Lewis, K., Van Dijken, G., and Arrigo, K. R., 2020, Changes in phytoplankton concentration now drive increased Arctic Ocean primary production: *Science*, v. 369, p. 198–202.

Li, W. K., 2014, The state of phytoplankton and bacterioplankton at the Compass Buoy Station: Bedford Basin monitoring program 1992–2013: Fisheries and Oceans Canada Pêches et Océans Canada, 138 p.

Li, W. K., McLaughlin, F. A., Lovejoy, C., and Carmack, E. C., 2009, Smallest algae thrive as the Arctic Ocean freshens: *Science*, v. 326, p. 539.

Lin, P., Pickart, R. S., Stafford, K. M., Moore, G., Torres, D. J., Bahr, F., and Hu, J., 2016, Seasonal variation of the Beaufort shelfbreak jet and its relationship to Arctic cetacean occurrence: *Journal of Geophysical Research: Oceans*, v. 121, p. 8434–8454.

Lin, P., Pickart, R. S., Fissel, D., Ross, E., Kasper, J., Bahr, F., Torres, D. J., O'Brien, J., Borg, K., and Melling, H., 2020, Circulation in the vicinity of Mackenzie Canyon from a year-long mooring array: *Progress in Oceanography*, v. 187, DOI: 10.1016/j.pocean.2020.102396.

Lloyd, J. M., 2006, Modern distribution of benthic foraminifera from Disko Bugt, West Greenland: *Journal of Foraminiferal Research*, v. 36, p. 315–331.

Luoto, T. P., Nevalainen, L., Kubischarta, F., Kultti, S., Knudsen, K. L., and Salonen, V. P., 2011, Late quaternary ecological turnover in high arctic Lake Einstaken, Nordaustlandet, Svalbard (80 N). *Geografiska Annaler: Series A: Physical Geography*, v. 93, p. 337–354.

Madsen, H. B., and Knudsen, K. L., 1994, Recent foraminifera in shelf sediments of the Scoresby Sund fjord, East Greenland: *Boreas*, v. 23, p. 495–504.

McDougall, K. A., Brouwers, E. M., and Smith, P., 1986, Micropaleontology and sedimentology of the PB borehole series, Prudhoe Bay, Alaska: U.S. Geological Survey Bulletin 1598, 62 p., DOI: 10.3133/b1598.

McLaughlin, F. A., and Carmack, E. C., 2010, Deepening of the nutricline and chlorophyll maximum in the Canada Basin interior, 2003–2009: *Geophysical Research Letters*, v. 37, DOI: 10.1029/2010GL045459.

Meier, W. N., Fetterer, F., Savoie, M., Mallory, S., Duerr, R., and Stroeve, J., 2017, NOAA/NSIDC Climate Data Record of Passive Microwave Sea Ice Concentration, Version 3. [goddard_merged_seaice_conc]. Boulder, Colorado USA. NSIDC: National Snow and Ice Data Center. [January 2020].

Meunier, A., 1919, Mikroplankton de la mer Flamande. III. Les Péridiniens: Mémoires du Musée Royal d'Histoire Naturelle de Belgique, v. 8, p. 1–116.

Mioduszewski, J., Vavrus, S., and Wang, M., 2018, Diminishing Arctic sea ice promotes stronger surface winds: *Journal of Climate*, v. 31, p. 8101–8119.

Moffitt, S. E., Hill, T. M., Ohkushi, K., Kennett, J. P., and Behl, R. J., 2014, Vertical oxygen minimum zone oscillations since 20 ka in Santa Barbara Basin: A benthic foraminiferal community perspective: *Paleoceanography*, v. 29, p. 44–57.

Nürnberg, D., 1996, Biogenic barium and opal in shallow Eurasian shelf sediments in relation to the pelagic Arctic Ocean environment, in Stein, R., et al. (eds.), *Surface-sediment Composition and Sedimentary Processes in the Central Arctic Ocean and Along the Eurasian Continental Margin: Berichte zur Polarforschung* 112, Bremerhaven, Alfred Wegener Institute, p. 96–118.

Obu, J., Lantuit, H., Fritz, M., Pollard, W. H., Sachs, T., and Günther, F., 2016, Relation between planimetric and volumetric measurements of permafrost coast erosion: A case study from Herschel Island, western Canadian Arctic: *Polar Research*, v. 35, DOI: 10.3402/polar.v35.30313.

Ogi, M., and Wallace, J. M., 2007, Summer minimum Arctic sea ice extent and the associated summer atmospheric circulation: *Geophysical Research Letters*, v. 34, DOI: 10.1029/2007GL029897.

Ogi, M., Rigor, I. G., McPhee, M. G., and Wallace, J. M., 2008, Summer retreat of Arctic sea ice: Role of summer winds: *Geophysical Research Letters*, v. 35, DOI: 10.1029/2008GL035672.

Oksanen, J., Blanchet, F. G., Kindt, R., Legendre, P., Minchin, P. R., O'Hara, R., Simpson, G. L., Solymos, P., Stevens, M. H. H., and Wagner, H., 2013, Package 'vegan', Community Ecology Package, version 2, 295 p.

Olausson, E., 1982, The Pleistocene/Holocene boundary in south-western Sweden: *Sveriges Geologiska Undersökning Ser. C*, v. 794, 288 p.

Osadchiev, A., Silvestrova, K., and Myslenkov, S., 2020, Wind-driven coastal upwelling near large river deltas in the Laptev and east-Siberian seas: *Remote Sensing*, v. 12, DOI: 10.3390/rs12050844.

Overeem, I., Anderson, R. S., Wobus, C. W., Clow, G. D., Urban, F. E., and Matell, N., 2011, Sea ice loss enhances wave action at the Arctic coast: *Geophysical Research Letters*, v. 38, DOI: 10.1029/2011GL048681.

Paranjape, M. A., 1987, The seasonal cycles and vertical distribution of tintinnines in Bedford Basin, Nova Scotia, Canada: *Canadian Journal of Zoology*, v. 65, p. 41–48.

Pfalz, G., 2017, Lateral transport of sediment and organic matter, derived from coastal erosion, into the nearshore zone of the southern Beaufort Sea, Canada: *Technische Universität Dresden*, Dresden, 66 p.

Pickart, R. S., 2004, Shelfbreak circulation in the Alaskan Beaufort Sea: Mean structure and variability: *Journal of Geophysical Research: Oceans*, v. 109, DOI: 10.1029/2003JC001912.

Pickart, R. S., Spall, M. A., Moore, G. W., Weingartner, T. J., Woodgate, R. A., Aagaard, K., and Shimada, K., 2011, Upwelling in the Alaskan Beaufort Sea: Atmospheric forcing and local versus non-local response: *Progress in Oceanography*, v. 88, p. 78–100.

Pickart, R. S., Spall, M. A., and Mathis, J. T., 2013, Dynamics of upwelling in the Alaskan Beaufort Sea and associated shelf–basin fluxes: Deep Sea Research Part I: Oceanographic Research Papers, v. 76, p. 35–51

Pierce, R. W., and Turner, J. T., 1993, Global biogeography of marine tintinnids: Marine Ecology Progress Series, v. 94, p. 11–26.

Poag, C. W., and Tresslar, R. C., 1981, Living foraminifers of West Flower Garden Bank, northernmost coral reef in the Gulf of Mexico: Micropaleontology, v. 27, p. 31–62.

Polyak, L., Korsun, S., Febo, L. A., Stanovoy, V., Khusid, T., Hald, M., Paulsen, B. E., and Lubinski, D. J., 2002, Benthic foraminiferal assemblages from the southern Kara Sea, a river-influenced Arctic marine environment: Journal of Foraminiferal Research, v. 32, p. 252–273.

Polyak, L., Stanovoy, V., and Lubinski, D. J., 2003, Stable isotopes in benthic foraminiferal calcite from a river-influenced Arctic marine environment, Kara and Pechora Seas: Paleoceanography, v. 18, DOI: 10.1029/2001PA000752.

R Core Team, 2021, R: A language and environment for statistical computing. R Foundation for Statistical Computing, Vienna, Austria, Retrieved from <https://www.R-project.org/>.

Radosavljevic, B., Lantuit, H., Pollard, W., Overduin, P., Couture, N., Sachs, T., Helm, V., and Fritz, M., 2016, Erosion and flooding—threats to coastal infrastructure in the Arctic: A case study from Herschel Island, Yukon Territory, Canada: Estuaries and Coasts, v. 39, p. 900–915.

Rainville, L., and Woodgate, R. A., 2009, Observations of internal wave generation in the seasonally ice-free Arctic: Geophysical Research Letters, v. 36, DOI: 10.1029/2009GL041291.

Rasband, W. S., 1997–2018, ImageJ, U. S. National Institutes of Health, Bethesda, Maryland, USA, <https://imagej.nih.gov/ij/>.

Reimnitz, E., McCormick, M., McDougall, K., and Brouwers, E., 1993, Sediment export by ice rafting from a coastal polynya, Arctic Alaska, USA: Arctic and Alpine Research, v. 25, p. 83–98.

Retamal, L., Bonilla, S., and Vincent, W. F., 2008, Optical gradients and phytoplankton production in the Mackenzie River and the coastal Beaufort Sea: Polar Biology, v. 31, p. 363–379.

Rogers, G., Roff, J., and Lynn, D., 1981, Tintinnids of Chesterfield Inlet, Northwest Territories: Canadian Journal of Zoology, v. 59, p. 2360–2364.

Sanchez-Cabeza, J., and Ruiz-Fernández, A., 2012, ^{210}Pb sediment radiochronology: An integrated formulation and classification of dating models: Geochimica et Cosmochimica Acta, v. 82, p. 183–200.

Schlitzer, R., 2018, Ocean Data View, Alfred Wegener Institute, <https://odv.awi.de>.

Schulze, L. M., and Pickart, R. S., 2012, Seasonal variation of upwelling in the Alaskan Beaufort Sea: Impact of sea ice cover: Journal of Geophysical Research: Oceans, v. 117, DOI: 10.1029/2012JC007985.

Scott, D. B., Schell, T., Rochon, A., and Blasco, S., 2008a, Benthic foraminifera in the surface sediments of the Beaufort Shelf and slope, Beaufort Sea, Canada: Applications and implications for past sea-ice conditions: Journal of Marine Systems, v. 74, p. 840–863.

Scott, D. B., Schell, T., Rochon, A., and Blasco, S., 2008b, Modern benthic foraminifera in the surface sediments of the Beaufort Shelf, Slope and Mackenzie Trough, Beaufort Sea, Canada: Taxonomy and summary of surficial distributions: Journal of Foraminiferal Research, v. 38, p. 228–250.

Seidenkrantz, M.-S., 2013, Benthic foraminifera as palaeo sea-ice indicators in the subarctic realm—examples from the Labrador Sea–Baffin Bay region: Quaternary Science Reviews, v. 79, p. 135–144.

Seidenstein, J. L., Cronin, T. M., Gemery, L., Keigwin, L. D., Pearce, C., Jakobsson, M., Coxall, H. K., Wei, E. A., and Driscoll, N. W., 2018, Late Holocene paleoceanography in the Chukchi and Beaufort Seas, Arctic Ocean, based on benthic foraminifera and ostracods: Arktos, v. 4, DOI: 10.1007/s41063-018-0058-7.

Semiletov, I., Pipko, I., Gustafsson, Ö., Anderson, L. G., Sergienko, V., Pugach, S., Dudarev, O., Charkin, A., Gukov, A., and Bröder, L., 2016, Acidification of East Siberian Arctic Shelf waters through addition of freshwater and terrestrial carbon: Nature Geoscience, v. 9, p. 361–365.

Serreze, M. C., and Barrett, A. P., 2011, Characteristics of the Beaufort Sea high: Journal of Climate, v. 24, p. 159–182.

Sherr, E. B., Sherr, B. F., and Hartz, A. J., 2009, Microzooplankton grazing impact in the Western Arctic Ocean: Deep Sea Research Part II: Topical Studies in Oceanography, v. 56, p. 1264–1273.

Simmonds, I., and Keay, K., 2009, Extraordinary September Arctic sea ice reductions and their relationships with storm behavior over 1979–2008: *Geophysical Research Letters*, v. 36, DOI: 10.1029/2009GL039810.

Smith, D. C., and Morison, J. H., 1998, Nonhydrostatic haline convection under leads in sea ice: *Journal of Geophysical Research: Oceans*, v. 103, p. 3233–3247.

Souto, S., 1973, Contribución al conocimiento de los tintínnidos de agua dulce de la República Argentina. I Río de la Plata y Delta del Paraná: *Physis*, v. 32, p. 249–254.

Stepanova, A., Taldenkova, E., and Bauch, H. A., 2003, Recent Ostracoda from the Laptev Sea (Arctic Siberia): Species assemblages and some environmental relationships: *Marine Micropaleontology*, v. 48, p. 23–48.

Stepanova, A., Taldenkova, E., Simstich, J., and Bauch, H. A., 2007, Comparison study of the modern ostracod associations in the Kara and Laptev seas: Ecological aspects: *Marine Micropaleontology*, v. 63, p. 111–142.

Stepanova, A., Obrochta, S., Quintana Krupinski, N. B., Hyttinen, O., Kotilainen, A., and Andrén, T., 2019, Late Weichselian to Holocene history of the Baltic Sea as reflected in ostracod assemblages: *Boreas*, v. 48, p. 761–778.

Terhaar, J., Lauerwald, R., Regnier, P., Gruber, N., and Bopp, L., 2021, Around one third of current Arctic Ocean primary production sustained by rivers and coastal erosion: *Nature Communications*, v. 12, DOI: 10.1038/s41467-020-20470-z.

Tian, S. Y., Yasuhara, M., Hong, Y., Huang, H.-H. M., Iwatani, H., Chiu, W.-T. R., Mamo, B., Okahashi, H., and Rasmussen, T. L., 2020, Deglacial–Holocene Svalbard paleoceanography and evidence of meltwater pulse 1B: *Quaternary Science Reviews*, v. 233, DOI: 10.1016/j.quascirev.2020.106237.

Tremblay, J.-É., Bélanger, S., Barber, D., Asplin, M., Martin, J., Darnis, G., Fortier, L., Gratton, Y., Link, H., and Archambault, P., 2011, Climate forcing multiplies biological productivity in the coastal Arctic Ocean: *Geophysical Research Letters*, v. 38, DOI: 10.1029/2011GL048825.

Tremblay, J.-É., Robert, D., Varela, D. E., Lovejoy, C., Darnis, G., Nelson, R. J., and Sastri, A. R., 2012, Current state and trends in Canadian Arctic marine ecosystems: I. Primary production: *Climatic Change*, v. 115, p. 161–178.

Tremblay, J.-É., Raimbault, P., Garcia, N., Lansard, B., Babin, M., and Gagnon, J., 2014, Impact of river discharge, upwelling and vertical mixing on the nutrient loading and productivity of the Canadian Beaufort Shelf: *Biogeosciences*, v. 11, p. 4853–4868.

Voltski, I., Korsun, S., Pillet, L., and Pawlowski, J., 2015, *Protoelphidium niveum* and the taxonomy of "lower" elphidiids: Journal of Foraminiferal Research, v. 45, p. 250–263.

Walkusz, W., Williams, W. J., Harwood, L. A., Moore, S. E., Stewart, B. E., and Kwasniewski, S., 2012, Composition, biomass and energetic content of biota in the vicinity of feeding bowhead whales (*Balaena mysticetus*) in the Cape Bathurst upwelling region (south eastern Beaufort Sea): Deep Sea Research Part I: Oceanographic Research Papers, v. 69, p. 25–35.

Weingartner, T. J., Danielson, S. L., Potter, R. A., Trefry, J. H., Mahoney, A., Savoie, M., Irvine, C., and Sousa, L., 2017, Circulation and water properties in the landfast ice zone of the Alaskan Beaufort Sea: Continental Shelf Research, v. 148, p. 185–198.

Whatley, R. C., 1983, The application of Ostracoda to palaeoenvironmental analysis, *in* Maddocks, R. F. (ed.), Applications of Ostracoda: University of Houston, Geoscience, Houston, p. 51–77.

Williams, B., and Carmack, E. C., 2012, Ocean water and sea ice, *in* Burn, C. R. (ed.), Herschel Island Qikiqtaryuk: A Natural and Cultural History of Yukon's Arctic Island, University of Calgary Press, Calgary, p. 54–59.

Williams, W. J., and Carmack, E. C., 2015, The "interior" shelves of the Arctic Ocean: Physical oceanographic setting, climatology and effects of sea-ice retreat on cross-shelf exchange: Progress in Oceanography, v. 139, p. 24–41.

Wollenburg, J. E., and Kuhnt, W., 2000, The response of benthic foraminifers to carbon flux and primary production in the Arctic Ocean: Marine Micropaleontology, v. 40, p. 189–231.

Wollenburg, J. E., and Mackensen, A., 1998, Living benthic foraminifers from the central Arctic Ocean: Faunal composition, standing stock and diversity: Marine Micropaleontology, v. 34, p. 153–185.

Wood, K. R., Bond, N. A., Danielson, S. L., Overland, J. E., Salo, S. A., Stabeno, P. J., and Whitefield, J., 2015, A decade of environmental change in the Pacific Arctic region: Progress in Oceanography, v. 136, p. 12–31.

1.9 Supplementary material

Figure 1-A.1 A northwest–southeast seismic profile that crosses the Herschel Island – Qikiqtaruk shore to the middle of the Herschel Basin. The red arrow marks the location of the UWITEC gravity core YC18-HB-GC01.

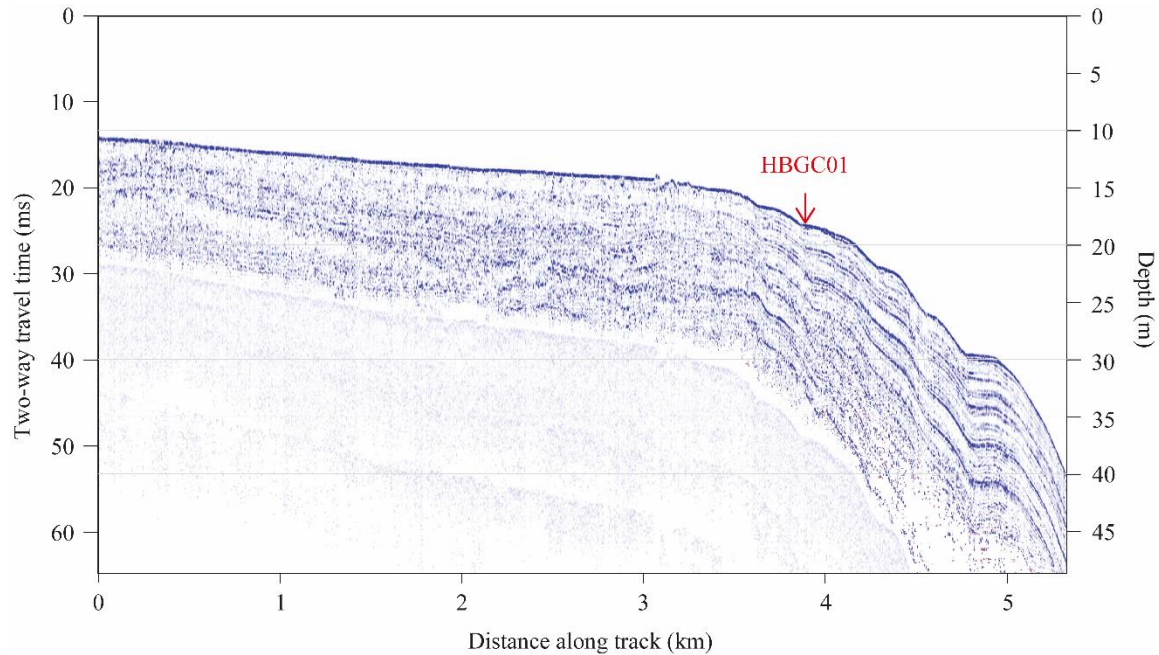


Figure 1-A.2 A near west–east seismic profile across the Herschel Basin showing the location of the PG2303 coring site. The red arrow marks the location of the UWITEC gravity core PG2303-1.

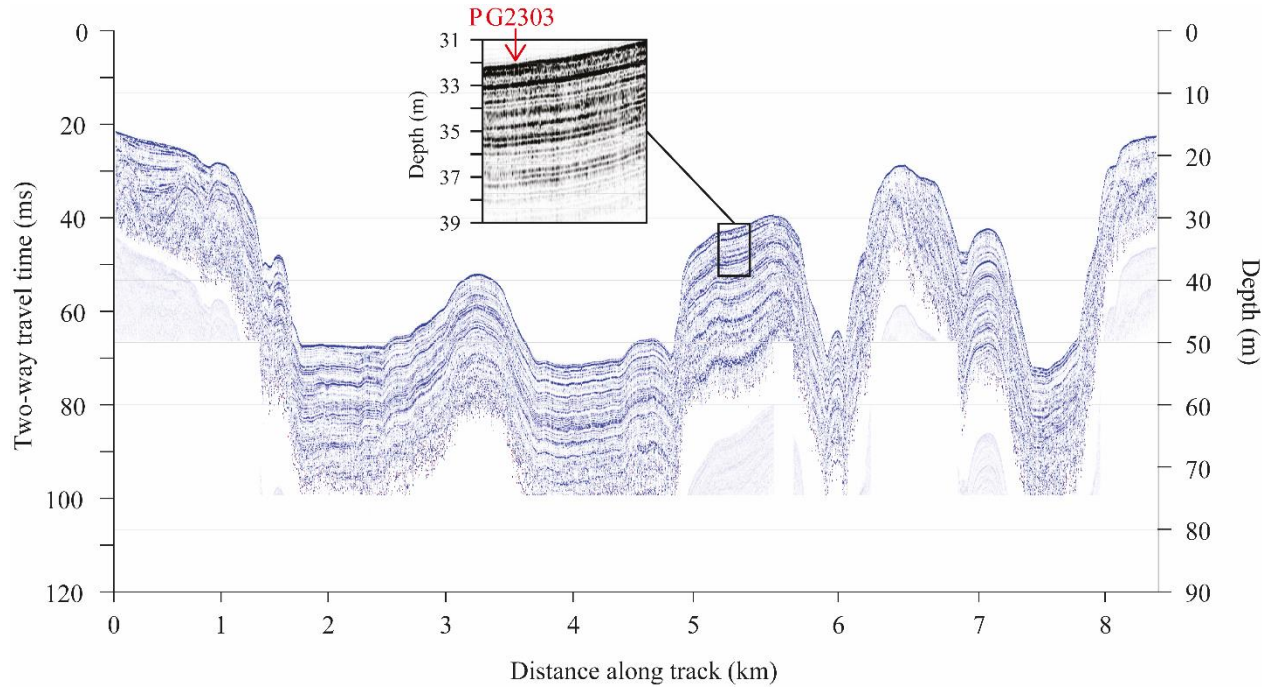


Figure 1-A.3 Photograph, CT-scan and density data of core YC18-HB-GC01.

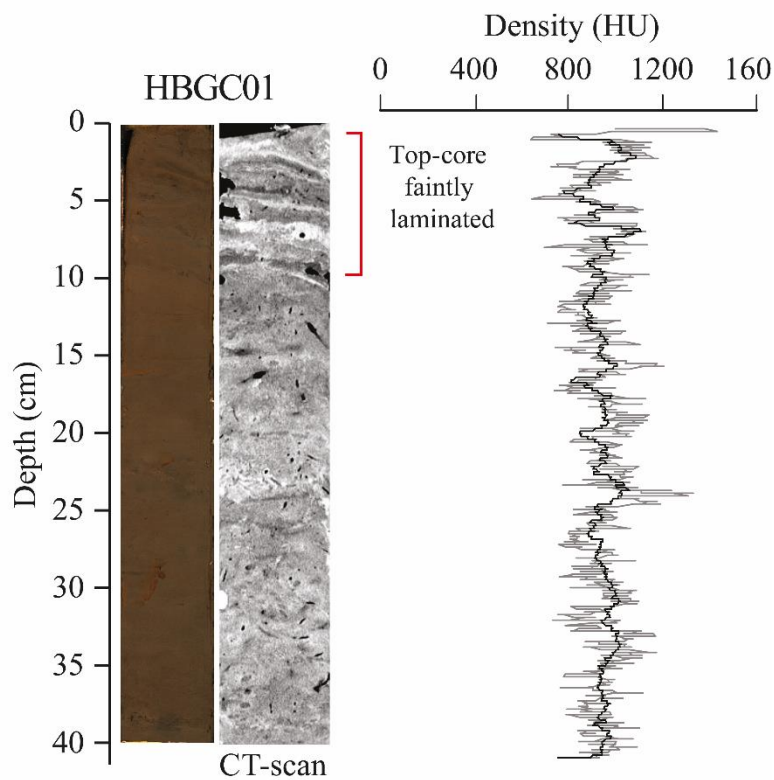


Figure 1-A.4 Original graph of the YC18-HB-GC01 age model produced by Plum.

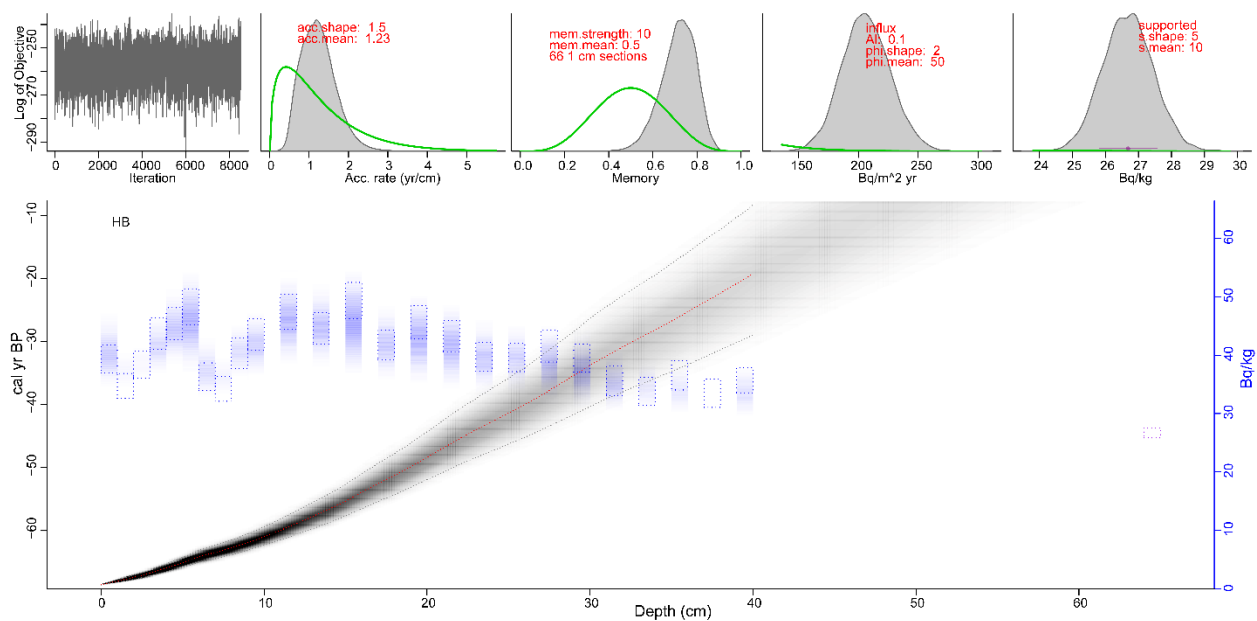
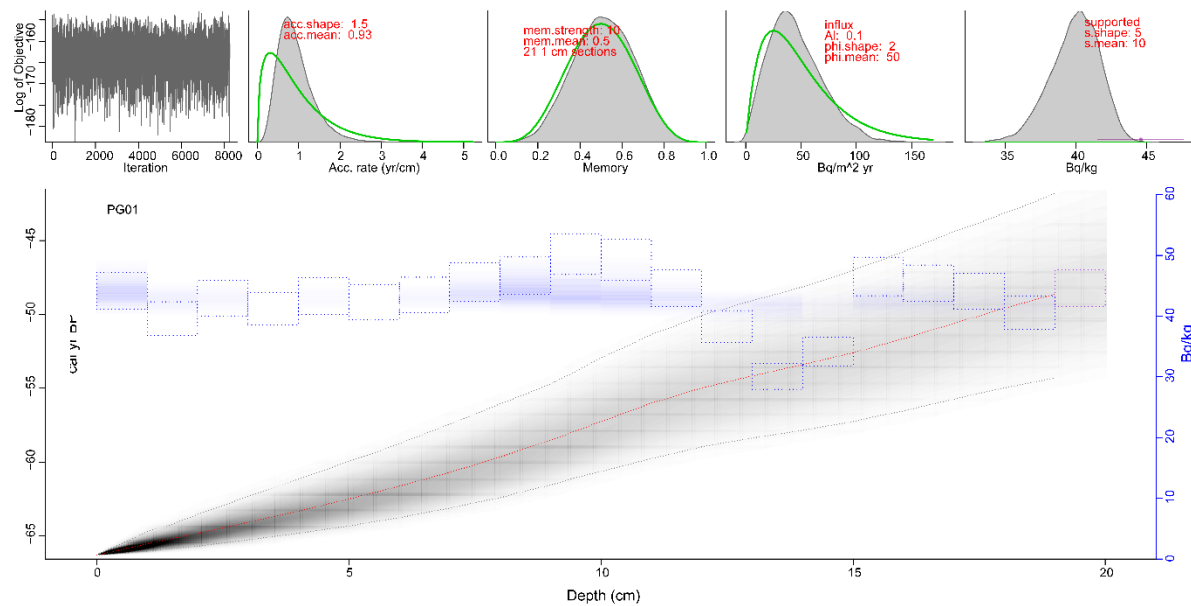


Figure 1-A.5 Original graph of the PG2303-1 age model produced by Plum.



CHAPITRE 2

IMPACTS OF STRONGER WINDS AND LONGER ICE-FREE SUMMERS ON CANADIAN BEAUFORT SEA SHELF ECOSYSTEMS SINCE THE LATE 1990S

Jade Falardeau^a, Anne de Vernal^a, Bianca Fréchette^a, Claude Hillaire-Marcel^a, Philippe Archambault^b, Michael Fritz^c, Colin Gallagher^d and George Tanski^c

- a. Geotop Research Center in Earth System Dynamics, Département des sciences de la Terre et de l'atmosphère, Université du Québec à Montréal, C.P. 8888 Succursale Centre-Ville, H3C 3P8, Montréal, Canada
- b. Québec Océan, ArcticNet, Takuvik, Département de biologie, Faculté des sciences et de génie, Université Laval, 1045 avenue de la Médecine, G1V 0A6, Québec, Canada
- c. Permafrost Research Unit, Alfred Wegener Institute, Helmholtz Centre for Polar and Marine Research, Telegrafenberg A45, 14773 Potsdam, Germany
- d. Fisheries and Oceans Canada, Arctic and Aquatic Research Division, Freshwater Institute, 501 University Crescent, Winnipeg, Manitoba, R3T-2N6, Canada

Cet article a été révisé à la suite de corrections mineures par les évaluateurs externes et soumis à nouveau à la revue *Estuarine, Coastal and Shelf Science* le 21 août 2023.

Les figures en matériel supplémentaire se retrouvent après les références de ce chapitre. Les tableaux supplémentaires ne seront accessibles qu'en ligne; voir les Annexes A à C pour les comptages micropaléontologiques bruts de la carotte YC18-HB-GC01.

Abstract

Continuous and multi-decadal records of faunal abundance and diversity helping to identify the impacts of ongoing global warming on aquatic ecosystems are rare in the coastal Arctic. Here, we used a 50-year-long microfaunal record from a sediment core collected in the Herschel Basin (YC18-HB-GC01; 18 m water depth) to document some of the environmental responses of the southern Canadian coastal Beaufort Sea to climate change. The microfaunal indicators include benthic foraminiferal assemblages, ostracods and tintinnids. The carbonated shells of two foraminiferal species were also analyzed for their stable isotope signatures ($\delta^{13}\text{C}$ and $\delta^{18}\text{O}$). We compiled environmental parameters from 1970–2019 for the coastal region, including sea ice data (break-up date, freeze-up date, open season length and mean summer concentration), the wind regime (mean speed, direction of strong winds and the number of storms), hydrological data (freshet date, freshet discharge and mean summer discharge of the Firth and the Mackenzie rivers), and air temperature. Large-scale atmospheric patterns were also taken into consideration. Time-constrained hierachal clustering analysis of foraminiferal assemblages and environmental parameters revealed a near-synchronous shift around the late 1990s. The microfaunal shift corresponds to an increased abundance of taxa tolerant to variable salinity, turbulent bottom water conditions, and turbid waters towards the present. The same time interval is marked by stronger easterly winds, more frequent storms, reduced sea-ice cover, and a pervasive anticyclonic circulation in the Arctic Ocean (positive Arctic Ocean Oscillation; AOO+). Deeper vertical mixing in the water column in response to intensified winds was fostered by reduced sea-ice cover with open surface waters leading to turbulence, increased particle loading and less saline bottom waters at the study site. Stronger easterly winds probably also resulted in enhanced resuspension events and coastal erosion in addition to a westward spreading of the Mackenzie River plume, altogether contributing to high particulate-matter transport. Increase food availability since ~2000 is probably essentially linked to enhanced degradation of terrestrial organic carbon, which also implies higher oxygen consumption. The sensitivity of microfaunal communities to environmental variations allowed capturing consequences of climate change on a marine Arctic shelf ecosystem over the last 50 years.

Keywords: Sea ice, Coastal erosion, Salinity, Benthic foraminifera, Tintinnids, Ostracods, Micropaleontology, Arctic Ocean

2.1 Introduction

Severe environmental changes in the coastal habitats of the southeastern Beaufort Sea due to global warming include sea-ice loss (Frey et al., 2015), increased coastal erosion rates (Irrgang et al., 2018), and the Mackenzie River plume spreading into open waters (Mulligan and Perrie, 2019). These modifications of the nearshore habitat can affect the distribution, quality, and diversity of marine resources (e.g., Brewster et al., 2016; Gallagher et al., 2021), with consequences on food security, culture, and economy of northern communities that rely on marine ecosystem for subsistence (Fritz et al., 2017). Identifying relationships between biota and their habitat can help local stakeholders to find adaptation strategies to climate change. However, studies that combine faunal and climatic records are sparse, and the existing records often cover too short or discontinuous observational periods, which makes it difficult to disentangle the impacts of recent anthropogenic climate warming versus natural climate and environmental variability. Paleoceanographic reconstructions with high temporal resolution can help fill the gap (e.g., Lapointe et al., 2017; Nguyen et al., 2017; Kutos et al., 2021; Gemery et al., 2023).

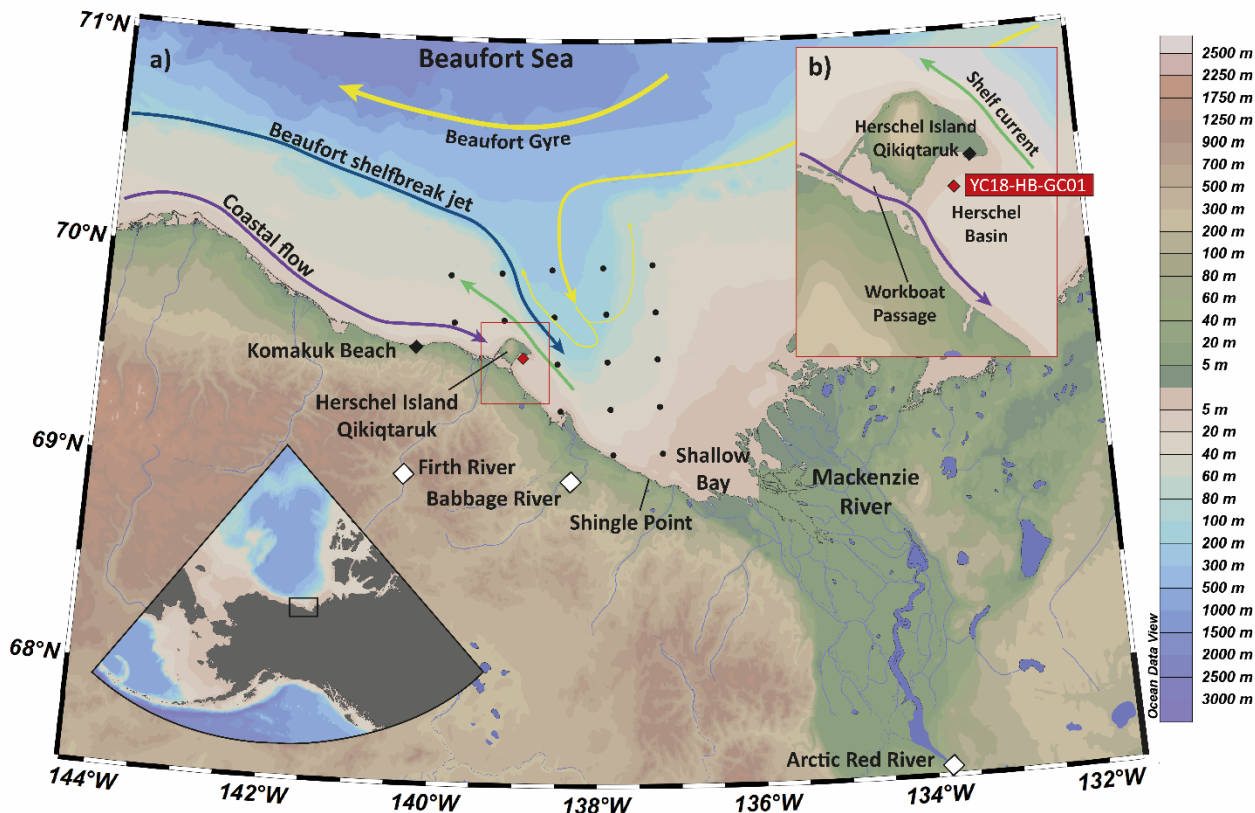
Microorganisms of Arctic Ocean shelves have been widely used as indicators of marine conditions. Their distribution is related to water temperature, salinity, oxygen levels, contaminants, and surface productivity (Cearreta et al., 2000; Wollenburg and Kuhnt, 2000; Polyak et al., 2002; Stepanova et al., 2003; Ruiz et al., 2005 and references therein; Gemery et al., 2017). In sediment archives, these microorganisms can be used to develop time series, providing that sedimentary processes are favorable to continuous and fine particle accumulation, which is uncommon in dynamic nearshore areas.

In this study, we established an ecological record spanning the last 50 years based on the analyses of microfaunal community changes in the Herschel Basin on the Beaufort Sea continental shelf, Canada. In addition to microfaunal assemblages, we analyzed the isotopic composition of the carbonate shells of two benthic foraminiferal species to further document bottom water conditions. In parallel, we compiled instrumental and satellite data of different environmental parameters including sea-ice, wind, hydrography, air temperature, and large-scale atmospheric pattern. By comparing both datasets, we seek to investigate potential relationships between ecological and environmental changes and to identify potential stressors in a rapidly evolving Arctic nearshore zone. This study also aims to validate the use of micropaleontological tools to reconstruct the impacts of recent climate changes on Arctic coastal areas, where in-situ measurements and ecosystem-based monitoring programs are limited (cf. Fritz et al., 2017; Brewster et al., 2021).

2.2 Study area

The Canadian Beaufort Sea continental shelf is ~530 km long and up to ~120 km wide. It is flanked by the Mackenzie Delta to the east and Herschel Island – Qikiqtaruk to the west (Fig. 2.1). East of the island, the Herschel Basin is 15 km wide, 40 km long, and has a maximum depth of 70 m (Fig. 2.1, EBA Engineering Consultants Ltd, 1992). As a natural sedimentary depocenter, it allows for a continuous accumulation of sediment and biological remains (Grotheer et al., 2020; Falardeau et al., 2023a). The shallow (< 20 m) part of the continental shelf is covered by persistent land-fast ice that forms in October and lasts until late June (Carmack and Macdonald, 2002). In summer, sea-ice meltwater and river discharge generate a stratified surface water layer of 7 to 15 m-thick (Carmack and Macdonald, 2002; Falardeau et al., 2023a).

Figure 2.1 a) Study area in the southern Canadian Beaufort Sea and b) close-up of the core site location. White and black diamonds represent the location of the hydrometric and weather stations, respectively. The black dots correspond to the grid used to calculate the mean summer sea-ice concentration. The purple arrow corresponds to the longshore current carrying low saline waters derived from the coastal river outflows and the extension of the Alaskan coastal waters; the blue arrow corresponds to the nutrient-rich and saline (>31.5) Pacific waters flowing through the “Beaufort Sea shelfbreak jet” (Pickart, 2004); the yellow arrows show the Beaufort Gyre and the associated recirculation currents and finally, the green arrow in (b) indicates the cold (<-1°C) and low salinity (<31) surface waters (<30 m) flowing through the shelf current (based on Lin et al., 2020). Maps were made in Ocean Data View (Schlitzer, 2018).



Predominant wind directions are an important component of the physical coastal environment. Under strong easterly winds, sea ice is pushed offshore, nutrient-rich subsurface waters upwell (Carmack and Macdonald, 2002; Pickart et al., 2011), and the Mackenzie River plume spread up to hundreds of kilometers westward (Mulligan and Perrie, 2019). Inversely, strong westerly winds tend to maintain sea ice and the river plume close to shore.

The Mackenzie River is among the four largest rivers discharging into the Arctic Ocean with an annual mean flux of $316 \text{ km}^3 \cdot \text{a}^{-1}$ (for 1999-2008; Holmes et al., 2012). The Mackenzie River plume, particularly during the spring freshet, brings fresh and particle-rich waters onto the shelf (Ehn et al., 2019). Two smaller rivers close to the study site, the Firth and Babbage rivers (Fig. 2.1), and smaller river systems, also contribute to freshwater with dissolved- and particulate-matter input (e.g., Coch et al., 2018).

2.3 Material and methods

2.3.1 Microfaunal analyses

Remains of microorganisms were analyzed in the sediment core YC18-HB-GC-01 (Fig. 2.1; 69.544°N - 138.970°W ; 18 m water depth; hereafter HBGC01) collected in the Herschel Basin in August 2018. The coring site is located approximately 4 km east of the Herschel Island coast and 125 km west of the Mackenzie River mouth at Shallow Bay (Fig. 2.1). The core was retrieved with a UWITEC gravity corer from a Zodiac inflatable boat and stored at $+4^\circ\text{C}$ until further analyses. The HBGC01 core was cut in halves lengthwise and subsampled at 1-cm intervals for micropaleontological and radio-isotope analyses. The 40 cm-long core spanned from ~ 1970 to 2018 with a mean sediment accumulation rate of $0.9 \pm 0.3 \text{ g} \cdot \text{cm}^{-2} \cdot \text{a}^{-1}$ allowing for a near-annual resolution (Falardeau et al., 2023a; Fig. 2-A.1d). The age model was built based on ^{210}Pb radiogenic activities and sediment density using the *Plum* package (Aquino-López et al., 2018) in R (R Core Team, 2021). Sediment laminations and a mixed ^{210}Pb excess signal in the core top 10 cm suggested reworking (Hill and Nadeau, 1989; Fig. 2-A.1a, c). However, the ^{210}Pb log-decrease between the bottom of the core and 10 cm led to estimating a mean sedimentation rate of $0.8 \text{ cm} \cdot \text{a}^{-1}$, which was fed into the *Plum* age model. An independent ^{137}Cs peak at 38-37 cm suggested an age of 1963 (Aoyama et al., 2006) that roughly matched the age interval of 1963-1981 given by the age model (Fig. 2-A.1d; see Falardeau et al. 2023a for more details).

For microfossil counts, 6-7 g of dry sediment per sample were wet-sieved at $63 \mu\text{m}$ and the upper fraction was observed under a stereo microscope at a magnification of 40 to 60X. The samples contain three main

types of microfossils: benthic foraminifera (calcareous and agglutinated, inclusively), ostracods, and tintinnids. Foraminifera were identified according to Feyling-Hanssen et al. (1971), Polyak et al. (2002), and Scott et al. (2008), while ostracods identification was based on Stepanova et al. (2003) and Gemery et al. (2017). The only species of tintinnid observed in the dried fraction >63 µm is *Tintinnopsis fimbriata* (Meunier, 1919), which is an agglutinated ciliate that inhabits the upper 40 m of the water column (Paranjape, 1987). For this study, the abundance of microfossils is expressed in fluxes (#·cm⁻²·a⁻¹), which is the number of specimens counted per gram of sediment in one sample (#·g⁻¹) multiplied by the accumulation rates (g·cm⁻²·a⁻¹). For more details on microfossil preparations, species identification, and microfaunal diversity in the Herschel Basin see Falardeau et al. (2023a).

We analyzed the assemblages of the benthic foraminifera and reported the relative abundance of species in percentages (%; calcareous and agglutinated foraminifera together). For the purpose of this paper, only the relative abundances of the taxa with clear ecological affinities are discussed (see Table 2.1).

2.3.2 Geochemistry

2.3.2.1 Carbonate shells

The carbonate shells of the two most abundant calcareous benthic foraminiferal species, *Elphidium clavatum*, and *Cassidulina reniforme*, were analyzed for their stable isotopic composition ($\delta^{18}\text{O}$ and $\delta^{13}\text{C}$, ‰ vs. VPDB) at the light stable isotope geochemistry laboratory of Geotop-UQAM following standard laboratory procedures. Briefly, the specimens from the >63 µm fraction of each species were weighed using a microbalance, which yielded between 50 and 120 µg of material per sample. The weighed specimens were subsequently transferred into conical glass vials, closed with septum caps, and heated at 90° for an hour before the analysis, which is performed using a Micromass Isoprime isotope ratio mass spectrometer coupled to a MultiCarb system in dual inlet mode. The results are normalized based on two internal references (UQ6: $\delta^{18}\text{O} = -1.48 \pm 0.03\text{‰}$ and $-14.25 \pm 0.05\text{‰}$; NBS18: $\delta^{13}\text{C} = 2.21 \pm 0.03\text{‰}$ and $-40.78 \pm 0.05\text{‰}$; see raw data in Table 2-A.1).

2.3.2.2 Bulk sediment

Geochemical analyses on the bulk sediments of core HBGC01 comprise the total organic carbon (TOC) and the total nitrogen (TN) together with the stable isotopic ratios of organic carbon ($\delta^{13}\text{C}_{\text{org}}$) and nitrogen ($\delta^{15}\text{N}$). For each subsample, about 1 g of homogenized freeze-dried sediment was weighed at UQAM before being sent to the Stable Isotope Facility of the University of California (Davis, USA). Following their

procedures, the inorganic carbon and moisture of ~5-30 mg of subsamples were removed by fumigation with hydrochloric acid (37%) for 72 hours and by treatment with NaOH pellets for 1 to 2 days, respectively, both at a temperature of 60°C. The TOC and TN were measured with an ECS 4010 Elemental Analyzer (Costech) and are given in weight percent (wt %). The $\delta^{13}\text{C}$ and $\delta^{15}\text{N}$ were measured using an Elementar Vario El Cube elemental analyzer coupled to an Isoprime VISION IRMS (Elementar) or a PDZ Europa 20-20 isotope ratio mass spectrometer (Sercon). The results are reported per mil relative to the Vienna Pee Dee Belemnite (‰ vs. VPDB) or the air standards (‰ vs. N air) for carbon and nitrogen, respectively. The atomic C/N ratio was obtained by multiplying the TOC/TN ratio with the atomic mass ratio of N/C (i.e. 14/12; see raw data in Table 2-A.2).

2.3.3 Environmental parameters

2.3.3.1 Sea-ice cover and seasonality

To quantify the daily sea-ice concentrations in the study area (area covered by sea ice in %), the mean of 18 grid points (25 km x 25 km) was calculated from the NOAA/NSIDC climate data record of passive microwave sea-ice concentration covering the 1979-2018 interval (data from Meier et al. 2017; see Fig. 2.1 for grid point locations). The metrics include the mean summer (June, July, August, and September; JJAS) sea-ice concentration followed by the break-up and freeze-up dates defined as 10 consecutive days with less than 50 % and over 50 % of sea-ice concentration, respectively, from which the length of the ice-free season was obtained.

Table 2.1 List of the microfaunal taxa, the corresponding abbreviation names, and their ecological affinities when applicable. *Selected ecological indicators

Abbreviation	Species	Ecological affinities	Reference
B. frig	<i>Buccella frigida</i>	Tolerant to low salinity in Arctic shelves	Polyak et al. (2002); Scott et al. (2008); Wollenburg and Kuhnt (2000)
C.ren	<i>Cassidulina reniforme</i>	Stable saline bottom waters	Polyak et al. (2002); Scott et al. (2008)
E.alb	<i>Elphidium albiumbilicatum</i>		
E.ask	<i>Elphidium asklundi</i>	Tolerant to low salinity	Falardeau et al. (2023a)
E.bart	* <i>Elphidium bartletti</i>	Varying and generally low salinities; Coarse-grained substrate	Polyak et al. (2002); Falardeau et al. (2023a)
E.clav	<i>Elphidium clavatum</i>		

E.pul	* <i>Eoepnidella pulchella</i>	Food availability and upwelling	Wollenburg and Kuhnt (2000); Scott et al. (2008); Falardeau et al. (2023a)
E.tak	<i>Epistominella takayanagii</i>		
H.orb	<i>Haynesina orbicularis</i>	Tolerant to low salinity in Arctic shelves	Polyak et al. (2002); Scott et al. (2008)
H.niv	* <i>Haynesina nivea</i>	Shallow environments; Fresh, warm and unstable water conditions	Voltski et al. (2015); Falardeau et al. (2023a)
I.hel	<i>Islandiella helenae</i>	Cold and relatively low salinity waters in shallow Arctic shelves; Near sea-ice margins	Cage et al. (2021)
I.nor	* <i>Islandiella norcrossi</i>	Stable saline waters	Polyak et al. (2002); Cage et al. (2021)
Poly	Polymorphinids		
Q.stalk	* <i>Quinqueloculina stalkeri</i>	Associated to glacier-proximal facies; Tolerate turbidity; Can feed on bacterial degradation products	Guilbault et al. (2003); Falardeau et al. (2023b)
R.turb	<i>Recurvooides turbinatus</i>		
S.fey	* <i>Stainforthia feylingi</i>	Sea-ice margin productivity	Seidenkrantz (2013)
S.bif	<i>Spiroplectammina biformis</i>	Rapid sedimentation and turbid meltwaters	Jennings and Helgadóttir (1994)
S.hor	* <i>Stetsonia horvathi</i>	Oligotrophic waters under permanently ice-covered regions; Can feed on bacterial degradation products	Wollenburg and Kuhnt (2000); Jennings et al. (2020); Falardeau et al. (2023b)
T.ear	* <i>Textularia earlandi</i>	Opportunistic; Can feed on bacterial degradation products; Tolerate turbidity	Alve (2010); Jennings et al. (2020); Falardeau et al. (2023b)
T.tor	<i>Textularia torquata</i>		
	<i>Tintinnopsis fimbriata</i>	Fresh sediment-loaded waters; Near river mouths	Echols and Fowler (1973); Falardeau et al. (2023a)

Table 2.2 List of the environmental parameters and their corresponding abbreviation names

T_sum_kom	Mean summer air temperature at Komakuk Beach (°C)
Fd_Tsi	Freshet date at Arctic Red River (Julian Day)
Md_Tsi	Mean summer discharge at Arctic Red River ($m^3 \cdot s^{-1}$)
Fv_Tsi	Freshet discharge value at Arctic Red River ($m^3 \cdot s^{-1}$)
Fd_Firth	Freshet date at Firth River (Julian Day)
Md_Firth	Mean summer discharge at Firth River ($m^3 \cdot s^{-1}$)
Fv_Firth	Freshet discharge value at Firth River ($m^3 \cdot s^{-1}$)
sum_sic	Mean summer sea-ice concentration (%)
break_up	Date of sea-ice break-up (Julian Day)
Op_seas	Number of ice-free days
Freeze_up	Date of sea-ice freeze-up (Julian Day)
mean_E_k	Mean easterly wind speed during the open water season at Komakuk Beach ($m \cdot s^{-1}$)
mean_W_k	Mean westerly wind speed during the open water season at Komakuk Beach ($m \cdot s^{-1}$)
east_storm_k	Number of easterly storms at Komakuk Beach
west_storm_k	Number of westerly storms at Komakuk Beach
tot_storm_k	Total number of storms at Komakuk Beach
NP	North Pacific Index
PDO	Pacific Decadal Oscillation
AOO	Arctic Ocean Oscillation
AO	Arctic Oscillation
AL	Aleutian Low-Beaufort Sea Anticyclone (ALBSA)
yr	Mean of the twelve months prior to the open water season (i.e., June)
sum	Summer mean (JJAS)
sb	Spring bloom (JJ) mean
fb	Fall bloom (AS) mean
lag1	Mean of the three months (MAM) before the open water season
lag2	Mean of the six months (DJFMAM) before the open water season

2.3.3.2 Wind data

We used the hourly wind data from the Komakuk Beach weather station (Fig. 2.1; Environment and Climate Change Canada Historical Climate Data, October 2020), which covers from 1973 to 2018. Measurements were made every 6 hours from 1973 to 1993, and every hour, from 1994 to 2018. Gaps that were smaller than 6 consecutive hours were interpolated from linear regression. The interpolated hourly 1994-2018 record was then subsampled every 6 hours to avoid an overrepresentation of the data in this interval. Only the hourly wind data within the open water season were considered for all calculated wind indices.

We analyzed the direction of winds $>10 m \cdot s^{-1}$, which exhibited a clear bimodal pattern (Fig. 2-A.2) as winds originated either from the east or the west (east: 45° - 135° and west: 225° - 315°). We calculated the mean

wind speed per open water season for both directions. We also calculated the annual frequency of storm events, which are described as six consecutive hours with winds $>10 \text{ m}\cdot\text{s}^{-1}$ (cf. Manson and Solomon, 2007). A storm event was thus recorded when two consecutive readings $>10 \text{ m}\cdot\text{s}^{-1}$ occurred. Data from the Herschel Island weather station are also available (Fig. 2.1b), but the temporal coverage is too short and discontinuous for being included in this study (see Fig. 2-A.2 and Table 2-A.3).

2.3.3.3 River discharge

Time-series of daily discharge data were retrieved online from the Firth River Near the Mouth, the Babbage River Below Caribou Creek, and the Mackenzie River at the Arctic Red River hydrometric stations (Fig. 2.1; Environment and Climate Change Canada Historical Hydrometric Data, April 2020). Discharge data cover 46 years (1972-2018), 18 years (1978-1994), and 44 years (1973-2017), respectively. Three hydrometric indices are used to describe the river dynamics: (1) the spring freshet date, (2) the freshet discharge, and (3) the mean summer discharge (July, August, and September; JAS), after the spring freshet date. The spring freshet date was defined as the day of the highest discharge between May and June. Due to its short temporal coverage, the Babbage River will not be discussed any further (see data in Fig. 2-A.3 and Table 2-A.3).

2.3.3.4 Air temperatures

Air temperature data were obtained from the Environment and Climate Change Canada Historical Climate Data (April 2020). The mean summer (JJAS) air temperature was calculated based on the daily mean air temperatures at Komakuk Beach (1958-2017) and at Herschel Island (1995-2018) weather stations (Fig. 2.1; Table 2-A.3), but only the longer record of Komakuk Beach was used for further analyses.

2.3.3.5 Atmospheric oscillation indices

We acquired the monthly means of different atmospheric oscillation indices including the North Pacific Index (NPI; Trenberth and Hurrell, 1994), the Aleutian Low-Beaufort Sea Anticyclone (ALBSA; Cox et al., 2019), the Arctic Oscillation (AO; Thompson and Wallace, 1998) and the Pacific Decadal Oscillation (PDO; Mantua et al., 1997) from the NOAA Physical Sciences Laboratory website (<https://psl.noaa.gov/>). Subsequently, we calculated the summer (JJAS) mean for these indices, in addition to the spring bloom (June and July) and the fall bloom (August and September) means. To evaluate if there was a level of predictability of the climate indices on the following summer environmental conditions, we also calculated the mean of the indices for the three months (March, April, and May; MAM), the six months (December

to May; DJFMAM) and the twelve months before the beginning of the summer season (June). Finally, the annual Arctic Ocean Oscillation index (AOO; Proshutinsky and Johnson, 1997; <https://www.whoi.edu/page.do?pid=66578>) was also used in this study. A summary of the atmospheric oscillation indices used in this study and their potential linkages with the southern Beaufort Sea environmental conditions are presented in Table 2-A.4.

2.3.4 Cluster analyses and rate of change

The continuous temporal coverage between the ecological indicators and the environmental parameters spans from 1979 to 2017. Data from the sediment core were treated independently because of uncertainties with regard to the age model and the irregular time steps between the sediment subsamples. To identify discontinuities in the time-series and to keep the chronological order, we used a time-constrained hierarchical cluster analysis. For the foraminiferal assemblages, we applied the *Bray-Curtis* dissimilarity on the square-root transformed foraminiferal relative abundances, i.e. the *Hellinger* transformed foraminiferal raw counts. The square-root transformation reduces the importance of the abundant taxa, and inversely, gives more importance to the lower-numbered taxa. Only the species recording >1 % in at least one sample were kept for statistical analyses (n=20 taxa; Fig. 2.2a). For the environmental dataset that includes parameters of different units and scales, the cluster was applied on the *Euclidean* distance of the z-scores transformed parameters (n=41 parameters; Fig. 2.2b). We used the constrained hierarchical clustering function (*chclust*) of the *rioja* package (Juggins, 2022) in R (R Core Team, 2021). Subsequently, the relative abundances of the taxa were normalized on a scale of 0 to 5 and ordered based on their weighted average from the cluster score using the *vegemite* function of the *vegan* package in R (Oksanen et al., 2013) and illustrated with a heat map (Fig. 2.2a). The same approach was used for the environmental parameters (Fig. 2.2b). Only the variables that demonstrated ruptures or changes within the covered time interval are discussed in this study.

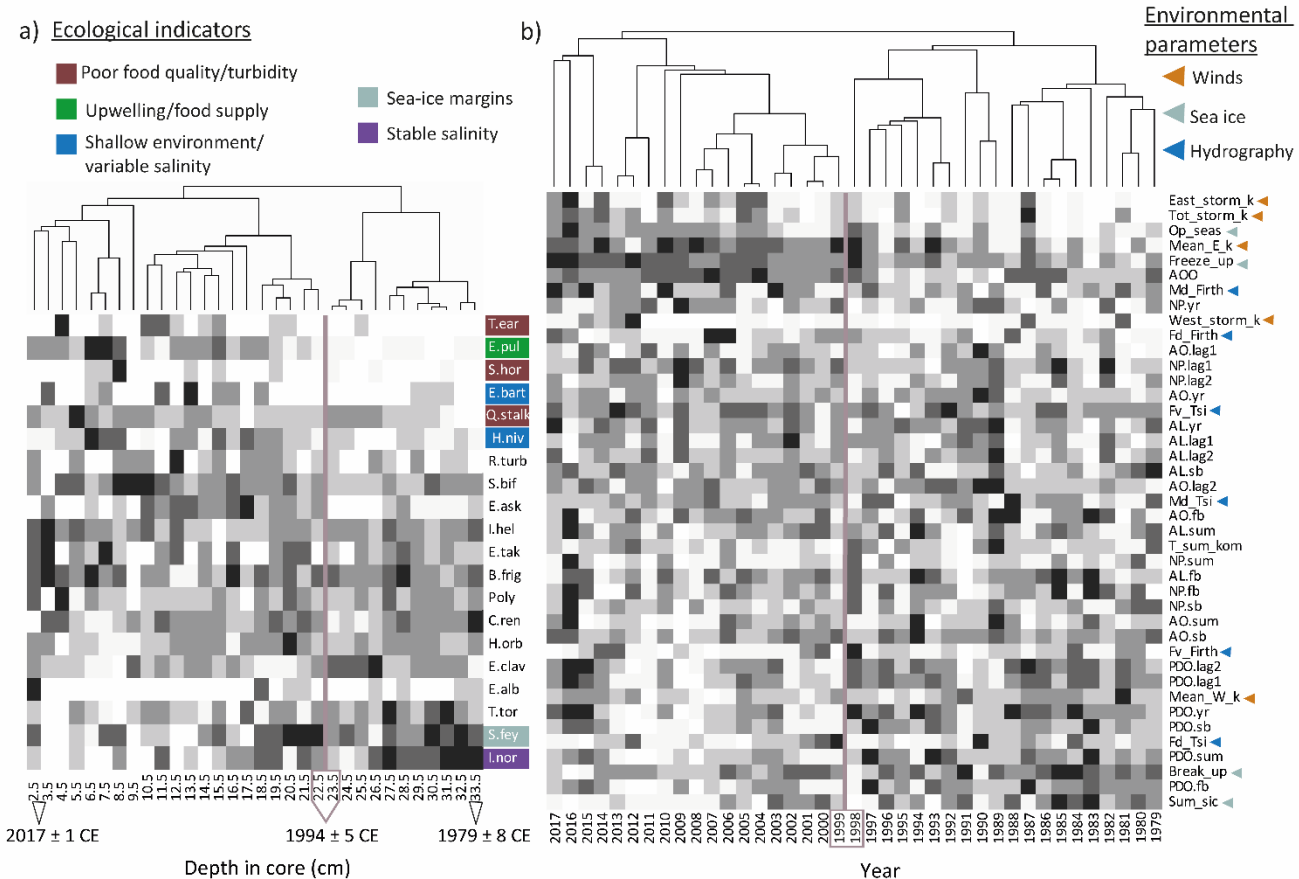
We also calculated an index of the rate of change per year for the foraminiferal and environmental data, which corresponds to the *Bray-Curtis* dissimilarity or the *Euclidean* distance for the foraminiferal assemblages and the environmental data, respectively, between adjacent samples or years in both chronosequences. The distance calculation was applied to the square-root transformed foraminiferal relative abundances and the z-score transformed environmental parameters. To obtain a rate of change per year, the *Euclidean* distance of the foraminiferal assemblages was divided by the elapsed time between samples. All the environmental data are available in Table 2-A.3.

2.4 Results and discussion

2.4.1 Environmental changes

The dendrogram of the time-constrained hierarchical clustering of the environmental parameters places the first division in 1998-1999 (Fig. 2.2b). The two resultant subsets are mainly determined by the intensification of easterly storms and the total number of storms (Figs. 2.2b, 2.3f). Accordingly, the mean easterly wind speeds increase towards the present and frequently reach values above $6 \text{ m}\cdot\text{s}^{-1}$ (Fig. 2.3e). Other important changes recorded around 1998 involve sea ice conditions (Fig. 2.2b). While the break-up occurred on average 18 days earlier in 1998-2017, the average freeze-up date was delayed by 15 days, implying an increased open water season of about one month (Table 2-A.3). This trend is reflected in the summer sea-ice concentration, which decreased from $34 \pm 14 \%$ before 1998 to $18 \pm 11 \%$ afterwards (Fig. 2.3d).

Figure 2.2 Heat maps and time-constrained hierachical clusters are illustrated as dendrograms of the (a) foraminiferal relative abundances, including the selected ecological indicators, and the (b) environmental parameters reordered based on their weighted average from the cluster score. See Tables 2.1 and 2.2 for the ecological affinity references and the abbreviation corresponding names.



The hydrographical indicators do not particularly stand out in the analysis, except for a possible increase in the Firth River mean summer discharge and an earlier freshet of the Mackenzie River towards the present (Figs. 2.2b, 2-A.2). The summer mean discharge of the Firth River increased by about $50 \text{ m}^3 \cdot \text{s}^{-1}$ over the 2005-2018 interval (Fig. 2-A.3). The waters of the Firth River and the organic matter they carry may reach the Herschel Basin as the currents flow dominantly from west to east through the Workboat Passage adjacent to the southern shore of Herschel Island (Fig. 2.1; Pelletier and Medioli, 2014). The Mackenzie River freshet occurred on average one week earlier since the beginning of the 1990s (Fig. 2-A.3). The PDO has generally been negative after 1998 (Fig. 2.2b) while the AOO became positive after 1997 (Fig. 2.2b, 2.3c). Lower environmental variability after 2000 is suggested by a decrease in the rate of change (Fig. 2.3b).

2.4.2 Changes in the marine habitat

2.4.2.1 Microfaunal community

The dendrogram of the time-constrained hierachal clustering for the foraminiferal assemblages places the main division of the full 1979-2017 time interval at 23 cm, which corresponds to an age of 1994 ± 5 years (Fig. 2.2a). The 1979-1994 subgroup was marked by abundant *Islandiella norcrossi* and *Stainforthia feylingi*, which decrease afterwards as *Textularia earlandi*, *Eoeponidella pulchella*, *Elphidium bartletti*, *Quinqueloculina stalkerii*, *Stetsonia horvathi* and *Haynesina nivea* increase (Fig. 2.2a).

The two main subsets of foraminiferal taxa are characterized by different levels of tolerance to low salinity waters and unstable conditions. While *Islandiella norcrossi* typically prefers stable saline conditions, *Haynesina nivea* and *Elphidium bartletti* occupy shallow environments with variable temperatures and salinities, along with relatively turbulent bottom waters (Table 2.1). The taxon *Stainforthia feylingi* is also more abundant at a deeper site of the Herschel Basin, which suggests a preference for calm and stable environmental conditions (Falardeau et al., 2023a). The height and number of branches in the dendrogram are higher in the 1994-2017 interval than from 1979 to 1994, which illustrates that neighboring assemblages are less comparable after ~1994 (Fig. 2.2a). Accordingly, the trend in the rate of change continuously increases and shows repeated peaks of particularly high values after ~1998 (Fig. 2.3a). This behavior is coherent with more dissimilar and changing foraminiferal assemblages, thus suggesting more unstable marine coastal habitat conditions during the last two decades.

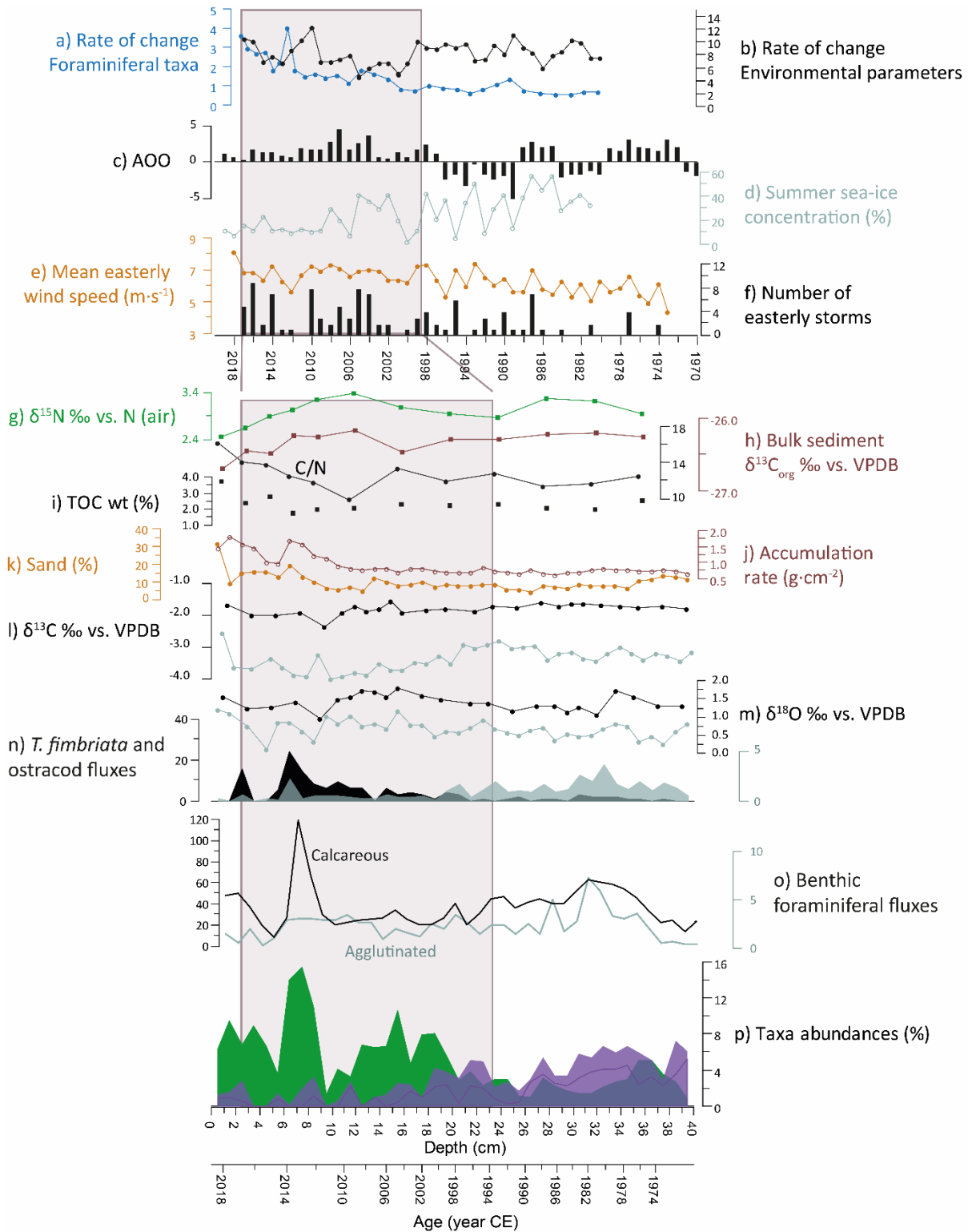
The two subsets of foraminiferal taxa may also reflect preferences for different types of food given the inverse relationship between species feeding on degradation products by bacteria (i.e. *Quinqueloculina stalker*, *Textularia earlandi* and *Stetsonia horvathi*) or on food associated with upwelling and primary productivity (i.e., *Eoepionidella pulchella*), and a species (i.e., *Stainforthia feylingi*) that feed near sea-ice margins (Table 2.1; Figs. 2.2a, 2.3p). The transition around 1994 is also marked by a decrease in ostracod fluxes from a mean of $1.5 \pm 0.8 \text{ valves} \cdot \text{cm}^{-2} \cdot \text{g}^{-1}$ before repeatedly near-zero values afterward. Inversely, the tintinnid *Tintinnopsis fimbriata* was nearly absent before ~ 1994 , after which its flux increased, peaking at $24 \text{ cm}^{-2} \cdot \text{g}^{-1}$ (Fig. 2.3n). The average calcareous benthic foraminiferal fluxes is lower after ~ 1994 (Fig. 2.3o, black line). However, the fluxes show large amplitude variations since ~ 2010 with a distinct high peak in calcareous foraminifera of $119 \text{ cm}^{-2} \cdot \text{g}^{-1}$ in ~ 2014 . Minimum values are recorded at the bottom and top of the core, which coincide with intervals of reduced agglutinated benthic foraminiferal fluxes (Fig. 2.3o).

2.4.2.2 Geochemistry and lithology

The $\delta^{13}\text{C}$ -values of *Elphidium clavatum* average $-3.4 \pm 0.3 \text{ ‰}$. Negative values characterize infaunal habitat, as the interstitial water of the sediment is depleted in ^{13}C (McCorkle et al., 1997). After ~ 2006 , the $\delta^{13}\text{C}$ -values slightly decrease reaching the lowest value of $-4.0 \pm 0.1 \text{ ‰}$ in ~ 2012 (Fig. 2.3l, gray). The $\delta^{13}\text{C}$ -values of *Cassidulina reniforme* remain constant throughout the record ($-1.8 \pm 0.2 \text{ ‰}$; Fig. 2.3l, black). The $\delta^{13}\text{C}$ of *E. clavatum* is lower than that of *C. reniforme*, suggesting that *E. clavatum* either lives at a greater depth in the sediment and/or have a faster metabolism (higher respiration rates; cf. Ravelo and Hillaire-Marcel, 2007; Cesbron et al., 2016). Decreased $\delta^{13}\text{C}$ -value in benthic foraminiferal shells can also relate to more depleted inorganic carbon in bottom waters due to high microbial respiration of organic matter (Mol et al., 2018). The $\delta^{18}\text{O}$ -values of *E. clavatum* ranged from 0.6 ‰ in the ~ 1970 -2000 interval to values $>1.0 \text{ ‰}$ towards the core top with two relatively low values around 2012 and 2016 (Fig. 2.3m, gray line). *C. reniforme* also shows a trend toward higher $\delta^{18}\text{O}$ -values upcore (Fig. 2.3m, black line). In estuarine-like environments, increased $\delta^{18}\text{O}$ suggests increased water salinity as these variables tend to have a positive linear relationship (Polyak et al., 2003; Lansard et al., 2012).

Figure 2.3 Summary figure of regional changes from the 1970s to 2018 as recorded in the study core, and the environmental and climatic archives. Rate of change of the a) benthic foraminiferal assemblages and the b) environmental parameters (see section 2.3.4). c), d), e), and f) Selected environmental indicators. g), h) and i) Geochemical measurements performed in the HBGC01 core together with the atomic C/N ratio (black line). j) Accumulation rates ($\text{g} \cdot \text{cm}^{-2}$) and k) concentration of sand (%). l) $\delta^{13}\text{C}$ and m) $\delta^{18}\text{O}$ of *Elphidium clavatum* (gray) and *Cassidulina reniforme* (black). n) Fluxes ($\# \cdot \text{cm}^{-2} \cdot \text{a}^{-1}$) of *Tintinnopsis fimbriata* (black shaded area) and ostracod valves (gray shaded area) and o) fluxes of calcareous (black line) and agglutinated (gray line) benthic foraminifera. p) Relative abundance (%) of *Eoepionidella pulchella* (green shaded area) and the cumulative abundance (%; purple

shaded area) of *Islandiella norcrossi* and *Stainforthia feylingi* from 1970 to 2018 (see Falardeau et al., 2023a). The solid purple line delineates the abundance of *S. feylingi* (below) and *I. norcrossi* (above). The gray shaded areas highlight the 1999–2017 and the 1994–2017 subsets of the foraminiferal taxa and the environmental parameters, respectively.



The TOC increased from 2.2 to 3.8 % towards the core top (Fig. 2.3i), and the $\delta^{13}\text{C}_{\text{org}}$ - and $\delta^{15}\text{N}$ -values of bulk sediment samples decreased after ~2009 (Fig. 2.3g, h). The C/N ratio >10 suggests dominant terrestrial organic matter sources, especially towards the core top (Fig. 2.3; cf. Magen et al., 2010; Jong et al., 2020). The changes in the grain-size distribution of the core are restricted to the last decade with sand content increasing from ~ 9 to 31 % (Fig. 2.3k).

2.4.3 Consequences of climate change on the coastal ecosystem

2.4.3.1 Easterly winds, sea ice, and unstable marine conditions

Winds and sea ice-related variables recorded the most significant changes along the southeastern Beaufort Sea coast over the last five decades. The relationship between easterly winds and the reduced sea-ice cover and/or persistence is known in the region (Ogi and Wallace, 2007; Wood et al., 2013; Frey et al., 2015), as easterly winds tend to push the ice away from the shore. At the regional scale, enhanced easterly winds occur under a strong anticyclonic regime (i.e., under positive AOO; Proshutinsky and Johnson, 1997; Ogi and Wallace, 2007; Fig. 2.3c, d, e; Table 2-A.4). Furthermore, the potential relationship between negative PDO and reduced sea ice (Fig. 2.2b) in the Arctic Ocean has been documented by Screen and Francis (2016) and Lapointe et al. (2017). Hence, negative PDO normally occurs when the Aleutian Low is weak (positive NPI; Table 2-A.4), which leads to dominant southerly winds in the northern Pacific, thus to the advection of warm Pacific air towards the central Arctic. However, the effects of a negative PDO/weak Aleutian Low on the sea-ice cover to the southern Beaufort Sea is equivocal, as it also favors westerly winds (downwelling events; Kirillov et al., 2016; see section 2.2). Ultimately, the strength of the anticyclonic circulation in the western Arctic better accounts for wind direction and sea-ice cover changes in the area (Ogi and Wallace, 2007; Kirillov et al., 2016; this study). On land, negative PDO leads to warmer atmosphere and enhanced precipitation in the northwestern Canadian Arctic (Lapointe et al., 2017; Kutos et al., 2021), which might result in higher mean river discharge (Coch et al., 2018), and possibly earlier freshet dates (Figs. 2.2b, 2-A.2). The environmental parameters that stand out the most from our cluster analysis are thus interrelated and complementary to each other (Table 2-A.4).

The environmental shift identified in 1998 is near-synchronous with the important marine habitat shift revealed by the microfaunal community in 1994 ± 5 years (Fig. 2.2; section 2.4.2.1). A reduced sea-ice cover, strong easterly winds, and the enhanced frequency of storms likely favored vertical mixing (Rainville and Woodgate, 2009; Schulze and Pickart, 2012) and a western dispersal of the Mackenzie River plume towards Herschel Island and beyond (Mulligan and Perrie, 2019). Altogether, they can account for more

variability in oceanographic conditions at depth in the Herschel Basin (section 2.4.2.1), in accordance with the foraminiferal rate of change recording the highest values (Fig. 2.3a). Interestingly, lower environmental variability was recorded after 1998 (Fig. 2.3b). The lower summer sea-ice concentration, thus the longer open water season, might have played an important role in coastal habitat instabilities. Although environmental variability was higher before 1998, more persistent land-fast ice probably acted as a shield from the variable climatic conditions (see Falardeau et al., 2023a).

The Mackenzie River hydrography does not seem to play an important role in the coastal area near the Herschel Basin (Fig. 2.2b). The influence of the plume at such a distance from the river mouth appears to be more determined by wind strength and direction and sea-ice than by freshet and summer mean discharge. However, nearby tributaries and small rivers result in freshwater and organic matter inputs that may be important locally (Fig. 2.2b; Coch et al., 2018).

Although most ecological indicators and environmental parameters point to enhanced freshwater in the Herschel Basin during the last two decades, higher $\delta^{18}\text{O}$ values are recorded after 2000 (Fig. 2.3m), which is somewhat counterintuitive (Lansard et al., 2012). The benthic $\delta^{18}\text{O}$ record could reflect a shallower halocline as recently identified in the Canada Basin (Rosenblum et al., 2022). However, during the seasonal sea-ice growth, ^{18}O -depleted brines are released and sink to the sea floor, whereas during summer, sea-ice melting releases positive $\delta^{18}\text{O}$ and low-salinity meltwater into the surface water layer (Ravelo and Hillaire-Marcel, 2007). As these processes blur the current $\delta^{18}\text{O}$ -salinity relationship, an unequivocal interpretation of the shift in $\delta^{18}\text{O}$ -values seems difficult to resolve here given the combination of changes in the sea ice regime, halocline depth, and continental runoff. Nevertheless, the negative $\delta^{18}\text{O}$ values after 2006 suggest higher variability in the parameters governing the isotopic composition of benthic foraminifera (Fig. 2.3m).

2.4.3.2 Food sources and turbidity

After 1998, strong easterly winds and more frequent storms (Fig. 2.3e, f) favored the mixing and upwelling of nutrient-rich subsurface Pacific waters (Pickart, 2004; Pickart et al., 2011), thus increasing the regional primary productivity (Tremblay et al., 2011). Enhanced food supply might be the reason for the increased abundance of *Eoeponidella pulchella* dated around 1994 ± 5 years (Fig. 2.3p; Table 2.1). A slight increase in $\delta^{15}\text{N}$ and $\delta^{13}\text{C}_{\text{org}}$, and a lower C/N around 2010 (Fig. 2.3g, h) may also indicate enhanced export of fresh marine algae (Magen et al., 2010). Alternatively, the concomitant increase of *T. fimbriata* (Fig. 2.3n, black

shaded area), *Quinqueloculina stalker*, *Textularia earlandi* and *Stetsonia horvathi* abundances after ~1998 (Fig. 2.2a; Table 2.1) suggests that the additional supply of degraded organic matter is mainly from terrestrial sources that can sustain nearshore marine food webs (Terhaar et al., 2021). Terrestrial organic matter could originate from the Mackenzie River plume (Magen et al., 2010) pushed by the strong easterly winds (Fig. 2.3e, f) or from the Firth River and other local river systems (Fig. 2.2b; section 2.2.4.1). It may also originate from permafrost degradation and coastal erosion (Jong et al., 2020) as sediment dispersal around Herschel Island is favored especially under easterly winds (Klein et al., 2019).

The intensified oxygen consumption associated with microbial degradation of organic matter (Mol et al., 2018) may explain the low abundances of ostracods after ~1998 (Fig. 2.3n, gray shaded area) as they are sensitive to hypoxia (e.g., Ruiz et al., 2005; Stepanova et al., 2019). Moreover, *T. fimbriata* inhabits environments near river mouths (Table 2.1), where degradation of organic matter is important. Hence, the inverse relationship between *T. fimbriata* and ostracod abundances in the sediment (Fig. 2.3n) could be explained by the increased input of organic matter leading to oxygen consumption.

After 2006, when sea-ice concentration was particularly low (Fig. 2.3d), the increased vulnerability of cliffs and permafrost-based coastlines to wave action may have led to maximal coastal erosion rates (Overeem et al., 2011; Irrgang et al., 2018). The subsequent large supply of terrestrial matter may account for increased TOC accumulation, well-reflected in the $\delta^{13}\text{C}$ -depleted TOC and the higher C/N values (Magen et al., 2010; Grotheer et al., 2020; Jong et al., 2020), and increased accumulation rates, which are all recorded in the recent years (Fig. 2.3h, i, j). Enhanced supply of terrestrial matter may also account for the lower $\delta^{13}\text{C}$ -values in *Elphidium clavatum* (Fig. 2.3l, gray), which can be indicative of enhanced respiration of ^{13}C depleted organic matter (cf. Ravelo and Hillaire-Marcel, 2007; Mol et al., 2018). Furthermore, terrestrial matter could result from the strengthened vertical mixing and bottom currents under more ice-free conditions (Rainville and Woodgate, 2009) that cause the resuspension of fine particles and reworking (Hill and Nadeau, 1989; Jong et al., 2020), which is documented by the relative enrichment in sand content (Fig. 2.3d, k). The parallel increase of sand and TOC might illustrate alternating episodes of accumulation vs. reworking (Jong et al., 2020), which add to unstable conditions in the nearshore marine habitat. A coarser sediment substrate can also account for changes in the benthic microfaunal assemblages (Polyak et al., 2002; Gemery et al., 2021; Falardeau et al., 2023a).

While the species diversity of foraminifera did not vary significantly over the last decades, the most notable impact of the recent climate change in the benthic foraminiferal community is recorded through a change in the proportions of accompanied species (Fig. 2.2a; Falardeau et al., 2023a). More importantly, the rate at which the assemblages changed since the late 1990s is unprecedented over the last millennia (Falardeau et al., 2023b). Additionally, the increase in sand content, which results from intense and frequent vertical mixing due to strong winds, is associated with lower benthic foraminiferal abundances, especially the agglutinated ones (Fig. 2.3k, o, gray line). A dilution of the microfossil content by detrital input cannot be discarded, but should be minimized by using microfaunal fluxes. Moreover, since the preservation of the microfossils remains good throughout the HBGC01 sediment core, their decreased abundance likely relates to reduced productivity of agglutinated foraminifera (Falardeau et al., 2023a).

2.5 Conclusions

At the onset of the 21st century, the coastal area of the southern Canadian Beaufort Sea was marked by the intensification of mean summer easterly wind speed and storm frequency accompanied by reduced summer sea-ice cover concentration and a longer open water season. Accordingly, the beginning of the 21st century also corresponds to a strong anticyclonic regime in the Arctic Ocean (AOO+), which favored easterly winds, and dominantly negative PDO, leading to reduced sea-ice cover and contributing to the advection of warm Pacific air in the western Arctic Ocean. Such environmental conditions were marked by a significant shift in the coastal benthic habitats as documented by the microfossil assemblages, geochemical tracers, and lithological indices.

After ~1994, the ecological indicators suggest more turbulent bottom water conditions with enhanced freshwaters leading to variable salinities in the coastal environment, most probably related to more intensive vertical mixing of the upper freshwater layer due to longer ice-free seasons and stronger winds. This phenomenon probably intensified during the last decade when particularly low sea-ice concentration led to increased sediment reworking and resuspension. In addition, the coastal Beaufort Sea was probably marked by an enhanced supply of terrestrial organic matter. Part of the terrestrial inputs may have been carried by the Mackenzie River plume, which also plays a role in freshwater fluxes, and from resuspension and erosion of the nearby coasts, both occurring under strong easterly winds.

The impacts of the environmental shift are mainly recorded in the proportions of many benthic foraminiferal species in the assemblages. The rapid rate at which these assemblages changed,

unprecedented on the time scale of centuries, emphasizes the importance to continue the monitoring of the benthic microfauna in the forthcoming years. Moreover, increased terrestrial input probably led to enhanced microbial degradation of organic matter. This process contributes to oxygen consumption, which may have negatively affected animals such as ostracods, and extend to other benthic organisms. Furthermore, the organic matter is mainly transported within particulate-rich waters. High turbidity can affect light penetration and raises concerns about the potential of primary producers to achieve photosynthetic activity, with consequences for primary consumers and higher trophic levels of the marine food web.

2.6 Acknowledgements

This study was possible thanks to the Fonds de Recherche du Québec Nature et Technologies (FRQNT) for their financial support to JF through scholarships and to the Geotop Research Centre. We also thank the Natural Sciences and Engineering Research Council (NSERC) who provided funds to AdV through a Discovery and a CREATE grant [432295; ArcTrain]. We acknowledge the Northern Scientific Training Program of Polar Knowledge Canada and the EU Horizon 2020 project Nunataryuk [grant no. 773421] for making the fieldwork on Herschel Island – Qikiqtaruk Territorial Park and the community consultations possible. In particular, we thank Chief Ranger Richard Gordon and his team. We thank Konstantin Klein and Léo Chassiot, who helped in the field. We wish to thank our colleagues who contributed to this study: Charles Brunette for sea-ice data, Pascal Bourgault for historical climate and hydrometric data extraction, Hussein Wazneh for his help in R coding, and Paul Myers for his advice on atmospheric oscillation indices. We finally wish to acknowledge the reviewers who helped in improving our manuscript and who provided us with insightful comments.

2.7 References

- Alve, E., 2010. Benthic foraminiferal responses to absence of fresh phytodetritus: A two-year experiment. *Marine Micropaleontology* 76, 67-75.
- Aoyama, M., Hirose, K., Igarashi, Y., 2006, Re-construction and updating our understanding on the global weapons tests ^{137}Cs fallout: *Journal of Environmental Monitoring* 8, 431-438.
- Aquino-López, M.A., Blaauw, M., Christen, J.A., Sanderson, N.K., 2018, Bayesian analysis of ^{210}Pb dating: *Journal of Agricultural, Biological and Environmental Statistics* 23, 317-333.

Brewster, J., Neumann, D., Ostertag, S., Loseto, L., 2016. Traditional Ecological Knowledge (TEK) at Shingle Point, YK: Observations on Changes in the Environment and Fish Populations. Characterizing the diet and habitat niches of coastal fish populations in the Beaufort Sea Tarium Niryutait Marine Protected Area 121.

Brewster, J.D., Hansen-Craik, K., Harwood, L., Blakeston, C., 2021. State of Tarium Niryutait Marine Protected Areas (TNMPA) Report: Inventory of Monitoring from 2010-2016. Department of Fisheries and Oceans Canada.

Cage, A.G., Pieńkowski, A.J., Jennings, A., Knudsen, K.L., Seidenkrantz, M.-S., 2021. Comparative analysis of six common foraminiferal species of the genera *Cassidulina*, *Paracassidulina*, and *Islandiella* from the Arctic–North Atlantic domain. *Journal of Micropalaeontology* 40, 37-60.

Carmack, E.C., Macdonald, R.W., 2002. Oceanography of the Canadian Shelf of the Beaufort Sea: a setting for marine life. *Arctic*, 29-45.

Cearreta, A., Irabien, M.J., Leorri, E., Yusta, I., Croudace, I., Cundy, A., 2000. Recent anthropogenic impacts on the Bilbao estuary, northern Spain: geochemical and microfaunal evidence. *Estuarine, Coastal and Shelf Science* 50, 571-592.

Cesbron, F., Geslin, E., Jorissen, F., Delgard, M.-L., Charrieau, L., Deflandre, B., Jézéquel, D., Anschutz, P., Metzger, E., 2016. Vertical distribution and respiration rates of benthic foraminifera: Contribution to aerobic remineralization in intertidal mudflats covered by *Zostera noltei* meadows. *Estuarine, Coastal and Shelf Science* 179, 23-38.

Coch, C., Lamoureux, S.F., Knoblauch, C., Eischeid, I., Fritz, M., Obu, J., Lantuit, H., 2018. Summer rainfall dissolved organic carbon, solute, and sediment fluxes in a small Arctic coastal catchment on Herschel Island (Yukon Territory, Canada). *Arctic Science* 4, 750-780.

Cox, C.J., Stone, R.S., Douglas, D.C., Stanitski, D., Gallagher, M., 2019. The Aleutian Low-Beaufort Sea Anticyclone: A climate index correlated with the timing of springtime melt in the Pacific Arctic cryosphere. *Geophysical Research Letters* 46, 7464-7473.

EBA Engineering Consultants Ltd., 1992. Proceedings of the Beaufort Sea granular resources workshop, Part 1: Reports on NOGAP regional studies, 11 pp.

Echols, R.J., Fowler, G.A., 1973. Agglutinated tintinnid loricae from some Recent and Late Pleistocene shelf sediments. *Micropaleontology* 19, 431-443.

Ehn, J.K., Reynolds, R.A., Stramski, D., Doxaran, D., Lansard, B., Babin, M., 2019. Patterns of suspended particulate matter across the continental margin in the Canadian Beaufort Sea during summer. *Biogeosciences* 16, 1583-1605.

Environment and Climate Change Canada Historical Climate Data, Retrieved April, 2020 from https://climate.weather.gc.ca/index_e.html.

Environment and Climate Change Canada Historical Climate Data, Retrieved October, 2020 from https://climate.weather.gc.ca/index_e.html.

Environment and Climate Change Canada Historical Hydrometric Data, Retrieved April, 2020 from https://wateroffice.ec.gc.ca/mainmenu/historical_data_index_e.html.

Falardeau, J., de Vernal, A., Seidenkrantz, M.-S., Cronin, T.M., Gemery, L., Chassiot, L., Fritz, M., Carnero-Bravo, V., Hillaire-Marcel, C., Archambault, P., 2023a. Microfaunal recording of recent environmental changes in the Herschel basin, western Arctic Ocean. *Journal of Foraminiferal Research* 53, 20-48.

Falardeau, J., de Vernal, A., Seidenkrantz, M.-S., Fritz, M., Cronin, T. M., Gemery, L., Rochon, A., Carnero-Bravo, V., Hillaire-Marcel, C., Pearce, C., Archambault, P., 2023b. A 1300-year microfaunal record from the Beaufort Sea shelf indicates exceptional climate-related environmental changes over the last two centuries. *Palaeogeography, Palaeoclimatology, Palaeoecology* 625, 111670.

Feyling-Hanssen, R.W., Jørgensen, J.A., Knudsen, K.L., Lykke-Andersen, A.-L., 1971. Late Quaternary Foraminifera from Vendsyssel, Denmark and Sandnes, Norway. *Geological Society of Denmark* 21, 67-317.

Frey, K.E., Moore, G., Cooper, L.W., Grebmeier, J.M., 2015. Divergent patterns of recent sea ice cover across the Bering, Chukchi, and Beaufort seas of the Pacific Arctic Region. *Progress in Oceanography* 136, 32-49.

Fritz, M., Vonk, J.E., Lantuit, H., 2017. Collapsing arctic coastlines. *Nature Climate Change* 7, 6-7.

Gallagher, C.P., Courtney, M.B., Seitz, A.C., Lea, E.V., Howland, K.L., 2021. Ocean-entry timing and marine habitat-use of Canadian Dolly Varden: Dispersal among conservation, hydrocarbon exploration, and shipping areas in the Beaufort Sea. *Estuarine, Coastal and Shelf Science* 262, DOI: 10.1016/j.ecss.2021.107609 .

Gemery, L., Cronin, T.M., Briggs, W.M., Brouwers, E.M., Schornikov, E.I., Stepanova, A., Wood, A.M., Yasuhara, M., 2017. An Arctic and Subarctic ostracode database: biogeographic and paleoceanographic applications. *Hydrobiologia* 786, 59-95.

Gemery, L., Cronin, T.M., Cooper, L.W., Dowsett, H.J., Grebmeier, J.M., 2021. Biogeography and ecology of Ostracoda in the US northern Bering, Chukchi, and Beaufort Seas. *PloS one* 16, DOI: 10.1371/journal.pone.0251164.

Gemery, L., Cronin, T.M., Cooper, L.W., Roberts, L.R., Keigwin, L.D., Addison, J.A., Leng, M.J., Lin, P., Magen, C., Marot, M.E., Schwartz, V., 2023. Multi-proxy record of ocean-climate variability during the last two millennia on the Mackenzie Shelf, Beaufort Sea. *Micropaleontology* 69, 345-366.

Grotheer, H., Meyer, V., Riedel, T., Pfalz, G., Mathieu, L., Hefter, J., Gentz, T., Lantuit, H., Mollenhauer, G., Fritz, M., 2020. Burial and origin of permafrost-derived carbon in the nearshore zone of the southern Canadian Beaufort Sea. *Geophysical Research Letters* 47, DOI: 10.1029/2019GL085897.

Guilbault, J.-P., Barrie, J.V., Conway, K., Lapointe, M., Radi, T., 2003. Paleoenvironments of the Strait of Georgia, British Columbia during the last deglaciation: microfaunal and microfloral evidence. *Quaternary Science Reviews* 22, 839-857.

Hill, P.R., Nadeau, O.C., 1989. Storm-dominated sedimentation on the inner shelf of the Canadian Beaufort Sea. *Journal of Sedimentary Research* 59, 455-468.

Holmes, R.M., McClelland, J.W., Peterson, B.J., Tank, S.E., Bulygina, E., Eglinton, T.I., Gordeev, V.V., Gurtovaya, T.Y., Raymond, P.A., Repeta, D.J., 2012. Seasonal and annual fluxes of nutrients and organic matter from large rivers to the Arctic Ocean and surrounding seas. *Estuaries and Coasts* 35, 369-382.

Irrgang, A.M., Lantuit, H., Manson, G.K., Günther, F., Grosse, G., Overduin, P.P., 2018. Variability in rates of coastal change along the Yukon coast, 1951 to 2015. *Journal of Geophysical Research: Earth Surface* 123, 779-800.

Jennings, A.E., Helgadóttir, G., 1994. Foraminiferal assemblages from the fjords and shelf of eastern Greenland. *Journal of Foraminiferal Research* 24, 123-144.

Jennings, A., Andrews, J., Reilly, B., Walczak, M., Jakobsson, M., Mix, A., Stoner, J., Nicholls, K.W., Cheseby, M., 2020. Modern foraminiferal assemblages in northern Nares Strait, Petermann Fjord, and beneath Petermann ice tongue, NW Greenland. *Arctic, Antarctic, and Alpine Research* 52, 491-511.

Jong, D., Bröder, L., Tanski, G., Fritz, M., Lantuit, H., Tesi, T., Haghipour, N., Eglinton, T.I., Vonk, J.E., 2020. Nearshore zone dynamics determine pathway of organic carbon from eroding permafrost coasts. *Geophysical research letters* 47, DOI: 10.1029/2020GL088561.

Juggins, S. (2022). rioja: Analysis of Quaternary Science Data. R package version 1.0-5, <https://cran.r-project.org/package=rioja>.

Kirillov, S., Dmitrenko, I., Tremblay, B., Gratton, Y., Barber, D., Rysgaard, S., 2016. Upwelling of Atlantic Water along the Canadian Beaufort Sea continental slope: Favorable

atmospheric conditions and seasonal and interannual variations. *Journal of Climate* 29, 4509-4523.

Klein, K.P., Lantuit, H., Heim, B., Fell, F., Doxaran, D., Irrgang, A.M., 2019. Long-term high-resolution sediment and sea surface temperature spatial patterns in Arctic nearshore waters retrieved using 30-year landsat archive imagery. *Remote Sensing* 11, DOI: 10.3390/rs11232791.

Kutos, O., Rochon, A., Montero-Serrano, J.C., 2021. Evolution of palaeo-sea-surface conditions and sediment dynamics over the last 2700 years on the Mackenzie Slope, Beaufort Sea (Canadian Arctic). *Boreas* 50, 893-914.

Lansard, B., Mucci, A., Miller, L.A., Macdonald, R.W., Gratton, Y., 2012. Seasonal variability of water mass distribution in the southeastern Beaufort Sea determined by total alkalinity and $\delta^{18}\text{O}$. *Journal of Geophysical Research: Oceans* 117, DOI: 10.1029/2011JC007299.

Lapointe, F., Francus, P., Lamoureux, S.F., Vuille, M., Jenny, J.-P., Bradley, R.S., Massa, C., 2017. Influence of North Pacific decadal variability on the western Canadian Arctic over the past 700 years. *Climate of the Past* 13, 411-420.

Lin, P., Pickart, R.S., Fissel, D., Ross, E., Kasper, J., Bahr, F., Torres, D.J., O'Brien, J., Borg, K., Melling, H., 2020. Circulation in the vicinity of Mackenzie Canyon from a year-long mooring array. *Progress in Oceanography* 187, DOI: 10.1016/j.pocean.2020.102396.

Magen, C., Chaillou, G., Crowe, S.A., Mucci, A., Sundby, B., Gao, A., Makabe, R., Sasaki, H., 2010. Origin and fate of particulate organic matter in the southern Beaufort Sea-Amundsen Gulf region, Canadian Arctic. *Estuarine, Coastal and Shelf Science* 86, 31-41.

Manson, G.K., Solomon, S.M., 2007. Past and future forcing of Beaufort Sea coastal change. *Atmosphere-Ocean* 45, 107-122.

Mantua, N.J., Hare, S.R., Zhang, Y., Wallace, J.M., Francis, R.C., 1997. A Pacific interdecadal climate oscillation with impacts on salmon production. *Bulletin of the American Meteorological Society* 78, 1069-1080.

McCorkle, D.C., Corliss, B.H., Farnham, C.A., 1997. Vertical distributions and stable isotopic compositions of live (stained) benthic foraminifera from the North Carolina and California continental margins. *Deep Sea Research Part I: Oceanographic Research Papers* 44, 983-1024.

Meier, W. N., Fetterer, F., Savoie, M., Mallory, S., Duerr, R., Stroeve, J., 2017, NOAA/NSIDC Climate Data Record of Passive Microwave Sea Ice Concentration, Version 3.

[goddard_merged_seaice_conc]. Boulder, Colorado USA. NSIDC: National Snow and Ice Data Center. [January 2020].

Meunier, A., 1919. Mikroplankton de la mer Flamande. III. Les Péridiniens : Mémoires du Musée Royal d'Histoire Naturelle de Belgique 8, 1-116.

Mol, J., Thomas, H., Myers, P.G., Hu, X., Mucci, A., 2018. Inorganic carbon fluxes on the Mackenzie Shelf of the Beaufort Sea. Biogeosciences 15, 1011-1027.

Mulligan, R.P., Perrie, W., 2019. Circulation and structure of the Mackenzie River plume in the coastal Arctic Ocean. Continental Shelf Research 177, 59-68.

Nguyen, L., Pilfold, N.W., Derocher, A.E., Stirling, I., Bohart, A.M., Richardson, E., 2017. Ringed seal (*Pusa hispida*) tooth annuli as an index of reproduction in the Beaufort Sea. Ecological Indicators 77, 286-292.

Ogi, M., Wallace, J.M., 2007. Summer minimum Arctic sea ice extent and the associated summer atmospheric circulation. Geophysical Research Letters 34, DOI: 10.1029/2007GL029897.

Oksanen, J., Blanchet, F. G., Kindt, R., Legendre, P., Minchin, P. R., O'Hara, R., Simpson, G. L., Solymos, P., Stevens, M. H. H., Wagner, H., 2013, Package 'vegan', Community Ecology Package, version 2, 295 pp.

Overeem, I., Anderson, R.S., Wobus, C.W., Clow, G.D., Urban, F.E., Matell, N., 2011, Sea ice loss enhances wave action at the Arctic coast: Geophysical Research Letters, v. 38, DOI: 10.1029/2011GL048681.

Paranjape, M.A., 1987. The seasonal cycles and vertical distribution of tintinnines in Bedford Basin, Nova Scotia, Canada. Canadian Journal of Zoology 65, 41-48.

Pelletier, B.R., Medioli, B. E., 2014. Environmental atlas of the Beaufort coastlands. Geological Survey of Canada.

Pickart, R.S., 2004. Shelfbreak circulation in the Alaskan Beaufort Sea: Mean structure and variability. Journal of Geophysical Research: Oceans 109, DOI: 10.1029/2003JC001912.

Pickart, R.S., Spall, M.A., Moore, G.W., Weingartner, T.J., Woodgate, R.A., Agaard, K., Shimada, K., 2011. Upwelling in the Alaskan Beaufort Sea: Atmospheric forcing and local versus non-local response. Progress in Oceanography 88, 78-100.

Polyak, L., Korsun, S., Febo, L.A., Stanovoy, V., Khusid, T., Hald, M., Paulsen, B.E., Lubinski, D.J., 2002. Benthic foraminiferal assemblages from the southern Kara Sea, a river-influenced Arctic marine environment. *Journal of Foraminiferal Research* 32, 252-273.

Polyak, L., Stanovoy, V., Lubinski, D.J., 2003. Stable isotopes in benthic foraminiferal calcite from a river-influenced Arctic marine environment, Kara and Pechora Seas: *Paleoceanography* 18, DOI: 10.1029/2001PA000752.

Proshutinsky, A.Y., Johnson, M.A., 1997. Two circulation regimes of the wind-driven Arctic Ocean. *Journal of Geophysical Research: Oceans* 102, DOI: 10.1029/97JC00738.

R Core Team, 2021. R: A language and environment for statistical computing. R Foundation for Statistical Computing, Vienna, Austria. URL <https://www.R-project.org/>.

Rainville, L., Woodgate, R.A., 2009. Observations of internal wave generation in the seasonally ice-free Arctic. *Geophysical Research Letters* 36, DOI: 10.1029/2009GL041291.

Ravelo, A.C., Hillaire-Marcel, C., 2007. Chapter eighteen the use of oxygen and carbon isotopes of foraminifera in paleoceanography. *Developments in marine geology* 1, 735-764.

Rosenblum, E., Stroeve, J., Gille, S.T., Lique, C., Fajber, R., Tremblay, L.B., Galley, R., Loureiro, T., Barber, D.G., Lukovich, J.V., 2022. Freshwater input and vertical mixing in the Canada Basin's seasonal halocline: 1975 versus 2006-2012. *Journal of Physical Oceanography* 52, DOI: 10.1175/JPO-D-21-0116.1.

Ruiz, F., Abad, M., Bodergat, A.-M., Carbonel, P., Rodríguez-Lázaro, J., Yasuhara, M., 2005. Marine and brackish-water ostracods as sentinels of anthropogenic impacts. *Earth-Science Reviews* 72, 89-111.

Schlitzer, R., 2018. Ocean Data View, Alfred Wegener Institute, <https://odv.awi.de>.

Schulze, L.M., Pickart, R.S., 2012. Seasonal variation of upwelling in the Alaskan Beaufort Sea: Impact of sea ice cover. *Journal of Geophysical Research: Oceans* 117, DOI: 10.1029/2012JC007985.

Scott, D.B., Schell, T., Rochon, A., Blasco, S., 2008. Modern benthic foraminifera in the surface sediments of the Beaufort Shelf, Slope and Mackenzie Trough, Beaufort Sea, Canada: Taxonomy and summary of surficial distributions. *Journal of Foraminiferal Research* 38, 228-250.

Screen, J.A., Francis, J.A., 2016. Contribution of sea-ice loss to Arctic amplification is regulated by Pacific Ocean decadal variability. *Nature Climate Change* 6, 856-860.

Seidenkrantz, M.-S., 2013. Benthic foraminifera as palaeo sea-ice indicators in the subarctic realm—examples from the Labrador Sea–Baffin Bay region. Quaternary Science Reviews 79, 135-144.

Stepanova, A., Taldenkova, E., Bauch, H.A., 2003. Recent Ostracoda from the Laptev Sea (Arctic Siberia): species assemblages and some environmental relationships. Marine Micropaleontology 48, 23-48.

Stepanova, A., Obrochta, S., Quintana Krupinski, N.B., Hyttinen, O., Kotilainen, A., Andrén, T., 2019. Late Weichselian to Holocene history of the Baltic Sea as reflected in ostracod assemblages. Boreas 48, 761-778.

Terhaar, J., Lauerwald, R., Regnier, P., Gruber, N., Bopp, L., 2021. Around one third of current Arctic Ocean primary production sustained by rivers and coastal erosion. Nature communications 12, 1-10.

Thompson, D.W., Wallace, J.M., 1998. The Arctic Oscillation signature in the wintertime geopotential height and temperature fields. Geophysical research letters 25, 1297-1300.

Tremblay, J.É., Bélanger, S., Barber, D., Aspin, M., Martin, J., Darnis, G., Fortier, L., Gratton, Y., Link, H., Archambault, P., 2011. Climate forcing multiplies biological productivity in the coastal Arctic Ocean. Geophysical Research Letters 38, DOI: 10.1029/2011GL048825.

Trenberth, K.E., Hurrell, J.W., 1994. Decadal atmosphere-ocean variations in the Pacific. Climate Dynamics 9, 303-319.

Voltski, I., Korsun, S., Pillet, L., Pawlowski, J., 2015. *Protelphidium niveum* (Lafrenz, 1963) and the taxonomy of “lower” elphidiids. Journal of Foraminiferal Research 45, 250-263.

Wollenburg, J.E., Kuhnt, W., 2000. The response of benthic foraminifers to carbon flux and primary production in the Arctic Ocean. Marine Micropaleontology 40, 189-231.

Wood, K.R., Overland, J.E., Salo, S.A., Bond, N.A., Williams, W.J., Dong, X., 2013. Is there a “new normal” climate in the Beaufort Sea? Polar Research 32, DOI: 10.3402/polar.v32i0.19552.

2.8 Supplementary material

Figure 2-A.1 Radiogenic isotope data and age model of core HBGCO1 slightly modified from Falardeau et al. (2023a). (a) CT-scan of core HBGCO1 in which laminations can be observed in the core top 10 cm. (b) Total ^{210}Pb (yellow), ^{226}Ra (orange), and ^{137}Cs (gray) activity profiles in core HBGCO1. The mean ^{226}Ra activity at $1.60 \pm 0.05 \text{ dpm}\cdot\text{g}^{-1}$ would represent the value of the supported ^{210}Pb , which was subtracted from the total ^{210}Pb activity to obtain the ^{210}Pb in excess. The pink dotted line marks the peak in ^{137}Cs at 38-37 cm. (c) Natural logarithm of excess ^{210}Pb (blue dots). The gray line marks the linear regression of the $\ln^{210}\text{Pb}_{\text{ex}}$ in excess below 10 cm. (d) HBGCO1 core age model obtained with *Plum* (mean ages = red line; minimum and maximum ages = gray dotted lines). The pink arrow marks the age of the nuclear weapon test in 1963 (Aoyama et al., 2006). The gray shaded areas in (c) and (d) represent the interval of the proposed mixed layer.

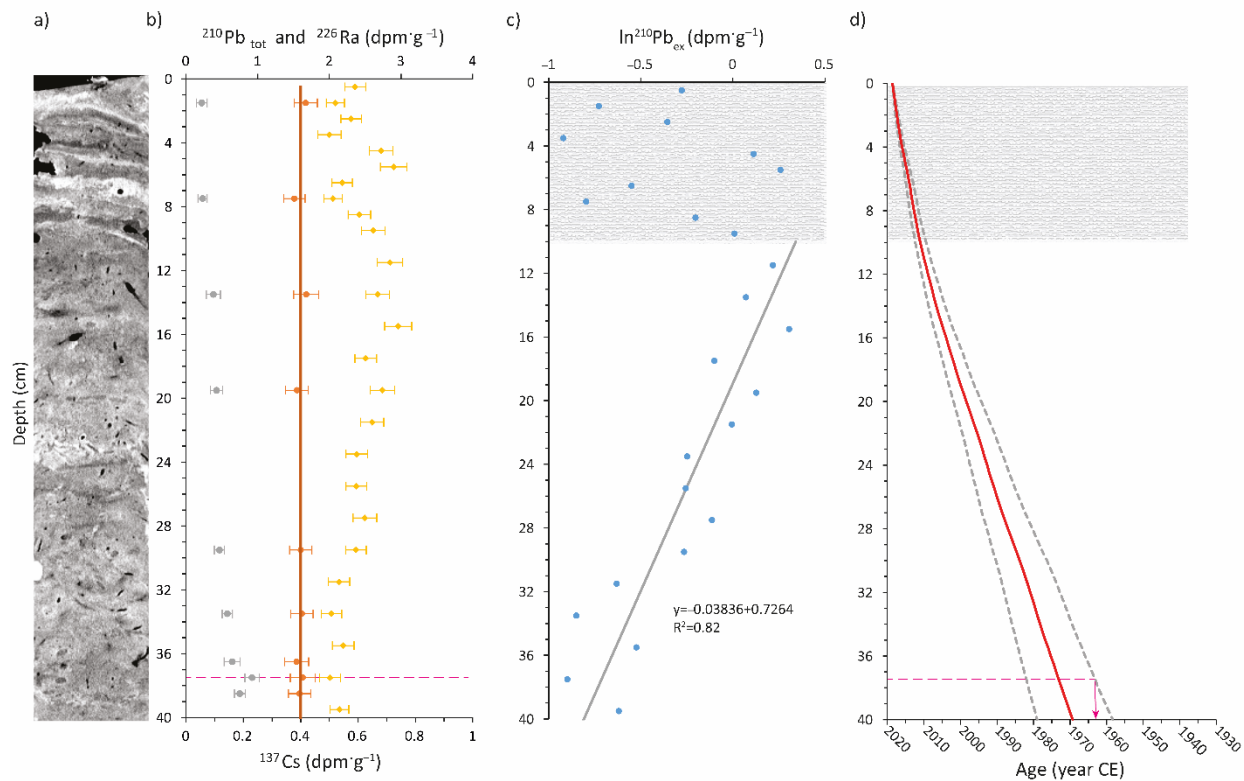


Figure 2-A.2 The direction of strong winds ($>10\text{m}\cdot\text{s}^{-1}$) during the open water season over the years at a) Herschel Island and b) Komakuk Beach weather stations.

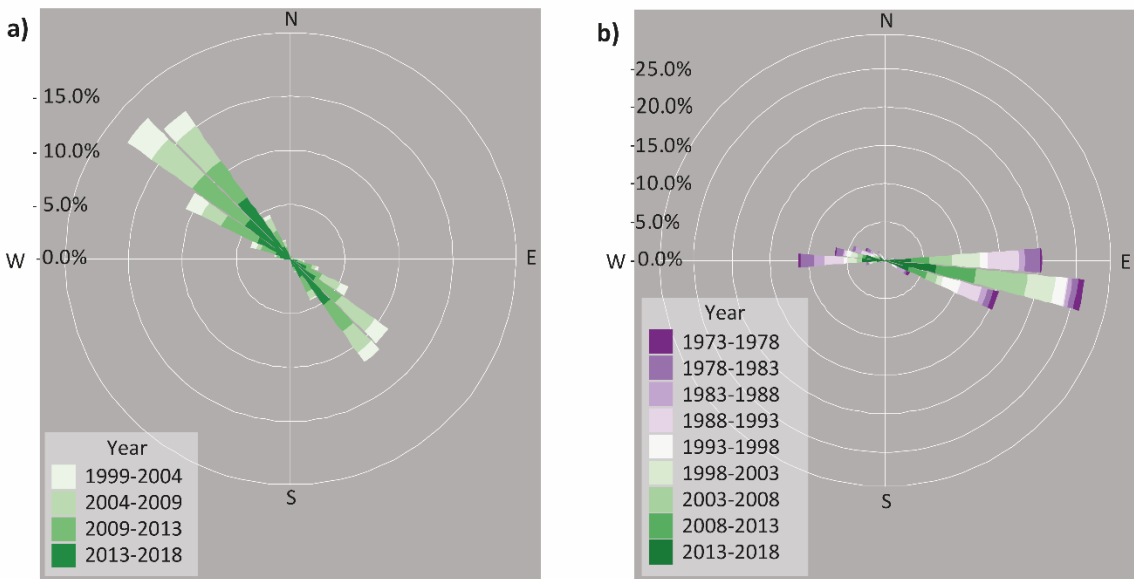
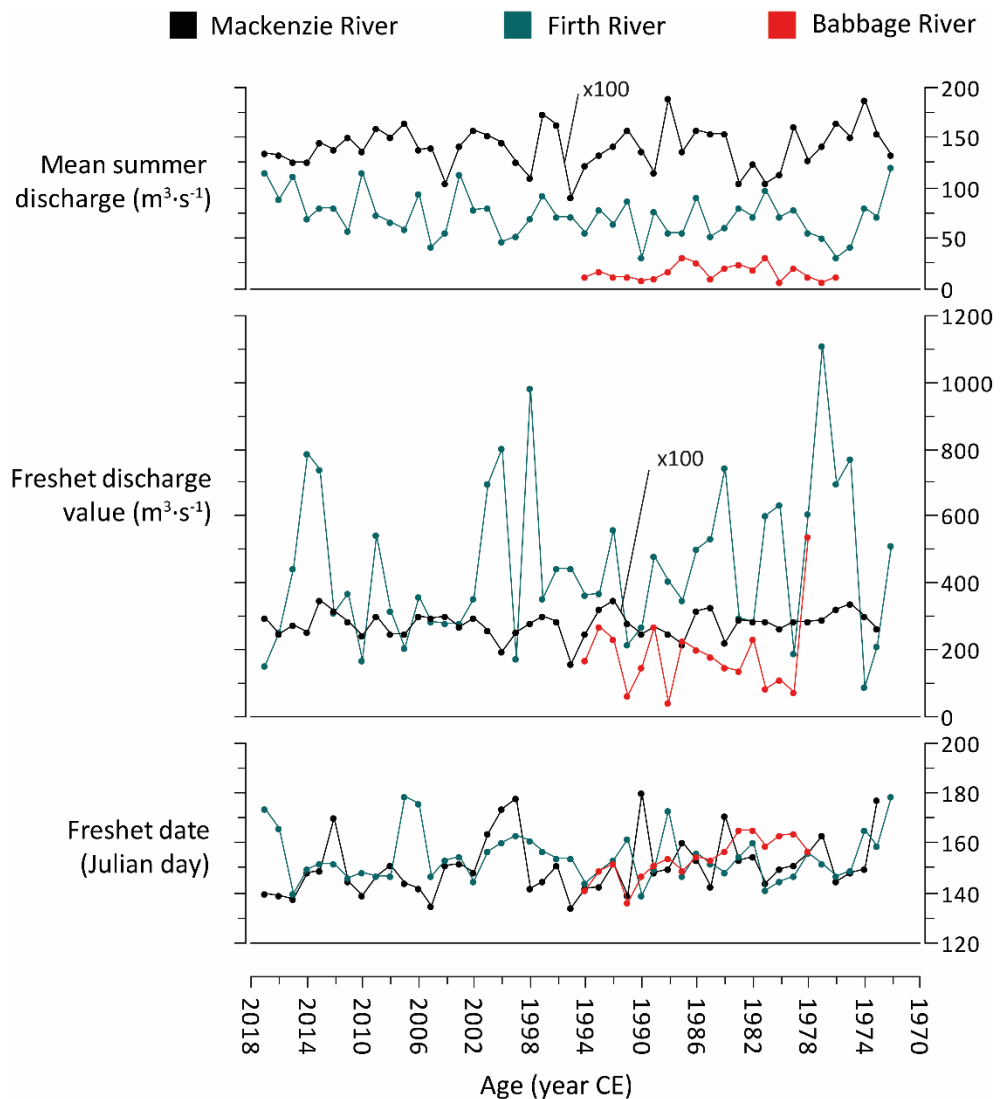


Figure 2-A.3 The hydrography of the Firth (blue), Babbage (red), and Mackenzie (black) rivers. The freshet discharge value and the mean summer discharge of the Mackenzie River were divided by 100.



CHAPITRE 3

A 1300-YEAR MICROFAUNAL RECORD FROM THE BEAUFORT SEA SHELF INDICATES EXCEPTIONAL CLIMATE-RELATED ENVIRONMENTAL CHANGES OVER THE LAST TWO CENTURIES

Jade Falardeau^{a*}, Anne de Vernal^a, Marit-Solveig Seidenkrantz^b, Michael Fritz^c, Thomas M. Cronin^d, Laura Gemery^d, André Rochon^{a,e}, Vladislav Carnero-Bravo^{a,f}, Claude Hillaire-Marcel^a, Christof Pearce^b and Philippe Archambault^g

- a. Geotop Research Center in Earth System Dynamics and Département des sciences de la Terre et de l'atmosphère, Université du Québec à Montréal, C.P. 8888 Succursale Centre-Ville, H3C 3P8, Montréal, Canada
- b. Paleoceanography and Paleoclimate Group, Department of Geoscience, Arctic Research Centre, and iClimate centre, Aarhus University, Høegh-Guldbergs Gade 2, DK-8000 Aarhus C, Denmark
- c. Permafrost Research Unit, Alfred Wegener Institute, Helmholtz Centre for Polar and Marine Research, Telegrafenberg A45, 14773 Potsdam, Germany
- d. U.S. Geological Survey, Florence Bascom Geoscience Center, 12201 Sunrise Valley Drive, National Center, Reston, VA, USA 20192
- e. Institut des sciences de la mer de Rimouski, Université du Québec à Rimouski, 310 allée des Ursulines, G5L 2Z9, Rimouski, Canada
- f. Instituto de Ecología, Universidad del Mar, Campus Puerto Ángel, 70902 Puerto Ángel, Oaxaca, México
- g. Québec Océan, ArcticNet, Takuvik, Département de biologie, Faculté des sciences et de génie, Université Laval, 1045 avenue de la Médecine, G1V 0A6, Québec, Canada

Cet article paraît dans le volume de septembre 2023 de la revue *Palaeogeography, Palaeoclimatology, Palaeoecology*.

Falardeau, J., de Vernal, A., Seidenkrantz, M.-S., Fritz, M., Cronin, T. M., Gemery, L., Rochon, A., Carnero-Bravo, V., Hillaire-Marcel, C., Pearce, C., Archambault, P., 2023b. A 1300-year microfaunal record from the Beaufort Sea shelf indicates exceptional climate-related environmental changes over the last two centuries. *Palaeogeography, Palaeoclimatology, Palaeoecology* 625, 111670.

Les textes et figures en matériel supplémentaire se retrouvent après les références de ce chapitre. Les tableaux supplémentaires ne seront accessibles qu'en ligne; voir les Annexes G à I pour les comptages micropaléontologiques bruts de la carotte PG2303.

Abstract

The environments of Arctic Ocean nearshore areas experience high intra- and inter-annual variability, making it difficult to evaluate the impact of anthropogenic warming. However, a sediment record from the southern Canadian Beaufort Sea allowed us to reconstruct the impacts of climate and environmental changes over the last 1300 years along the northern Yukon coast, Canada. The coring site (PG2303; 69.513°N, 138.895°W; water depth 32 m) is located in the Herschel Basin, where high sedimentation rates (0.1–0.5 cm a⁻¹) allowed analyses at sub-centennial to decadal resolutions. Benthic foraminiferal, ostracod, and tintinnid assemblages, as well as the stable isotope composition of the foraminifera *Elphidium clavatum* and *Cassidulina reniforme* were used as paleoclimatic and ecological indicators, while the age model was based on the combined radiometric data of ¹⁴C, ²¹⁰Pb and ¹³⁷Cs. From ca 700 to 1050 CE, our data suggest penetration of offshore shelf-break waters inferred by the dominance of *C. reniforme* followed by the relatively abundant *Triloculina trihedra* in the foraminiferal assemblages as both species are associated with stable saline conditions. Afterwards, the occurrence of ostracods *Kotoracythere arctoborealis* and *Normanicythere leioderma* suggests influx of Pacific-sourced waters until ca. 1150 CE. From ~1150–1650 CE, persistent frigid waters, limited sediment supply, and low abundances of microfossils suggest cold conditions with pervasive annual sea-ice cover that may have restricted upwelling of oceanic waters. After ~1800 CE, the co-occurrence of *Tintinnopsis fimbriata* and bacterial/complex organic carbon feeder foraminifera (*Quinqueloculina stalkerii*, *Textularia earlandi* and *Stetsonia horvathi*), suggest an increased influence of freshwater rich in particulate organic matter, which may be related to the spreading of the Mackenzie River plume and/or increased coastal permafrost erosion during longer ice-free seasons. Based on these proxy data, the shift at ~1800 CE marks the onset of regional warming, which further intensified after ~1955 CE, likely in response to the anthropogenic forcing.

Keywords: Benthic foraminifera, Ostracods, Tintinnids, Beaufort Sea, Arctic coasts, Climate change

3.1 Introduction

Sea ice is a key parameter for marine food webs in nearshore Arctic ecosystems, as it influences the timing, flux, and export of primary producers (Grebmeier and Barry, 2007; Nadaï et al., 2021), the up-welling of nutrient-rich subsurface waters onto the continental shelves (Schulze and Pickart, 2012), and vertical mixing and/or stratification (Rainville and Woodgate, 2009; Blais et al., 2017). In the Beaufort Sea, sea-ice cover extent decreased ten times faster from 2000 to 2012 CE (-12.84 days a^{-1}) than during the two previous decades (1979–2000 CE; Frey et al., 2015). The ongoing climate warming likely plays an important role in the decreasing sea-ice cover trend (Notz and Stroeve, 2016), but its temporal and spatial extent also depends on dynamic and thermodynamic factors (Spreen et al., 2011; Frey et al., 2015; Belter et al., 2021). Numerous relationships between the sea-ice cover and large-scale modes of atmospheric circulation, as indicators of dominant wind and thus water mass transport patterns, have been identified (Rigor et al., 2002; Screen and Francis, 2016; Cox et al., 2019; Zhang et al., 2019). These indices may have undergone significant amplitude variations over the last few millennia, notably in relation to the Pacific Decadal Oscillation (PDO; Mantua and Hare, 2002) and the Arctic Oscillation (AO; Thompson and Wallace, 1998) as suggested by terrestrial and marine proxies (MacDonald and Case, 2005; Darby et al., 2012; Lapointe et al., 2017).

For a complete understanding of climate dynamics in the past, long time series are needed to assess the interplay between different environmental forcings, including their relationships to sea-ice cover and, thus, how they influence oceanic conditions and productivity. Furthermore, these time series help identify natural variability, which in turn can serve to sort out the effects and the magnitude of recent anthropogenic climate changes. To a certain extent, reconstructions of past conditions in the nearshore environments could also offer insights into marine biological resources and their tolerance to changes over centuries of harvesting, i.e. fisheries, in the Beaufort Sea (Usher, 2002; Friesen et al., 2020). Over the last two millennia, large-amplitude climatic events have been inferred in the terrestrial environment of northwestern America based on tree rings and sediment cores in lakes (e.g. Rühland et al., 2003; Bird et al., 2009; Viau and Gajewski, 2009; Fritz et al., 2012; Anchukaitis et al., 2013; Porter et al., 2013; Wolter et al., 2017; Nicolle et al., 2018) and in offshore marine environments of the Beaufort Sea (Richerol et al., 2008; Schell et al., 2008; Bringue' and Rochon, 2012; Scott et al., 2009; Kutos et al., 2021). However, Canadian Beaufort Sea continental shelf records are rare (Seidenstein et al., 2018; Gemery et al., 2023), especially near the coasts.

The first objective of this study is to reconstruct the environmental conditions of the Canadian Beaufort Sea shelf over the last millennium, where harvesting of marine biological resources has been and still is extremely important for local communities. Our study's second objective is to disentangle the effect of anthropogenic activities from the natural variability. To meet these objectives, we document past marine conditions, focusing on evaluating changes in sea ice, water temperature and salinity, as well as marine productivity. We base the study on microfossil investigations of two marine sediment cores retrieved at the same site (PG2303) in the Herschel Basin, northern Yukon, Canada. The study site is in an area of relatively high and continuous sediment accumulation, which enables sub-decadal temporal resolution over millennia (Grotheer et al., 2020), together with abundant, diverse, and well-preserved microfossils (Falardeau et al., 2023).

3.2 Regional setting

Coring site PG2303 is in the Herschel Basin on the continental shelf off northern Canada (Fig. 3.1a, b). The basin is located 3 km west of Herschel Island-Qikiqtaruk, and 7 km north of the Yukon coast (Fig. 3.1b). The organic carbon sequestered in Herschel Basin is dominated by terrestrial sources. It is derived either from coastal erosion of Herschel Island-Qikiqtaruk and the mainland coast or from particulate matter transported by the Mackenzie River (Grotheer et al., 2020), with the Mackenzie River mouth located at Shallow Bay ca 130 km east of our study site (Fig. 3.1b). Today, suspended particulate matter from the Mackenzie River reaches the study site during the spring freshet when turbidity is at a maximum (Juhls, 2021) and under easterly winds (Wood et al., 2015). The spring freshet occurs from mid-May to the end of June (Carmack and Macdonald, 2002; Mulligan and Perrie, 2019). On average, the sea ice break-up occurs by the end of June, and sea ice forms again around mid-October (Carmack and Macdonald, 2002; Frey et al., 2015).

Hydrographic conditions in the area depend on local winds. Generally, the Beaufort shelfbreak jet flows eastward, transporting cold and saline nutrient-rich Pacific winter waters (blue arrow; Fig. 3.1b; Pickart, 2004; hereafter referred to as Pacific waters). They are also known as the Remnant Winter Water (Lin et al., 2020). These Pacific waters overlay the dense, warm, and saline Atlantic waters (dotted red arrow; Fig. 3.1a; Lin et al., 2020). Alongshore, the coastal flow transports warmed meteoric waters or sea-ice meltwaters and possibly warmer and less saline Pacific summer waters towards the east (purple arrow; Fig. 3.1b; Lin et al., 2020). Offshore, the Beaufort Gyre circulates clockwise, causing recirculation in the Mackenzie Trough (yellow arrows; Fig. 3.1a, b; Lin et al., 2020). Dominant winds are either from the

northwest or the east-south-east (Fig. 3.1b; Radosavljevic et al., 2016). Easterly wind events favor the upwelling of shelf-break waters onto the continental shelf, decreased sea-ice cover, and enhanced primary productivity (Tremblay et al., 2011, 2012; Pickart et al., 2013). In contrast, westerly winds are unfavorable for upwelling and lead to persistent sea-ice cover (Carmack and Macdonald, 2002; Pickart et al., 2011). The water column in the Herschel Basin is stratified in summer with a freshwater layer 7–15 m thick at the surface above the frigid (< 0°C) and saline waters at the bottom (Fig. 3.1c; Mulligan et al., 2010). The Herschel Basin bottom waters are formed by a mixture of brines from sea-ice formation in winter and upwelled waters from the shelf break (Williams and Carmack, 2012).

3.3 Methods

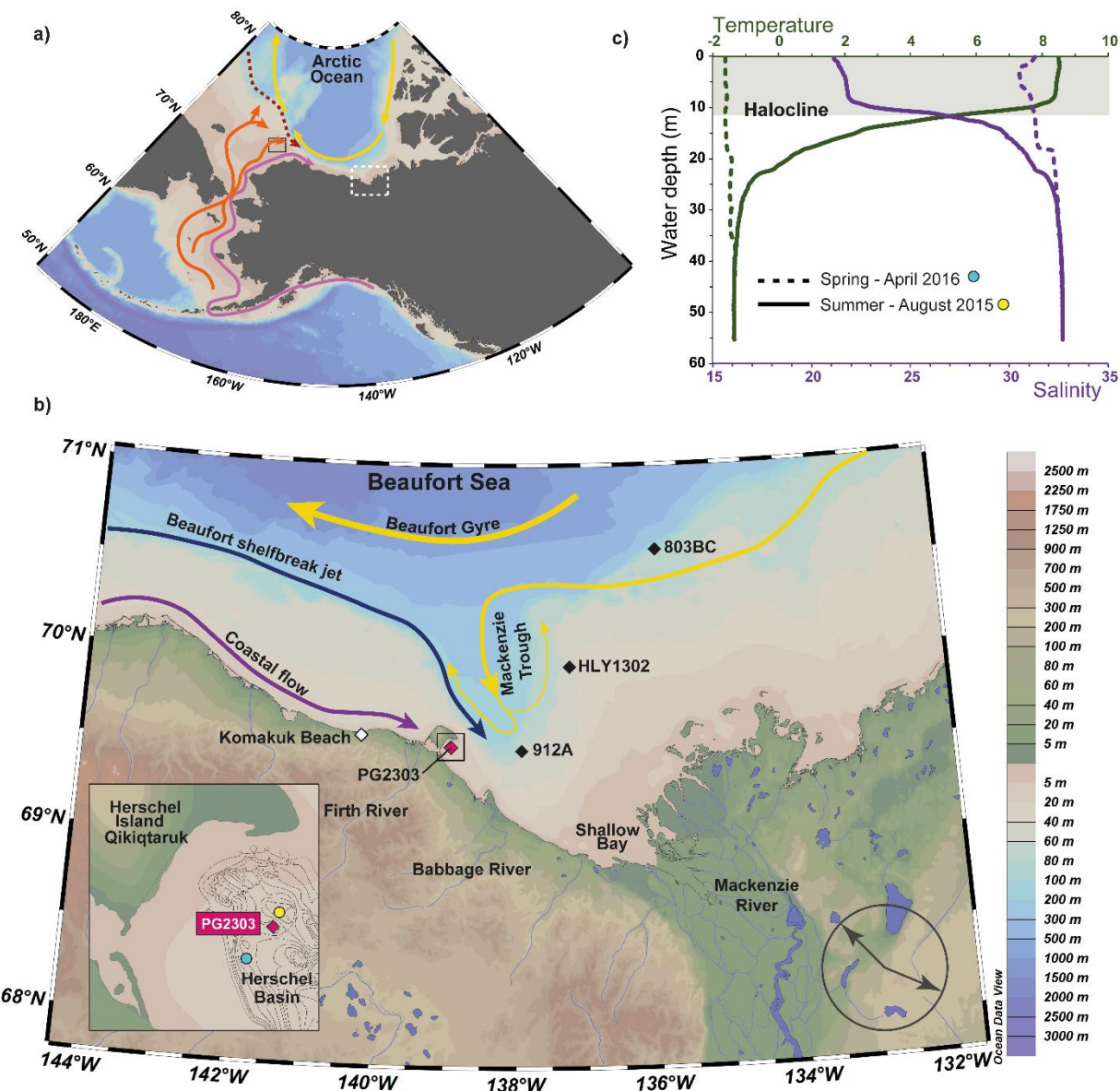
3.3.1 Sediment cores

Marine sediment core PG2303 was collected with a UWITEC piston corer on April 20th, 2016, using a tripod placed on the sea ice, as part of the Yukon Coast spring expedition led by the Alfred Wegener Institute in Potsdam, Germany (Fig. 3-A.1). The 12.3 m long core was collected in 32 m water depth at 69.513°N and 138.895°W in clastic mud (Falardeau et al., 2023). The sediment record is constructed as a composite sequence of five overlapping core segments that were correlated based on magnetic susceptibility (Pfälz, 2017). It covers about 4000 years of sedimentation (Grotheer et al., 2020). In this study, we focus on the upper 322 cm of the core, which encompasses the last 1300 years (see Section 3.4.1; Fig. 3.2; Table 3-A.1). The core was subsampled at 10-cm intervals from 322 to 62 cm and at 5-cm intervals from 62 cm to the top of the core (Table 3-A.2); subsamples were 1-cm thick. During the same expedition, a short surface sediment core of 20 cm in length (PG2303-1) was collected at the same site using a UWITEC gravity corer to recover the water-sediment interface better. It was stored cool before subsampling at 1-cm intervals using a vertical extruder. The short core likely covers the last two decades (see Section 3.4.1; Fig. 3-A.2; Appendix 3-A.1; Falardeau et al., 2023).

3.3.2 Grain size

A minimum of 0.2 g of dry sediment per sample was weighed for grain size analysis. Next, the sediment was mixed with hydrogen peroxide (30%) to remove organic matter. Once the reaction was complete, the samples were measured in the Microtrac MRB Bluewave laser diffraction instrument at the Geotop-UQAM. The instrument can detect grain sizes from 0.01 to 2000 µm. The data were processed in GRADISTAT (Blott, 2010), which defines sand as particles between 2 mm and 63 µm, silt between 63 and 2 µm, and clays <2 µm. Results are reported in Table 3-A.3.

Figure 3.1 a) Regional map showing the location of the study area (dotted white square) and the Hanna Shoal (black square). The pink and orange arrows indicate the flow of the Alaskan Coastal Waters (ACW) and other Pacific water branches (winter/summer water masses), respectively; the dotted red arrow shows the path of the subsurface Atlantic Water along the continental margin, and the yellow arrows represent the Beaufort Gyre based on Grebmeier et al. (2006). b) Map of the study area showing the coastal flow (purple arrow), the Beaufort shelfbreak jet (dark blue arrow), and the waters recirculating in the Mackenzie Trough under the Beaufort Gyre influence (yellow arrows) based on Lin et al. (2020). The gray arrows in the lower right corner mark the dominant wind directions (Radosavljevic et al., 2016), the black diamonds show the location of cores mentioned in the text, and the white diamond shows the location of the Komakuk Beach weather station. In the lower-left corner is a close-up of the study area with the core site location (pink diamond) and bathymetry of the Herschel Basin (EBA Engineering Consultants Ltd., 1992). c) Salinity (purple) and temperature (green) profiles in the Herschel Basin in August 2015 (solid line) and April 2016 (dotted lines) from CTD data (Falardeau et al., 2023). The blue and yellow dots refer to the location of the CTD measurements shown in the close-up of Fig. 3.1b, while the gray shading area separates the local surface waters from the bottom waters.



3.3.3 Radiometric chronology

The age models were defined based on radiometric analyses, combining ^{210}Pb , ^{226}Ra , ^{137}Cs and ^{14}C measurements; fore core PG2303 all methods were used, while for PG2303–1 we concentrated on ^{210}Pb , ^{226}Ra , and ^{137}Cs . The age model for PG2303–1 has previously been presented by Falardeau et al. (2023), who showed that the bottom of this core may be dated to 1999 ± 6 CE. For core PG2303, fifteen samples in the upper 75 cm of the core were analyzed for ^{210}Pb , ^{226}Ra and ^{137}Cs at Geotop-UQAM (Table 3-A.2). For ^{210}Pb , a spike of ^{209}Po was added into the ground sediment samples (~ 1 g), before it was successively digested in three different acids (HNO_3 ; HCl , HF and HNO_3), and in hydrogen peroxide with acid (H_2O_2 and HNO_3). Then, the residue was dissolved in HCl 0.5 N with ascorbic acid.

The ^{209}Po (recovery of the internal tracer) and the ^{210}Po activities (sample) were measured by alpha spectrometry using ORTEC detectors coupled to Maestro™ data acquisition software on silver disks. We calculated ^{210}Pb by assuming secular equilibrium between ^{210}Pb and ^{210}Po . The ^{226}Ra and ^{137}Cs were measured using high-resolution gamma spectrometry with a germanium detector (ORTEC). Samples were dried and sealed in plastic containers for at least 3 weeks prior to measurement. The ^{226}Ra activity average can represent the value of supported lead ($^{210}\text{Pb}_{\text{sup}}$) in the core. The excess of ^{210}Pb ($^{210}\text{Pb}_{\text{ex}}$) is obtained by subtracting the $^{210}\text{Pb}_{\text{sup}}$ from the total activity of ^{210}Pb ($^{210}\text{Pb}_{\text{tot}}$).

Table 3.1 ^{14}C ages on core PG2303 calibrated according to Marine20 with the CALIB 8.20 calibration program (Stuiver and Reimer, 1993) in consideration of a ΔR of 330 ± 41 years. The ^{14}C age in gray was not considered in the model. The ^{14}C ages with a laboratory sample ID starting with AWI and COL were measured at AWI MICADAS and at the University of Cologne, respectively.

Date name as reported in Figure 3.2	Depth (cm)	Uncalibrated ^{14}C age (years BP)	Calibrated age range (2 sigma) (cal. years BP)	Median age (cal. years BP)	Median age (years CE)	Dated material	Reference	Laboratory sample ID
Outlier	112-113	2313 ± 80	1164-1618	1385	565	Benthic foraminifera (n=1); <i>Vaginulina</i> sp.	This study	AWI-7126.1.1
PG4	151-152	1865 ± 41	738-1099	921	1029	Bivalve; <i>Nuculana</i> sp.	Grotheer et al. (2020)	COL4367.1.1
PG3	237-238	2024 ± 67	898-1283	1089	861	Benthic foraminifera (n=1); <i>Vaginulina</i> sp.	This study	AWI-7127.1.1
PG2	246.5-247.5	1955 ± 65	813-1231	1018	932	Mollusk	This study	AWI-7148.1.1
PG1	673.5	3062 ± 47	2050-2492	2269	-319	Bivalve; <i>Nuculana</i> sp.	Grotheer et al. (2020)	COL4368.1.1

Four ^{14}C ages on biogenic carbonates, i.e. mollusk shells and large specimens of the benthic foraminifera *Vaginulina* sp., measured at the AMS facility at the University of Cologne and the Alfred Wegener Institute (AWI) MICADAS laboratory were used to constrain the age model of core PG2303 (Table 3.1). The two ^{14}C ages at 248–246 cm and 238–237 cm delivered similar ages ranging \sim 861–932 CE (Table 3.1), offering a robust age anchor at this core depth interval. The model was constructed using the OxCal program (version 4.4; Bronk Ramsey, 2008, 2009) and we applied the Marine20 curve (Heaton et al., 2020). We used a ΔR of 330 ± 41 years based on a 3600-year-old tephra layer in a sediment core of the Chukchi Sea (Pearce et al., 2017; West et al., 2022). It is similar to the ΔR of 308 ± 111 years based on ^{14}C ages of seven mollusks collected in the nearshore areas of Alaska prior to bomb testing (Table 3-A.4; cf. McNeely et al., 2006). These two independent ΔR suggest that the reservoir effect in the area was most probably constant over the last few millennia.

While the overall age model of PG2303 is based on radiocarbon dating, the radiogenic isotope activity of ^{210}Pb , ^{226}Ra , and ^{137}Cs in the top 75 cm helped constrain the upper part of the age model. We used the core depth at which the supported ^{210}Pb is reached, i.e. 1906 CE at 46 \pm 2 cm (Fig. 3-A.2), as an age marker (Fig. 3.2). Moreover, we assumed that the drop in ^{137}Cs recorded at 14.5–9.5 cm core depth (midpoint at 12 cm; Fig. 3-A.2) correlated to the drop in atmospheric ^{137}Cs fallout at \sim 1980 CE (Kuzyk et al., 2013). As the tintinnid concentrations and grain size data between the top of core PG2303 and the bottom of core PG2303–1 show no communalities (Fig. 3.3), we interpret the top of core PG2303 to be older than the age at the bottom of core PG2303–1 and that there is no overlap between the cores. Thus, the top of core PG2303 must be older than 1999 ± 6 CE (cf. Falardeau et al., 2023). Nevertheless, the total inventory of ^{137}Cs in PG2303 indicates that only a limited amount of surface sediment has been lost in the coring process (cf. Kuzyk et al., 2013). Using levels for the drop in ^{137}Cs and for the supported ^{210}Pb , we calculated a mean sedimentation rate of $0.44 \pm 0.06 \text{ cm a}^{-1}$ for this interval and extrapolated the age upwards. This gave an age of 2010 ± 20 CE for the core top, but due to the maximal possible age of 1999 ± 6 CE at the core top, we reduced the possible range to 1990–2005 CE (Fig. 3.2; see Fig. 3-A.2 and Appendix 3-A.1 for more details).

The sediment mass accumulation ($\text{g cm}^{-2}\text{a}^{-1}$) results from the calculated mean sedimentation rates (cm a^{-1}) based on the OxCal age model multiplied by the mean density of $1.05 \pm 0.05 \text{ g cm}^{-3}$. The mean density was calculated from the fifteen samples measured for ^{210}Pb , which showed homogeneous values (Table 3-

A.5). Uncertainties on the accumulation rates follow the propagation of the errors on the ages and the density.

3.3.4 Micropaleontological preparations

A total of 39 subsamples (~ 6 g of dried sediment) from core PG2303 were dried, weighed, and subsequently wet sieved at $63\text{ }\mu\text{m}$. The $>63\text{ }\mu\text{m}$ fraction was used to observe and count microfossils under a binocular microscope at $40\times$. In three samples, fine sand was abundant, and we used dense liquid (tetrachlorethylene, C_2Cl_4) to separate mineral grains from biogenic remains (Table 3-A.2). The most common microfossils were benthic foraminifera, ostracods, and tintinnids.

The identification of foraminifera largely follows previous work by Feyling-Hanssen et al. (1971), Polyak et al. (2002), Scott et al. (2008a), and Jennings et al. (2020). All benthic foraminiferal taxa identified in this study are the same as those found in the short core PG2303–1 collected at the same site in the Herschel Basin (Table 3.2a). For a detailed description of the micropaleontological content in the gravity core PG2303–1, see Falardeau et al. (2023). All calcareous benthic foraminiferal taxa belonging to the Polymorphinoidea superfamily were grouped as “polymorphinids” (Table 3-A.6).

For the ostracod community, some taxa occurred exclusively in core PG2303. Among these, *Acanthocythereis dunelmensis*, *Roundstonia globulifera*, *Cytheropteron biconvexa*, *Kotoracythere arctoborealis* and *Normanicythere leioderma* are reported here for the first time in the Herschel Basin (Table 3.2b). Their identification is based on Gemery et al. (2017) and Stepanova et al. (2003). The ostracods are categorized into two groups following their tolerance to salinity (Table 3.2b); the low salinity tolerant (LST) taxa and the euhaline taxa, which prefer salinity >30 psu.

The only reported species of tintinnids in cores PG2303 and PG2303–1 is *Tintinnopsis fimbriata* (Meunier, 1919; Agatha, 2008). *T. fimbriata* is an agglutinated ciliate that uses small mineral particles to build its shell (lorica). It was reported as *Tintinnopsis rioplatensis* (Souto, 1973) in Scott et al. (2008a).

We calculated the concentrations (# g^{-1} sediment) of calcareous benthic foraminifera, agglutinated benthic foraminifera, ostracods, and *T. fimbriata* by dividing the total counts by the dry mass in each sample. For microfossil fluxes (# $\text{cm}^{-2}\text{a}^{-1}$), we multiplied the concentrations (# g^{-1}) with the accumulation rates ($\text{g cm}^{-2}\text{a}^{-1}$). We considered the uncertainties in accumulation rates to calculate the errors in the fluxes.

Next, we calculated the relative abundance (%) of benthic foraminiferal and ostracod taxa. The benthic foraminiferal counts are reported as the relative frequency of the taxa versus the total benthic foraminiferal (calcareous and agglutinated) assemblage. The agglutinated foraminifera are found in lower numbers, but we also calculated the percentage of the calcareous and agglutinated species separately, together with the total foraminiferal concentrations and fluxes (Fig. 3-A.3). Finally, we used the Arctic Ostracode Database 2020 (AOD2020; Cronin et al., 2021) and built distribution maps of selected species using Ocean Data View (Schlitzer, 2018; Fig. 3-A.4).

The percentages of foraminifera are considered statistically significant for dominant taxa (>5%) when a minimum of 100 foraminiferal tests are counted per sample, although >300 specimens should normally be counted to fully account for the proportions of rare species (Fatela and Taborda, 2002). For ostracods, we considered abundances of ≥ 10 valves as significant. All counts of calcareous benthic foraminifera satisfied the minimum threshold value of 100 with a mean of 458 ± 173 specimens per sample, with one exception (sample at 63–62 cm; 1790 ± 30 CE; 78 foraminifera counted; Table 3-A.6). When calcareous and agglutinated foraminiferal specimens are combined, counts <300 are reached in only seven samples, among those two have a sum <200. Thus, we are confident in the robustness of the foraminiferal assemblage data. Ostracod valve counts ranged from one to 45 with a mean of 15 ± 11 valves per sample (Table 3-A.6). We calculated the percentages of ostracod taxa for all samples, but assemblages should be considered with caution especially with low abundance counts of <10 valves. For *T. fimbriata*, there were <10 loricae counted per sample below 53 cm, but the counts reached a mean of 53 ± 31 specimens in the upper part of the core. Only the concentrations and fluxes are presented for the tintinnids as one species was identified.

Table 3.2 a) List of benthic foraminiferal and tintinnid taxa identified in the cores (x = present). b) List of ostracod taxa identified in the cores (x = present).

a)		PG2303	PG2303-1
Calcareous foraminifera			
<i>Bolivinellina pseudopunctata</i> (Höglund, 1947)	x	x	
<i>Buccella frigida</i> (Cushman, 1922)	x	x	
<i>Cassidulina reniforme</i> Nørvang, 1945	x	x	
<i>Cornuspira involvens</i> (Reuss, 1850)	x	x	
<i>Elphidiella groenlandica</i> (Cushman, 1933)	x	-	
<i>Elphidium albumbilicatum</i> (Weiss, 1954)	x	x	
<i>Elphidium asklundi</i> Brotzen, 1943	x	x	
<i>Elphidium bartletti</i> Cushman, 1933	x	x	
<i>Elphidium clavatum</i> Cushman, 1930	x	x	

<i>Elphidium hallandense</i> Brotzen, 1943	x	x			
<i>Eoeponidella pulchella</i> (Parker, 1952a)	x	x			
<i>Epistominella takayanagii</i> Iwasa, 1955	x	x			
<i>Haynesina nivea</i> (Lafrenz, 1963)	x	x			
<i>Haynesina orbicularis</i> (Brady, 1881a)	x	x			
<i>Islandiella helena</i> Feyling-Hanssen & Buzas, 1976	x	x			
<i>Islandiella norcrossi</i> (Cushman, 1933)	x	x			
<i>Nonionellina labradorica</i> (Dawson, 1860)	x	x			
Polymorphinoidea	x	x			
<i>Pyrgo williamsoni</i> (Sylvestri, 1923)	x	x			
<i>Quinqueloculina stalkeri</i> Loeblich & Tappan, 1953*	x	x			
<i>Quinqueloculina seminulum</i> (Linnaeus, 1758)	x	x			
<i>Stainforthia feylingi</i> Knudsen & Seidenkrantz, 1994	x	x			
<i>Stainforthia loeblichi</i> (Feyling-Hanssen, 1954)	x	x			
<i>Stetsonia horvathi</i> Green, 1960	x	x			
<i>Triloculina trihedra</i> Loeblich & Tappan, 1953	x	x			
<i>Vaginulina trondheimensis</i> (Feyling-Hanssen, 1964)	x	-			
<i>Valvularineria</i> spp. Cushman (1926)	x	x			
Agglutinated foraminifera					
<i>Ammotium cassis</i> (Parker, 1870)	-	x			
<i>Cribrostomoides crassimargo</i> (Norman, 1892)	x	x			
<i>Eggerelloides advenus</i> (Cushman, 1922)	x	x			
<i>Lagenammina diffugiformis</i> (Brady, 1876)	x	x			
<i>Portetrochammina karica</i> Shchedrina, 1946	x	x			
<i>Recurvooides turbinatus</i> (Brady, 1881b)	x	x			
<i>Spiroplectammina biformis</i> (Parker & Jones, 1865)	x	x			
<i>Textularia earlandi</i> Parker, 1952b	x	x			
<i>Textularia torquata</i> Parker, 1952a	x	x			
Tintinnids					
<i>Tintinnopsis fimbriata</i> Meunier, 1919	x	x			
b)					
			Low Salinity		
			Tolerant	Euhaline	References
<i>Acanthocythereis dunelmensis</i> (Norman, 1869)	x	-	x		5
<i>Cluthia cluthae</i> (Brady, Crosskey & Robertson, 1874)	x	-		x	1, 5, 6
<i>Cytheropteron biconvexa</i> Whatley and Masson, 1979	x	-		x	1, 3
<i>Cytheropteron brastadensis</i> Lord, 1981/ <i>Cytheropteron discoveria</i> Brouwers, 1994	x	x		x	1, 2, 6
<i>Cytheropteron elaeeni</i> Cronin, 1989	x	x		x	2, 4, 5
<i>Cytheropteron sulense</i> Lev, 1972	x	x		x	5
<i>Cytheropteron suzdalskyi</i> Lev, 1972	x	x		x	2
<i>Eucythere</i> spp.: <i>Eucythere argus</i> (Sars, 1866); <i>Eucythere declivis</i> (Norman, 1865)	x	x	x		5
<i>Eucytherura delineata</i> Whatley & Eynon, 1996	x	x		x	4
<i>Heterocyprideis sorbyana</i> (Jones, 1857)	x	x	x		3, 5, 6

<i>Kotoracythere arctoborealis</i> Schornikov & Zenina, 2006	x	-		x	7
<i>Loxoconcha venepidermoidea</i> (Swain, 1963)	x	x	x		2
<i>Normanicythere leioderma</i> (Norman, 1869)	x	-		x	1, 2, 5
<i>Paracyprideis pseudopunctillata</i> Swain, 1963	x	x	x		2, 3, 4, 5
<i>Rabilimis mirabilis</i> (Brady, 1868)	x	x		x	1, 2, 5
<i>Roundstonia globulifera</i> (Brady, 1868)	x	-	x		5
<i>Semicytherura complanata</i> (Brady, Crosskey & Robertson, 1874)	x	x		x	6

- 1- Olausson (1982)
- 2- McDougall et al. (1986)
- 3- Stepanova et al. (2003)
- 4- Gemery et al. (2017)
- 5- Stepanova et al. (2019)
- 6- Tian et al. (2020)
- 7- Gemery et al. (2021)

3.3.5 PCA analyses and community diversity

We performed a principal component analysis (PCA) to guide the identification of significant shifts and to divide the record of benthic foraminiferal and ostracod assemblages in the composite sequence of cores PG2303–1 and PG2303 into ecozones. For the abundant and diverse benthic foraminiferal assemblages (calcareous and agglutinated taxa included), we included taxa that occurred in at least 20 out of the 74 samples of the composite core and that were $\geq 2\%$ of the assemblages in at least one sample. Then, we analyzed the samples with ≥ 300 test counts. For ostracods, all taxa were kept, but we ran the analysis only on samples with counts of 10 valves or more. For the PCA, we used the vegan package (Oksanen et al., 2013) on the standardized (z-scores) relative abundances using the R software (R Core Team, 2021).

The Shannon diversity index (Shannon, 1948) was used as an indicator of diversity, which is the exponential of the Shannon entropy. The Shannon diversity index was calculated on the Hellinger-transformed raw counts of foraminifera and ostracods of the composite core in the vegan package under R. For foraminifera, the specimens identified to the genus level were discarded, except those belonging to specimens usually identified at the genus level, such as *Valvularia* spp. (see Table 3.2a). We calculated the Shannon diversity index at the genus level for the ostracods.

3.3.6 Stable isotopes

The isotopic composition ($\delta^{18}\text{O}$ and $\delta^{13}\text{C}$ ‰ vs. VPDB) of benthic foraminiferal tests was measured on *Elphidium clavatum* and *Cassidulina reniforme*. For each species, between 50 and 120 µg from the >63 µm fraction (equivalent to about 80–200 specimens of *E. clavatum* and 60–150 specimens of *C. reniforme*) were weighed with a microbalance and transferred into conical glass vials. The vials were closed with septum caps and heated at 90°C for an hour prior to the analysis at Geotop-UQAM. The laboratory uses a Micromass Isoprime isotope ratio mass spectrometer coupled to a MultiCarb system in dual inlet mode. In some intervals, successive samples were grouped to reach a suitable mass of calcium carbonate. Some samples could not be measured due to insufficient mass (Table 3-A.7). The results were normalized using two internal reference materials ($\delta^{18}\text{O} = -1.48 \pm 0.03\text{ ‰}$ and $-14.25 \pm 0.05\text{ ‰}$; $\delta^{13}\text{C} = 2.21 \pm 0.03\text{ ‰}$ and $-40.78 \pm 0.05\text{ ‰}$). The analytical uncertainty is less than $\pm 0.05\text{ ‰}$ and $\pm 0.08\text{ ‰}$ for $\delta^{18}\text{O}$ and $\delta^{13}\text{C}$, respectively.

E. clavatum tests have shown a disequilibrium of around -0.6 to -1.0 ‰ vs. VPDB (Erlenkeuser and von Grafenstein, 1999; Polyak et al., 2003), but also a positive one of +1.0 ‰ vs. VPDB (Bauch et al., 2004), for $\delta^{18}\text{O}$ in other studies of Arctic sediments. *E. clavatum* is known to have different offsets depending on water salinity (Polyak et al., 2003; Bauch et al., 2004). Therefore, although it is one of the most common species on Arctic Ocean shelves, *E. clavatum* is not ideal for isotopic analysis in shallow estuarine environments. Nevertheless, since the studied core site is from the deeper part of the basin, below the pycnocline (Fig. 3.1c), the isotope data should reflect a relatively stable and saline environment. *C. reniforme* normally calcifies close to equilibrium with a low vital offset of $0.13 \pm 0.2\text{ ‰}$ (Austin and Kroon, 1996).

Negative $\delta^{13}\text{C}$ values of *E. clavatum* have been reported in previous studies (Erlenkeuser and von Grafenstein, 1999; Polyak et al., 2003; Bauch et al., 2004), which would suggest infaunal habitats where pore waters are depleted in ^{13}C (McCorkle et al., 1990). Indeed, *E. clavatum* often lives as shallow infaunals in the upper millimeters of sediment (Murray, 2006) and can tolerate high sedimentation rates and burial (Ullrich et al., 2009), while *Cassidulina* can be both epifaunal and infaunal (Murray, 2006).

Seawater samples were poured from a water sampler at the sampling site directly into 30 mL narrowneck LDPE bottles. Samples were stored dark and cool at +4 °C prior to analysis. The oxygen ($\delta^{18}\text{O}$) and hydrogen ($\delta^2\text{H}$) stable isotope compositions of precipitation were measured in the Stable Isotope Facility of the

Alfred Wegener Institute in Potsdam (Germany), using a Finnigan MAT Delta-S mass spectrometer ($1\sigma < 0.1 \text{ ‰}$ for $\delta^{18}\text{O}$, $1\sigma < 0.8 \text{ ‰}$ for $\delta^2\text{H}$; Meyer et al., 2000). Values are given as per mil (‰) difference from the Vienna Standard Mean Ocean Water (VSMOW) standard (see data in Table 3-A.8). The $\delta^{18}\text{O}$ in the water was used to calculate the equilibrium calcite $\delta^{18}\text{O}$ as a function of salinity using the equation of Shackleton (1974) modified for the PDB scale (Hut, 1987) based on Polyak et al. (2003) and assuming stable water temperatures of -1 °C (Fig. 3.1c). The equation is:

$$\text{Equilibrium calcite } \delta^{18}\text{O} = \delta^{18}\text{O}_{\text{water}} - 0.27 + (\text{Temperature}[\text{°C}] - 16.9)/-4.0$$

3.4 Results

3.4.1 PG2303 grain size and age model

The ratios between sand, silt, and clay are relatively constant throughout core PG2303, with concentrations ranging from 1 to 4%, 63–74%, and 23–36%, respectively. The OxCal model performed on the ^{14}C data for core PG2303 yielded ages of $690 \pm 150 \text{ CE}$ in the bottom sample (322–321 cm) up to $1998 \pm 8 \text{ CE}$ at core top (Fig. 3.2). The mean mass accumulation rates are $0.38 \pm 0.02 \text{ g cm}^{-2}\text{a}^{-1}$ from the bottom to $1160 \pm 130 \text{ CE}$, then they decrease to $0.15 \text{ g cm}^{-2}\text{a}^{-1}$, subsequently again increasing to $0.52 \text{ g cm}^{-2}\text{a}^{-1}$ from $1910 \pm 10 \text{ CE}$ to the core top (Fig. 3.3). The bottom of the short core PG2303–1 is younger than the top of the long piston core PG2303 in accord with high $^{210}\text{Pb}_{\text{tot}}$ values and sedimentological and micropaleontological data (see Section 3.3.3; Fig. 3-A.2; Appendix 3-A.1; Falardeau et al., 2023).

3.4.2 PG2303 Microfossil abundances

The most abundant microfossils reported in this study are calcareous benthic foraminifera with mean concentrations of $72 \pm 25 \text{ g}^{-1}$. The concentrations decrease by half towards the core top, with values of $\sim 106 \text{ g}^{-1}$ at the bottom of the core ($690 \pm 150 \text{ CE}$) down to mean values of $55 \pm 20 \text{ g}^{-1}$ at $< 110 \text{ cm}$ ($> 1440 \pm 90 \text{ CE}$; Fig. 3.3). The flux of calcareous foraminifera is estimated at $25 \pm 13 \text{ cm}^{-2}\text{a}^{-1}$, with recurrent higher values prior to $1160 \pm 130 \text{ CE}$ (mean of $33 \pm 7 \text{ cm}^{-2}\text{a}^{-1}$).

The concentrations of agglutinated benthic foraminifera average $11 \pm 8 \text{ g}^{-1}$ and their fluxes average $4 \pm 4 \text{ cm}^{-2}\text{a}^{-1}$. A distinct interval of low agglutinated foraminiferal abundances occurs around 120–50 cm (~ 1330 – 1880 CE) with mean concentrations of $7 \pm 4 \text{ g}^{-1}$ and mean fluxes of $1 \pm 1 \text{ cm}^{-2}\text{a}^{-1}$. However, the presence of calcareous and agglutinated foraminifera throughout the record suggests good preservation.

The concentration of ostracods ranges from 1 to 6 valves g⁻¹, except for a maximum of 9 valves g⁻¹ at 1160 ± 130 CE (Fig. 3.3), corresponding to a maximum flux of 4 ± 1 valves cm⁻²a⁻¹. *Tintinnopsis fimbriata* abundance is low until 53 cm (1825 ± 20 CE; <1 g⁻¹). Afterward, mean *T. fimbriata* concentrations are 8 ± 5 g⁻¹ and fluxes are 4 ± 3 cm⁻²a⁻¹.

Figure 3.2 Core PG2303 age model based on OxCal (version 4.4; Bronk Ramsey, 2008, 2009). The vertical gray bar indicates the length of the core section used for this study. The blue shading indicates the 2-sigma probability range of the age depth model. Details on the two constrained ages based on ²¹⁰Pb and ¹³⁷Cs activity profiles at the top of the core can be found in the methods Section 3.3.3 and Appendix 3-A.1. The age model of core PG2303-1 (20–0 cm) from Falardeau et al. (2023) is illustrated in the gray rectangle in the top right corner.

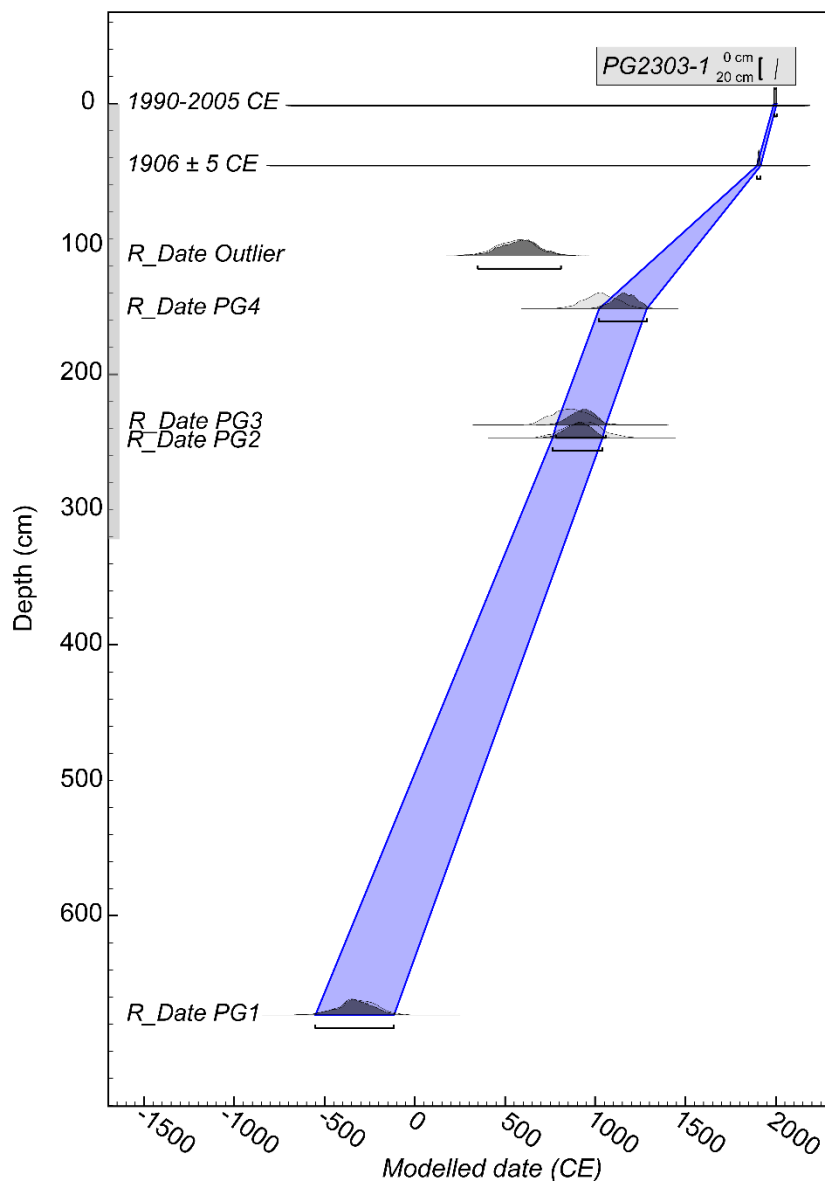
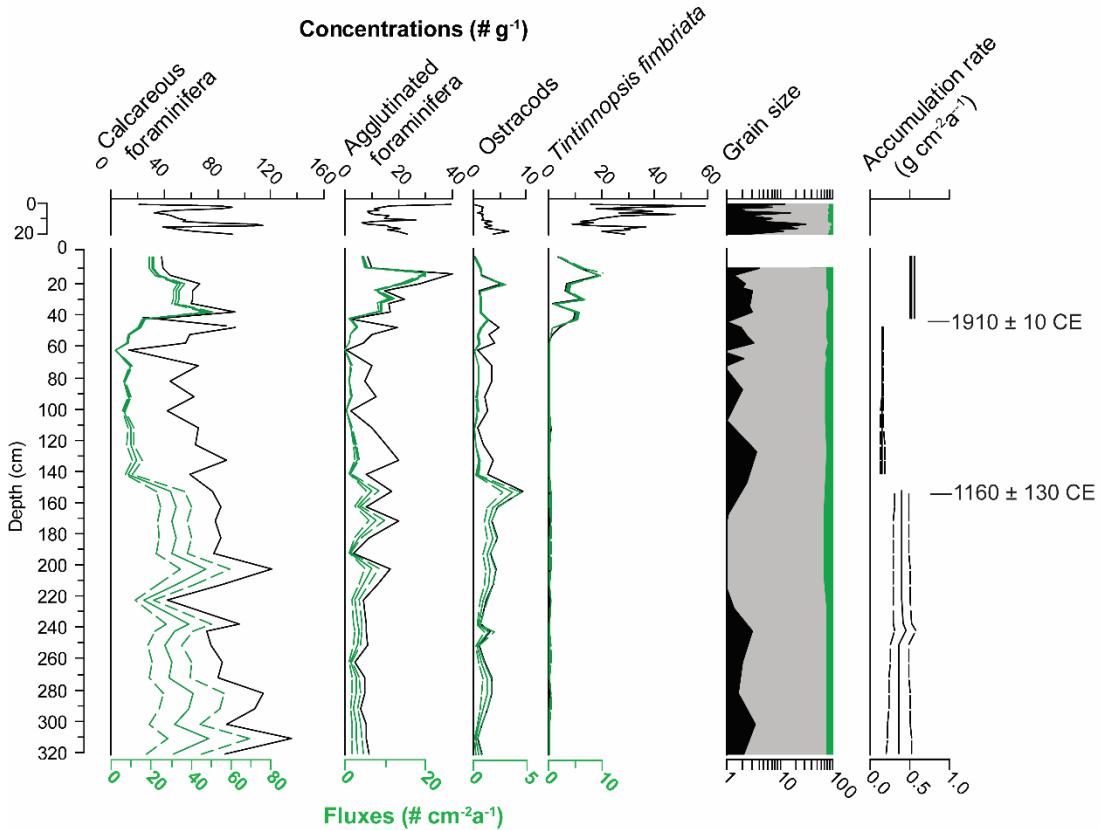


Figure 3.3 Microfossil concentrations (black lines), fluxes (green lines), grain size (black = sand; gray = silt; green = clay), and mass accumulation rates of the composite sequence of cores PG2303–1/PG2303 as a function of depth (cm). Dashed lines represent the flux and mass accumulation rate errors.



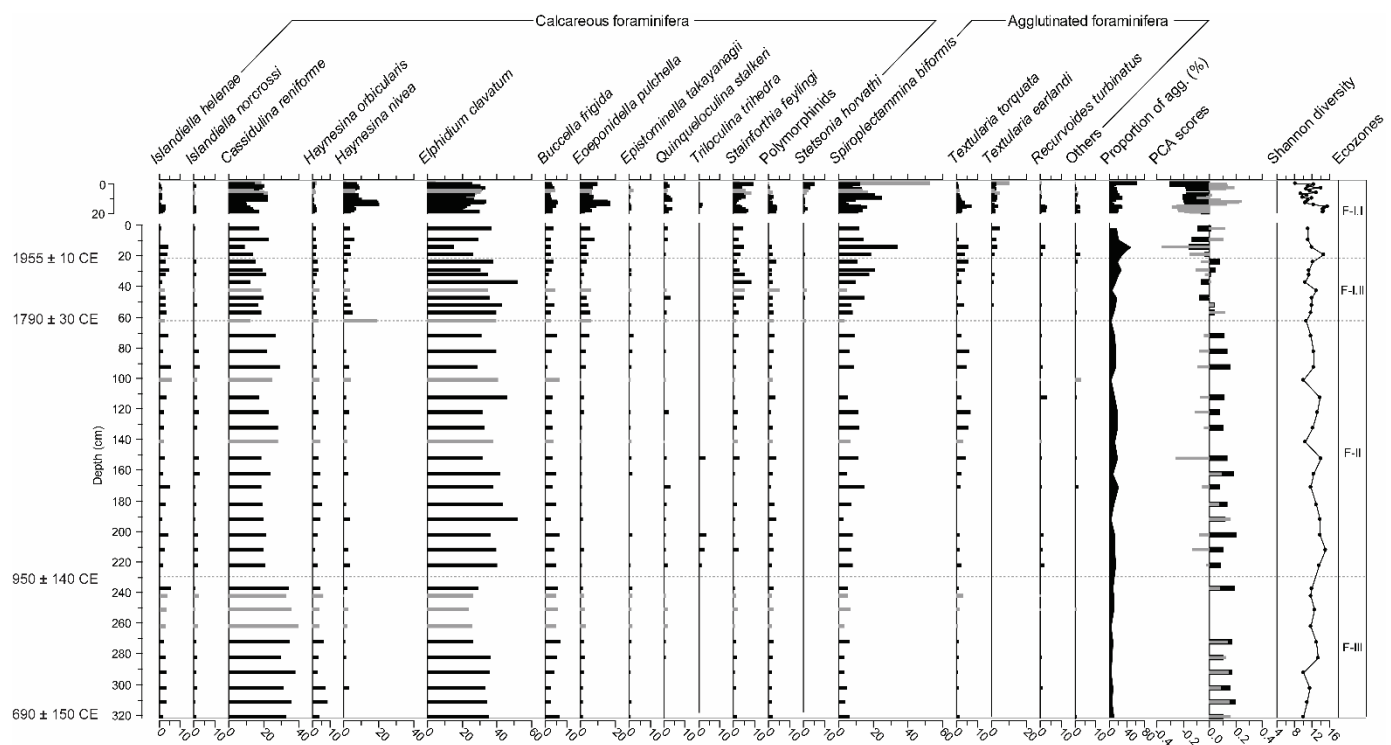
3.4.3 Benthic foraminiferal assemblages

A total of 22 species of calcareous and 11 species of agglutinated benthic foraminiferal taxa were identified (Table 3.2a). There was no indication of dissolution of the carbonate tests. The Shannon diversity index is 12 ± 2 in cores PG2303–1/PG2303 but reaches recurrent lower values towards the present (<10; Fig. 3.4). *Elphidium clavatum* and *Cassidulina reniforme* dominate the assemblages of core PG2303 with percentages of $35 \pm 7\%$ and $24 \pm 8\%$ of the calcareous and agglutinated assemblage, respectively. *Spiroplectammina biformis* is the dominant agglutinated taxa with relative abundances ranging from 5 to 35%. *Islandiella helena*, *Haynesina orbicularis*, *Haynesina nivea*, *Buccella frigida*, *Eoepionidella pulchella*, *Stainforthia feylingi*, polymorphinids, and *Textularia torquata* are occasional accompanying taxa (0–10%). *Islandiella norcrossi*, *Elphidium asklundi*, *Epistominella takayanagii*, *Quinqueloculina stalker*, *Triloculina trihedra*, *Stetsonia horvathi*, *Textularia earlandi*, and *Recurvorides turbinatus* are common, but occur in low percentages (<3%; Fig. 3.4; Table 3-A.6). *Stainforthia loeblichii* and *Bolivinellina pseudopunctata* were also

recovered in addition to rare specimens of *Cornuspira* spp., *Elphidium bartletti* and the agglutinated *Cibrostromoides crassimargo*, *Portrochammina karica* and *Eggerelloides advenus* (Tables 3.2a and 3-A.6).

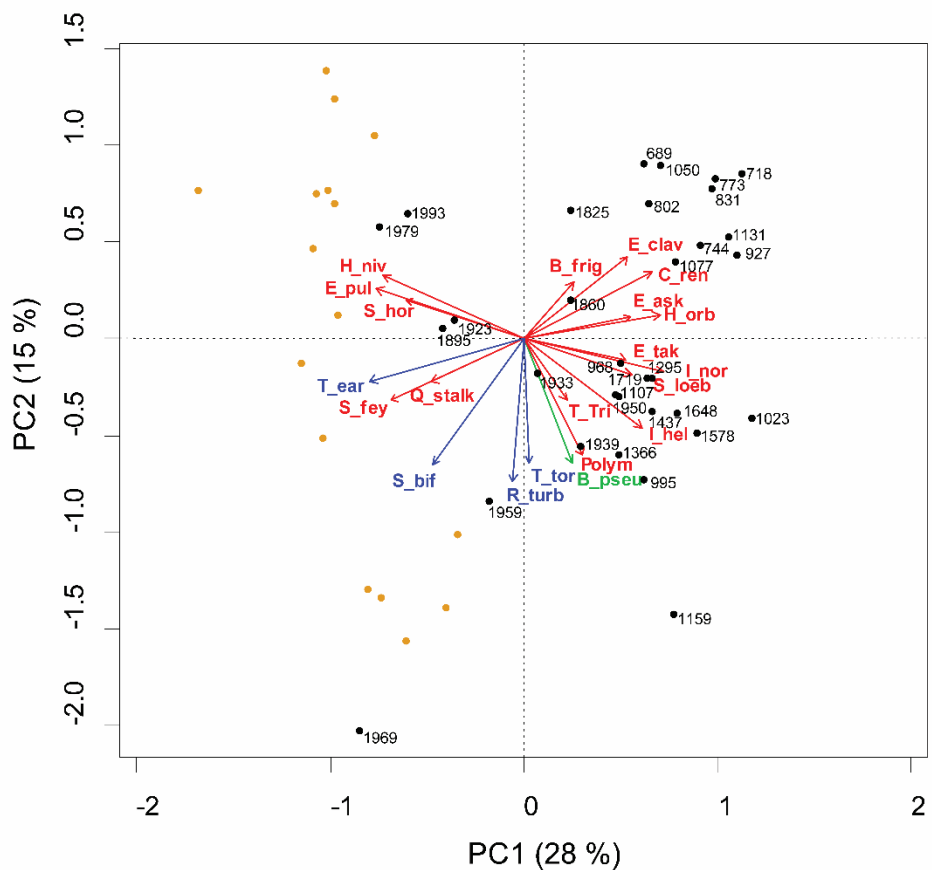
The PCA of benthic foraminiferal assemblages revealed that the first principal component (PC1) explains 28% of the variance (Fig. 3.5; See Table 3.3 for the corresponding abbreviation names). Negative PC1 scores characterize the modern assemblages (samples younger than 1790 ± 30 CE; Fig. 3.5), which are marked by the increase of *T. earlandi*, *S. feylingi*, *E. pulchella*, *H. nivea*, *S. horvathi*, *S. biformis*, and *Q. stalker* (Figs. 3.4-5). The second principal component (PC2) explains 15% of the variance. It shows an opposition between the agglutinated taxa *R. turbinatus*, *S. biformis* and *T. torquata* together with the calcareous taxon *B. pseudopunctata* against *H. nivea*, *E. clavatum*, *E. pulchella*, and *B. frigida* (Fig. 3.5).

Figure 3.4 Percentages of benthic foraminiferal taxa in the composite sediment sequence of cores PG2303–1/PG2303 as a function of depth (cm). The assemblages calculated with <300 foraminiferal tests are represented in gray. The principal component analysis (PCA) scores are represented by thick black bars (PC1) and thin gray bars (PC2). The ecozones were defined based on the PCA of the foraminiferal assemblages (see Fig. 3.5) and a shift in the dominant taxa.



The foraminiferal assemblages were divided into three ecozones based on the PCA results. Ecozone F-III is distinguished by positive PC2 values from 690 ± 150 to 950 ± 140 CE (Figs. 3.4-5). However, Ecozone F-III, is more importantly defined by the abundance of *C. reniforme*, which dominates the assemblages only during this interval (Fig. 3.4). In Ecozone F-II, PC1 scores positive and PC2 scores negative values until 1790 ± 30 CE. Finally, in Ecozone F-I, PC1 values decrease to near zero values and then oscillate (Ecozone F-I.II) until a clear shift to negative values at ~ 1955 CE occurs (Ecozone F-I.I; Fig. 3.4).

Figure 3.5 PCA plot of foraminiferal assemblages in the composite sediment sequence of cores PG2303–1/PG2303 (black dots for piston core PG2303 samples and orange dots for the short gravity PG2303–1 core samples). Agglutinated foraminifera are shown in blue, the low-oxygen tolerant calcareous species *Bolivinellina pseudopunctata* (*B_pseu*) is in green, while the remaining calcareous species are shown in red. See Table 3.3 for the full names of the abbreviations used.

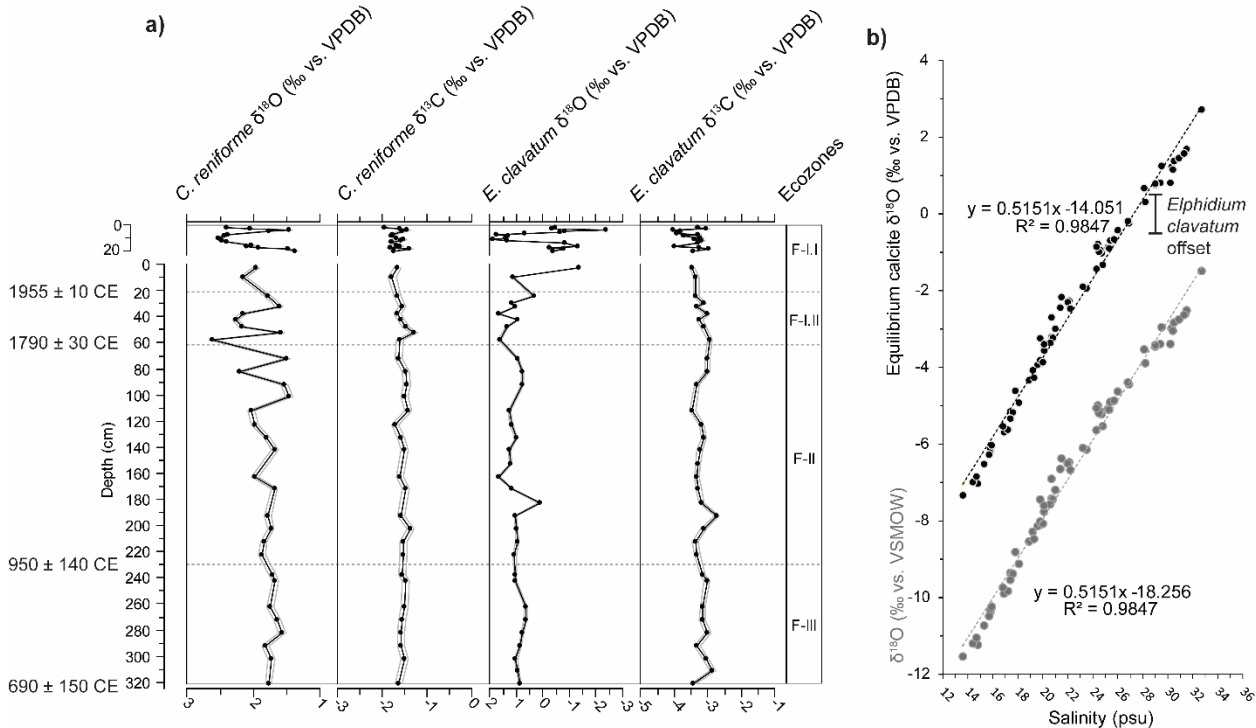


3.4.4 Stable isotopes

The $\delta^{18}\text{O}$ of *Cassidulina reniforme* ($\delta^{18}\text{O}_{\text{CR}}$) mostly ranges from 1.5 to 2.5 ‰ (mean = 1.9 ± 0.3 ‰) throughout the composite sequence. It shows little variations nearly through ecozones F-III to F-II, after which large amplitude oscillations of ± 1.0 ‰ occur (Fig. 6a). The stable carbon isotope of *C. reniforme* ($\delta^{13}\text{C}_{\text{CR}}$) records mean values of -1.6 ± 0.1 ‰.

The $\delta^{18}\text{O}$ of *Elphidium clavatum* ($\delta^{18}\text{O}_{\text{EC}}$) ranges between 0.2 and 1.6 ‰ before 1955 ± 10 CE (mean = 1.0 ± 0.2 ‰; Fig. 3.6a). Above, in Ecozone F-I.I, the $\delta^{18}\text{O}_{\text{EC}}$ shows a decrease accompanied by large amplitude oscillations of up to 4.0 ‰, with values ranging from -2.5 to 2.0 ‰. On the other hand, the $\delta^{13}\text{C}_{\text{EC}}$ is relatively uniform prior to 1790 ± 30 CE with a mean of -3.2 ± 0.1 ‰ and slowly decreases in the upper part of the sequence to reach values of -4.0 ± 0.1 ‰ at the core top (see raw data in Table 3-A.7).

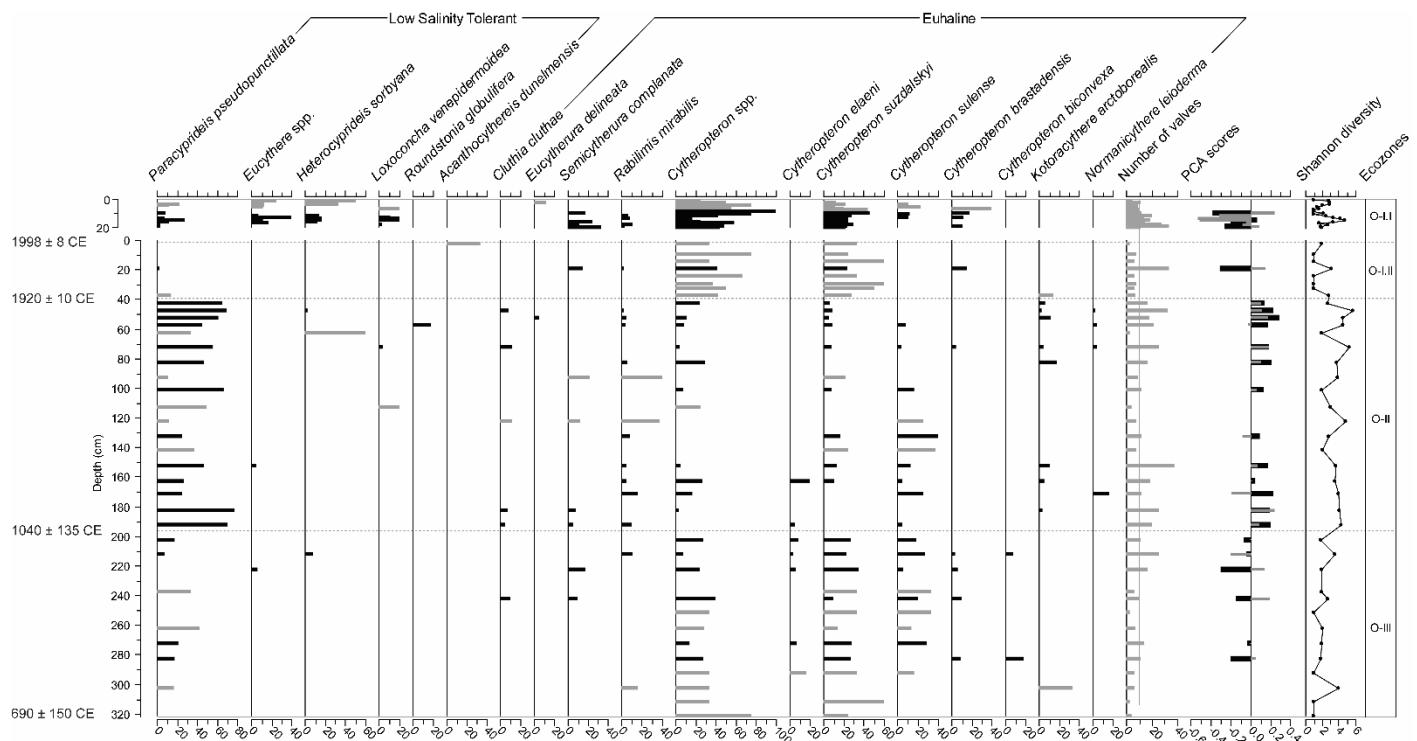
Figure 3.6 a) Stable isotope ratios ($\delta^{18}\text{O}$ and $\delta^{13}\text{C}$) of *Elphidium clavatum* and *Cassidulina reniforme* in the composite sediment sequence of cores PG2303-1/PG2303 as a function of depth (cm). The thin lines surrounding the main curves illustrate the analytical uncertainty. b) The equilibrium calcite $\delta^{18}\text{O}$ as a function of salinity (black dots; Table 3-A.7) calculated from $\delta^{18}\text{O}$ in the water column measured in the Herschel Basin at different depths in summer 2015 (gray dots; Table 3-A.8). A negative offset of 1.0 ‰ for *Elphidium clavatum* is depicted.



3.4.5 Ostracod assemblages

In total, 19 ostracod taxa were identified. Among those, six are low salinity tolerant (LST) and 11 are euhaline (Table 3.2b; Fig. 3.7). The recurrent euhaline taxa are *Cytheropteron* spp., *Cytheropteron suzdalskyi*, and *Cytheropteron sulense* (cf. McDougall et al., 1986; Stepanova et al., 2019). *Paracyprideis pseudopunctillata* is the dominant LST taxa. The Shannon diversity index indicates that one to five ostracod genera compose the assemblages (Fig. 3.7). *Kotoracythere arctoborealis* occurs at three distinctive intervals, often accompanied by *Normanicysthere leioderma*.

Figure 3.7 Relative abundances of ostracod taxa in the composite sediment sequence of cores PG2303–1/PG2303 as a function of depth (cm). The assemblages calculated with <10 ostracod valves are represented in gray. The principal component analysis scores are represented by thick black bars (PC1) and thin gray bars (PC2). The ecozones were defined based on the PCA of the ostracod assemblages (see Fig. 3.8).



The PCA of the ostracod assemblages shows an opposite trend between two groups of species on the first axis, which explains 22% of the variance (PC1, Fig. 3.8; see Table 3.3 for the corresponding abbreviation names). The first group of PC1 includes *C. suzdalskyi*, *Cytheropteron brastadensis*, *Semicytherura complanata*, and *Cytheropteron* spp. scoring negatively, and the second group of PC1 is composed of *P. pseudopunctillata*, *K. arctoborealis*, *Cluthia cluthae*, *N. leioderma*, and *Rabilimis mirabilis* scoring positively. PC2, which explains 14% of the variance, is mainly characterized by *Heterocyprideis sorbyana* and *Loxoconcha venepidermoidea* scoring negative values in contrast to *S. complanata*, *C. cluthae* and *C.*

brastadensis (Fig. 3.8). PC2 seems to discriminate ostracod taxa based on their salinity preference (Table 3.2b). The Ecozones O-III, O-II, and O-I division is based on PC1. In Ecozone O-III, from 690 ± 150 to 1040 ± 135 CE, *Cytheropteron* spp. and *C. suzdalskyi* largely dominate the assemblages ($57 \pm 23\%$), which corresponds to negative PC1 scores and low species diversity (means of 2 ± 1 ; Figs. 3.7-8). In Ecozone O-II, PC1 values are positive with abundant *P. pseudopunctillata* ($46 \pm 20\%$ of the assemblages). In Ecozone O-I, from 1920 ± 10 CE to the top of the record, PC1 values shift back to negative scores with the dominance of *Cytheropteron* spp. and *C. suzdalskyi* ($65 \pm 29\%$), and the species diversity drops (means of 2 ± 1). Ecozone O-I was subdivided into two subzones, based on marked negative PC2 scores after 1998 ± 8 CE associated with a notable increase of LST taxa occurrences (Fig. 3.7).

Figure 3.8 PCA plot of the ostracod assemblages in the composite sediment sequence of cores PG2303–1/PG2303 (black dots for piston core PG2303 samples and orange dots for the short gravity PG2303–1 core samples). The LST taxa are in blue and the euhaline taxa are in red. See Table 3.3 for the full names of the abbreviations used.

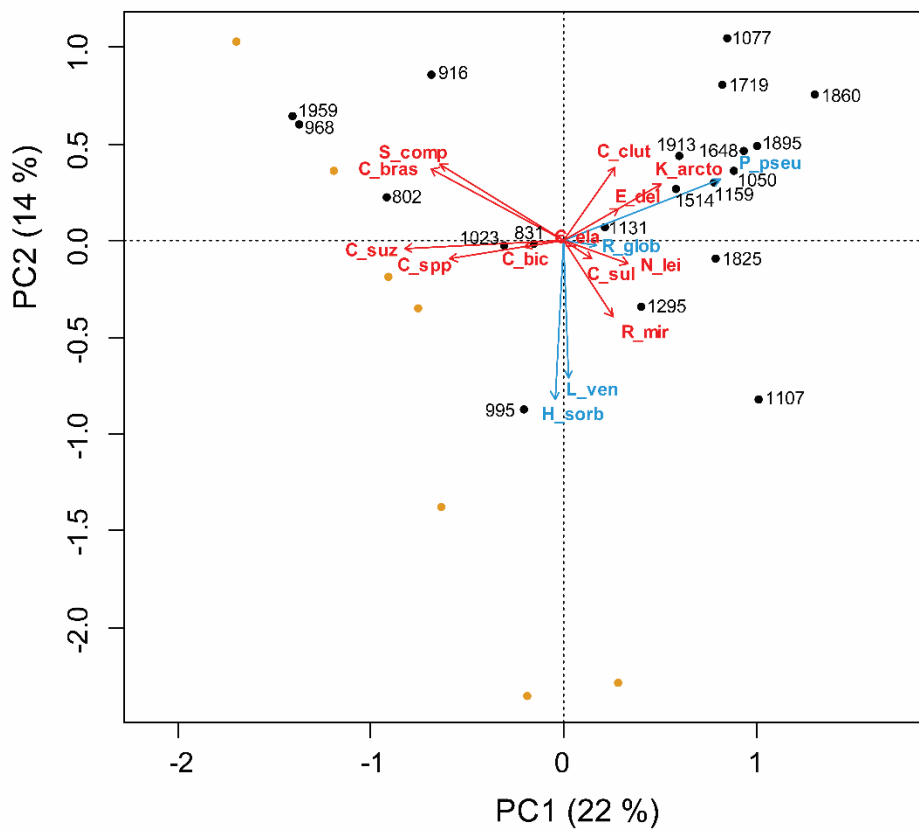


Table 3.3 List of abbreviations for foraminiferal and ostracod taxa in the Figs. 3.5 and 3.8.

Benthic foraminifera:

B_frig	<i>Buccella frigida</i>
B_pseu	<i>Bolivinellina pseudopunctata</i>
C_ren	<i>Cassidulina reniforme</i>
E_ask	<i>Elphidium asklundi</i>
E_clav	<i>Elphidium clavatum</i>
E_pul	<i>Eoeponidella pulchella</i>
E_tak	<i>Epistominella takayanagii</i>
H_niv	<i>Haynesina nivea</i>
H_orb	<i>Haynesina orbicularis</i>
I_hel	<i>Islandiella helenae</i>
I_nor	<i>Islandiella norcossi</i>
Polym	Polymorphinids
Q_stalk	<i>Quinqueloculina stalkeri</i>
R_turb	<i>Recurvoides turbinatus</i>
S_bif	<i>Spiroplectammina biformis</i>
S_fey	<i>Stainforthia feylingi</i>
S_hor	<i>Stetsonia horvathi</i>
S_loeb	<i>Stainforthia loeblichii</i>
T_ear	<i>Textularia earlandi</i>
T_tor	<i>Textularia torquata</i>
T_Tri	<i>Triloculina trihedra</i>

Ostracods:

C_bic	<i>Cytheropteron biconvexa</i>
C Bras	<i>Cytheropteron brastadensis</i>
C_clut	<i>Cluthia cluthae</i>
C_elia	<i>Cytheropteron elaeeni</i>
C_spp	<i>Cytheropteron spp.</i>
C_sul	<i>Cytheropteron sulense</i>
C_suz	<i>Cytheropteron suzdalskyi</i>
E_del	<i>Eucytherura delineata</i>
H_sorb	<i>Heterocyprideis sorbyana</i>
K_arcto	<i>Kotoracythere arctoborealis</i>
L_ven	<i>Loxoconcha venepidermoidea</i>
N_lei	<i>Normanicythere leioderma</i>
P_pseu	<i>Paracyprideis pseudopunctillata</i>
R_glob	<i>Roundstonia globulifera</i>
R_mir	<i>Rabilimis mirabilis</i>
S_comp	<i>Semicytherura complanata</i>

3.4.6 Ecozones and ecological shifts

The ostracod and foraminiferal ecozones are nearly similar in range, although the transitions from ecozones III to II, and from ecozones II to I, both occur later for ostracods than for the foraminifera (Figs. 3.4 and 3.7). The ecozones are compared in the summary Fig. 3.9, which is shown in function of depth due to the poorly constrained age model, especially prior to 1790 ± 30 CE (Fig. 3.2). Interpretations and comparisons with the literature are thus cautious for this interval. However, one important ecological shift at 1160 ± 130 CE was identified independently from the ecozones (see Section 3.5.2.2; Fig. 3.9). The two main ecological shifts identified are based on the more diverse and abundant foraminiferal assemblages, i.e. ecozones F-I.II and F-I.I, an interval where the age model is supported by additional radiogenic isotope data, and thus better constrained (i.e. after ~ 1800 CE; Figs. 3.2 and 3-A.2; Appendix 3-A.1).

3.5 Discussion

3.5.1 Identification of environmental conditions from micropaleontological proxies

3.5.1.1 Variable salinities and turbidity on Arctic shelves

The nearshore PG2303–1/PG2303 cores were retrieved at a relatively shallow depth (32 m), around 20 m below the summer halocline (Mulligan et al., 2010; Fig. 3.1c), and within the propagation limit of the Mackenzie River plume (Wood et al., 2015). Our microfossil assemblages reflect the highly variable salinity, temperature, and sediment discharge typical of Arctic estuaries, with the occurrence of *Elphidium clavatum*, *Haynesina orbicularis*, and *Buccella frigida* (cf. Khusid and Korsum, 1996; Polyak et al., 2002). *Haynesina nivea*, which occurs throughout the sequence and records high percentages in the upper part of the core, is indicative of shallow environments with fluctuating low salinity (light blue in Fig. 3.9) and relatively warm waters (Madsen and Knudsen, 1994; Luoto et al., 2011; Voltski et al., 2015; Falardeau et al., 2023). The other common taxa include *Cassidulina reniforme*, *Islandiella helenae*, *Spiroplectammina biformis*, and *Textularia* spp. that are typical of Arctic Ocean shelves (Jennings and Helgadóttir, 1994; Scott et al., 2008a; Cage et al., 2021). They also include *Eoepionidella pulchella* that thrives in particularly nutrient-rich waters (Wollenburg and Kuhnt, 2000; Knudsen et al., 2008; Scott et al., 2008b; Falardeau et al., 2023), and together with *Epistominella takayanagii* (light green in Fig. 3.9), it may relate to enhanced productivity.

The presence of LST ostracods (light blue in Fig. 3.9; except *Paracyprideis pseudopunctillata*), notably *Heterocyprideis sorbyana* found in river-influenced shallow environments (Stepanova et al., 2007; Gemery

et al., 2021), also suggests varying salinity. Interestingly, the euhaline taxon *Cytheropteron sulense* reaches its highest abundance near the river mouths (Fig. 3-A.4b), similar to the tintinnid *Tintinnopsis fimbriata*, characteristic of sediment-loaded freshwaters (Echols and Fowler, 1973; Burkovsky, 1976; Rogers et al., 1981; Scott et al., 2008a; Falardeau et al., 2023). The relationship between *C. sulense* and estuaries is not clear yet, but this shallow-water taxon found at littoral depths may tolerate turbidity and feed on the seasonal supply of food from river discharges.

3.5.1.2 Relationships to sea ice and food requirements

The nearshore study site is influenced by sea ice with land-fast ice that persists for nearly 9 months per year, from October to June (Carmack and Macdonald, 2002). The dominance of *Cassidulina reniforme* and *Elphidium clavatum* is compatible with such an environment and often constitute sea-ice proximal assemblages in fjords and glacial tongues (Hald and Korsun, 1997; Korsun and Hald, 2000; Jennings et al., 2020). The ostracod *Semicytherura complanata*, which records maximum abundance in polynyas of the Bering and Siberian shelves (Barber and Massom, 2007; Fig. 3-A.4f), may indicate enhanced sea-ice formation and brine rejections (Stepanova et al., 2003). The ostracod *Paracyprideis pseudopunctillata*, although also tolerant to low salinity (light blue in Fig. 3.8), may relate to an environment characterized by brine rejections (Gemery et al., 2021). Hence, *P. pseudopunctillata* is widely distributed along the Arctic nearshore areas, particularly where new sea ice is formed year-round on the East Siberian shelf (Fig. 3-A.4e). *P. pseudopunctillata* accompanied by *S. complanata* and *Cluthia cluthae* forms an assemblage similar to those of Hanna Shoal, NW Alaska (Fig. 3.1a), where frigid winter waters (dark blue in Fig. 3.9; Gemery et al., 2021) are accompanied with brine rejections. Furthermore, *Stainforthia feylingi* has a connection with sea ice as it typically thrives in the high-productivity areas near sea-ice margins (dark green in Fig. 3.9; Seidenkrantz, 2013).

Textularia earlandi and *Stetsonia horvathi* usually dominate oligotrophic waters under permanent sea-ice cover (Wollenburg and Mack-ensen, 1998; Wollenburg and Kuhnt, 2000; Jennings et al., 2020). However, in this study, we propose that the presence of *T. earlandi* and *S. horvathi* may be controlled by their feeding strategy. Both taxa can feed on complex organic carbon or bacterial degradation products that constitute food of poor quality (Alve, 2010; Jennings et al., 2020). *Quinqueloculina stalker* is a more bacterial feeder than a fresh algal feeder and can tolerate high turbidity (Guilbault et al., 2003). Hence, the three taxa, *T. earlandi*, *S. horvathi*, and *Q. stalker*, are here grouped as bacterial/complex carbon feeders (brown in Fig. 3.9). The bacterial/complex carbon feeders may represent opportunistic behavior taking advantage of

increased food supply regardless of the food type (cf. also Mäkelä et al., 2018). Intervals of more depleted $\delta^{13}\text{C}$ in the tests of benthic foraminifera may point to enhanced organic carbon fluxes and remineralization (Mackensen, 2008).

3.5.1.3 The shelf-break waters

The shelf-break waters, which are mainly derived from Pacific waters and the slightly saltier and warmer Atlantic waters (Lin et al., 2020), are important components of the Herschel Basin hydrography. They upwell along the margin and fill the bottom of the basin (Williams and Carmack, 2012). These water masses have a more oceanic signatures and may be associated with species that prefer cool stable saline bottom waters such as *Islandiella norcrossi* (cf. Polyak et al., 2002), a species which has been found associated with chilled Atlantic Water (Rytter et al., 2002; Cage et al., 2021; Seidenkrantz et al., 2021), and *Cassidulina reniforme* (cf. Polyak et al., 2002; Scott et al., 2008a). The occurrence of *Triloculina trihedra*, even in relatively low numbers, also suggests inflow of stable and saline bottom waters as miliolids thrive in such conditions (Murray, 1991; Polyak et al., 2002). Moreover, *T. trihedra* was previously found in assemblages dominated by the Atlantic-water indicator *Cassidulina neoteretis* (cf. Seidenkrantz et al., 2021) in the Kara Sea (Husum et al., 2015) and the Eurasian Basin (Wollenburg and Mackensen, 1998). However, although these taxa suggest stable and saline bottom waters, they do not necessarily provide evidence of Atlantic waters in the Herschel Basin.

Kotoracythere arctoborealis today reaches its maximum abundance in the Bering and Chukchi Seas (Fig. 3-A.4c; Gemery et al., 2021; orange in Fig. 3.9), while *Normanicythere leioderma* is found in relation to productive bottom waters in the Bering-Chukchi-Beaufort Seas (Fig. 3-A.4d; Gemery et al., 2021), and often co-occurs with *K. arctoborealis* (Fig. 3.7). Together, the intermittent occurrence of these species in our record may indicate variable presence of nutrient-rich Pacific waters (green and orange in Fig. 3.9) and thus, that influx of Pacific-sourced waters has occurred in pulses in the Herschel Basin during the last millennium (orange in Fig. 3.9); this may be partly due to its bathymetric features. Hence, intensified penetration of shelf-break water masses into the basin may occur during events of particularly favorable climatic conditions for upwelling on the Beaufort Sea shelf and/or for the eastward flow of Pacific waters.

3.5.2 History of environmental conditions prior to ~1800 CE

3.5.2.1 Influence of oceanic waters in the Herschel Basin from ~700 to 1150 CE

In Ecozone F-III, the dominance of *Cassidulina reniforme* and the occurrence of *Islandiella norcrossi* (Fig. 3.4) suggest influx of relatively saline bottom waters from the open shelf (see discussion in Section 3.5.1.3). The enhanced inflow of oceanic waters persisted slightly into Ecozone F-II as *Triloculina trihedra* relative abundance increases from 950 ± 140 to 1040 ± 135 CE (Fig. 3.9). Yet, the frequent occurrence of *Cytheropteron sulense* through Ecozone O-III (~690–1040 CE; Figs. 3.7, 3-A.4b) rather suggests estuarine-like conditions (Section 3.5.1.1) with episodes of freshwater discharge consistent with the abundance of *Haynesina orbicularis* and *Buccella frigida* (Fig. 3.4; Polyak et al., 2002). Altogether, the foraminiferal and ostracod assemblages thus suggest a combination between relatively high inflow of oceanic waters as well as relatively strong outflow of lower-salinity waters presumably derived from river runoff and/or snow and sea-ice melt. Similarly, oscillations in the oxygen stable isotope signals of ostracod valves and in the agglutinated foraminiferal abundances in the more offshore core HLY1302 (Fig. 3.1b) suggest fluctuating salinity and temperature in bottom waters between 800 and 1200 CE (Gemery et al., 2023).

In contrast, the $\delta^{18}\text{O}_{\text{EC}}$ and $\delta^{18}\text{O}_{\text{CR}}$ are relatively stable and oscillate close to 1.0 ‰ and 1.8 ‰ , respectively, through Ecozone F-III (Fig. 3.6a). Based on the strong linear relationship between $\delta^{18}\text{O}$ of seawater and salinity in the Herschel Basin, these values would correspond to a salinity of ~31 psu if assuming a negative offset of 1.0 ‰ for *Elphidium clavatum* (Fig. 3.6b; Erlenkeuser and von Grafenstein, 1999; Polyak et al., 2003). This is within the current mean annual (summer to winter) range for the bottom water salinity (ranging 28–32 psu; Mulligan et al., 2010; referred to as Polar Mixed Layer). Thus, the temporal resolution captured by the $\delta^{18}\text{O}_{\text{EC}}$ and $\delta^{18}\text{O}_{\text{CR}}$ is likely not sufficient to be used as indicators of summer bottom water salinity variations in this interval (cf. Gemery et al., 2023).

At 1040 ± 135 CE, the presence of *Paracyprideis pseudopunctillata* accompanied by *Cluthia cluthae* and *Semicytherura complanata* supports persistent frigid and saline bottom waters through Ecozone O-II (Section 3.5.1.2). Concurrently, the presence of *Rabilimis mirabilis* (Fig. 3.7) may indicate the development of stable cold and saline bottom waters as this species thrives in the upper limit of the Arctic Ocean halocline (Cronin et al., 2022). Such conditions may suggest enhanced sea-ice formation and brine rejections leading to poorly mixed bottom waters and strong stratification. The increased occurrence of the calcareous low-oxygen tolerant species *Bolivinellina pseudopunctata* (Alve and Bernhard, 1995; Patterson et al., 2000) combined with the relatively high frequencies of agglutinated foraminifera in

Ecozone F-II (Figs. 3.4-5; Table 3-A.6), suggests episodes of reduced bottom-water ventilation and increased rejection of corrosive brines (Nardelli et al., 2023), respectively. However, conditions on the continental shelf were likely still favorable for biological productivity with continuous influence of shelf-break waters until 1160 ± 130 CE as suggested from the occurrence of Pacific water indicators (orange and green, Fig. 3.9).

3.5.2.2 The culmination of a regional cooling between ~ 1150 and 1650 CE

Afterwards, for a few hundred years, from 1160 ± 130 CE to 1650 ± 50 CE, there is no indication of strong oceanic inflow (Section 3.5.1.3). We associate this interval with the coldest phase of our record. It was likely marked by dense sea-ice cover, limited upwelling to the shelf (Schulze and Pickart, 2012), and low productivity as illustrated by low microfossil abundances and fluxes (Fig. 3.3). This interval was characterized by low sediment accumulation rates (Fig. 3.3), which concurs with a pervasive sea-ice cover limiting sediment supply from coastal erosion, floating ice, or the spreading of the Mackenzie River plume. The transition towards these cold conditions at 1160 ± 130 CE is probably synchronous with a decrease in air temperatures over Alaska (~ 1150 CE; cf. Nicolle et al., 2018; Fig. 3.9) and with an increase of Arctic sea-ice extent (Kinnard et al., 2011; Fig. 3.9). This time period also approximately corresponds to the period of the Little Ice Age (Mann et al., 2009).

3.5.2.3 The early decline of harsh climate conditions near the coast, ~ 1650 - 1800 CE

Towards the end of Ecozone F-II, at 1650 ± 50 CE, bio-productivity increased slightly (light green, Fig. 3.9) while Pacific waters were reintroduced (orange, Fig. 3.9). The combination of productivity and influx of Pacific waters suggests longer sea-ice-free seasons and recurrence of milder conditions on the Beaufort Sea shelf. This agrees with the conclusions of Richerol et al. (2008), who documented high cyst concentrations of phototrophic dinoflagellate taxa as early as ~ 1624 CE in a site close to the coast in the Mackenzie Trough (core 912A, Fig. 3.1b), and about 300 years earlier than what was recorded at more offshore study sites (cores 906B, 803BC and HLY1302; Fig. 3.1b; Richerol et al., 2008; Bringué and Rochon, 2012; Gemery et al., 2023). Notably, the $\delta^{18}\text{O}_{\text{CR}}$ signal starts to oscillate of about 1.0 ‰ at approximately the same time (~ 1580 CE) in our record (end of Ecozone F-II; Fig. 3.6a). These oscillations may suggest larger amplitude salinity variations of ± 2 psu (Fig. 3.6), albeit still within the present seasonal salinity variations (Mulligan et al., 2010).

3.5.3 The modern warming after ~1800 CE

3.5.3.1 The environmental impact of the gradual warming from ca 1800 to 2000 CE

At 1790 ± 30 CE, both benthic foraminiferal and ostracod records suggest a short but strong freshwater pulse (light blue; Fig. 3.9). Bringué and Rochon (2012) also reported a low salinity event at 1790 CE (core 803BC; Fig. 3.1b), which they linked to a release of freshwater accumulated by the Beaufort Gyre, due to a shift from anticyclonic to cyclonic regime. Shortly after this freshwater pulse, the concentrations of *Tintinnopsis fimbriata*, which lives at depths of 0–40 m in the water column (Paranjape, 1987), increased significantly at our study site, which suggests enhanced inflow of fresh and sediment-loaded waters (Echols and Fowler, 1973; Scott et al., 2008a; Falardeau et al., 2023; light blue, Fig. 3.9). The high accumulation rates (Fig. 3.3) also point to high sediment supply, which is in agreement with increased abundance of *Spiroplectammina biformis* (Fig. 4), a taxon tolerant to rapid sedimentation and turbid meltwater (Jennings and Helgadóttir, 1994). Concurrently, enhanced input of terrestrial organic carbon is illustrated by the increase in bacterial/complex feeders (brown, Fig. 3.9; Section 3.5.1.2).

The input of terrestrial particles may be linked to a westward spread of the Mackenzie River plume (Ehn et al., 2019; Juhls, 2021) or could alternatively originate from coastal erosion (Grotheer et al., 2020; Jong et al., 2020). Fluvial inputs and coastal erosion can both be linked to a more extended open-water season with a more rapid response of the river plume to wind stress (Mulligan and Perrie, 2019). Increased permafrost degradation in response to an enhanced wave impact under ice-free conditions may also be a cause (Overeem et al., 2011; Günther et al., 2015; Mioduszewski et al., 2018). Moreover, longer ice-free seasons would facilitate the recorded increase in biological productivity (light and dark green, Fig. 3.9). Altogether, the low and variable salinity in surface/subsurface waters (light blue, Fig. 3.9) and the increased terrestrial organic input and productivity (brown and green, Fig. 3.9) illustrate the beginning of the modern warming at the onset of foraminiferal Ecozone F-I (Fig. 3.9).

A break-up of the cold and saline bottom winter waters at around 1920 ± 10 CE is inferred from the ostracod assemblages mainly as *Paracyprideis pseudopunctillata* decreases drastically (Figs. 3.7 and 3.9). This coincides with the reduced abundances of *Islandiella norcrossi*, which prefers stable saline waters (after sample 43–42 cm; Fig. 3.4; Cage et al., 2021; Falardeau et al., 2023). Thus, this transition may relate to enhanced seasonal mixing/renewal of the bottom waters, causing increased variability of the bottom-water salinity, which is often characterized by open waters in nearshore settings. A sea-ice break-up earlier in the summer season, and thus a more extended open-water season, would coincide with enhanced sea-

ice margin productivity, as it is also suggested by increased abundance of the foraminifera *Stainforthia feylingi* (Figs. 3.4 and 3.9; Section 3.5.1.2). Reduced summer sea-ice cover may have favored offshore inputs of terrestrial matter as reworked palynomorphs peaked on the slope of the Mackenzie shelf around 1920 CE (core 803BC; Fig. 3.1b; Bringué and Rochon, 2012). The microfaunal transition around 1920 ± 10 CE coincides with the regional warming inferred from other records on land using varves (Bird et al., 2009), pollen (Wolter et al., 2017), and tree-ring series (Porter et al., 2013).

All the above listed indicators of warming reach maximum values after 1955 ± 10 CE (Ecozone F-I.I; Fig. 3.9), which could be the regional signature of the main onset of anthropogenic warming. The 1955 CE shift corresponds to a significant decrease in Arctic sea-ice extent (Kinnard et al., 2011; Fetterer et al., 2017; Fig. 3.9) and accelerated atmospheric warming (Anchukaitis et al., 2013; Porter et al., 2013; Nicolle et al., 2018; Fig. 3.9). The timing of the onset and the acceleration of the modern warming are consistent with those in the synthesis of Abram et al. (2016) at 1830 CE and 1930 CE, respectively, for the Arctic region.

3.5.3.2 The post-2000 CE environmental conditions

After ~ 2000 CE, the Herschel Basin bottom waters are characterized by low salinity excursions, expressed by large $\delta^{18}\text{O}_{\text{EC}}$ oscillations, abundant *Haynesina nivea* and LST ostracods (light blue, Fig. 3.9). The $\delta^{18}\text{O}_{\text{EC}}$ signal would correspond to high salinity variations ranging from 24.5 to 33 psu (Fig. 3.6a, b). Although, the large amplitudes might to some extent be an artifact of changing internal offsets of *Elphidium clavatum* in low salinities (Polyak et al., 2003; Bauch et al., 2004), the peaks of depleted $\delta^{18}\text{O}_{\text{EC}}$ still strongly suggest episodes of low salinity. The low salinity fluctuations observed at depth in the basin may be explained by enhanced vertical mixing under seasonal sea-ice-free conditions (Rainville and Woodgate, 2009), in agreement with the low summer sea-ice concentrations recorded after ~ 2000 CE (Fetterer et al., 2017; Falardeau et al., 2023). Hence, low sea-ice leading to the increased impact of storms (Mioduszewski et al., 2018) probably have fostered mixing and turbulence in the water column.

Stronger easterly winds have been recorded at the Komakuk Beach weather station after 1996 CE (Fig. 3.1b; Environment Canada, 2020). Such winds foster the spreading of the Mackenzie River plume, particularly during ice-free conditions (Wood et al., 2015; Mulligan and Perrie, 2019). This could explain the high *Tintinnopsis fimbriata* concentrations (Figs. 3.3 and 3.9). Concomitantly, easterly winds favoring upwelling of cold and saline subsurface waters (Carmack and Macdonald, 2002; Pickart et al., 2011) may have resulted in salinity variations (light blue, Fig. 3.9) and enhanced productivity (light green, Fig. 3.9;

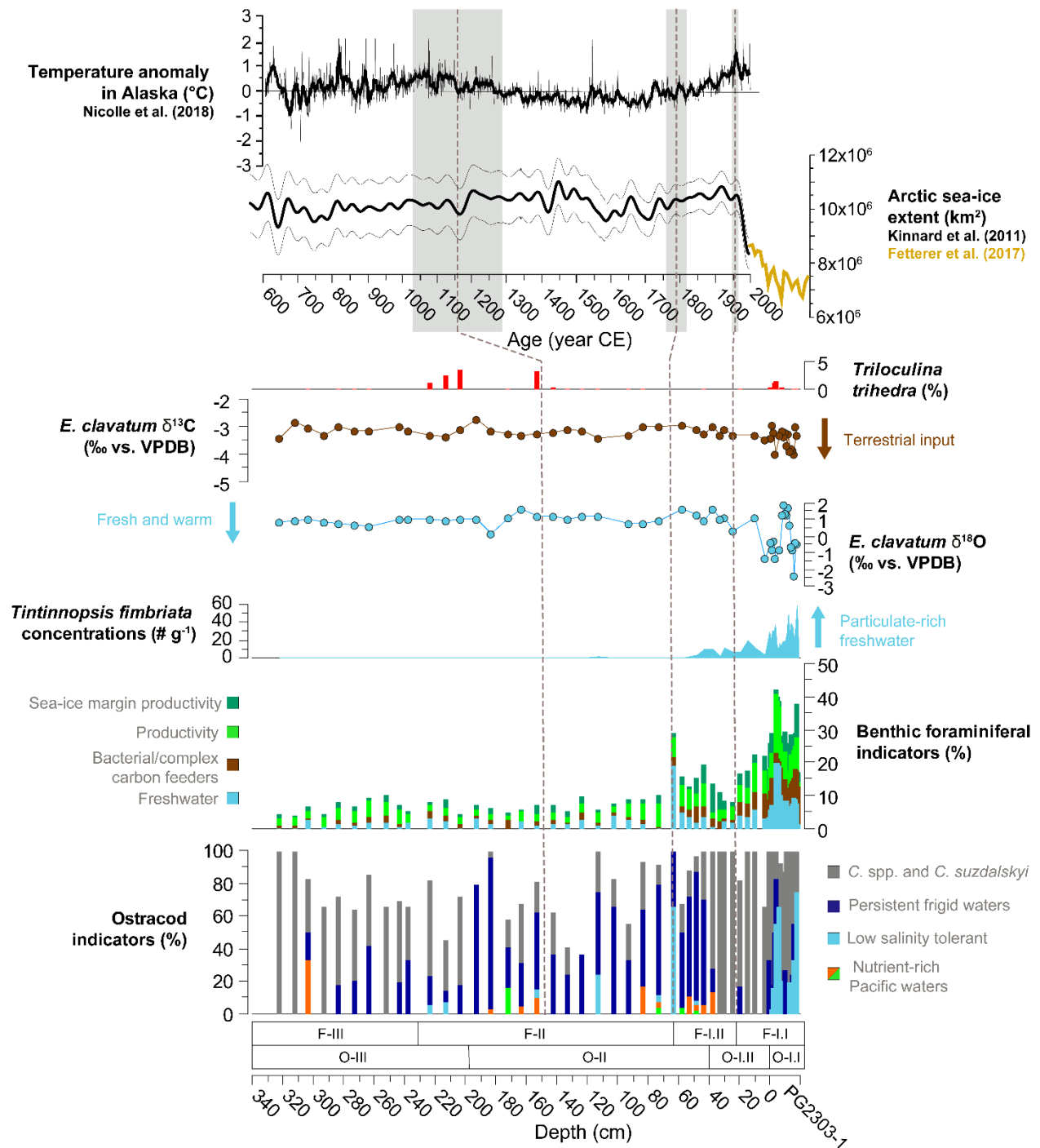
Tremblay et al., 2011, 2012; Pickart et al., 2013). Easterly winds are also associated with sediment resuspension and turbidity around Herschel Island-Qikiqtauruk (Klein et al., 2019), in agreement with increased erosion rates recorded since 2000 CE (Jones et al., 2009; Obu et al., 2016; Radosavljevic et al., 2016), which may have contributed to maximum terrestrial inputs in accord with the depleted $\delta^{13}\text{C}_{\text{EC}}$ signal (Figs. 3.6a and 3.9; Polyak et al., 2003; Mackensen, 2008; Grotheer et al., 2020).

3.6 Conclusion

The unique setting of the Herschel Basin as a sedimentary depocenter with high accumulation rates in the nearshore zone of the western Canadian Arctic yields microfossil records that allow us to reconstruct changes in the nearshore environments of the Canadian Beaufort Sea at high temporal resolution over the last 1300 years. The foraminiferal, ostracod, and tintinnid data, together with the isotopic composition of foraminiferal tests, provide complementary information about bottom (benthic foraminifera and ostracods) and surface (tintinnids) water conditions (temperature, salinity), sea-ice coverage, and organic matter fluxes through productivity and terrestrial input.

The records also enable inferences about regional climate changes, which appear related to terrestrial temperature anomalies in Alaska and sea-ice cover extent in the Arctic Ocean. A particularly cold interval was recorded between 1150 CE and 1650 CE as marked by persistent frigid winter waters, together with hampered upwelling of shelf-break waters, low productivity, and limited sediment supply to the basin, most probably in response to heavy annual sea-ice cover.

Figure 3.9 Summary figure of paleoecological data from the Herschel Basin site PG2303 in function of depth (cm) compared with existing data of temperature anomalies in Alaska (Nicolle et al., 2018) and summer sea-ice extent in the Arctic Ocean from 600 to 2000 CE (Kinnard et al., 2011; black line) with a close-up from 2000 to 2022 CE (Fetterer et al., 2017; yellow line) in function of age (year CE). Three important shifts are identified: at 1160 ± 130 CE, a transition to particularly cold conditions, and at 1790 ± 30 CE and at 1955 ± 10 CE to mark the early onset and the acceleration of the modern warming, respectively. For the ostracod indicators (cumulative percentages): Pacific waters (orange) = *Kotoracythere arctoborealis*; Productivity (light green) = *Normanicythere leioderma*; Low salinity tolerant (light blue) = *Heterocyprideis sorbyana*, *Loxoconcha venepidermoidea* and *Eucythere* spp.; Persistent frigid waters (dark blue) = *Paracyprideis pseudopunctillata*, *Cluthia cluthae* and *Semicytherura complanata*. For the benthic foraminiferal indicators (cumulative percentages): Variable salinity (light blue) = *Haynesina nivea*; Bacterial/complex organic carbon feeders (brown) = *Textularia earlandi*, *Stetsonia horvathi* and *Quinqueloculina stalker*; Productivity (light green) = *Eoeponidella pulchella* and *Epistominella takayanagii*; Sea-ice margin productivity (dark green) = *Stainforthia feylingi*. *Triloculina trihedra* refers to cool and stable saline waters (red).



The most salient feature of this study is the regional signature of the ongoing global climate warming that was recorded as early as 1790 ± 30 CE, but increased sharply after 1955 ± 10 CE, likely in response to the ongoing anthropogenic forcing. It seems to coincide with the onset and emergence of the industrial-age warming, as evidenced by Abram et al. (2016) on an hemispheric scale and more regionally, in Alaska, as shown by Nicolle et al. (2018).

The impacts of climate changes include salinity variations in surface water that may be caused by the Mackenzie River plume extent and sea- ice melt. They also include higher terrestrial input with regards to the Mackenzie River plume and coastal erosion. These impacts reach maxima after 2000 CE and are marked by particularly high fluctuations of bottom water conditions because of intensified vertical mixing. All the above-listed impacts of climate change are probably directly or indirectly related to reduced summer sea-ice cover. Finally, we can conclude that the magnitude of these impacts in the post 2000 CE interval is unprecedented over the last 1300 years and thus over the history of traditional harvesting in the nearshore waters of the Canadian Beaufort Sea by the Inuvialuit and their ancestors.

3.7 Acknowledgements

We acknowledge the Fonds de Recherche du Quebec Nature et Technologies (FRQNT) that funded JF through scholarships. This study was also possible thanks to Natural Sciences and Engineering Research Council (NSERC) of Canada funds through a Discovery grant to AdV and a CREATE grant to ArcTrain [grant no. 432295]. We wish to thank the Geotop Research Center for equipment and laboratory access and more personally, to Jean-François Hélie and Agnieszka Adamowicz-Walczak for their help and support in the preparation of the stable isotope analyses. TC and LG are funded by the U.S. Geological Survey, Climate Research and Development Program. Any use of trade, firm, or product names is for descriptive purposes only and does not imply endorsement by the U.S. Government. MSS is funded by the Independent Research Fund Denmark [grant no. 0135-00165B; GreenShelf] and the European Union's Horizon 2020 research and innovation program [grant agree- ment no. 869383; ECOTIP]. MF and JF have received financial support by the Nunataryuk project, which is funded by the European Union's Horizon 2020 research and innovation program [grant no. 773421]. VCB received a National Council of Science and Technology (CONACYT) postdoc grant from Mexico [CVU no. 174856]. We express our thanks to the Yukon Territorial Government and the Yukon Parks (Herschel Island – Qiqiktaruk Territorial Park). The authors acknowledge the support of the Aurora Research Institute (ARI, Inuvik) for the field component. We finally wish to thank all the people that contributed to the realization of this study: George Tanski, Jan Kahl and Boris Biskaborn who supported sediment coring; Margaux Rougier and Estelle Allan for the ostracod distribution maps and support with Ocean Data View, respectively; Bianca Fréchette for her advice in statistical analyses; Diogo Barnetche for the location of equipment at the Département des Sciences de la Terre; Tiffany Audet and Anna To for micropaleontological sample preparations; and Philippe Roberge for the grain size analyses

3.8 References

- Abram, N.J., McGregor, H.V., Tierney J.E., Evans M.N., McKay N.P., Kaufman D.S. and the PAGES 2k Consortium (Thirumalai K., Martrat B., Goosse H., Phipps S.J., Steig E.J., Kilbourne, K.H., Saenger, C.P., Zinke J., Leduc G., Addison J.A., Mortyn P.G., Seidenkrantz M.-S., Sicre M.A., Selvaraj K., Filipsson, H.L., Neukom, R., Gergis, J., Mark A.J., Curran M.A.J., Gunten L.), 2016. Early and asynchronous onset of industrial-era warming. *Nature* 536, 411-415. DOI: 10.1038/nature19082.
- Agatha, S., 2008. Redescription of the tintinnid ciliate *Tintinnopsis fimbriata* Meunier, 1919 (Spirotricha, Choretrichida) from coastal waters of Northern Germany. *Denisia* 23, 261-272.
- Alve, E., 2010. Benthic foraminiferal responses to absence of fresh phytodetritus: A two-year experiment. *Marine Micropaleontology* 76, 67-75.
- Alve, E., Bernhard, J.M., 1995. Vertical migratory response of benthic foraminifera to controlled oxygen concentrations in an experimental mesocosm. *Marine Ecology Progress Series* 116, 137-151.
- Anchukaitis, K.J., D'Arrigo, R.D., Andreu-Hayles, L., Frank, D., Verstege, A., Curtis, A., Buckley, B.M., Jacoby, G.C., Cook, E.R., 2013. Tree-ring-reconstructed summer temperatures from northwestern North America during the last nine centuries. *Journal of Climate* 26, 3001-3012.
- Austin, W.E.N., Kroon, D., 1996. Lateglacial sedimentology, foraminifera and stable isotope stratigraphy of the Hebridean Continental Shelf, Northwest Scotland. In: Andrews, J., Austin, W., Bergsten, H., Jennings, A. (Eds.), *The Lateglacial Palaeoceanography of the North Atlantic Margins*, Geological Society of London 111, 187-213.
- Barber, D.G., Massom, R.A., 2007. The role of sea ice in Arctic and Antarctic polynyas. *Elsevier Oceanography Series* 74, 1-54.
- Bauch, H., Erlenkeuser, H., Bauch, D., Müller-Lupp, T., Taldenkova, E., 2004. Stable oxygen and carbon isotopes in modern benthic foraminifera from the Laptev Sea shelf: implications for reconstructing proglacial and profluvial environments in the Arctic. *Marine Micropaleontology* 51, 285-300.
- Belter, H.J., Krumpen, T., von Albedyll, L., Alekseeva, T.A., Birnbaum, G., Frolov, S.V., Hendricks, S., Herber, A., Polyakov, I., Raphael, I., 2021. Interannual variability in Transpolar Drift summer sea ice thickness and potential impact of Atlantification. *The Cryosphere* 15, 2575-2591.
- Bird, B.W., Abbott, M.B., Finney, B.P., Kutchko, B., 2009. A 2000 year varve-based climate record from the central Brooks Range, Alaska. *Journal of Paleolimnology* 41, 25-41.

- Blais, M., Ardyna, M., Gosselin, M., Dumont, D., Bélanger, S., Tremblay, J.-É., Gratton, Y., Marchese, C., and Poulin, M., 2017, Contrasting interannual changes in phytoplankton productivity and community structure in the coastal Canadian Arctic Ocean. *Limnology and Oceanography* 62, 2480-2497.
- Blott, S., 2010. GRADISTAT ver. 8.0: A grain size distribution and statistics package for the analysis of unconsolidated sediments by sieving or laser granulometer. Kenneth Pye Associates, Solihull, UK.
- Bringué, M., Rochon, A., 2012. Late Holocene paleoceanography and climate variability over the Mackenzie slope (Beaufort sea, Canadian Arctic). *Marine Geology* 291, 83-96.
- Bronk Ramsey, C., 2008. Deposition models for chronological records. *Quaternary Science Reviews* 27, 42-60.
- Bronk Ramsey, C., 2009. Bayesian analysis of radiocarbon dates. *Radiocarbon* 51, 337-360.
- Burkovsky, I., 1976. Ecology of Tintinnida (Ciliata) of the White Sea. *Zoologicheskii Zhurnal* 55, 497-507.
- Cage, A.G., Pieńkowski, A.J., Jennings, A., Knudsen, K.L., Seidenkrantz, M.-S., 2021. Comparative analysis of six common foraminiferal species of the genera *Cassidulina*, *Paracassidulina*, and *Islandiella* from the Arctic–North Atlantic domain. *Journal of Micropalaeontology* 40, 37-60.
- Carmack, E.C., Macdonald, R.W., 2002. Oceanography of the Canadian Shelf of the Beaufort Sea: a setting for marine life. *Arctic* 55, 29-45.
- Cox, C.J., Stone, R.S., Douglas, D.C., Stanitski, D., Gallagher, M., 2019. The Aleutian Low-Beaufort Sea Anticyclone: A climate index correlated with the timing of springtime melt in the Pacific Arctic cryosphere. *Geophysical Research Letters* 46, 7464-7473.
- Cronin, T. M., Gemery, L.J., Briggs, W.M., Brouwers, E.M., Schornikov, E.I., Stepanova, A., Wood, A.M., Yasuhara, M., Siu, S. (2021-01-08). NOAA/WDS Paleoclimatology - Arctic Ostracode Database 2020 (AOD2020). [Data Table]. NOAA National Centers for Environmental Information. DOI: 10.25921/grn9-9029. Accessed [2020-11-03].
- Cronin, T.M., Gemery, L., Baylee, M.O., Regnier, A.M., Poirier, R., Sienna, S., 2022. Abrupt Quaternary Ocean-ice Events in the Arctic: Evidence from the *Ostracod Rabiliensis*. *Micropaleontology* 68, 232-242.
- Darby, D.A., Ortiz, J.D., Grosch, C.E., Lund, S.P., 2012. 1,500-year cycle in the Arctic Oscillation identified in Holocene Arctic sea-ice drift. *Nature Geoscience* 5, 897-900.

EBA Engineering Consultants Ltd., 1992. Proceedings of the Beaufort Sea granular resources workshop, Part 1: Reports on NOGAP regional studies, 11 pp.

Echols, R.J., Fowler, G.A., 1973. Agglutinated tintinnid loricae from some Recent and Late Pleistocene shelf sediments. *Micropaleontology* 19, 431-443.

Ehn, J.K., Reynolds, R.A., Stramski, D., Doxaran, D., Lansard, B., Babin, M., 2019. Patterns of suspended particulate matter across the continental margin in the Canadian Beaufort Sea during summer. *Biogeosciences* 16, 1583-1605.

Environment Canada, 2020. Historical climate data. Retrieved from <http://climate.weather.gc.ca>, Accessed [2020-10-12].

Erlenkeuser, H., von Grafenstein, U., 1999. Stable oxygen isotope ratios in benthic carbonate shells of ostracoda, foraminifera, and bivalvia from surface sediments of the Laptev Sea, summer 1993 and 1994. In: Thiede, J., Tomovkhov, L.A. (Eds.), Land-Ocean Systems in the Siberian Arctic. Springer, Berlin, Heidelberg, pp. 503-514.

Falardeau, J., de Vernal, A., Seidenkrantz, M.-S., Cronin, T.M., Gemery, L., Chassiot, L., Fritz, M., Carnero-Bravo, V., Hillaire-Marcel, C., and Archambault, P., 2023. Microfaunal recording of recent environmental changes in the Herschel Basin, western Arctic Ocean. *Journal of Foraminiferal Research* 53, 20-48.

Fatela, F., Taborda, R., 2002. Confidence limits of species proportions in microfossil assemblages. *Marine Micropaleontology* 45, 169-174.

Fetterer, F., Knowles, K., Meier, W. N., Savoie, M., Windnagel, A. K., 2017. Sea Ice Index, Version 3 [Sea Ice Index Monthly Data with Statistics]. Boulder, Colorado USA, National Snow and Ice Data Center, DOI:10.7265/N5K072F8. Date Accessed 11-23-2022.

Feyling-Hanssen, R.W., Jørgensen, J.A., Knudsen, K.L., Lykke-Andersen, A.-L., 1971. Late Quaternary Foraminifera from Vendsyssel, Denmark and Sandnes, Norway. *Bulletin of the Geological Society of Denmark* 21, 67-317.

Frey, K.E., Moore, G., Cooper, L.W., Grebmeier, J.M., 2015. Divergent patterns of recent sea ice cover across the Bering, Chukchi, and Beaufort seas of the Pacific Arctic Region. *Progress in Oceanography* 136, 32-49.

Friesen, T.M., Finkelstein, S.A., Medeiros, A.S., 2020. Climate variability of the Common Era (AD 1–2000) in the eastern North American Arctic: Impacts on human migrations. *Quaternary International* 549, 142-154Fritz, M., Vonk, J.E., Lantuit, H., 2017. Collapsing Arctic coastlines. *Nature Climate Change* 7, 6-7.

Fritz, M., Herzschuh, U., Wetterich, S., Lantuit, H., De Pascale, G.P., Pollard, W.H., Schirrmeister, L., 2012. Late glacial and Holocene sedimentation, vegetation, and climate history from easternmost Beringia (northern Yukon Territory, Canada). *Quaternary Research* 78, 549-560. DOI:10.1016/j.yqres.2012.07.007

Gemery, L., Cronin, T.M., Briggs, W.M., Brouwers, E.M., Schornikov, E.I., Stepanova, A., Wood, A.M., Yasuhara, M., 2017. An Arctic and Subarctic ostracod database: biogeographic and paleoceanographic applications. *Hydrobiologia* 786, 59-95.

Gemery, L., Cronin, T.M., Cooper, L.W., Dowsett, H.J., Grebmeier, J.M., 2021. Biogeography and ecology of Ostracoda in the US northern Bering, Chukchi, and Beaufort Seas. *Plos one* 16, DOI: 10.1371/journal.pone.0251164.

Gemery, L., Cronin, T.M., Cooper, L.W., Roberts, L.R., Keigwin, L.D., Addison, J.A., Leng, M.J., Lin, P., Magen, C., Marot, M.E., Schwartz, V., 2023. Multi-proxy record of ocean-climate variability during the last two millennia on the Mackenzie Shelf, Beaufort Sea. *Micropaleontology* 69, 345-366.

Grebmeier, J.M., Cooper, L.W., Feder, H.M., Sirenko, B.I., 2006. Ecosystem dynamics of the Pacific-influenced northern Bering and Chukchi Seas in the Amerasian Arctic. *Progress in Oceanography* 71, 331-361.

Grebmeier, J., Barry, J., 2007. Benthic processes in polynyas. *Elsevier Oceanography Series* 74, 363-390.

Grotheer, H., Meyer, V., Riedel, T., Pfalz, G., Mathieu, L., Hefter, J., Gentz, T., Lantuit, H., Mollenhauer, G., Fritz, M., 2020. Burial and origin of permafrost-derived carbon in the nearshore zone of the southern Canadian Beaufort Sea. *Geophysical Research Letters* 47, DOI: 10.1029/2019GL085897.

Guilbault, J.-P., Barrie, J.V., Conway, K., Lapointe, M., Radi, T., 2003. Paleoenvironments of the Strait of Georgia, British Columbia during the last deglaciation: microfaunal and microfloral evidence. *Quaternary Science Reviews* 22, 839-857.

Günther, F., Overduin, P. P., Yakshina, I. A., Opel, T., Baranskaya, A. V., Grigoriev, M. N., 2015. Observing Muostakh disappear: permafrost thaw subsidence and erosion of a ground-ice-rich island in response to arctic summer warming and sea ice reduction. *The Cryosphere*, 9, 151-178.

Hald, M., Korsun, S., 1997. Distribution of modern benthic foraminifera from fjords of Svalbard, European Arctic. *Journal of Foraminiferal Research* 27, 101-122.

Heaton, T.J., Köhler, P., Butzin, M., Bard, E., Reimer, R.W., Austin, W.E., Ramsey, C.B., Grootes, P.M., Hughen, K.A., Kromer, B., 2020. Marine20—the marine radiocarbon age calibration curve (0–55,000 cal BP). *Radiocarbon* 62, 779-820.

Husum, K., Hald, M., Stein, R., Weißschnur, M., 2015. Recent benthic foraminifera in the Arctic Ocean and Kara Sea continental margin. *Arktos* 1, 5.

Hut, G., 1987. Consultants' group meeting on stable isotope reference samples for geochemical and hydrological investigations, IAEA, Vienna 16-18 September 1985 : Report to the Director General, 42 pp.

Jennings, A.E., Helgadóttir, G., 1994. Foraminiferal assemblages from the fjords and shelf of eastern Greenland. *Journal of Foraminiferal Research* 24, 123-144.

Jennings, A., Andrews, J., Reilly, B., Walczak, M., Jakobsson, M., Mix, A., Stoner, J., Nicholls, K.W., Cheseby, M., 2020. Modern foraminiferal assemblages in northern Nares Strait, Petermann Fjord, and beneath Petermann ice tongue, NW Greenland. *Arctic, Antarctic, and Alpine Research* 52, 491-511.

Jernas, P., Klitgaard-Kristensen, D., Husum, K., Koç, N., Tverberg, V., Loubere, P., Prins, M., Dijkstra, N., Gluchowska, M., 2018. Annual changes in Arctic fjord environment and modern benthic foraminiferal fauna: Evidence from Kongsfjorden, Svalbard. *Global and planetary change* 163, 119-140.

Jones, B.M., Arp, C.D., Jorgenson, M.T., Hinkel, K.M., Schmutz, J.A., Flint, P.L., 2009. Increase in the rate and uniformity of coastline erosion in Arctic Alaska. *Geophysical Research Letters* 36, DOI: 10.1029/2008GL036205.

Jong, D., Bröder, L., Tanski, G., Fritz, M., Lantuit, H., Tesi, T., Haghipour, N., Eglinton, T.I., Vonk, J.E., 2020. Nearshore zone dynamics determine pathway of organic carbon from eroding permafrost coasts. *Geophysical research letters* 47, DOI: 10.1029/2020GL088561.

Juhls, B., 2021. Land-Ocean Interactions in Arctic Coastal Waters: Ocean Colour Remote Sensing and Current Carbon Fluxes to the Arctic Ocean. Freie Universität Berlin. 165 pp. <https://refubium.fu-berlin.de/handle/fub188/29262>

Khusid, T.A., Korsum, S.A., 1996, Modern benthic foraminiferal assemblages in the Kara Sea. In: Stein, R., et al. (Eds.), *Surface-sediment Composition and Sedimentary Processes in the Central Arctic Ocean and Along the Eurasian Continental Margin: Berichte zur Polarforschung* 112, Bremerhaven, Alfred Wegener Institute, pp. 96-118.

Kinnard, C., Zdanowicz, C.M., Fisher, D.A., Isaksson, E., de Vernal, A., Thompson, L.G., 2011. Reconstructed changes in Arctic sea ice over the past 1,450 years. *Nature* 479, 509-512.

Klein, K.P., Lantuit, H., Heim, B., Fell, F., Doxaran, D., Irrgang, A.M., 2019. Long-term high-resolution sediment and sea surface temperature spatial patterns in Arctic nearshore

waters retrieved using 30-year landsat archive imagery. *Remote Sensing* 11, DOI: 10.3390/rs11232791.

Knudsen, K.L., Stabell, B., Seidankrantz, M.S., Eiriksson, J., Blake Jr, W., 2008. Deglacial and Holocene conditions in northernmost Baffin Bay: sediments, foraminifera, diatoms and stable isotopes. *Boreas* 37, 346-376

Korsun, S., Hald, M., 2000. Seasonal dynamics of benthic foraminifera in a glacially fed fjord of Svalbard, European Arctic. *Journal of Foraminiferal Research* 30, 251-271.

Kutos, O., Rochon, A., Montero-Serrano, J.C., 2021. Evolution of palaeo-sea-surface conditions and sediment dynamics over the last 2700 years on the Mackenzie Slope, Beaufort Sea (Canadian Arctic). *Boreas* 50, 893-914.

Kuzyk, Z.Z.A., Gobeil, C., Macdonald, R.W., 2013. ^{210}Pb and ^{137}Cs in margin sediments of the Arctic Ocean: controls on boundary scavenging. *Glob. Biogeochem. Cycles* 27, 422-439.

Lapointe, F., Francus, P., Lamoureux, S.F., Vuille, M., Jenny, J.-P., Bradley, R.S., Massa, C., 2017. Influence of North Pacific decadal variability on the western Canadian Arctic over the past 700 years. *Climate of the Past* 13, 411-420.

Lin, P., Pickart, R.S., Fissel, D., Ross, E., Kasper, J., Bahr, F., Torres, D.J., O'Brien, J., Borg, K., Melling, H., 2020. Circulation in the vicinity of Mackenzie Canyon from a year-long mooring array. *Progress in Oceanography* 187, DOI: 10.1016/j.pocean.2020.102396.

Luoto, T.P., Nevalainen, L., Kubischarta, F., Kultti, S., Knudsen, K.L., Salonen, V.P., 2011. Late quaternary ecological turnover in high arctic Lake Einstaken, Nordaustlandet, Svalbard (80 N). *Geografiska Annaler: Series A, Physical Geography* 93, 337-354.

MacDonald, G.M., Case, R.A., 2005. Variations in the Pacific Decadal Oscillation over the past millennium. *Geophysical Research Letters* 32, DOI: 10.1029/2005GL022478.

Mackensen, A., 2008. On the use of benthic foraminiferal $\delta^{13}\text{C}$ in palaeoceanography: constraints from primary proxy relationships. *Geological Society, London, Special Publications* 303, 121-133.

Madsen, H.B., Knudsen, K.L., 1994. Recent foraminifera in shelf sediments of the Scoresby Sund fjord, East Greenland. *Boreas* 23, 495-504.

Mäkelä, A., Witte, U., Archambault, P., 2018. Short-term processing of ice algal-and phytoplankton-derived carbon by Arctic benthic communities revealed through isotope labelling experiments. *Marine Ecology Progress Series* 600, 21-39.

Mann, M.E., Zhang, Z., Rutherford, S., Bradley, R.S., Hughes, M.K., Shindell, D., Ammann, C., Faluvegi, G., Ni, F., 2009. Global signatures and dynamical origins of the Little Ice Age and Medieval Climate Anomaly. *Science* 326, 1256-1260

Mantua, N.J., Hare, S.R., 2002. The Pacific decadal oscillation. *Journal of Oceanography* 58, 35-44.

McCorkle, D.C., Keigwin, L.D., Corliss, B.H., Emerson, S.R., 1990. The influence of microhabitats on the carbon isotopic composition of deep-sea benthic foraminifera. *Paleoceanography* 5, 161-185.

McDougall, K. A., Brouwers, E. M., Smith, P., 1986, Micropaleontology and sedimentology of the PB borehole series, Prudhoe Bay, Alaska: U.S. Geological Survey Bulletin 1598, 62 pp., DOI: 10.3133/b1598.

McNeely, R., Dyke, A., Southon, J., 2006. Canadian marine reservoir ages: preliminary data assessment. *Geological Survey of Canada (Open File 5049)*, 3 pp.

Meunier, A., 1919. Mikroplankton de la mer Flamande. III. Les Péridiniens: Mémoires du Musée Royal d'Histoire Naturelle de Belgique 8, 1-116.

Meyer, H., Schönicke, L., Wand, U., Hubberten, H. W., Friedrichsen, H., 2000. Isotope studies of hydrogen and oxygen in ground-ice experiences with the equilibration technique. *Environmental and Health Studies* 36, 133–149, DOI: 10.1080/10256010008032939.

Mioduszewski, J., Vavrus, S., Wang, M., 2018. Diminishing Arctic sea ice promotes stronger surface winds. *Journal of Climate* 31, 8101-8119.

Mulligan, R.P., Perrie, W., Solomon, S., 2010. Dynamics of the Mackenzie River plume on the inner Beaufort shelf during an open water period in summer. *Estuarine, Coastal and Shelf Science* 89, 214-220.

Mulligan, R.P., Perrie, W., 2019. Circulation and structure of the Mackenzie River plume in the coastal Arctic Ocean. *Continental Shelf Research* 177, 59-68.

Murray, J.W., 1991. *Ecology and Palaeoecology of Benthic Foraminifera*. Longman, Harlow, p. 397.

Murray, J.W., 2006. *Ecology and applications of benthic foraminifera*. Cambridge University Press, 440 pp.

Nadaï, G., Nöthig, E.-M., Fortier, L., Lalande, C., 2021. Early snowmelt and sea ice breakup enhance algal export in the Beaufort Sea. *Progress in Oceanography* 190, DOI: 10.1016/j.pocean.2020.102479.

Nicolle, M., Debret, M., Massei, N., Colin, C., de Vernal, A., Divine, D., Werner, J.P., Hormes, A., Korhola, A., Linderholm, H.W., 2018. Climate variability in the subarctic area for the last 2 millennia. *Climate of the Past* 14, 101-116.

Notz, D., Stroeve, J., 2016. Observed Arctic sea-ice loss directly follows anthropogenic CO₂ emission. *Science* 354, 747-750.

Obu, J., Lantuit, H., Fritz, M., Pollard, W. H., Sachs, T., Günther, F., 2016. Relation between planimetric and volumetric measurements of permafrost coast erosion: a case study from Herschel Island, western Canadian Arctic. *Polar Research* 35, DOI: 10.3402/polar.v35.30313.

Oksanen, J., Blanchet, F.G., Kindt, R., Legendre, P., Minchin, P.R., O'hara, R., Simpson, G.L., Solymos, P., Stevens, M.H.H., Wagner, H., 2013. Package 'vegan'. Community ecology package, version 2, 1-295.

Olausson, E., 1982, The Pleistocene/Holocene boundary in south-western Sweden: Sveriges Geologiska Undersökning. Ser. C, v. 794, 288 p.

Overeem, I., Anderson, R.S., Wobus, C.W., Clow, G.D., Urban, F.E., Matell, N., 2011. Sea ice loss enhances wave action at the Arctic coast. *Geophysical Research Letters* 38, DOI: 10.1029/2011GL048681.

Paranjape, M.A., 1987. The seasonal cycles and vertical distribution of tintinnines in Bedford Basin, Nova Scotia, Canada. *Canadian Journal of Zoology* 65, 41-48.

Patterson, R.T., Guilbault, J.-P., Thomson, R.E., 2000. Oxygen level control on foraminiferal distribution in Effingham Inlet, Vancouver Island, British Columbia, Canada. *Journal of Foraminiferal Research* 30, 321-335.

Pearce, C., Varhelyi, A., Wastegård, S., Muschitiello, F., Barrientos, N., O'Regan, M., Cronin, T.M., Gemery, L., Semiletov, I., Backman, J., 2017. The 3.6 ka Aniakchak tephra in the Arctic Ocean: a constraint on the Holocene radiocarbon reservoir age in the Chukchi Sea. *Climate of the Past* 13, 303-316.

Pfälz, G., 2017. Lateral transport of sediment and organic matter, derived from coastal erosion, into the nearshore zone of the southern Beaufort Sea, Canada. Technische Universität Dresden, 86 pp., <https://epic.awi.de/id/eprint/44364/>

Pickart, R.S., 2004. Shelfbreak circulation in the Alaskan Beaufort Sea: Mean structure and variability. *Journal of Geophysical Research: Oceans* 109, DOI: 10.1029/2003JC001912.

Pickart, R.S., Spall, M.A., Moore, G.W., Weingartner, T.J., Woodgate, R.A., Aagaard, K., Shimada, K., 2011. Upwelling in the Alaskan Beaufort Sea: Atmospheric forcing and local versus non-local response. *Progress in Oceanography* 88, 78-100.

Pickart, R.S., Spall, M.A., Mathis, J.T., 2013. Dynamics of upwelling in the Alaskan Beaufort Sea and associated shelf–basin fluxes. *Deep Sea Research Part I: Oceanographic Research Papers* 76, 35-51

Polyak, L., Korsun, S., Febo, L.A., Stanovoy, V., Khusid, T., Hald, M., Paulsen, B.E., Lubinski, D.J., 2002. Benthic foraminiferal assemblages from the southern Kara Sea, a river-influenced Arctic marine environment. *Journal of Foraminiferal Research* 32, 252-273.

Polyak, L., Stanovoy, V., Lubinski, D.J., 2003. Stable isotopes in benthic foraminiferal calcite from a river-influenced Arctic marine environment, Kara and Pechora Seas. *Paleoceanography* 18, DOI: 10.1029/2001PA000752.

Porter, T.J., Pisaric, M.F., Kokelj, S.V., 2013. A ring-width-based reconstruction of June–July minimum temperatures since AD 1245 from white spruce stands in the Mackenzie Delta region, northwestern Canada. *Quaternary Research* 80, 167-179.

R Core Team, 2021. R: A language and environment for statistical computing. R Foundation for Statistical Computing, Vienna, Austria. URL <https://www.R-project.org/>.

Radosavljevic, B., Lantuit, H., Pollard, W., Overduin, P., Couture, N., Sachs, T., Helm, V., Fritz, M., 2016. Erosion and flooding—threats to coastal infrastructure in the Arctic: a case study from Herschel Island, Yukon Territory, Canada. *Estuaries and Coasts* 39, 900-915.

Rainville, L., Woodgate, R.A., 2009. Observations of internal wave generation in the seasonally ice-free Arctic. *Geophysical Research Letters* 36, DOI: 10.1029/2009GL041291.

Richerol, T., Rochon, A., Blasco, S., Scott, D.B., Schell, T.M., Bennett, R.J., 2008. Evolution of paleo sea-surface conditions over the last 600 years in the Mackenzie Trough, Beaufort Sea (Canada). *Marine Micropaleontology* 68, 6-20.

Rigor, I.G., Wallace, J.M., Colony, R.L., 2002. Response of sea ice to the Arctic Oscillation. *Journal of Climate* 15, 2648-2663.

Rogers, G., Roff, J., Lynn, D., 1981. Tintinnids of Chesterfield Inlet, Northwest Territories. *Canadian Journal of Zoology* 59, 2360-2364.

Rühland, K., Priesnitz, A., Smol, J.P., 2003. Paleolimnological evidence from diatoms for recent environmental changes in 50 lakes across Canadian Arctic treeline. *Arctic, Antarctic, and Alpine Research* 35, 110-123.

Rytter, F., Knudsen, K.L., Seidenkrantz, M.-S., Eiríksson, J., 2002. Modern distribution of benthic foraminifera on the North Icelandic shelf and slope. *J. Foraminifer. Res.* 32, 217-244.

Sanchez-Cabeza, J., Ruiz-Fernández, A., 2012. ^{210}Pb sediment radiochronology: an integrated formulation and classification of dating models. *Geochimica et Cosmochimica Acta* 82, 183-200.

Schell, T.M., Scott, D.B., Rochon, A., Blasco, S., 2008. Late Quaternary paleoceanography and paleo-sea ice conditions in the Mackenzie Trough and Canyon, Beaufort Sea. *Canadian Journal of Earth Sciences* 45, 1399-1415.

Schlitzer, R., 2018. Ocean Data View, Alfred Wegener Institute, <https://odv.awi.de>.

Schulze, L.M., Pickart, R.S., 2012. Seasonal variation of upwelling in the Alaskan Beaufort Sea: Impact of sea ice cover. *Journal of Geophysical Research: Oceans* 117, DOI: 10.1029/2012JC007985.

Scott, D.B., Schell, T., Rochon, A., Blasco, S., 2008a. Modern benthic foraminifera in the surface sediments of the Beaufort Shelf, Slope and Mackenzie Trough, Beaufort Sea, Canada: Taxonomy and summary of surficial distributions. *Journal of Foraminiferal Research* 38, 228-250.

Scott, D.B., Schell, T., Rochon, A., Blasco, S., 2008b. Benthic foraminifera in the surface sediments of the Beaufort Shelf and slope, Beaufort Sea, Canada: Applications and implications for past sea-ice conditions. *Journal of Marine Systems* 74, 840-863

Scott, D.B., Schell, T., St-Onge, G., Rochon, A., Blasco, S., 2009. Foraminiferal assemblage changes over the last 15,000 years on the Mackenzie-Beaufort Sea Slope and Amundsen Gulf, Canada: Implications for past sea ice conditions. *Paleoceanography* 24, DOI: 10.1029/2007PA001575.

Screen, J.A., Francis, J.A., 2016. Contribution of sea-ice loss to Arctic amplification is regulated by Pacific Ocean decadal variability. *Nature Climate Change* 6, 856-860.

Seidenkrantz, M.-S., 2013. Benthic foraminifera as palaeo sea-ice indicators in the subarctic realm—examples from the Labrador Sea–Baffin Bay region. *Quaternary Science Reviews* 79, 135-144.

Seidenkrantz, M.-S., Kuijpers, A., Aagaard-Sørensen, S., Lindgreen, H., Olsen, J., Pearce, C., 2021. Evidence for influx of Atlantic water masses to the Labrador Sea during the Last Glacial Maximum. *Scientific reports* 11, 1-14.

Seidenstein, J.L., Cronin, T.M., Gemery, L., Keigwin, L.D., Pearce, C., Jakobsson, M., Coxall, H.K., Wei, E.A., Driscoll, N.W., 2018. Late Holocene paleoceanography in the Chukchi and Beaufort Seas, Arctic Ocean, based on benthic foraminifera and ostracods. *Arktos* 4, DOI: 10.1007/s41063-018-0058-7.

Shackleton, N., 1974. Attainment of isotopic equilibrium between ocean water and the benthonic foraminifera genus *Uvigerina*: isotopic changes in the ocean during the last glacial. *Colloques Internationaux du C.N.R.S.* 219, 203-209.

Shannon, C.E., 1948. A mathematical theory of communication. *The Bell System Technical Journal* 27, 379-423.

Souto, S., 1973. Contribución al conocimiento de los tintínnidos de agua dulce de la República Argentina. I Río de la Plata y Delta del Paraná. *Physis* 32, 249-254.

Spreen, G., Kwok, R., Menemenlis, D., 2011. Trends in Arctic sea ice drift and role of wind forcing: 1992–2009. *Geophysical Research Letters* 38, DOI: 10.1029/2011GL048970.

Stepanova, A., Taldenkova, E., Bauch, H.A., 2003. Recent Ostracoda from the Laptev Sea (Arctic Siberia): species assemblages and some environmental relationships. *Marine Micropaleontology* 48, 23-48.

Stepanova, A., Taldenkova, E., Simstich, J., Bauch, H.A., 2007. Comparison study of the modern ostracod associations in the Kara and Laptev seas: Ecological aspects. *Marine Micropaleontology* 63, 111-142.

Stepanova, A., Obrochta, S., Quintana Krupinski, N. B., Hyttinen, O., Kotilainen, A., and Andrén, T., 2019, Late Weichselian to Holocene history of the Baltic Sea as reflected in ostracod assemblages: *Boreas*, v. 48, p. 761–778.

Stuiver, M., Reimer, P.J., 1993. Extended ^{14}C data base and revised CALIB 3.0 ^{14}C age calibration program. *Radiocarbon* 35, 215-230.

Thompson, D.W., Wallace, J.M., 1998. The Arctic Oscillation signature in the wintertime geopotential height and temperature fields. *Geophysical research letters* 25, 1297-1300.

Tian, S. Y., Yasuhara, M., Hong, Y., Huang, H.-H. M., Iwatani, H., Chiu, W.-T. R., Mamo, B., Okahashi, H., and Rasmussen, T. L., 2020, Deglacial–Holocene Svalbard paleoceanography and evidence of meltwater pulse 1B: *Quaternary Science Reviews*, v. 233, DOI: 10.1016/j.quascirev.2020.106237.

Tremblay, J.-É., Bélanger, S., Barber, D., Asplin, M., Martin, J., Darnis, G., Fortier, L., Gratton, Y., Link, H., Archambault, P., 2011. Climate forcing multiplies biological productivity

in the coastal Arctic Ocean. *Geophysical Research Letters* 38, DOI: 10.1029/2011GL048825.

Tremblay, J.-É., Robert, D., Varela, D.E., Lovejoy, C., Darnis, G., Nelson, R.J., Sastri, A.R., 2012. Current state and trends in Canadian Arctic marine ecosystems: I. Primary production. *Climatic Change* 115, 161-178.

Ullrich, A.D., Cowan, E.A., Zellers, S.D., Jaeger, J.M., Powell, R.D., 2009. Intra-annual variability in benthic foraminiferal abundance in sediments of Disenchantment Bay, an Alaskan glacial fjord. *Arctic, Antarctic, and Alpine Research* 41, 257-271.

Usher, P.J., 2002. Inuvialuit use of the Beaufort Sea and its resources, 1960-2000. *Arctic*, 18-28.

Viau, A.E., Gajewski, K., 2009. Reconstructing millennial-scale, regional paleoclimates of boreal Canada during the Holocene. *Journal of Climate* 22, 316-330.

Voltski, I., Korsun, S., Pillet, L., Pawlowski, J., 2015. *Protoelphidium niveum* and the taxonomy of "lower" elphidiids. *Journal of Foraminiferal Research* 45, 250-263.

Williams, B., Carmack, E., 2012. Ocean water and sea ice. In: Burn, C.R. (Ed.), *Herschel Island Qikiqtaryuk: A Natural and Cultural History of Yukon's Arctic Island*. University of Calgary Press, Calgary, pp. 54-59.

Wollenburg, J.E., Mackensen, A., 1998. Living benthic foraminifera from the central Arctic Ocean: faunal composition, standing stock and diversity. *Marine Micropaleontology* 34, 153-185.

Wollenburg, J.E., Kuhnt, W., 2000. The response of benthic foraminifera to carbon flux and primary production in the Arctic Ocean. *Marine Micropaleontology* 40, 189-231.

Wolter, J., Lantuit, H., Herzschuh, U., Stettner, S., Fritz, M., 2017. Tundra vegetation stability versus lake-basin variability on the Yukon Coastal Plain (NW Canada) during the past three centuries. *The Holocene* 27, 1846-1858.

Wood, K.R., Bond, N.A., Danielson, S.L., Overland, J.E., Salo, S.A., Stabeno, P.J., Whitefield, J., 2015. A decade of environmental change in the Pacific Arctic region. *Progress in Oceanography* 136, 12-31.

Zhang, M., Perrie, W., Long, Z., 2019. Springtime North Pacific Oscillation and summer sea ice in the Beaufort sea. *Climate Dynamics* 53, 671-686.

3.9 Supplementary material

3.9.1 Appendix 3-A.1 – Interpretations of $^{210}\text{Pb}_{\text{tot}}$, ^{226}Ra , ^{137}Cs activity profiles of cores PG2303 and PG2303-1

Sedimentological and micropaleontological data of cores PG2303 and PG2303-1 do not overlap, as illustrated by distinct grain size and tintinnid concentrations in PG2303-1 vs. PG2303 core top (Fig. 3). The hiatus is also illustrated by the higher $^{210}\text{Pb}_{\text{tot}}$ content of core PG2303-1 (Fig. S2a). However, the inventory of ^{137}Cs of $\sim 4.98 \text{ dpm cm}^{-2}$ in core PG2303 is close to the maximum ^{137}Cs fallout recorded in Arctic Ocean sediments of about 5.7 dpm cm^{-2} up to 2007 CE (Kuzyk et al., 2013). Thus, only a limited amount of surface sediment could have been lost in the coring of PG2303 and the age gap between the two cores is probably small.

The age model developed for the short gravity core PG2303-1 (Falardeau et al., 2023) suggests that it covers the interval of $1999 \pm 6 \text{ CE}$ (at 19 cm) to 2016 CE (year of collection). In consequence, the age of the surface sediment in core PG2303 should not exceed $1999 \pm 6 \text{ CE}$.

In the long core PG2303, the ^{137}Cs activity of the 48–13 cm interval varies between 0.05 ± 0.01 and $0.19 \pm 0.01 \text{ dpm g}^{-1}$ (Fig. S2a; Table S5). It falls to ~ 0 , within error bars, in the 14.5–9.5 cm interval, which can reasonably be associated with the drop in atmospheric ^{137}Cs fallout after 1980 CE (Kuzyk et al., 2013). Above 9.5 cm, samples were not available for gamma counting. Consequently, the 1986 CE Chernobyl peak could not be identified, although it is recorded in sedimentary archives of the area (Carnero-Bravo et al., 2021, Falardeau et al., 2023). Within these constraints, we hypothesize an age of about 1983 CE between 9.5 and 14.5 cm ($12 \pm 3 \text{ cm}$) for PG2303. The presence of ^{137}Cs activity in core PG2303-1 (Fig. S2a) probably reflects the tail of the Chernobyl peak followed by the Fukushima event, whose associated ^{137}Cs peak penetrated the Arctic Ocean around 2014 CE (Kumamoto et al., 2017).

The $^{210}\text{Pb}_{\text{tot}}$ activity in core PG2303 decreases from a maximum of $3.0 \pm 0.2 \text{ dpm g}^{-1}$ at 15–14 cm to a relatively steady value of $1.72 \pm 0.11 \text{ dpm g}^{-1}$ below 47.5 cm (Fig. S2a), while the parent isotope ^{226}Ra has a mean activity of $2.16 \pm 0.26 \text{ dpm g}^{-1}$ throughout core PG2303. The large uncertainty for ^{226}Ra in the top two samples is due to poor counting statistics for the small samples available. In contrast, core PG2303-1 yielded a statistically distinct ^{226}Ra activity of 1.78 ± 0.04 at ± 1 standard deviation, but not necessarily distinct at 2 standard deviations, although some ^{226}Ra loss towards the sediment/water interface in PG2303-1 cannot be ruled out when compared with PG2303 (e.g., Not et al., 2008). Nonetheless, whatever

the effective ^{226}Ra activity in the sediment (mean activity of $2.05 \pm 0.27 \text{ dpm g}^{-1}$ for both cores), it is difficult to calculate $^{210}\text{Pb}_{\text{ex}}$ values using the activity of its parent ^{226}Ra as an estimate of the supported ^{210}Pb fraction. Some loss of the intermediate gaseous ^{222}Rn isotope could perhaps explain the unbalance in the ^{226}Ra - $^{210}\text{Pb}_{\text{tot}}$ radioactive series. We thus retained the ^{210}Pb activity of $1.72 \pm 0.11 \text{ dpm g}^{-1}$ near core bottom as the best estimate of the supported ^{210}Pb fraction. The decay of the excess in ^{210}Pb in the core, within error bars of the $^{210}\text{Pb}_{\text{tot}}\text{-}^{210}\text{Pb}_{\text{sup}}$ estimate ($\pm 0.16 \text{ dpm g}^{-1}$; Table S5) is reached between 44.5 cm and 47.5 cm downcore. Assigning a time span of ~ 110 years (i.e., ~ 5 half-lives of ^{210}Pb) for the decay of $^{210}\text{Pb}_{\text{ex}}$ (~ 5 half-lives), an age of ~ 1906 CE could be assigned to this depth. Using the anchor ages of 1983 CE at the depth of 12 ± 3 cm, as estimated above, and of ~ 1906 CE at 46 ± 2 cm, a sedimentation rate of about $0.44 \pm 0.06 \text{ cm a}^{-1}$ can be proposed for the $\sim 46\text{-}12$ cm interval. This estimated sedimentation rate would encompass the calculated sedimentation rate from the linear trend of the $^{210}\text{Pb}_{\text{ex}}$ natural logarithm using a $^{210}\text{Pb}_{\text{sup}}$ of 1.72 dpm g^{-1} (0.41 cm a^{-1} ; Fig. S2b), which consolidate that it most probably respects the mean sedimentation rate in the top tens of centimeters of core PG2303. Extrapolating this sedimentation rate to the core surface from the 1906 CE anchor would lead to a proposed age of 2010 ± 20 CE. As we estimated that the core top age of PG2303 could not exceed 1999 ± 6 CE, based on the offset between cores PG2303-1 and PG2303 and the above assumptions, a final “best estimate” of the age of core PG2303 top would be between 1990 and 2005 CE.

In core PG2303, the measurable ^{137}Cs activities down to 48 cm are not compatible with the above chronology as the nuclear fallout of ^{137}Cs in the atmosphere started in 1945 CE (Aoyama et al., 2006). Moreover, the ^{137}Cs distribution in the core does not show any clear peaking activity and rather depicts a relatively smooth profile. Some diffusion of ^{137}Cs seems thus likely (cf. Ali et al., 2008). As one cannot discard such a diffusion upwards, the anchor age of 1983 CE at the depth of 12 ± 3 cm retained above, remains open to question. Nevertheless, we assume that the effective age of the core top should not depart much from the 1990-2005 CE estimate and so is the mean sedimentation rate of $0.44 \pm 0.06 \text{ cm a}^{-1}$ between ~ 46 and 12 cm.

To conclude, the following estimated ages: 1990-2005 CE at 0 cm and 1906 CE at 46 ± 2 cm, were retained and fed into the *OxCal* program to constrain the age model at the top of the PG2303 core. Since the *OxCal* program does not accept errors on the core depth, we translated the ± 2 cm error of 1906 CE at 46 ± 2 cm into 1906 ± 5 years at 46 cm based on the mean sedimentation rate of $0.44 \pm 0.06 \text{ cm a}^{-1}$.

Figure 3-A.1 Photograph of PG2303 core sampling in April 2016 during the Yukon Coast spring expedition led by the Alfred Wegener Institute in Potsdam. Photo credit: Michael Fritz

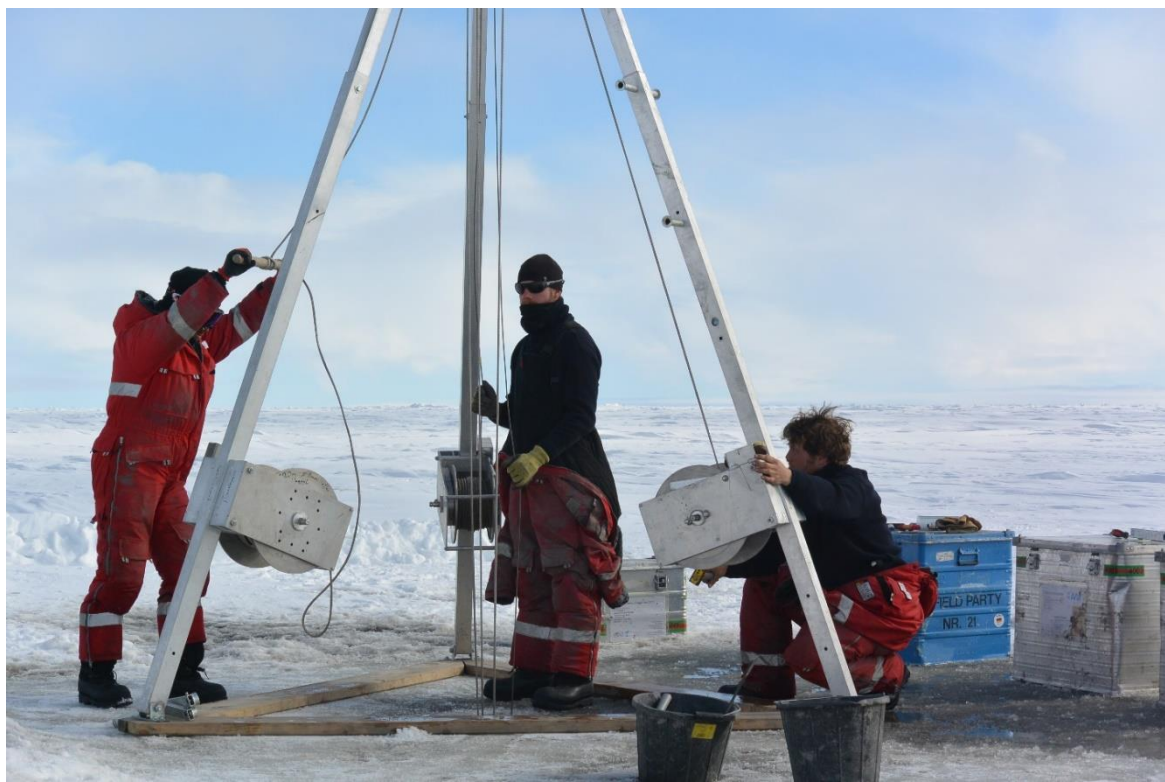


Figure 3-A.2 $^{210}\text{Pb}_{\text{tot}}$, ^{226}Ra , and ^{137}Cs of cores PG2303 and PG2303-1 activity profiles. The red vertical dotted lines indicate the mean of the measured ^{226}Ra in both cores, separately, with their respective error represented at the top and bottom of the dotted line. b) The natural logarithm of the $^{210}\text{Pb}_{\text{ex}}$ natural logarithm using a $^{210}\text{Pb}_{\text{sup}}$ of 1.72 dpm g $^{-1}$. By dividing the disintegration constant (Sanchez-Cabeza & Ruiz-Fernández, 2012) with the rate of the linear trend between 44.5 cm and 9.5 cm, we obtain a mean sedimentation rate of 0.41 cm a $^{-1}$.

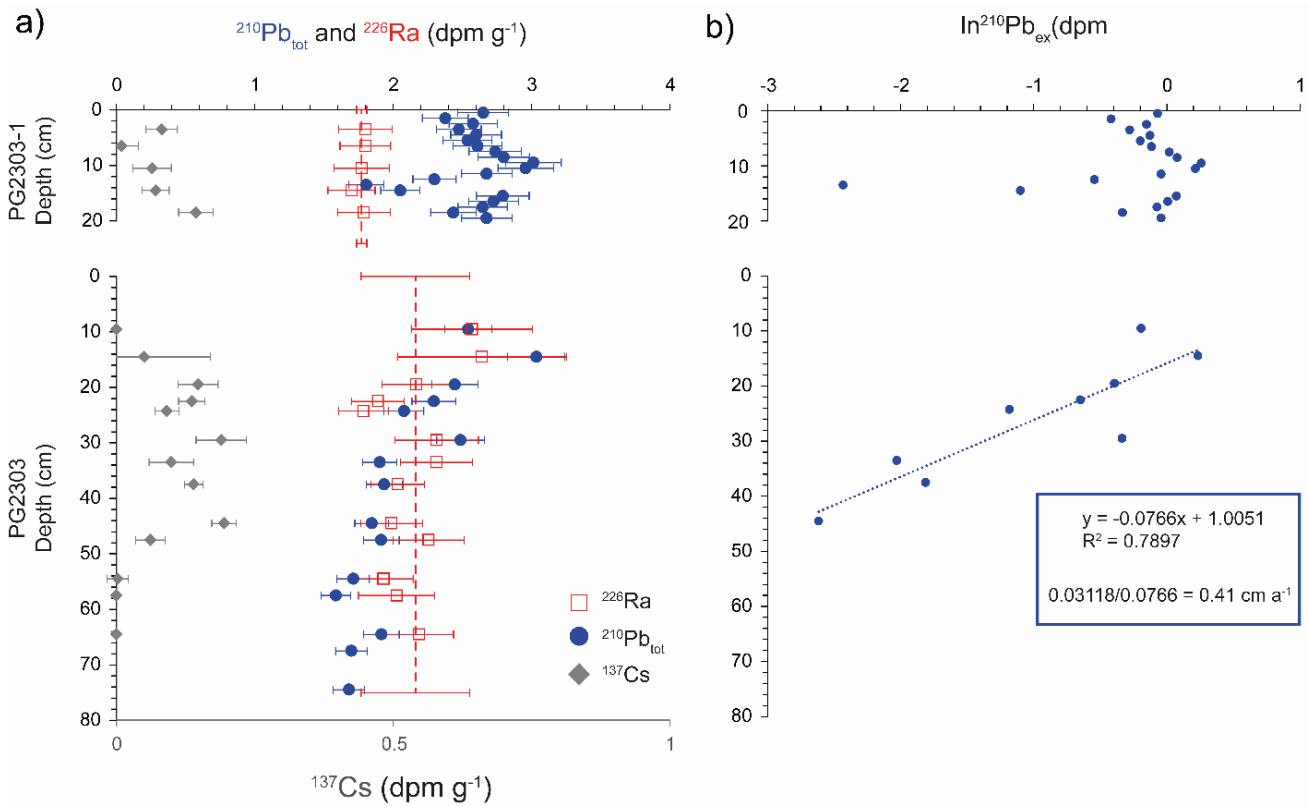


Figure 3-A.3 Assemblages of calcareous benthic foraminifera (black bars) and agglutinated benthic foraminifera (gray bars) calculated separately together with the total benthic foraminifera (calcareous and agglutinated included) concentrations (black line) and fluxes (green line) with its associated errors in dotted green lines as a function of depth (cm).

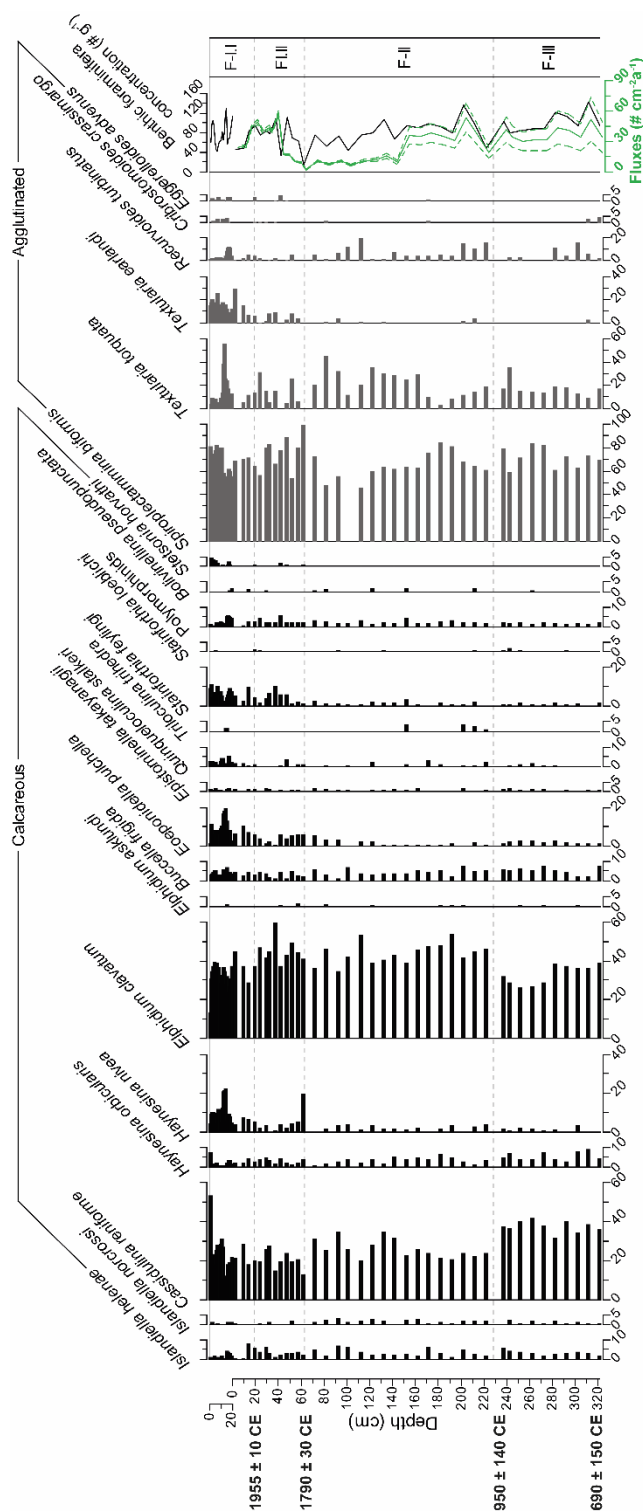
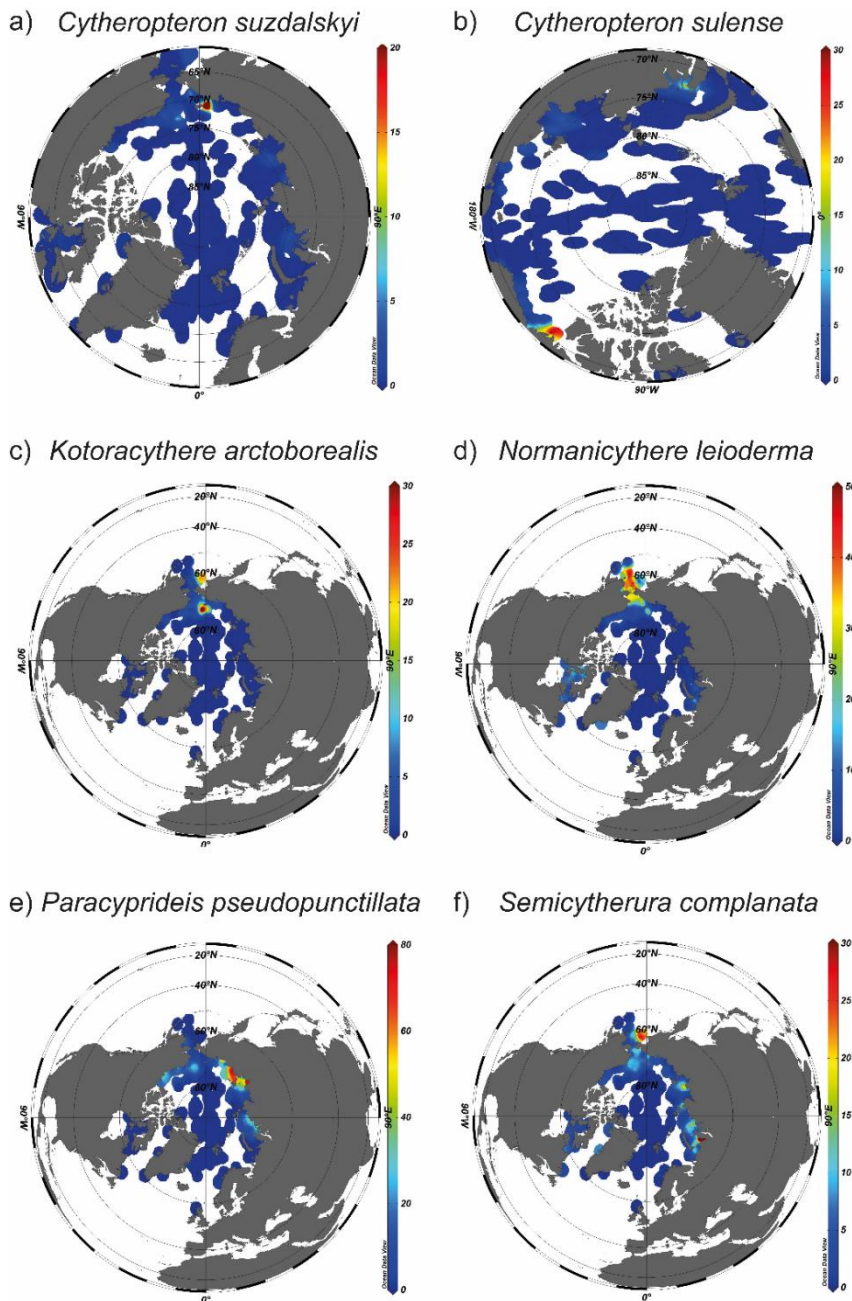


Figure 3-A.4 Distribution maps of selected ostracod taxa relative abundances using the Arctic Ostracode Database 2020 (AOD2020; Cronin et al., 2021). Prior to the relative abundance calculations, we did a preliminary validation of the coordinates using GEBCO 2014 and IBCAO 2012 combined to ensure the points yielded below water level values. 47 points were discarded. Furthermore, we only kept the samples that comprised 10 counted ostracod shells or more to allow a minimum significance of the calculated assemblages. Out of the 1574 points, 1137 were left. The maps were developed using Ocean Data View (Schlitzer, 2018).



3.9.2 References

- Ali, A.A., Ghaleb, B., Garneau, M., Asnong, H., Loisel, J., 2008. Recent peat accumulation rates in minerotrophic peatlands of the Bay James region, Eastern Canada, inferred by ^{210}Pb and ^{137}Cs radiometric techniques. *Applied Radiation and Isotopes* 66, 1350-1358.
- Aoyama, M., Hirose, K., Igarashi, Y., 2006. Re-construction and updating our understanding on the global weapons tests ^{137}Cs fallout. *Journal of Environmental Monitoring* 8, 431-438.
- Carnero-Bravo, V., Falardeau, J., Chassiot, L., Tanski, G., Hillaire-Marcel, C., Ghaleb, B., de Vernal, A., Vonk, J.E., Lantuit, H., Fritz, M., and Preda, M., 2021, Sediment structure and deposition rates in the Yukon coast: PANGAEA, DOI: 10.1594/PANGAEA.937387.
- Cronin, T.M., Gemery, L.J., Briggs, W.M., Brouwers, E.M., Schornikov, E.I., Stepanova, A., Wood, A.M., Yasuhara, M., Siu, S. (2021-01-08). NOAA/WDS Paleoclimatology - Arctic Ostracode Database 2020 (AOD2020). [Data Table]. NOAA National Centers for Environmental Information. DOI:10.25921/grn9-9029. Accessed [2020-11-03].
- Falardeau, J., de Vernal, A., Seidenkrantz, M.-S., Cronin, T.M., Gemery, L., Chassiot, L., Fritz, M., Carnero-Bravo, V., Hillaire-Marcel, C., and Archambault, P., 2023. Microfaunal recording of recent environmental changes in the Herschel basin, western Arctic Ocean. *Journal of Foraminiferal Research* 53, 20-48.
- Kumamoto, Y., Aoyama, M., Hamajima, Y., Nishino, S., Murata, A., Kikuchi, T., 2017. Radiocesium in the western subarctic area of the North Pacific Ocean, Bering Sea, and Arctic Ocean in 2013 and 2014. *Applied Radiation and Isotopes* 126, 88-92.
- Kuzyk, Z.Z. A., Gobeil, C., Macdonald, R.W., 2013. ^{210}Pb and ^{137}Cs in margin sediments of the Arctic Ocean: Controls on boundary scavenging. *Global biogeochemical cycles* 27, 422-439.
- Sanchez-Cabeza, J., and Ruiz-Fernández, A., 2012. ^{210}Pb sediment radiochronology: an integrated formulation and classification of dating models: *Geochimica et Cosmochimica Acta* 82, 183-200.
- Schlitzer, R., 2018. Ocean Data View, Alfred Wegener Institute, <https://odv.awi.de>.

CONCLUSION

4.1 La capacité d'analyse

Les enregistrements paléocénographiques démontrent que la région du sud-est de la mer de Beaufort a enregistré des variations climatiques de relativement grandes amplitudes, marquées par des intervalles de climat plus doux à plus froid, au cours du dernier millénaire (Bringué et Rochon; 2012; Gemery *et al.*, 2023; Kutos *et al.*, 2021; Seidenstein *et al.*, 2018). Les changements climatiques préindustriels sont associés à des changements dans les modes de circulation atmosphérique tels ceux de l'oscillation décennale du Pacifique (Mantua *et al.*, 1997) ou l'oscillation arctique (Thompson et Wallace, 1998). Ces dernières accompagneraient les variations de l'intensité du courant qui transporte les eaux pacifiques vers l'est, l'intensité et la direction du gyre de Beaufort, ainsi que la température de l'air et les précipitations en milieu terrestre, jouant à leur tour un rôle sur l'apport de nutriments, la séquestration/libération d'eau douce et les apports fluviatiles (Bringué et Rochon, 2012; Durantou *et al.*, 2012; Kutos *et al.*, 2021). Le réchauffement atmosphérique causé par l'activité anthropique se démarque dans les enregistrements à partir d'environ 1900 CE (Abram *et al.*, 2016; Bringué et Rochon, 2012; Gemery *et al.*, 2023; Nicolle *et al.*, 2018). Toutefois, peu d'études ont documenté les effets de ces variations environnementales sur la zone littorale, un milieu sous-représenté dans les reconstitutions paléocénographiques à l'échelle de l'Arctique (Heikkilä *et al.*, 2022). Pourtant, il s'agit d'un milieu influencé par l'érosion des côtes, les apports des rivières et les effets des tempêtes et des vagues en zone peu profonde, donc particulièrement sensible vis-à-vis du réchauffement du climat (Fritz *et al.*, 2017; Mulligan et Perrie, 2019; Rainville et Woodgate, 2009). Le plateau continental se distingue aussi par sa propre dynamique de glace de mer. La zone littorale pourrait donc répondre différemment aux changements climatiques régionaux (Richerol *et al.*, 2008). De plus, c'est à proximité des côtes que les activités de chasse et de pêche ont lieu (Fechhelm *et al.*, 2007; Papik *et al.*, 2003). L'étude de la réponse des habitats côtiers à des extrêmes climatiques (p. ex., petit âge glaciaire et réchauffement récent) est donc pertinente dans une perspective de changement climatique pour une gestion appropriée des ressources halieutiques.

De plus, bien que les effets du réchauffement climatique accéléré des dernières décennies sont évidents dans les enregistrements dendrochronologiques (Anchukaitis *et al.*, 2013; Porter *et al.*, 2013) ou autres compilations de données terrestres (Abram *et al.*, 2016; Kinnard *et al.*, 2011; Nicolle *et al.*, 2018), ils restent peu accessibles dans les enregistrements paléocénographiques disponibles (Tableau 0.1; Figure 0.2). Dans ce contexte, l'objectif général de cette thèse était de reconstituer les conditions marines de la zone

littorale du sud-est de la mer de Beaufort, Canada. Les séries temporelles développées devaient couvrir un intervalle suffisamment long et avoir une résolution temporelle d'analyse assez élevée pour permettre de distinguer les effets des changements anthropiques récents de la variabilité naturelle du milieu. Pour répondre à cet objectif, j'ai d'abord (1) développé une approche méthodologique basée sur les assemblages de foraminifères benthiques et d'ostracodes dans des archives sédimentaires du bassin Herschel. Par la suite, j'ai (2) démontré l'utilité de ces microfossiles comme traceurs écologiques et (3) évalué les effets des changements climatiques récents sur l'habitat pour, finalement, (4) les utiliser pour retracer les effets des variations climatiques des 1300 dernières années (voir modèle à la Figure 4.1).

4.2 Les différences entre la marge et le fond du bassin – Carottes HBGC01 et PG2303-1

Le carottage par gravité aux sites PG2303-1 et HBGC01 (Figures 0.3 et 0.4) a permis de prélever du matériel sédimentaire récent caractérisé par des taux élevés d'accumulation du sédiment dans le bassin Herschel. Le modèle d'âge développé pour la carotte HBGC01 à partir des analyses des isotopes radiogéniques, ^{210}Pb et ^{226}Ra , indique que la carotte couvre de 1979 à 2018 CE (Figure 1.4D) avec une vitesse de sédimentation moyenne de $0.8 \text{ cm} \cdot \text{a}^{-1}$. Un modèle d'âge fiable n'a pas pu être développé pour la carotte PG2303-1. Toutefois, la comparaison des inventaires de ^{210}Pb entre les deux carottes, a permis de confirmer que la carotte PG2303-1 renferme du sédiment récent, probablement accumulé après 2000 CE (Figure 1.15B). Pour ce qui est de la carotte longue par piston, le modèle d'âge développé à partir de quatre mesures ^{14}C a une marge d'erreur assez grande entre ~710 CE et 1800 CE (Figure 3.2), mais elle se resserre vers la surface, grâce à des informations supplémentaires provenant de mesures du ^{210}Pb .

La fraction $> 63 \mu\text{m}$ du sédiment des carottes contient principalement des foraminifères benthiques, des ostracodes et des tintinnides. Les foraminifères benthiques et les ostracodes illustrent une diversité taxonomique élevée avec 26 et 15 espèces recensées, respectivement, et des concentrations moyennes de 70 tests g^{-1} et 2 valves g^{-1} de sédiment. Ces microfossiles sont bien préservés dans le sédiment. Toutefois, les dénombrements d'ostracodes sont en général faibles et ne sont pas considérés comme significatifs lorsqu'ils sont inférieurs à 10 valves par échantillon (p. ex., Figure 3.7). Plus de matériel aurait été nécessaire pour des dénombrements plus élevés permettant d'analyser statistiquement les assemblages d'ostracodes afin de les utiliser comme traceurs écologiques. Une seule espèce de tintinnides a été identifiée. Il s'agit de *Tintinnopsis fimbriata* (Figure 1.10-4 à 1.10-6) qui est présente surtout vers le sommet des séquences sédimentaires. Nous ne croyons pas que ce phénomène soit attribuable à une mauvaise préservation, puisque les foraminifères agglutinants qui ont une composition similaire sont bien

préservés, mais plutôt à des changements de l'habitat. Les tintinnides ont aussi tendance à être plus gros ($> 63 \mu\text{m}$) lorsqu'ils sont plus abondants (Rogers *et al.*, 1981). Ainsi, les carottes sédimentaires utilisées pour cette thèse ont livré des résultats qui permettent de répondre aux objectifs initialement fixés (Tableau 0.1).

4.3 La transition de 1998 CE

Une importante transition dans les assemblages de foraminifères benthiques survient à l'aube du 21^e siècle dans la carotte HBGC01 (Figure 2.2a). La transition marque un passage vers un habitat plus instable, c'est-à-dire avec des salinités fluctuantes et des courants marins profonds plus dynamiques, accompagné d'une augmentation des apports terrigènes et de la productivité primaire. La concentration moyenne de la glace de mer en été dans la région enregistre une diminution ténue après 2003 CE et plus marquée après 2006 CE (Figure 1.3). Comme le site est relativement peu profond, il est proposé que la banquise joue le rôle de « bouclier » préservant la stratification de la colonne d'eau et favorisant des eaux de fond plus stables avant 2000 CE. Le rôle de la glace de mer sur la structure de l'habitat aquatique pélagique et benthique serait donc majeur.

Afin de mieux circonscrire les effets du climat sur l'habitat, d'autres variables environnementales ont été compilées. Elles incluent la glace de mer, les vents, les débits de rivières, la température de l'air et des indices d'oscillation atmosphérique régionale. Les résultats indiquent une transition à 1998 CE basée sur une analyse de regroupement des séries temporelles couvrant de 1979 à 2017 CE (Figure 2.2b). Cette transition serait attribuable à des tempêtes plus fréquentes, des vents d'est plus forts et un régime AOO positif avec un gyre de Beaufort renforcé, en plus d'une concentration de glace de mer plus faible en été après 1998 CE. Ce « nouveau régime climatique » (Wood *et al.*, 2013) caractérisé par des eaux libres de glace de mer entraîne des mélanges verticaux plus profonds (Rainville et Woodgate, 2012), une augmentation de l'érosion côtière et de la remise en suspension des particules (Klein *et al.*, 2019) et la dispersion du panache de la rivière Mackenzie vers le site d'échantillonnage des carottes sédimentaires (Mulligan *et al.*, 2010; Wood *et al.*, 2015). Ensemble, ces variables intrinsèquement liées (Wood *et al.*, 2013) auraient provoqué une instabilité accrue de l'habitat. Cette thèse a permis de mettre en évidence le rôle important des vents et des tempêtes, et aussi de démontrer que les changements climatiques récents affectent l'habitat et la biodiversité de la zone littorale.

4.4 Les 1300 dernières années

Les effets récents des changements climatiques incluant des salinités variables et une augmentation de la turbidité et des apports terrigènes ont été comparés aux conditions des 1300 dernières années reconstituées à partir de la carotte sédimentaire longue PG2303 (Figures 0.3 et 0.4). L'enregistrement démontre peu de changements de grandes amplitudes avant 1800 CE (Figure 3.9). Les faibles variations avant 1800 CE pourraient indiquer que malgré des variations climatiques régionales de relativement grandes amplitudes (p. ex., Gemery *et al.*, 2023; Nicolle *et al.*, 2018), les eaux de fond du bassin Herschel, qui est presque isolé, sont restées assez stables et baignées par des eaux froides. Une telle stabilité dépend sans doute de la banquise qui persiste sur le plateau continental (près de 9 mois par année en moyenne; Carmack et Macdonald, 2002). Toutefois, la physiographie du bassin a néanmoins permis l'enregistrement d'événements de remontées et/ou de flux prononcés des masses d'eau océaniques circulant le long du talus continental. Alors que la dépression du Mackenzie est continuellement baignée par ces masses d'eau océaniques, salées et relativement chaudes (Figure 0.2; carotte HLY1302; Gemery *et al.*, 2023; Seidenstein *et al.*, 2018), elles auraient occupé le bassin Herschel plutôt par intermittence (Figure 3.9). C'est ainsi que nous proposons un intervalle de températures minimales de 1130 ± 150 à 1640 ± 60 CE, alors qu'un couvert de glace de mer étendu empêchait la remontée des masses d'eau du talus continental (Schulze et Pickart, 2012) et que des eaux froides persistantes ne se renouvelant pas saisonnièrement occupaient le fond du bassin. La période froide s'imbrique entre deux périodes plus chaudes de ~710-1130 CE et ~1640-1790 CE, ce qui correspond approximativement aux conclusions tirées des compilations paléoclimatiques terrestres de Nicolle *et al.* (2018) et aux reconstitutions de la glace de mer de Kinnard *et al.* (2011; Fig. 3.9). Le début d'une période climatique plus clémence à ~1640 CE concorde avec les résultats micropaléontologiques de la carotte 912A (1650 CE; Figure 0.2; Richerol *et al.*, 2008). Cet événement semble synchrone régionalement et indiquerait une diminution de la glace de mer précoce dans la zone littorale par rapport au milieu hauturier.

Le réchauffement récent, qui débute vers 1790 CE, s'amplifie à partir de 1950 CE et atteint des valeurs sans précédent au cours des deux dernières décennies. Les conditions exceptionnelles enregistrées après 1950 CE tranchent ainsi avec les conditions stables qui dominaient depuis plus de 1300 ans. Ces années charnières, 1790 CE et 1950 CE, recoupent approximativement celles du début d'un réchauffement en milieu terrestre et de son accélération dans l'Arctique (Abram *et al.*, 2016), ce qui suppose une influence du climat continental importante sur la zone littorale. Il est alors possible de confirmer notre hypothèse initiale qui supposait que les changements récents engendreraient des effets au-delà des oscillations

climatiques naturelles. Ces effets occasionnent des modifications de la diversité des microorganismes, certes, mais ne semblent pas *a priori* contrevenir, ni favoriser, la productivité de ceux-ci, mis à part les ostracodes dont l'abondance a diminué au cours des dernières décennies.

4.5 Les traceurs écologiques et les questions qu'ils soulèvent

Nos traceurs micropaléontologiques indiquent une augmentation simultanée des apports nutritifs terrigènes et marins (Figure 2.2a) au cours des deux dernières décennies. Une diminution du $\delta^{13}\text{C}$ concorde avec une augmentation du carbone organique (Mackensen, 2008; Ravelo et Hillaire-Marcel, 2007), donc des apports nutritifs, mais il a été toutefois impossible de distinguer l'apport relatif entre le carbone d'origine terrigène et d'origine marine. Les flux particulaires élevés le long des côtes rendent le signal dans le sédiment uniforme et donc peu sensible aux changements de productivité primaire dans la colonne d'eau (Grotheer *et al.*, 2020). Il serait intéressant d'avoir recours à d'autres approches analytiques qui permettraient de les distinguer, comme ces derniers ont des effets différents sur les populations de phytoplancton et de zooplancton (Bell *et al.*, 2016; Comeau *et al.*, 2011) et donc, éventuellement sur les niveaux trophiques supérieurs.

La reconstitution des apports terrigènes se basait sur l'augmentation du foraminifère benthique *Quinqueloculina stalker* (Figure 1.6-5) qui tolère la turbidité et peut se nourrir de carbone organique terrigène biodégradé (Guilbault *et al.*, 2003). Les espèces *Textularia earlandi* et *Stetsonia hovarthi* (Figures 1.7-3 et 1.6-11) ont également été considérées comme traceurs d'apports terrigènes. Toutefois, ces espèces sont généralement associées à des milieux oligotrophes où la couverture de glace est pérenne (Jennings *et al.*, 2020; Wollenburg et Kuhnt, 2000) et leur augmentation récente paraît peu cohérente. Le même phénomène est observé dans la carotte PG2303 (Figure 3.3). Dans le contexte environnemental de notre étude, c'est probablement la capacité de ces espèces à se nourrir de produits de dégradation microbienne (Alve, 2010; Jennings *et al.*, 2020) qui a été le paramètre le plus déterminant. Cela soulève des questions importantes sur l'interprétation et l'utilisation des foraminifères comme traceurs de glace de mer et souligne l'importance d'évaluer les affinités écologiques des traceurs micropaléontologiques dans chaque région d'étude. Par exemple, une augmentation du couvert de glace de mer récent (~ 100 dernières années) est reconstituée dans la mer de Beaufort par Bringé et Rochon (2012) à partir des assemblages de dinokystes et par Schell *et al.* (2008) et Scott *et al.* (2009) à partir du ratio de tests agglutinants/calcaires, ce qui est fort peu probable (cf. Fetterer *et al.*, 2017). Les reconstitutions des conditions des eaux de surface à partir des dinokystes (voir Tableau 0.1) pourraient être revues après un

examen critique de la chronologie et aussi avec la nouvelle base de données qui incluent depuis plus de sites localisés dans la mer des Tchouktches et dans le nord-ouest du Canada (de Vernal *et al.*, 2020).

L'un des deux traceurs de glace de mer utilisés pour cette thèse était un marqueur indirect de la présence de la banquise, soit *Islandiella norcrossi*. En effet, ce taxon (Figure 1.6-4) occupe des habitats de salinités stables (Cage *et al.*, 2021; Polyak *et al.*, 2002), favorisés lorsque la glace agit comme « bouclier ». L'utilisation d'*Islandiella norcrossi* comme traceur de glace de mer s'appliquerait donc à notre site d'étude, mais pourrait s'étendre à des contextes bathymétriques semblables. L'utilisation de différents traceurs pour reconstituer la glace de mer, comme les biomarqueurs (Kolling *et al.*, 2020), serait néanmoins pertinente dans la perspective d'une représentation de la dynamique de la glace de mer de la zone littorale.

Au cours des mille dernières années, des apports d'eaux pacifiques épisodiques ont été enregistrés, à ~1050-1150 CE et ~1625-1900 CE, à partir de l'abondance de deux espèces d'ostracodes caractéristiques de la mer et du détroit de Béring, *Kotoracythere arctoborealis* et *Normanicysthere leioderma* (Figures 3-A.4c-d et 4.1). Des apports d'eaux pacifiques riches en nutriments sur le plateau continental favorisent des floraisons phytoplanctoniques (Pickart *et al.*, 2013; Tremblay *et al.*, 2011) qui ne se perçoivent toutefois pas à partir de nos traceurs de productivité dans la carotte PG2303. Il serait intéressant d'explorer plus en détail la relation productivité primaire-eaux pacifiques dans le bassin Herschel en jumelant les assemblages d'ostracodes à d'autres traceurs paléocénographiques. Par ailleurs, des reconstitutions quantitatives des conditions des masses d'eau à partir de la méthode des analogues modernes sur les assemblages d'ostracodes sont envisageables (cf. Gemery *et al.*, 2017) et permettraient de mieux caractériser l'environnement associé à ces intervalles d'apports d'eaux pacifiques.

4.6 Contributions et travaux futurs

Cette étude est adressée à des micropaléontologues, des écologistes et des paléocénographes. À travers les trois chapitres, cette thèse à contribuer à (1) établir un registre de diversité des foraminifères benthiques, des ostracodes et des tintinnides dans un milieu littoral arctique; (2) démontrer que les traceurs micropaléontologiques sont complémentaires, sensibles aux changements locaux et à échelles temporelles courtes; (3) identifier que l'instabilité des eaux profondes (salinité variable et turbulence des courants) et les apports terrigènes, principalement en lien avec des vents d'est forts dominants et une réduction du couvert de glace de mer, affectent les assemblages microfaunistiques et donc la biodiversité; (4) confirmer que les changements observés, dès 1950 CE et particulièrement après 2000 CE, excèdent

largement ceux de la variabilité naturelle du milieu (Figure 4.1). De plus, cette thèse présente les premières reconstitutions des conditions marines de la zone littorale du sud-est de la mer de Beaufort. Les traceurs paléoécologiques ont également pu être évalués, puisque les enregistrements couvraient la période de données instrumentales. Finalement, la résolution temporelle des analyses a permis de capter les effets du changement climatique récent, contrairement à d'autres enregistrements marins du sud-est de la mer de Beaufort. Les travaux présentés n'arrivent toutefois pas à répondre entièrement à la motivation initiale de la thèse qui avait pour ambition de faire des liens plus directs avec les ressources halieutiques. Les reconstitutions restent approximatives dans le temps, avec des marges d'erreur de plusieurs années pour chaque échantillon. De plus, chaque microorganisme peut se reproduire à des moments distincts, comme à la débâcle ou à la fin de l'été, et donc enregistrer un événement précis dans l'année. Des reconstitutions quantitatives de salinité et de température ne peuvent pas être obtenues, les reconstitutions restent relatives et qualitatives. Jongler entre les données environnementales réelles et les reconstitutions micropaléontologiques représentait aussi un défi de taille. L'exercice donnait parfois l'impression d'un cercle vicieux : on évalue les effets de l'environnement sur la biodiversité et l'abondance des espèces, mais en retour on utilise la biodiversité et l'abondance des espèces pour caractériser le milieu.

Parmi les principales perspectives de travaux futurs, les reconstitutions paléocénographiques du bassin Herschel devraient inclure d'autres traceurs paléoécologiques. Les biomarqueurs (PIP₂₅; Kolling *et al.*, 2020) et les analyses palynologiques, incluant l'utilisation de fonctions de transfert et de la technique des analogues modernes sur les assemblages de dinokystes (de Vernal *et al.*, 2020), offriraient des reconstitutions plus directes de la glace de mer, en plus de rendre compte de la productivité primaire. De surcroît, les concentrations de palynomorphes terrestres et remaniés pourraient conforter les indices d'apports terrigènes proposés dans cette thèse (e.g., Kutos *et al.*, 2021). Les assemblages de diatomées seraient également des marqueurs des flux d'eaux pacifiques, en plus de la durée de la saison libre de glace de mer (Astakhov *et al.*, 2020). Une telle approche multitraceurs permettrait de répondre aux lacunes soulevées précédemment dans la conclusion, c'est-à-dire le besoin (1) d'élucider la question entourant la diminution précoce de glace de mer dans la zone littorale (~1650 CE; cette étude; Richerol *et al.*, 2008), (2) de distinguer les apports d'éléments nutritifs issus du milieu marin de ceux des apports terrigènes et (3) d'approfondir la relation entre les apports d'eaux pacifiques et la productivité primaire. Un site tel que le bassin Herschel serait l'occasion de valider les affinités écologiques de ces traceurs paléoécologiques et de consolider leurs interprétations dans des contextes physiographiques similaires. La faisabilité d'analyses palynologiques a déjà été évaluée dans le bassin Herschel (Annexe J) et les

conditions de préservation sont probablement propices à l'identification de diatomées, des valves de *Coscinodiscus* sp. ayant été observées dans les échantillons (Figure 1.7-7).

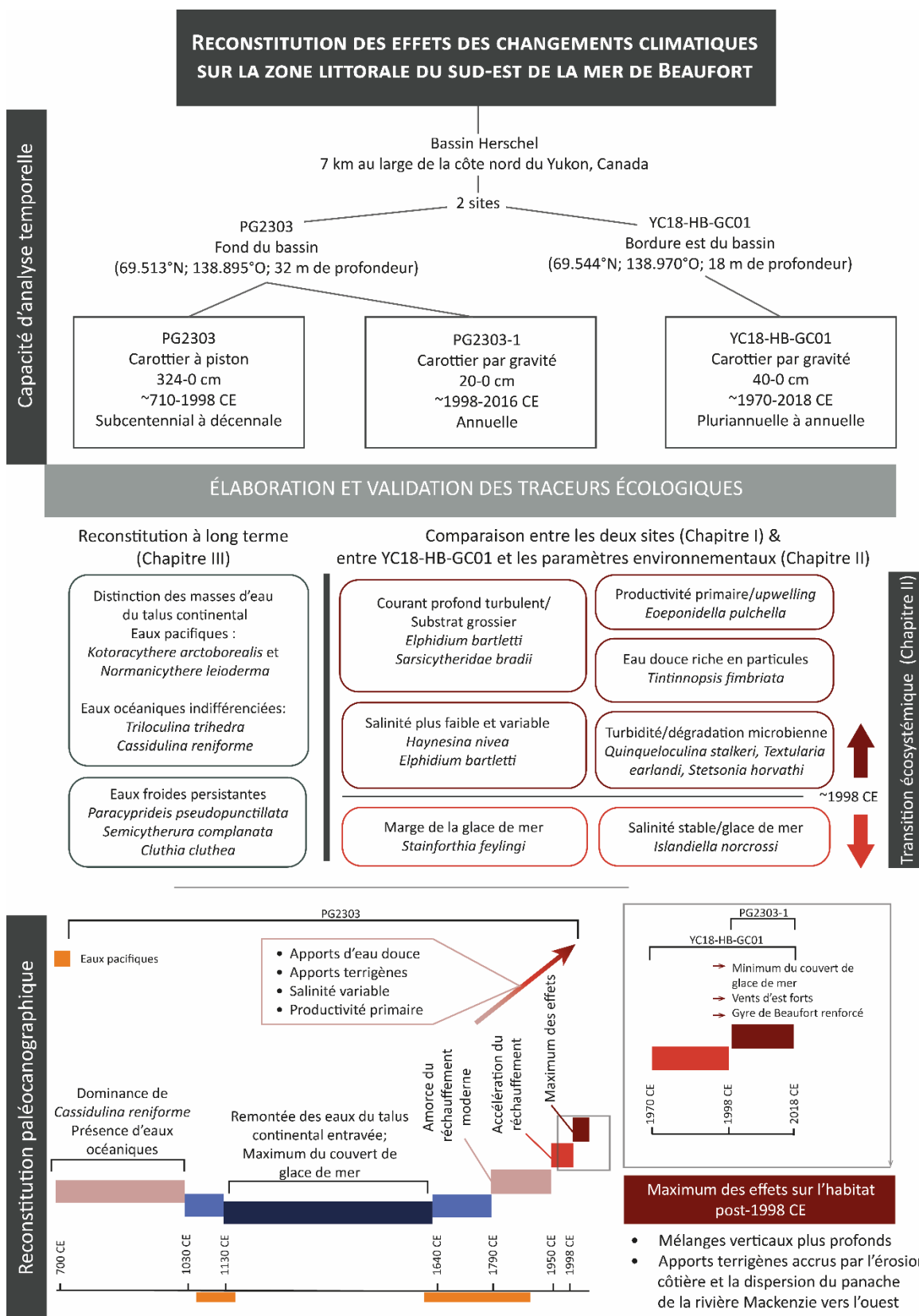
Avec l'augmentation des tempêtes, de l'érosion côtière et de la dispersion du panache de la rivière Mackenzie et à l'inverse de la diminution du couvert de glace de mer, un enjeu qui ne pourra qu'augmenter et qui sera à surveiller est la turbidité. Ses répercussions sur la production primaire et la qualité des pêches sont déjà connues (Retamal *et al.*, 2008; Scharffenberg *et al.*, 2019) et cette thèse a soulevé des questions importantes sur les effets de la turbidité sur les écosystèmes, en particulier sur la désoxygénation. La désoxygénation reste à ce jour notre meilleure hypothèse pour expliquer la diminution récente de la concentration des ostracodes. Il serait donc pertinent de poursuivre les recherches traitant des effets de la turbidité sur la chaîne trophique et sur les niveaux d'oxygène dans les eaux profondes du littoral arctique. Des mesures de mitigation de la turbidité de l'eau sur la qualité des pêches restent toutefois limitées. Les conditions environnementales des dernières décennies, telles qu'une débâcle hâtive et des vents favorables aux *upwellings*, pourraient toutefois mener à des conditions de pêche favorables (Falardeau, M. *et al.*, 2022; Walkusz *et al.*, 2012) et inciteront probablement l'adoption de nouvelles habitudes de chasse et pêche. La capacité d'adaptation des communautés est bien exprimée dans les paroles d'un membre d'Aklavik où il est question de la chasse à la baleine dans un contexte de changements climatiques récents:

I guess our people, as we, as time goes by, we just learned to adapt to it and have to go with it and lucky our people, we've been around here long enough we know there is other places we gotta go like for instance when we go whaling in the summertime. There are all these places that are shallow now, but then they find their ways you know. They know their land. (Falardeau, J. et Ouellet-Bernier, en prép., p. 17).

Le futur de la recherche est dans la cocréation et le partage de savoir. Bien que la paléocéanographie peut paraître abstraite d'un œil extérieur, elle est utile pour alimenter des dialogues sur les perspectives des changements du climat; la tradition orale et les reconstitutions climatiques ayant chacune leurs histoires à raconter (voir Falardeau, J. et Ouellet-Bernier, en prép.). Le bassin Herschel fait d'ailleurs partie de ces histoires orales. Il y a de cela des milliers d'années, le bassin Herschel aurait été un lieu de chasse réputé, car il était un lac d'eau douce où les animaux s'arrêtaient pour boire (Richard Gordon, conversation personnelle). Mise à part la turbidité, un autre élément qui mérite une attention particulière et qui engagerait la cocréation de savoir est la surveillance de proliférations de diatomées et de dinoflagellés libérant des toxines. La diminution du couvert de glace de mer et le réchauffement des eaux de surface

favorisent les espèces responsables de la libération de ces toxines qui se bioaccumulent et qui entraînent des effets neurologiques nocifs sur les mammifères, incluant les humains, jusqu'à la mort. Enregistrées dans le nord-ouest de l'Alaska (Anderson *et al.*, 2021; Lefebvre *et al.*, 2016), la prolifération d'algues nuisibles et la contamination pourraient raisonnablement s'étendre jusque dans le sud-est de la mer de Beaufort, en territoire Inuvialuit. Un tel risque nécessitera des suivis autant dans les sédiments marins et les conditions des masses d'eau de surface, en particulier la température et la salinité, que dans le comportement et la concentration en toxine des mammifères marins chassés. De tels programmes de surveillance et de prévision de proliférations d'algues nuisibles ont déjà été mis sur pied dans le golfe du Saint-Laurent et la côte est américaine (Boivin-Rioux *et al.*, 2021; Li, Y. *et al.*, 2009).

Figure 4.1 Modèle résumant la structure de la thèse



J'aimerais finalement terminer cette thèse sur une note qui me tient à cœur, la communication scientifique. Au cours des cinq dernières années à travailler sur ce projet de thèse, j'ai participé à des ateliers comme le *Sprint de Science*, édité et coécrit le livret *ArcTrain*, qui explique au grand public les méthodes pour documenter le climat, et surtout élaboré la trousse pédagogique intitulée *Stories about Climate* avec Marie-Michèle Ouellet-Bernier (voir exemple à la Figure 4.2). Je me suis aussi déplacée à Aklavik et Inuvik dans les Territoires du Nord-Ouest (Figure 0.2), où j'ai échangé avec des membres des communautés sur les enjeux de la région. En tant que membre de la communauté scientifique, je crois avoir apporté ma pièce de puzzle à la compréhension de la dynamique climatique terrestre. Toutefois, je crois qu'il est primordial de remodeler ou de repenser cette pièce du puzzle dans un cadre plus général, afin qu'elle soit transmise au grand public, accessible, ludique et qu'elle éveille des discussions, et ce tout particulièrement pour les jeunes générations. La science a un sens pour moi quand elle est utile et au service de la communauté, particulièrement à un moment aussi critique que celui que nous vivons collectivement actuellement.

Figure 4.2 Extrait de la bande dessinée créée dans le cadre du projet *Stories about Climate* (Falardeau, J. et Ouellet-Bernier, en prép.). On y voit le personnage principal échantillonner une carotte de sédiment accompagné de nul autre que moi-même et d'autres membres de l'équipe. Gracieuseté de Mark-Antoine Thibodeau Breault.



ANNEXE A

COMPTAGES BRUTS DES FORAMINIFÈRES BENTHIQUES CALCAIRES DANS LA CAROTTE YC18-

HB-GC01

Profondeur (cm)	<i>Islandiella helena</i>	<i>Islandiella norcrossi</i>	<i>Islandiella</i> spp.	<i>Cassidulina reniforme</i>	<i>Haynesina orbicularis</i>	<i>Haynesina nivea</i>	<i>Haynesina</i> spp.	<i>Elphidium clavatum</i>	<i>Elphidium</i> spp.	<i>Elphidium albiumbilicatum</i>	<i>Elphidium asklundi</i>	<i>Elphidium haliandense</i>	<i>Elphidium bartletti</i>	<i>Elphidiella aeroenlandica</i>	<i>Buccella</i> spp.	<i>Buccella frigida</i>	<i>Eoepitonidella pulchella</i>	<i>Epistomina takavanaaii</i>	<i>Quinqueloculina stalkerii</i>	<i>Quinqueloculina</i> spp.	<i>Quinqueloculina seminulum</i>	<i>Quinqueloculina tata</i>	<i>Triloculina trihedra</i>	<i>Pyrgo williamsoni</i>	<i>Stainforthia feylingi</i>	<i>Stainforthia loeblichii</i>	<i>Bolivinellina pseudobunctorata</i>	polymorphinids	<i>Cornuspira involvens</i>	<i>Variinulina trondheimensis</i>	<i>Nonionellina labradorica</i>	<i>Valvulinaria</i> spp.	<i>Stetsonia horvathi</i>	Autre	Non-identifié					
0.5	8	2	1	30	10	10	0	137	0	0	0	0	0	0	0	0	2	19	4	3	0	0	0	0	0	0	0	0	0	0	0	0	0	0	0	0	0	0	0	
1.5	12	2	0	15	4	0	0	127	1	1	1	0	2	0	0	0	5	19	4	3	0	0	0	0	0	0	0	0	0	0	0	0	0	0	0	0	0	0	0	
2.5	7	1	0	8	4	6	0	103	0	3	0	0	0	0	0	0	0	9	12	2	4	0	0	0	0	0	0	0	0	0	0	0	0	0	0	0	0	0	0	
3.5	5	0	0	14	2	3	0	47	0	0	1	0	1	0	0	0	5	8	2	1	0	0	0	0	0	0	0	0	0	0	0	0	0	0	0	0	0	5		
4.5	1	0	0	9	0	4	0	32	0	0	0	0	0	0	0	0	0	2	4	0	1	0	0	0	0	0	0	0	0	0	0	0	0	0	0	0	0	0	0	
5.5	7	2	0	18	5	14	0	124	2	0	0	0	0	0	0	0	5	8	2	19	0	0	0	0	0	0	1	0	0	1	0	0	0	0	0	0	0	0	0	
6.5	9	0	0	39	5	82	0	231	0	0	2	0	1	0	0	0	28	72	2	20	0	0	1	1	0	1	0	0	10	3	1	0	2	2	0	1	1			
7.5	8	0	0	18	2	40	3	143	0	0	0	0	2	1	0	0	8	46	6	3	0	0	0	0	0	6	0	0	3	0	0	0	0	0	0	0	0	0	0	
8.5	2	2	0	18	1	23	0	73	0	0	1	0	0	0	0	0	9	20	1	5	3	0	0	0	0	4	0	0	2	0	0	0	0	0	0	0	5	1	3	
9.5	4	0	0	17	1	3	0	100	0	0	0	0	0	0	0	0	0	2	0	6	0	0	0	0	0	0	0	0	0	0	0	0	0	0	0	0	0	0	0	0
10.5	7	0	0	19	3	9	0	107	0	0	3	0	0	0	0	0	6	8	0	8	1	0	0	0	0	1	0	0	2	0	0	0	0	0	0	0	0	0	1	
11.5	1	4	0	30	4	5	0	102	0	0	2	0	2	0	0	0	3	6	2	2	0	2	0	1	0	1	0	0	2	0	0	0	0	0	0	0	0	0	0	0
12.5	8	0	0	33	6	21	0	147	0	0	4	0	0	2	0	1	18	3	4	0	0	0	0	0	0	0	0	2	0	0	0	0	0	0	0	0	0	3		
13.5	2	2	0	28	6	21	0	120	0	0	3	0	3	0	0	1	14	0	6	0	0	0	1	0	0	0	0	1	0	0	0	0	0	0	0	1	0	2		
14.5	4	0	0	37	11	13	0	176	0	0	2	0	0	2	0	0	8	20	2	8	0	0	0	0	0	4	0	0	3	1	0	0	0	0	0	0	0	4		
15.5	0	1	0	28	8	27	0	118	0	0	2	0	1	0	0	0	3	25	0	2	0	0	0	0	0	5	0	2	3	0	0	0	0	0	1	0	0	0	0	0
16.5	2	3	0	17	1	10	0	99	0	0	3	0	1	1	0	1	11	8	2	3	0	0	0	0	1	0	0	1	0	0	0	0	0	0	0	0	5			
17.5	2	2	0	19	6	23	0	97	0	0	5	0	0	0	0	0	3	15	0	0	0	0	0	0	0	0	0	0	0	0	0	0	0	0	0	0	0	0		
18.5	3	5	0	31	10	24	0	107	0	2	1	0	1	0	0	0	12	19	0	2	0	0	0	0	0	5	0	0	3	0	0	0	0	0	0	0	0	3		
19.5	9	8	0	48	12	25	0	163	0	0	4	0	0	0	0	0	9	19	2	3	0	1	0	0	0	5	0	0	4	1	0	0	1	1	0	0	0	0	0	0
20.5	5	1	0	36	29	23	0	153	0	1	3	0	0	0	0	0	13	9	4	5	0	0	0	0	3	9	0	0	9	2	0	0	0	0	0	0	4			
21.5	8	7	0	51	9	17	3	173	1	1	2	0	0	1	0	4	12	4	4	0	0	0	0	2	9	0	0	7	0	0	0	0	0	0	0	0	4			
22.5	3	6	0	37	6	14	0	188	0	0	3	0	0	0	0	0	10	7	0	4	0	2	0	1	2	9	0	1	3	0	0	0	1	0	0	0	0	0	0	
23.5	8	4	0	35	10	29	0	313	0	0	0	0	0	0	0	0	15	14	2	11	0	1	0	0	1	6	0	0	4	2	0	0	0	1	0	1				
24.5	6	1	0	29	4	16	0	200	0	0	0	0	0	0	1	6	9	0	11	0	1	0	0	0	7	1	0	3	3	0	0	0	0	0	0	0	0			
25.5	10	2	0	33	12	10	0	316	0	0	0	0	0	0	0	0	12	5	4	14	1	1	1	0	0	6	0	3	10	1	0	0	1	0	1	5				
26.5	3	11	0	38	4	8	0	299	0	1	0	0	0	0	0	0	8	4	2	10	0	0	0	0	0	1	0	0	2	0	0	0	0	1	0	0	0	0	0	
27.5	16	17	0	57	17	10	0	256	0	0	2	0	0	1	0	1	17	15	4	5	0	0	0	0	0	9	0	0	12	0	0	0	0	0	0	0	1	0	0	0

28.5	9	11	0	61	15	24	0	243	0	1	4	0	0	1	0	23	10	6	6	0	0	0	0	0	4	1	0	4	1	0	0	0	0	0	3
29.5	7	11	0	64	11	23	0	296	0	0	1	1	1	0	0	13	8	3	4	0	0	0	0	1	5	0	0	9	0	0	0	0	0	1	1
30.5	7	21	0	86	16	25	0	391	0	0	1	0	1	0	0	15	10	3	9	0	1	0	0	3	19	1	0	10	1	0	0	0	0	0	0
31.5	10	20	0	62	9	22	0	310	0	0	1	0	1	1	0	8	7	3	2	0	1	0	0	2	8	0	0	11	2	0	0	1	1	2	0
32.5	13	22	1	73	10	29	0	309	1	1	1	0	0	0	0	14	11	2	0	0	0	0	0	4	13	2	0	6	0	0	0	0	0	0	2
33.5	18	18	0	85	17	18	0	213	0	1	2	0	0	0	0	19	12	2	0	0	0	0	0	0	8	0	0	8	1	0	1	0	0	1	1
34.5	5	17	0	44	18	17	0	210	0	0	0	0	0	0	0	14	11	2	1	0	0	0	0	0	8	2	1	3	0	0	0	0	1	0	1
35.5	5	6	0	36	4	19	0	133	0	0	0	0	0	0	0	13	13	1	2	0	0	0	0	1	9	0	0	1	0	0	0	0	2	1	0
36.5	15	7	1	26	11	1	0	119	0	1	0	0	0	0	0	2	11	6	2	0	0	0	0	0	4	0	0	7	0	0	0	0	0	0	4
37.5	5	4	0	20	4	7	0	105	0	0	0	0	0	0	0	11	6	0	1	0	0	0	0	0	1	0	0	5	1	0	1	0	1	0	0
38.5	0	4	0	15	5	2	0	68	0	1	0	0	0	0	0	4	3	0	2	0	0	0	0	1	4	0	0	2	0	0	0	0	0	0	0
39.5	10	13	0	38	4	5	0	155	0	0	0	0	0	0	0	9	2	2	1	1	1	0	0	1	2	0	0	7	0	1	0	0	0	1	0

ANNEXE B

COMPTAGES BRUTS DES FORAMINIFÈRES BENTHIQUES AGGLUTINANTS ET AUTRES TYPES DE MICROFOSSILES DANS LA CAROTTE YC18-HB-GC01

Profondeur (cm)	Foraminifères benthiques agglutinants										Autres types de microfossiles						
	<i>Spiroplectammina biformis</i>	<i>Textularia torquata</i>	<i>Textularia earlandi</i>	<i>Recurvoides turbinatus</i>	<i>Cribrostomoides crassimargo</i>	<i>Sigmoilopsis schlumbergeri</i>	Agg. unidentified	<i>Ammotium cassis</i>	<i>Lagenammina diffugiformis</i>	<i>Eggerelloides advenus</i>	<i>Porotrachammina karica</i>	<i>Tintinnopsis fimbriata</i>	Grain de pollen	Foraminifère planctonique	Valve de diatomée	<i>Spongotorachus glacialis</i>	Fragment de bivalve
0.5	5	1	0	0	0	0	0	0	0	0	0	1	NA	1	0	0	0
1.5	0	0	0	1	0	0	0	0	0	0	0	1	NA	0	0	0	0
2.5	5	1	0	1	0	0	1	0	0	0	0	70	9	0	Présent	0	2
3.5	0	0	0	0	0	0	0	0	0	0	0	2	4	0	Présent	0	0
4.5	3	0	1	0	0	0	2	0	0	0	0	0	1	0	0	0	0
5.5	11	5	0	1	0	0	4	0	0	0	0	41	0	0	10	0	0
6.5	9	3	0	0	0	0	0	0	0	0	0	107	0	1	10	0	0
7.5	8	1	1	0	0	0	2	0	0	0	0	64	3	0	Présent	0	0
8.5	14	0	0	1	0	0	0	0	0	0	0	52	3	0	0	0	0
9.5	14	2	0	1	0	0	0	0	0	0	0	43	0	0	5	0	0
10.5	15	4	2	1	0	0	3	0	0	0	0	76	0	0	4	0	0
11.5	9	5	2	0	0	0	0	0	0	0	0	45	0	0	10	0	0
12.5	11	3	1	4	0	0	4	0	0	0	0	58	0	0	2	0	0
13.5	2	3	0	0	0	0	0	0	0	0	0	3	0	1	Présent	0	0
14.5	8	1	1	1	0	0	3	0	0	0	1	58	1	0	3	0	0
15.5	6	4	1	1	0	0	0	0	0	0	0	32	0	0	0	0	0
16.5	8	0	0	0	0	0	0	0	0	0	0	38	0	1	0	0	0
17.5	8	8	0	1	0	1	1	0	0	0	0	25	0	0	1	0	Présent
18.5	10	1	0	1	0	0	3	0	0	0	0	6	0	0	0	0	0
19.5	15	7	1	2	0	0	0	0	0	0	0	37	0	0	0	0	0
20.5	16	5	1	1	0	0	0	0	0	0	0	30	1	0	0	0	2
21.5	4	1	0	0	0	0	7	0	0	0	0	2	1	0	0	0	0
22.5	8	5	0	1	0	0	0	0	0	0	0	5	1	0	0	0	0
23.5	11	9	0	1	0	0	0	0	0	0	0	5	1	0	0	0	0
24.5	6	4	0	0	0	0	0	0	0	0	0	9	0	0	0	0	0
25.5	8	12	1	0	0	0	3	0	0	0	0	19	0	0	0	0	0
26.5	5	4	0	2	0	0	0	0	0	0	0	0	0	0	0	0	0
27.5	22	29	0	1	0	0	0	0	0	0	0	8	0	0	0	0	0

28.5	9	7	0	0	0	0	0	0	0	0	0	6	0	0	0	0	0	0
29.5	11	7	0	2	0	0	2	0	0	0	0	4	0	0	0	0	0	0
30.5	38	31	0	0	0	0	0	0	0	0	0	30	1	0	0	0	0	0
31.5	15	27	0	1	0	0	0	0	1	0	1	18	0	0	0	0	0	0
32.5	13	12	0	1	0	0	0	0	0	0	0	15	0	1	0	0	2	0
33.5	14	6	0	0	0	0	1	0	0	0	0	16	0	0	0	0	0	0
34.5	16	9	0	1	0	0	0	0	0	0	0	5	1	0	0	10	2	Présent
35.5	7	4	0	0	0	0	2	0	0	0	0	5	0	0	0	0	0	0
36.5	1	0	0	1	0	0	1	0	0	0	0	0	6	0	0	0	0	0
37.5	2	0	0	0	0	0	1	0	0	0	0	5	6	0	0	0	0	0
38.5	1	0	0	0	0	0	0	0	0	0	0	0	0	1	0	0	0	0
39.5	0	0	0	1	0	0	0	0	0	0	0	0	3	0	0	0	2	0

ANNEXE C

COMPTAGES BRUTS DES OSTRACODES DANS LA CAROTTE YC18-HB-GC01

Profondeur (cm)	<i>Sarsicytheridea bradii</i>	<i>Cluthia cluthae</i>	<i>Loxoconcha venepidermoidea</i>	<i>Rabilimis mirabilis</i>	<i>Cytheropteron suzdaletskiyi</i>	<i>Cytheropteron sulense</i>	<i>Cytheropteron discoveria ou brasiliensis</i>	<i>Cytheropteron elaeini</i>	<i>Cytheropteron</i> spp.	<i>Eucytherura delineata</i>	<i>Eucythere</i> spp.	<i>Semicytherura complanata</i>	<i>Heterocyprideis sorbyana</i>	<i>Paracyprideis pseudopuntillata</i>	Nombre de valves identifiées	Nombre de valves comptées
0.5	0	0	0	0	0	0	0	0	0	0	0	0	0	0	0	1
1.5	0	0	0	0	0	0	0	0	0	0	0	0	0	0	0	0
2.5	0	0	0	0	0	0	0	0	0	0	0	0	1	0	1	3
3.5	0	0	0	0	0	0	0	0	0	0	0	0	0	0	0	0
4.5	0	2	0	0	0	0	0	0	0	0	0	0	0	0	0	2
5.5	0	0	0	0	0	0	0	0	0	0	0	0	0	1	1	1
6.5	0	0	3	1	0	0	0	0	0	0	1	0	0	3	8	10
7.5	0	0	1	0	0	0	0	0	0	0	0	0	0	0	1	1
8.5	0	0	0	1	0	0	0	0	0	0	0	0	0	0	1	3
9.5	0	0	0	0	0	0	0	0	1	1	0	0	0	1	3	3
10.5	0	1	0	0	1	0	0	1	1	0	0	0	0	0	4	4
11.5	0	0	0	0	1	0	0	0	0	0	0	0	0	0	1	3
12.5	0	0	0	0	0	0	0	0	1	0	0	0	1	0	2	2
13.5	0	0	0	0	0	0	0	0	0	2	0	0	0	0	2	2
14.5	0	0	1	0	1	0	0	1	0	0	0	0	0	0	3	6
15.5	0	0	0	0	0	0	0	0	2	0	0	0	0	0	2	4
16.5	0	0	0	0	0	0	0	0	0	1	0	0	0	1	2	3
17.5	1	1	0	0	0	0	0	0	1	0	0	0	0	1	4	5
18.5	0	0	0	0	1	0	0	0	0	0	0	0	0	0	1	1
19.5	1	1	0	0	0	0	0	0	2	0	0	0	0	2	6	8
20.5	1	0	0	0	0	0	0	2	4	0	0	0	2	3	12	16
21.5	0	0	0	0	1	0	0	1	1	0	0	0	0	1	4	4
22.5	1	0	0	0	1	0	0	0	0	0	2	0	0	3	7	8
23.5	2	14	0	0	0	0	0	0	0	0	0	0	0	1	17	19
24.5	0	0	0	1	1	0	0	2	1	0	0	0	0	1	6	8
25.5	2	1	0	0	1	0	0	0	1	0	0	0	0	2	7	11
26.5	0	0	0	0	2	0	0	4	0	0	0	0	0	1	7	8
27.5	1	6	0	0	0	0	0	5	0	0	0	0	0	4	16	18
28.5	2	0	0	0	3	0	0	0	0	0	2	0	0	2	9	10

29.5	1	2	0	0	1	0	0	3	0	0	1	0	0	1	9	10
30.5	2	2	0	2	0	0	0	0	2	0	6	0	0	5	19	26
31.5	2	2	0	0	0	0	0	2	1	0	0	0	0	4	11	16
32.5	2	4	0	0	0	0	0	3	0	1	1	1	0	4	16	32
33.5	1	1	0	0	0	0	0	0	1	0	3	2	0	3	11	13
34.5	0	1	1	2	0	0	0	3	1	0	0	0	0	1	9	9
35.5	3	0	0	1	0	0	0	2	0	0	2	0	1	2	11	14
36.5	2	2	0	0	0	0	0	0	0	0	2	1	0	2	9	10
37.5	0	3	0	0	0	0	0	0	0	0	1	0	2	2	8	13
38.5	1	0	0	1	1	0	0	1	0	0	0	1	0	4	9	11
39.5	2	0	1	0	0	0	0	0	0	0	0	0	0	2	5	6

ANNEXE D

COMPTAGES BRUTS DE FORAMINIFÈRES BENTHIQUES CALCAIRES DANS LA CAROTTE PG2303-

1

Profondeur (cm)	<i>Islandiella helena</i>	<i>Islandiella norcrossi</i>	<i>Cassidulina reniforme</i>	<i>Haynesina orbicularis</i>	<i>Haynesina nivea</i>	<i>Elphidium clavatum</i>	<i>Elphidium albiumbilicatum</i>	<i>Elphidium asklundii</i>	<i>Elphidium hallandense</i>	<i>Elphidium bartletti</i>	<i>Eospionidella pulchella</i>	<i>Epistominella takayanagii</i>	<i>Quinqueloculina stalkeri</i>	<i>Quinqueloculina</i> spp.	<i>Quinqueloculina seminulum</i>	<i>Triloculina trihedra</i>	<i>Pyrgo williamsoni</i>	<i>Stainforthia feylungi</i>	<i>Stainforthia loebichi</i>	<i>Bolivinellina pseudopunctata</i>	polymorphinids	<i>Compspira involvens</i>	<i>C. involvens</i> cf.	<i>Bolivina</i> spp.	<i>Nonionellina labradorica</i>	<i>Valvularia</i> spp.	<i>Stetsonia horvathi</i>	Non identifié	
0.5	1	0	35	5	3	9	0	0	0	0	0	1	1	1	0	0	0	0	0	1	0	0	0	0	0	0	1		
1.5	3	1	75	8	38	128	0	2	0	0	0	15	49	1	8	0	0	0	0	27	0	1	3	0	0	0	22	4	
2.5	7	9	131	10	58	195	0	0	0	0	23	43	2	18	0	0	0	0	0	27	0	1	3	0	0	0	22	4	
3.5	4	2	99	5	49	172	1	0	1	1	22	39	4	5	1	1	2	0	17	3	0	4	0	1	0	0	17	5	
4.5	5	1	61	1	27	108	0	0	0	1	15	18	3	4	1	0	0	0	14	0	0	0	0	0	0	1	9	2	
5.5	2	0	37	4	18	79	0	0	0	0	12	17	5	5	0	0	0	0	15	2	0	2	0	0	0	1	7	2	
6.5	2	1	49	5	17	74	0	1	0	0	4	6	2	3	0	0	0	0	11	0	1	5	1	0	0	0	1	4	2
7.5	2	2	66	3	11	84	0	0	0	0	8	20	0	0	0	0	0	0	25	1	0	4	0	0	0	0	5	1	
8.5	4	0	62	2	28	86	0	0	1	0	7	17	0	4	0	0	0	0	16	1	1	1	0	0	0	0	1	0	
9.5	5	1	91	0	35	90	0	0	0	0	11	31	3	10	0	0	0	0	25	0	0	10	0	0	0	0	2	0	
11	7	2	101	3	17	99	0	0	0	0	8	34	2	16	1	0	2	0	18	1	1	9	0	0	0	0	0	1	0
12	2	1	85	4	39	101	0	0	0	0	12	27	1	15	0	0	0	0	9	0	1	3	0	0	1	0	0	4	4
13	1	1	44	2	86	151	0	0	0	0	25	70	2	2	0	0	0	0	8	0	0	3	1	0	1	0	1	3	5
14	4	1	69	5	141	228	0	0	0	0	41	121	2	3	0	1	1	0	8	0	0	14	0	1	0	0	0	5	1
15	6	2	76	8	147	180	0	0	0	0	38	127	5	2	2	1	12	0	9	0	1	7	4	0	0	0	1	3	4
16	10	1	27	6	13	69	0	3	0	1	16	29	4	4	0	0	4	0	10	0	1	12	1	0	0	0	2	1	0
17	11	4	45	7	23	77	1	0	0	1	11	21	0	5	0	1	0	0	16	1	1	16	1	0	0	1	0	3	0
18	12	5	57	11	30	74	0	0	0	2	14	24	6	17	0	0	1	0	24	0	2	17	1	0	0	0	0	8	2
19	12	0	61	11	26	84	0	0	0	2	14	27	2	8	0	0	2	0	30	1	3	16	0	5	1	0	0	4	2
20	6	5	60	5	14	102	0	0	1	2	12	9	1	7	0	0	0	1	22	1	5	14	0	1	0	0	0	1	1

ANNEXE E

COMPTAGES BRUTS DE FORAMINIFÈRES BENTHIQUES AGGLUTINANTS ET AUTRES TYPES DE MICROFOSSILES DANS LA CAROTTE PG2303-1

Profondeur (cm)	Foraminifères benthiques agglutinants									Autres types de microfossiles			
	<i>Spiroplectammina biformis</i>	<i>Textularia torquata</i>	<i>Textularia earlandi</i>	<i>Recunvoides turbinatus</i>	<i>Cribrostomoides crassimargo</i>	<i>Ammotium cassis</i>	<i>Lagenammina diffugiformis</i>	<i>Eggerelloides advenus</i>	<i>Portatracammina karica</i>	Non-identifié	<i>Tintinnopsis fimbriata</i>	Grain de pollen	Foraminifère planctonique
0.5	99	0	20	2	0	0	0	0	0	1	49	24	0
1.5	64	4	16	0	0	0	0	0	1	0	295	5	0
2.5	54	8	18	2	0	0	0	2	0	0	214	6	0
3.5	45	1	11	1	1	0	0	0	0	1	99	1246	0
4.5	47	4	10	2	0	0	0	0	1	2	177	0	0
5.5	36	4	6	0	0	0	0	0	0	0	217	6	0
6.5	42	0	6	2	0	0	0	1	0	0	154	13	0
7.5	35	3	16	1	2	0	0	0	1	2	268	1	0
8.5	66	5	6	1	0	0	0	3	0	1	141	20	0
9.5	62	9	15	3	0	0	0	0	0	0	116	0	1
10.5	##	8	17	2	1	0	0	0	0	2	100	1	0
11.5	37	9	12	2	2	0	0	1	0	1	70	13	1
12.5	21	14	1	0	0	0	0	0	0	0	94	6	0
13.5	21	29	0	0	0	0	0	0	0	1	52	21	0
14.5	45	23	15	4	0	0	0	0	0	0	90	48	0
15.5	40	22	12	8	4	0	1	0	0	2	197	6	0
16.5	61	19	6	13	1	1	0	4	1	3	151	36	0
17.5	57	11	8	12	1	1	0	0	0	2	180	9	0
18.5	59	12	10	12	0	0	0	3	0	2	100	3	0
19.5	39	9	9	3	0	0	0	0	0	9	85	8	0

ANNEXE F
COMPTAGES BRUTS DES OSTRACODES DANS LA CAROTTE PG2303-1

Profondeur (cm)	<i>Loxconcha venepidermoidea</i>	<i>Rabilimis mirabilis</i>	<i>Cytheropteron suzdalskyi</i>	<i>Cytheropteron sulense</i>	<i>Cytheropteron discovery ou brasiliensis</i>	<i>Cytheropteron eleeni</i>	<i>Cytheropteron spp.</i>	<i>Eucytherura delineata</i>	<i>Eucythere spp.</i>	<i>Semicytherura complanata</i>	<i>Heterocyprideis sorbyana</i>	<i>Paracyprideis pseudopuntillata</i>	Nombre de valves identifiées	Nombre de valves comptées
0.5	0	0	0	0	0	0	0	0	0	0	0	0	0	0
1.5	0	0	0	0	0	0	1	0	1	0	2	0	4	5
2.5	0	0	1	0	0	0	4	1	1	0	1	0	8	11
3.5	0	0	2	1	0	0	1	0	0	0	3	2	9	9
4.5	0	0	0	0	0	0	6	0	1	0	0	0	1	8
5.5	0	0	1	2	0	0	5	0	1	0	0	0	0	9
6.5	1	0	1	0	2	0	1	0	0	0	0	0	0	5
7.5	0	0	4	0	0	0	5	0	0	0	0	0	0	10
8.5	0	0	0	0	0	0	7	0	0	0	0	0	0	8
9.5	0	0	5	0	2	0	1	0	0	2	0	1	11	12
10.5	0	0	1	1	0	0	6	0	0	0	0	0	0	8
11.5	0	1	4	0	0	0	6	0	1	0	2	0	14	20
12.5	1	0	0	1	1	0	1	0	4	0	1	0	9	12
13.5	3	1	3	0	0	0	2	0	0	0	2	1	12	14
14.5	5	0	0	0	0	0	3	0	2	0	3	5	18	19
15.5	0	0	2	0	0	0	2	0	0	2	1	1	8	11
16.5	0	0	3	0	0	0	7	0	2	0	0	0	12	15
17.5	1	3	8	0	0	0	11	0	0	3	0	1	27	28
18.5	0	1	7	0	3	0	14	0	0	3	0	1	29	34
19.5	0	0	2	0	0	0	4	0	0	3	0	0	9	11

ANNEXE G

COMPTAGES BRUTS DES FORAMINIFÈRES BENTHIQUES CALCAIRES DANS LA CAROTTE PG2303

Profondeur réelle (cm)	<i>Islandiella heleneae</i>	<i>Islandiella helenae juvenile</i>	<i>Islandiella norcrossi</i>	<i>Islandiella</i> spp.	<i>Cassidulina reniforme</i>	<i>Haynesina orbicularis</i>	<i>Haynesina nivea</i>	<i>Haynesina</i> spp.	<i>Elphidium clavatum</i>	<i>Elphidium</i> spp.	<i>Elphidium albumbilicatum</i>	<i>Elphidium asklundii</i>	<i>Elphidium hallandense</i>	<i>Elphidium bartletti</i>	<i>Elphidiella aroenlandica</i>	<i>Buccella frigida</i>	<i>Eoeporinidella putchellae</i>	<i>Epistominella takayanagii</i>	<i>Quinqueloculina stalkerii</i>	<i>Quinqueloculina seminulum</i>	<i>Triloculina trihedra</i>	<i>Pyrao williamsoni</i>	<i>Stainforthia feylingi</i>	<i>Polymorphinids</i>	<i>Bolivinellina</i>	<i>Cycloairia involvens</i>	<i>Bolivina</i> spp.	<i>Vaainulicina trondheimensis</i>	<i>Nanionellina labradorica</i>	<i>Valvulinaria</i> spp.	<i>Stetsonia horvathi</i>	Non-identifié		
2.5	4	0	4	0	91	12	19	0	192	0	1	0	0	1	0	0	0	8	26	1	5	0	0	0	0	0	0	0	0	0	0	0	6	
9.5	2	0	2	0	71	6	19	0	92	0	0	1	0	0	0	0	0	8	26	1	5	0	0	0	0	0	0	0	0	0	0	0		
14.5	16	7	0	0	49	13	19	0	78	0	0	1	0	2	0	0	13	20	4	3	0	0	0	0	0	0	0	0	0	0	0	0		
19.5	17	8	3	1	84	12	25	0	155	0	0	0	2	3	0	0	15	26	6	6	0	0	1	0	19	7	12	1	1	0	0	5	1	
24.25	14	1	5	1	72	15	9	0	172	0	0	2	0	1	0	0	17	16	1	2	0	0	0	0	7	5	18	0	0	0	0	2	3	
29.5	26	1	2	0	107	21	14	0	168	0	0	1	0	0	0	0	16	6	8	0	0	0	0	0	0	16	2	10	4	0	0	0	1	0
32.5	10	7	8	0	123	16	1	0	199	0	1	0	1	0	0	0	10	12	8	2	0	0	0	0	31	2	11	1	0	0	0	0	0	0
37.5	9	0	2	0	83	11	7	0	340	0	0	1	0	0	1	8	7	4	1	0	0	0	0	0	57	0	14	2	0	0	0	0	4	1
42.5	4	3	2	0	49	11	10	0	91	0	0	2	0	0	1	12	16	3	3	0	0	1	0	15	0	15	0	0	0	0	0	5	0	
47.5	23	4	3	0	168	19	17	1	302	0	0	3	0	5	0	10	31	2	28	0	0	0	0	42	0	19	1	0	0	0	0	7	5	
52.5	16	4	11	0	104	8	25	0	260	0	0	1	0	0	0	0	27	30	7	3	1	0	0	0	7	1	13	1	1	0	0	0	1	0
57.5	14	1	1	1	74	10	20	0	158	0	0	7	0	0	1	11	23	3	6	0	0	0	0	10	0	10	0	3	0	0	0	0	0	0
62.5	2	0	0	0	10	3	15	0	31	0	0	0	0	0	0	2	5	0	1	0	1	0	0	1	0	2	0	1	0	0	0	1	0	
72.5	28	0	9	0	164	5	3	2	190	0	1	2	0	0	0	34	31	12	1	0	0	0	0	16	2	18	4	0	0	0	0	0	0	0
82.5	7	0	9	0	79	7	6	0	144	0	0	4	0	0	0	11	11	6	4	0	0	1	0	5	1	10	4	0	0	0	0	0	0	0
92.5	21	5	14	0	128	11	13	0	127	0	0	2	0	0	0	5	13	5	0	1	0	1	0	5	4	7	1	1	0	0	0	0	1	0
101.5	11	1	3	0	47	8	8	0	76	0	0	0	0	0	0	0	13	1	2	2	0	0	0	0	2	1	4	0	0	0	0	0	0	0
112.5	15	1	8	0	76	9	6	0	198	0	1	2	0	0	0	15	10	2	1	0	0	1	0	4	3	14	1	1	0	1	0	2	0	
122.5	8	3	14	0	123	19	16	0	170	0	0	4	0	0	2	17	11	4	12	0	0	2	0	11	1	6	8	0	0	0	0	0	1	
132.5	12	1	10	0	150	10	9	0	175	0	0	3	0	0	0	18	5	4	1	0	0	1	0	10	5	11	2	0	0	0	0	1	0	
141.5	4	1	0	0	58	10	4	0	78	0	0	1	0	0	0	8	2	3	1	0	0	1	0	4	0	0	0	0	0	0	1	0		
152.5	10	2	11	0	84	16	6	0	143	1	0	1	1	0	16	4	5	6	2	0	15	0	13	2	18	7	0	0	0	0	0	0	2	
162.5	8	2	17	0	127	25	13	0	222	0	0	2	0	1	0	27	5	10	1	0	2	0	0	4	1	11	2	0	0	1	0	0	1	
171.5	18	0	3	0	63	11	0	0	125	0	0	1	0	3	0	12	3	2	10	0	0	1	0	2	2	5	1	0	0	0	0	0	0	
182.5	17	3	9	0	122	38	11	0	275	0	1	6	0	0	0	32	7	4	8	0	2	0	0	12	1	19	4	0	0	0	0	1	0	
192.5	7	1	6	0	114	28	21	0	294	0	0	6	0	2	1	15	8	2	4	0	0	2	6	2	21	1	0	1	0	0	1	1		
202.5	28	1	13	0	140	19	3	0	241	0	0	6	0	1	0	45	4	12	6	4	1	24	0	5	4	14	3	0	0	0	2	0		
212.5	27	0	19	0	191	14	26	0	378	0	0	2	0	1	0	42	18	5	9	1	1	24	3	24	9	24	15	0	2	0	0	0	1	
222.5	7	1	10	0	102	15	17	0	198	0	0	0	0	0	0	25	5	4	10	0	1	7	0	3	3	9	2	0	1	0	0	1		
237.5	25	2	3	0	159	22	9	0	136	0	1	1	0	1	0	27	6	7	0	0	0	0	4	4	12	1	0	0	1	0	0	1		
242.5	10	1	7	0	86	17	2	0	69	0	0	1	0	0	0	14	6	5	2	0	0	0	0	3	5	5	0	0	0	0	0	1	1	
251.5	9	0	2	0	91	10	6	0	60	0	0	2	0	0	0	15	7	3	4	0	0	0	0	5	3	6	1	0	0	0	0	1	0	
262.5	9	1	7	1	118	12	6	0	77	0	0	0	0	0	0	16	9	5	6	0	0	1	0	3	0	5	3	0	0	1	0	0	2	

272.5	7	0	4	0	120	24	4	0	91	0	0	3	0	0	0	25	7	5	3	0	0	1	0	4	1	9	1	0	0	0	1	0	1	1
282.5	12	1	8	0	125	16	7	0	152	0	0	1	0	0	0	23	12	3	4	0	0	1	0	8	1	9	0	1	1	0	0	3	1	1
292.5	15	0	5	0	162	13	3	0	151	0	0	2	0	0	0	18	8	4	1	0	0	0	4	5	7	0	0	0	0	0	0	0	1	
302.5	12	2	6	0	116	28	12	0	123	0	0	4	0	1	0	9	6	2	1	0	0	1	0	5	0	7	1	0	0	0	0	0	0	0
311.5	18	2	5	0	197	48	3	0	186	0	0	3	0	1	0	13	8	7	2	0	0	0	0	3	3	9	0	1	0	0	0	0	0	0
321.5	7	0	4	0	118	15	2	0	127	0	0	1	0	0	0	25	5	3	2	0	0	0	1	6	0	8	0	0	0	0	0	0	0	

ANNEXE H

COMPTAGES BRUTS DES FORAMINIFÈRES BENTHIQUES AGGLUTINANTS ET AUTRES TYPES DE MICROFOSSILES DANS LA CAROTTE PG2303

Profondeur réelle (cm)	Foraminifères benthiques agglutinants										Autres types de microfossiles			
	<i>Spiroplectammina biformis</i>	<i>Textularia torquata</i>	<i>Textularia earlandi</i>	<i>Recuvioides turbinatus</i>	<i>Cribrostomoides crassimargo</i>	<i>Eggerelloides advenus</i>	<i>Eggerelloides</i> sp.	<i>Portrochammina karica</i>	<i>Logenammina diffugiformis</i>	Non-identifié	<i>Tintinnopsis fimbriata</i>	Foraminifère planctonique	Valve de diatomée	Grain de pollen
2.5	62	0	27	1	0	0	0	0	0	0	41	1	2	0
9.5	45	4	10	2	0	1	0	0	0	1	74	0	0	1
14.5	174	31	19	14	0	2	0	0	1	2	##	0	0	0
19.5	111	24	12	7	2	2	5	0	2	6	43	0	0	1
24.25	49	27	1	2	1	0	0	0	0	6	38	0	0	0
29.5	116	23	4	0	1	0	0	0	0	0	78	1	0	0
32.5	101	8	11	1	0	0	0	0	0	0	13	0	0	0
37.5	66	16	10	3	1	0	1	0	0	2	59	0	0	0
42.5	14	0	0	0	0	0	1	0	0	3	77	0	0	0
47.5	128	7	5	1	0	0	1	0	0	1	30	0	0	0
52.5	47	23	8	5	0	0	0	0	0	3	12	0	0	0
57.5	34	3	2	0	0	0	0	0	1	2	1	0	0	0
62.5	3	0	0	0	0	0	0	0	0	0	1	0	0	1
72.5	58	17	0	4	0	0	0	0	0	1	0	0	0	0
82.5	25	24	1	1	1	0	0	0	0	0	0	0	0	0
92.5	38	22	3	5	0	0	0	0	0	0	1	0	1	0
101.5	0	1	0	1	0	0	0	3	0	3	0	0	0	2
112.5	26	12	1	14	0	0	0	0	0	3	5	0	0	0
122.5	62	37	0	2	0	0	0	0	0	2	3	0	0	0
132.5	64	31	2	2	0	0	0	0	0	1	3	0	0	1
141.5	15	7	0	2	0	0	0	0	0	0	0	0	0	0
152.5	53	21	0	4	0	0	0	0	0	5	2	0	0	0
162.5	29	14	0	2	0	0	0	0	0	1	2	0	1	1
171.5	51	7	0	3	1	0	1	1	0	3	2	0	0	0
182.5	51	2	0	3	0	0	0	0	0	4	2	0	0	0
192.5	18	2	0	1	0	0	0	0	0	1	2	0	0	0
202.5	55	10	2	12	0	0	0	0	0	1	2	0	0	1
212.5	77	18	5	13	0	0	0	0	0	6	1	0	0	2

222.5	41	13	0	11	0	0	0	0	0	2	7	0	0	0
237.5	27	6	0	0	0	0	0	1	0	0	0	0	0	0
242.5	15	9	0	1	0	0	0	0	0	0	0	0	0	0
251.5	18	4	0	1	0	0	0	0	0	2	1	0	0	0
262.5	11	2	0	0	0	0	0	0	0	0	1	0	0	2
272.5	24	4	0	0	0	0	0	0	0	1	0	0	0	1
282.5	16	5	0	3	0	1	0	1	0	0	2	0	0	0
292.5	16	4	0	1	0	0	0	0	0	1	1	0	0	0
302.5	19	4	0	5	0	0	0	0	0	2	0	1	0	0
311.5	22	3	1	2	1	0	0	1	0	0	0	0	0	0
321.5	24	6	0	1	2	0	0	0	0	1	0	0	0	0

ANNEXE I
COMPTAGES BRUTS DES OSTRACODES DANS LA CAROTTE PG2303

Profondeur réelle (cm)	<i>Paracyprideis pseudopunctillata</i>	<i>Eucythere spp.</i>	<i>Heterocyprideis sorbyana</i>	<i>Loxoconcha venepidermoidea</i>	<i>Roundstomia globulifera</i>	<i>Acanthocythereis danheimensis</i>	<i>Cluthia clutiae</i>	<i>Eucytherura delineata</i>	<i>Semicytherura complanata</i>	<i>Rubilimis mirabilis</i>	<i>Cytheropteron spp.</i>	<i>Cytheropteron elaeani</i>	<i>Cytheropteron suzdalskyi</i>	<i>Cytheropteron sulense</i>	<i>Cytheropteron discoveria ou brastadensis</i>	<i>Cytheropteron biconvexa</i>	<i>Kotoracythere arctoborealis</i>	<i>Normancythere leioderma</i>	Nombre de valves identifiées	Nombre de valves comptées
2.5	0	0	0	0	0	1	0	0	0	0	1	0	0	0	0	0	0	0	3	4
9.5	0	0	0	0	0	0	0	0	0	0	6	0	2	0	0	0	0	0	8	9
14.5	0	0	0	0	0	0	0	0	0	0	2	0	4	0	0	0	0	0	6	9
19.5	1	0	0	0	0	0	0	0	5	1	14	0	8	0	5	0	0	0	34	34
24.25	0	0	0	0	0	0	0	0	0	0	4	0	2	0	0	0	0	0	6	7
29.5	0	0	0	0	0	0	0	0	0	0	3	0	5	0	0	0	0	0	8	9
32.5	0	0	0	0	0	0	0	0	0	0	3	0	3	0	0	0	0	0	6	10
37.5	1	0	0	0	0	0	0	0	0	0	3	0	2	0	0	0	1	0	7	8
42.5	11	0	0	0	0	0	0	0	0	0	4	0	1	0	0	0	1	0	17	21
47.5	23	0	1	0	0	0	3	0	0	1	0	0	3	0	0	0	1	1	33	37
52.5	11	0	0	0	0	0	0	1	0	1	2	0	1	0	0	0	2	0	18	27
57.5	10	0	0	0	4	0	0	0	0	1	2	0	2	2	0	0	0	1	22	26
62.5	1	0	2	0	0	0	0	0	0	0	0	0	0	0	0	0	0	0	3	4
72.5	14	0	0	1	0	0	3	0	0	0	1	0	2	1	1	0	1	1	25	27
82.5	8	0	0	0	0	0	0	0	0	1	5	0	0	0	0	0	3	0	17	24
92.5	1	0	0	0	0	0	0	0	2	4	0	0	2	0	0	0	0	0	9	13
101.5	8	0	0	0	0	0	0	0	0	0	1	0	1	2	0	0	0	0	12	12
112.5	2	0	0	1	0	0	0	0	0	0	0	1	0	0	0	0	0	0	4	5
122.5	1	0	0	0	0	0	1	0	1	3	0	0	0	2	0	0	0	0	8	12
132.5	3	0	0	0	0	0	0	0	0	1	0	0	2	6	0	0	0	0	12	19
141.5	3	0	0	0	0	0	0	0	0	0	0	0	2	3	0	0	0	0	8	8
152.5	18	2	0	0	0	0	0	0	0	2	2	0	5	5	0	0	4	0	38	45
162.5	5	0	0	0	0	0	0	0	0	1	5	4	2	1	0	0	1	0	19	27
171.5	3	0	0	0	0	0	0	0	0	2	2	0	0	3	0	0	0	2	12	12
182.5	20	0	0	0	0	0	2	0	2	0	1	0	0	0	0	0	1	0	26	32
192.5	14	0	0	0	0	0	1	0	1	2	0	1	0	1	0	0	0	0	20	23
202.5	2	0	0	0	0	0	0	0	0	0	3	1	3	2	0	0	0	0	11	20
212.5	2	0	2	0	0	0	0	0	0	3	2	1	6	7	1	2	0	0	26	37
222.5	0	1	0	0	0	0	0	0	3	0	4	1	6	1	1	0	0	0	17	25
237.5	2	0	0	0	0	0	0	0	0	0	0	0	2	2	0	0	0	0	6	6

242.5	0	0	0	0	0	0	1	0	1	0	4	0	1	2	1	0	0	0	10	11
251.5	0	0	0	0	0	0	0	0	0	0	1	0	1	1	0	0	0	0	3	3
262.5	3	0	0	0	0	0	0	0	0	0	2	0	1	1	0	0	0	0	7	7
272.5	3	0	0	0	0	0	0	0	0	0	2	1	4	4	0	0	0	0	14	14
282.5	2	0	0	0	0	0	0	0	0	0	3	0	3	0	1	2	0	0	11	12
292.5	0	0	0	0	0	0	0	0	0	0	2	1	2	1	0	0	0	0	6	10
302.5	1	0	0	0	0	0	0	0	0	1	2	0	0	0	0	0	2	0	6	6
311.5	0	0	0	0	0	0	0	0	0	0	1	0	2	0	0	0	0	0	3	3
321.5	0	0	0	0	0	0	0	0	0	0	3	0	1	0	0	0	0	0	4	6

ANNEXE J
COMPTAGES DES PALYNOMORPHES DANS LA CAROTTE PG2303

	Profondeur réelle (cm)		19.5	72.5	212.5	311.5
Grain de pollen	Arbre	<i>Abies</i>	1			
		<i>Picea</i>	40	37	63	19
		<i>Picea 1/3</i>	34	19	35	20
		<i>Pinus</i>	9	6	7	4
		<i>Pinus 1/3</i>	6	4	9	9
		<i>Thuia/Juniperus</i>	1		1	
		<i>Quercus</i>		3		
		<i>Betula</i>	36	32	48	42
		<i>Alnus spp.</i>				32
	Arbuste	<i>Alnus crispa</i>	56	58	50	
		<i>Alnus incana</i>			1	
		<i>Ericaceae</i>	8	6	8	7
		<i>Salix</i>	6	5	6	3
		<i>Ambrosia</i>			1	
		<i>Artemisia</i>	18	6	12	4
		<i>Liguliflore</i>		1		
		<i>Tubuliflore</i>	4	5	3	3
		<i>Caryophyllaceae</i>			2	
		<i>Chenopodiaceae</i>		2	3	1
Herbe	Herbe	<i>Cyperaceae</i>	79	42	73	31
		<i>Poaceae</i>	40	11	28	14
		<i>Rosaceae</i>	2	2		
		Type Rumex		3		
		<i>Thallictrum</i>			1	
		Autre		3		5
		Non-identifié	6	7	9	1
		<i>Lycopodium annotinum</i>	1		2	4
		<i>Lycopodium clavatum</i>	1	1		4
		<i>Hunerzia type selago</i>			1	
Spore		<i>Selaginella</i>			2	
		Spore monolete	18	20	15	14
		Spore trilete	9	4	3	1
		<i>Sphagnum</i>	34	22	29	19
		<i>Bitectatodinium tepikiense</i>	1			
		<i>Impagidinium pallidum</i>	1			
		<i>Operculodinium centrocarpum</i>	32	5	1	
Dinokyste		<i>O. cent. var. arctic</i>	9			
		<i>Spiniferites elongatus</i>	1			

	<i>Cyst of pentapharsodinium dalei</i>	2			1
	<i>Islandinium brevispinosum</i>	4	4		2
	<i>Islandinium minutum</i>	22	8	8	3
	<i>I. cf. cezare</i>	12	2	3	4
	<i>Echinidinium karaense</i>	2		1	
	<i>Brigantedinium spp.</i>	16	6	13	14
	<i>Brigantedinium simplex</i>	3		1	
	<i>Protoperidinium americanum</i> (type)			5	
	<i>Polykrikos quadratus</i>	5	8	3	
	<i>Peridinium</i>	1		7	
Remanié	Grain de pollen	3	1	3	1
	Gymnosperme	36	8	14	
	Spore monolète				1
	Spore trilète	47	23	36	18
	Autre spore		2	4	1
	Acritarche	1			3
Divers	Dinokyste	8		8	5
	<i>Halodinium</i>	7	11	8	3
	<i>Cymetiosphaera</i>	2		1	
	<i>Pediastrum</i>	26	4	12	2
	Tintinnide	1			
	Lignine de foraminifères	26	8	11	
	<i>Sigmopolis</i>	7		4	5
	Thecamoebien	2	15	14	
	Œuf de copépode		10	5	3
	Vertébré	16	17	39	16
	Mandibule	2	5	2	
	Spore de champignon	20		7	1
	<i>Radiosperma</i>				3

RÉFÉRENCES

- Abram, N. J., McGregor, H. V., Tierney, J. E., Evans, M. N., McKay, N. P. et Kaufman, D. S. (2016). Early onset of industrial-era warming across the oceans and continents. *Nature*, 536(7617), 411-418.
- Agatha, S. (2008). Redescription of the tintinnid ciliate *Tintinnopsis fimbriata* Meunier, 1919 (Spirotricha, Choretrichida) from coastal waters of Northern Germany. *Denisia*, 23, 261.
- Allan, E., de Vernal, A., Seidenkrantz, M. S., Briner, J. P., Hillaire-Marcel, C., Pearce, C., . . . Nielsen, M. T. (2021). Insolation vs. meltwater control of productivity and sea surface conditions off SW Greenland during the Holocene. *Boreas*, 50(3), 631-651.
- Alve, E. (2003). A common opportunistic foraminiferal species as an indicator of rapidly changing conditions in a range of environments. *Estuarine, Coastal and Shelf Science*, 57(3), 501-514.
- Alve, E. (2010). Benthic foraminiferal responses to absence of fresh phytodetritus: A two-year experiment. *Marine Micropaleontology*, 76(3-4), 67-75.
- Anchukaitis, K. J., D'Arrigo, R. D., Andreu-Hayles, L., Frank, D., Verstege, A., Curtis, A., . . . Cook, E. R. (2013). Tree-ring-reconstructed summer temperatures from northwestern North America during the last nine centuries. *Journal of Climate*, 26(10), 3001-3012.
- Anderson, D. M., Fachon, E., Pickart, R. S., Lin, P., Fischer, A. D., Richlen, M. L., . . . Bahr, F. (2021). Evidence for massive and recurrent toxic blooms of *Alexandrium catenella* in the Alaskan Arctic. *Proceedings of the National Academy of Sciences*, 118(41), e2107387118.
- Andrachuk, M. et Pearce, T. (2010). Vulnerability and adaptation in two communities in the Inuvialuit Settlement Region. Dans *Community adaptation and vulnerability in arctic regions* (p. 63-81). Springer.
- Arrigo, K. R. et van Dijken, G. L. (2015). Continued increases in Arctic Ocean primary production. *Progress in Oceanography*, 136, 60-70.
- Astakhov, A., Shi, X., Darin, A., Kalugin, I., Hu, L., Tsoy, I., . . . Babich, V. (2020). Reconstructing ice conditions in the southern Chukchi Sea during the last millennium based on chemical composition of sediments and diatom assemblages. *Marine Geology*, 427, 106220.

Austin, W.E.N. et Kroon, D., 1996. Lateglacial sedimentology, foraminifera and stable isotope stratigraphy of the Hebridean Continental Shelf, northwest Scotland. *Geological Society of London* 111(1), 187-213.

Bauch, H., Erlenkeuser, H., Bauch, D., Müller-Lupp, T. et Taldenkova, E. (2004). Stable oxygen and carbon isotopes in modern benthic foraminifera from the Laptev Sea shelf: implications for reconstructing proglacial and profluvial environments in the Arctic. *Marine Micropaleontology*, 51(3-4), 285-300.

Bélanger, S., Babin, M. et Tremblay, J. É. (2013). Increasing cloudiness in Arctic damps the increase in phytoplankton primary production due to sea ice receding. *Biogeosciences*, 10(6), 4087-4101

Bell, L. E., Bluhm, B. A. et Iken, K. (2016). Influence of terrestrial organic matter in marine food webs of the Beaufort Sea shelf and slope. *Marine Ecology Progress Series*, 550, 1-24.

Bereiter, B., Eggleston, S., Schmitt, J., Nehrbass-Ahles, C., Stocker, T. F., Fischer, H., . . . Chappellaz, J. (2015). Revision of the EPICA Dome C CO₂ record from 800 to 600 kyr before present. *Geophysical Research Letters*, 42(2), 542-549.

Bird, B. W., Abbott, M. B., Finney, B. P. et Kutchko, B. (2009). A 2000 year varve-based climate record from the central Brooks Range, Alaska. *Journal of Paleolimnology*, 41(1), 25-41.

Blais, M., Ardyna, M., Gosselin, M., Dumont, D., Bélanger, S., Tremblay, J. É., . . . Poulin, M. (2017). Contrasting interannual changes in phytoplankton productivity and community structure in the coastal Canadian Arctic Ocean. *Limnology and Oceanography*, 62(6), 2480-2497.

Boivin-Rioux, A., Starr, M., Chassé, J., Scarratt, M., Perrie, W. et Long, Z. (2021). Predicting the effects of climate change on the occurrence of the toxic dinoflagellate *Alexandrium catenella* along Canada's east coast. *Frontiers in Marine Science*, 7, 1171.

Bonsell, C. et Dunton, K. H. (2018). Long-term patterns of benthic irradiance and kelp production in the central Beaufort sea reveal implications of warming for Arctic inner shelves. *Progress in Oceanography*, 162, 160-170.

Brewster, J., Neumann, D., Ostertag, S. et Loseto, L. (2016). Traditional Ecological Knowledge (TEK) at Shingle Point, YK: Observations on Changes in the Environment and Fish Populations. *Characterizing the diet and habitat niches of coastal fish populations in the Beaufort Sea Tarium Niryutait Marine Protected Area*, 121.

Bringué, M. et Rochon, A. (2012). Late Holocene paleoceanography and climate variability over the Mackenzie slope (Beaufort sea, Canadian Arctic). *Marine Geology*, 291, 83-96.

- Burkovsky, I. (1976). Ecology of Tintinnida (Ciliata) of the White Sea. *Zool. zh*, 55, 497-507.
- Cage, A. G., Pieńkowski, A. J., Jennings, A., Knudsen, K. L. et Seidenkrantz, M.-S. (2021). Comparative analysis of six common foraminiferal species of the genera Cassidulina, Paracassidulina, and Islandiella from the Arctic–North Atlantic domain. *Journal of Micropalaeontology*, 40(1), 37-60.
- Carmack, E. C. et Macdonald, R. W. (2002). Oceanography of the Canadian Shelf of the Beaufort Sea: a setting for marine life. *Arctic*, 29-45.
- Cearreta, A., Irabien, M. J., Leorri, E., Yusta, I., Croudace, I. et Cundy, A. (2000). Recent anthropogenic impacts on the Bilbao estuary, northern Spain: geochemical and microfaunal evidence. *Estuarine, Coastal and Shelf Science*, 50(4), 571-592.
- Cesbron, F., Geslin, E., Jorissen, F., Delgard, M.-L., Charrieau, L., Deflandre, B., . . . Metzger, E. (2016). Vertical distribution and respiration rates of benthic foraminifera: Contribution to aerobic remineralization in intertidal mudflats covered by *Zostera noltei* meadows. *Estuarine, Coastal and Shelf Science*, 179, 23-38.
- Choudhury, A. et Dick, T. A. (1997). Parasites of the broad whitefish from the Mackenzie Delta.
- Clark, P. U., Alley, R. B. et Pollard, D. (1999). Northern Hemisphere ice-sheet influences on global climate change. *Science*, 286(5442), 1104-1111.
- Comeau, A. M., Li, W. K., Tremblay, J.-É., Carmack, E. C. et Lovejoy, C. (2011). Arctic Ocean microbial community structure before and after the 2007 record sea ice minimum. *PloS one*, 6(11), e27492.
- Couture, N. J. et Pollard, W. H. (2017). A model for quantifying ground-ice volume, Yukon Coast, Western Arctic Canada. *Permafrost and Periglacial Processes*, 28(3), 534-542.
- Cronin, T. M., Gemery, L., Olds, B. M., Regnier, A. M., Poirier, R. K. et Sui, S. (2022). Abrupt Quaternary Ocean-ice Events in the Arctic: Evidence from the Ostracode Rabilimis. *Micropaleontology*, 68(3), 232-242.
- Davin, S. (2019). Oceanographic changes off Canadian coasts in the 20th and 21st centuries: geochemical perspectives from deep-water corals. [Thèse de doctorat, Université du Québec à Montréal].
- de Vernal, A., Radi, T., Zaragosi, S., Van Nieuwenhove, N., Rochon, A., Allan, E., . . . Limoges, A. (2020). Distribution of common modern dinoflagellate cyst taxa in surface sediments of the Northern Hemisphere in relation to environmental parameters: The new n= 1968 database. *Marine Micropaleontology*, 159, 101796.

Doxaran, D., Devred, E. et Babin, M. (2015). A 50% increase in the mass of terrestrial particles delivered by the Mackenzie River into the Beaufort Sea (Canadian Arctic Ocean) over the last 10 years. *Biogeosciences*, 12(11), 3551-3565.

Dunton, K. H., Weingartner, T. et Carmack, E. C. (2006). The nearshore western Beaufort Sea ecosystem: circulation and importance of terrestrial carbon in arctic coastal food webs. *Progress in Oceanography*, 71(2-4), 362-378.

Durantou, L., Rochon, A., Ledu, D., Massé, G., Schmidt, S. et Babin, M. (2012). Quantitative reconstruction of sea-surface conditions over the last 150 yr in the Beaufort Sea based on dinoflagellate cyst assemblages: the role of large-scale atmospheric circulation patterns. *Biogeosciences*, 9(12), 5391-5406.

EBA Engineering Consultants Ltd. (1992). *Proceedings of the Beaufort Sea granular resources workshop*. Part 1: Reports on NOGAP regional studies.

Echols, R. J. et Fowler, G. A. (1973). Agglutinated tintinnid loricae from some Recent and Late Pleistocene shelf sediments. *Micropaleontology*, 431-443.

Ehn, J. K., Reynolds, R. A., Stramski, D., Doxaran, D., Lansard, B. et Babin, M. (2019). Patterns of suspended particulate matter across the continental margin in the Canadian Beaufort Sea during summer.

Environnement et changement climatique Canada. (2020). Données historiques climatiques. Récupéré le 9 octobre 2020 de https://climate.weather.gc.ca/index_e.html.

Environnement et changement climatique Canada. (2020). Données hydrométriques historiques. Récupéré le 25 avril 2020 de https://eau.ec.gc.ca/mainmenu/historical_data_index_f.html.

Erlenkeuser, H. et von Grafenstein, U. (1999). Stable oxygen isotope ratios in benthic carbonate shells of ostracoda, foraminifera, and bivalvia from surface sediments of the Laptev Sea, summer 1993 and 1994. Dans *Land-Ocean Systems in the Siberian Arctic* (p. 503-514). Springer.

Falardeau, J. et Ouellet-Bernier, M.-M. (en prép.). *Stories about Climate*. [Cahier d'activités].

Falardeau, M., Bennett, E. M., Else, B., Fisk, A., Mundy, C., Choy, E. S., ... Moore, J.-S. (2022). Biophysical indicators and Indigenous and Local Knowledge reveal climatic and ecological shifts with implications for Arctic Char fisheries. *Global Environmental Change*, 74, 102469.

Fechhelm, R. G., Streever, B. et Gallaway, B. J. (2007). The Arctic cisco (*Coregonus autumnalis*) subsistence and commercial fisheries, Colville River, Alaska: a conceptual model. *Arctic*, 421-429.

Fetterer, F., Knowles, K., Meier, W. N., Savoie, M. et Windnagel, A. K. (2017). Sea Ice Index, Version 3 [Sea Ice Index Monthly Data with Statistics]. Boulder, Colorado USA, National Snow and Ice Data Center. Récupéré le 23 novembre 2022 de <https://doi.org/10.7265/N5K072F8>.

Ford, J., Clark, D., Pearce, T., Berrang-Ford, L., Copland, L., Dawson, J., . . . Harper, S. (2019). Changing access to ice, land and water in Arctic communities. *Nature Climate Change*, 9(4), 335-339.

Frey, K. E., Moore, G., Cooper, L. W. et Grebmeier, J. M. (2015). Divergent patterns of recent sea ice cover across the Bering, Chukchi, and Beaufort seas of the Pacific Arctic Region. *Progress in Oceanography*, 136, 32-49.

Fritz, M., Vonk, J. E. et Lantuit, H. (2017). Collapsing arctic coastlines. *Nature Climate Change*, 7(1), 6-7.

Gallagher, C. P., Courtney, M. B., Seitz, A. C., Lea, E. V. et Howland, K. L. (2021). Ocean-entry timing and marine habitat-use of Canadian Dolly Varden: Dispersal among conservation, hydrocarbon exploration, and shipping areas in the Beaufort Sea. *Estuarine, Coastal and Shelf Science*, 262, 107609.

Gemery, L., Cronin, T. M., Briggs, W. M., Brouwers, E. M., Schornikov, E. I., Stepanova, A., . . . Yasuhara, M. (2017). An Arctic and Subarctic ostracode database: biogeographic and paleoceanographic applications. *Hydrobiologia*, 786(1), 59-95.

Gemery, L., Cronin, T. M., Cooper, L. W., Dowsett, H. J. et Grebmeier, J. M. (2021). Biogeography and ecology of Ostracoda in the US northern Bering, Chukchi, and Beaufort Seas. *PloS one*, 16(5), e0251164.

Gemery, L., Cronin, T. M., Cooper, L. W. et Grebmeier, J. M. (2013). Temporal changes in benthic ostracode assemblages in the Northern Bering and Chukchi Seas from 1976 to 2010. *Deep Sea Research Part II: Topical Studies in Oceanography*, 94, 68-79.

Gemery, L., Cronin, T.M., Cooper, L. W., Roberts, L. R., Keigwin, L. D., Addison, J. A., Leng, M. J., . . . Schwartz, V. (2023). Multi-proxy record of ocean-climate variability during the last two millennia on the Mackenzie Shelf, Beaufort Sea. *Micropaleontology*, 69(3), 345-366.

George, J. C., Druckenmiller, M. L., Laidre, K. L., Suydam, R. et Person, B. (2015). Bowhead whale body condition and links to summer sea ice and upwelling in the Beaufort Sea. *Progress in Oceanography*, 136, 250-262.

Global Climate Change: Evidence. (2021). Récupéré le 23 février 2021 de <http://climate.nasa.gov/evidence/>

Global Monitoring Laboratory. (2021). Trends in Atmospheric Carbon Dioxide, Carbon Cycle Greenhouse Gases, National Oceanic and Atmospheric Administration. Récupéré le 23 février 2021 de <https://www.esrl.noaa.gov/gmd/ccgg/trends/>

Grebmeier, J. M. (2012). Shifting patterns of life in the Pacific Arctic and sub-Arctic seas. *Annual review of marine science*, 4, 63-78.

Grebmeier, J. M. et Barry, J. (2007). Benthic processes in polynyas. *Elsevier oceanography series*, 74, 363-390.

Grotheer, H., Meyer, V., Riedel, T., Pfalz, G., Mathieu, L., Heftet, J., . . . Fritz, M. (2020). Burial and origin of permafrost-derived carbon in the nearshore zone of the southern Canadian Beaufort Sea. *Geophysical Research Letters*, 47(3), e2019GL085897.

Guilbault, J.-P., Barrie, J. V., Conway, K., Lapointe, M. et Radi, T. (2003). Paleoenvironments of the Strait of Georgia, British Columbia during the last deglaciation: microfaunal and microfloral evidence. *Quaternary Science Reviews*, 22(8-9), 839-857.

Günther, F., Overduin, P. P., Yakshina, I. A., Opel, T., Baranskaya, A. V. et Grigoriev, M. N. (2015). Observing Muostakh disappear: permafrost thaw subsidence and erosion of a ground-ice-rich island in response to arctic summer warming and sea ice reduction. *The Cryosphere*, 9(1), 151-178.

Hart, L. M., Bond, M. H., May-McNally, S. L., Miller, J. A. et Quinn, T. P. (2015). Use of otolith microchemistry and stable isotopes to investigate the ecology and anadromous migrations of Northern Dolly Varden from the Egegik River, Bristol Bay, Alaska. *Environmental Biology of Fishes*, 98(6), 1633-1643.

Heikkilä, M., Ribeiro, S., Weckström, K. et Pieńkowski, A. J. (2022). Predicting the future of coastal marine ecosystems in the rapidly changing Arctic: The potential of palaeoenvironmental records. *Anthropocene*, 37, 100319.

Hill, P. R. et Nadeau, O. C. (1989). Storm-dominated sedimentation on the inner shelf of the Canadian Beaufort Sea. *Journal of Sedimentary Research*, 59, 455-468.

Holmes, R. M., McClelland, J. W., Peterson, B. J., Tank, S. E., Bulygina, E., Eglinton, T. I., . . . Repeta, D. J. (2012). Seasonal and annual fluxes of nutrients and organic matter from large rivers to the Arctic Ocean and surrounding seas. *Estuaries and Coasts*, 35(2), 369-382.

IPCC (2014). Pachauri, R. et Meyer, L. Climate Change 2014: Synthesis Report. Contribution of Working Groups I, II and III to the Fifth Assessment Report of the Intergovernmental Panel on Climate Change.

IPCC (2021). Masson-Delmotte, V., Zhai, P., Pirani, A., Connors, S. L., Péan, C., Berger, S., . . . Gomis, M. Climate change 2021: the physical science basis. *Contribution of working group I to the sixth assessment report of the intergovernmental panel on climate change*, 2.

Irrgang, A. M., Lantuit, H., Gordon, R. R., Piskor, A. et Manson, G. K. (2019). Impacts of past and future coastal changes on the Yukon coast—threats for cultural sites, infrastructure, and travel routes. *Arctic Science*, 5(2), 107-126.

Jennings, A., Andrews, J., Reilly, B., Walczak, M., Jakobsson, M., Mix, A., . . . Cheseby, M. (2020). Modern foraminiferal assemblages in northern Nares Strait, Petermann Fjord, and beneath Petermann ice tongue, NW Greenland. *Arctic, Antarctic, and Alpine Research*, 52(1), 491-511.

Jong, D., Bröder, L., Tanski, G., Fritz, M., Lantuit, H., Tesi, T., . . . Vonk, J. E. (2020). Nearshore zone dynamics determine pathway of organic carbon from eroding permafrost coasts. *Geophysical research letters*, 47(15), e2020GL088561.

Jouzel, J., Masson-Delmotte, V., Cattani, O., Dreyfus, G., Falourd, S., Hoffmann, G., . . . Chappellaz, J. (2007). Orbital and millennial Antarctic climate variability over the past 800,000 years. *science*, 317(5839), 793-796.

Juhls, B. (2021). Land-Ocean Interactions in Arctic Coastal Waters: Ocean Colour Remote Sensing and Current Carbon Fluxes to the Arctic Ocean [Thèse de doctorat, Freie Universität Berlin].

Kinnard, C., Zdanowicz, C. M., Fisher, D. A., Isaksson, E., de Vernal, A. et Thompson, L. G. (2011). Reconstructed changes in Arctic sea ice over the past 1,450 years. *Nature*, 479(7374), 509-512.

Klein, K. P., Lantuit, H., Heim, B., Fell, F., Doxaran, D. et Irrgang, A. M. (2019). Long-term high-resolution sediment and sea surface temperature spatial patterns in Arctic nearshore waters retrieved using 30-year landsat archive imagery. *Remote Sensing*, 11(23), 2791.

Kohlbach, D., Ferguson, S. H., Brown, T. A. et Michel, C. (2019). Landfast sea ice-benthic coupling during spring and potential impacts of system changes on food web dynamics in Eclipse Sound, Canadian Arctic. *Marine Ecology Progress Series*, 627, 33-48.

Kolling, H. M., Stein, R., Fahl, K., Sadatzki, H., de Vernal, A. et Xiao, X. (2020). Biomarker distributions in (sub)-Arctic surface sediments and their potential for sea ice reconstructions. *Geochemistry, Geophysics, Geosystems*, 21(10), e2019GC008629.

Korsun, S. et Hald, M. (2000). Seasonal dynamics of benthic foraminifera in a glacially fed fjord of Svalbard, European Arctic. *The Journal of Foraminiferal Research*, 30(4), 251-271.

Kulikov, E., Carmack, E. et Macdonald, R. (1998). Flow variability at the continental shelf break of the Mackenzie Shelf in the Beaufort Sea. *Journal of Geophysical Research: Oceans*, 103(C6), 12725-12741.

Kutos, O., Rochon, A. et Montero-Serrano, J. C. (2021). Evolution of palaeo-sea-surface conditions and sediment dynamics over the last 2700 years on the Mackenzie Slope, Beaufort Sea (Canadian Arctic). *Boreas*.

Lansard, B., Mucci, A., Miller, L. A., Macdonald, R. W. et Gratton, Y. (2012). Seasonal variability of water mass distribution in the southeastern Beaufort Sea determined by total alkalinity and $\delta^{18}\text{O}$. *Journal of Geophysical Research: Oceans*, 117(C3).

Lantuit, H., Overduin, P. P., Couture, N., Wetterich, S., Aré, F., Atkinson, D., . . . Forbes, D. L. (2012). The Arctic coastal dynamics database: a new classification scheme and statistics on Arctic permafrost coastlines. *Estuaries and Coasts*, 35(2), 383-400.

Lefebvre, K. A., Quakenbush, L., Frame, E., Huntington, K. B., Sheffield, G., Stimmelmayr, R., . . . Goldstein, T. (2016). Prevalence of algal toxins in Alaskan marine mammals foraging in a changing arctic and subarctic environment. *Harmful Algae*, 55, 13-24.

Lewis, K., Van Dijken, G. et Arrigo, K. R. (2020). Changes in phytoplankton concentration now drive increased Arctic Ocean primary production. *Science*, 369(6500), 198-202.

Li, W. K. W., McLaughlin, F. A., Lovejoy, C. et Carmack, E. C. (2009). Smallest algae thrive as the Arctic Ocean freshens. *Science*, 326(5952), 539-539.

Li, Y., He, R., McGillicuddy Jr, D. J., Anderson, D. M. et Keafer, B. A. (2009). Investigation of the 2006 *Alexandrium fundyense* bloom in the Gulf of Maine: in-situ observations and numerical modeling. *Continental Shelf Research*, 29(17), 2069-2082.

Lin, P., Pickart, R. S., Fissel, D., Ross, E., Kasper, J., Bahr, F., . . . Melling, H. (2020). Circulation in the vicinity of Mackenzie Canyon from a year-long mooring array. *Progress in Oceanography*, 187, 102396.

Lin, P., Pickart, R. S., Stafford, K. M., Moore, G., Torres, D. J., Bahr, F. et Hu, J. (2016). Seasonal variation of the Beaufort shelfbreak jet and its relationship to Arctic cetacean occurrence. *Journal of Geophysical Research: Oceans*, 121(12), 8434-8454.

Lisiecki, L. E. (2010). Links between eccentricity forcing and the 100,000-year glacial cycle. *Nature geoscience*, 3(5), 349-352.

Logerwell, E., Rand, K., Danielson, S. et Sousa, L. (2018). Environmental drivers of benthic fish distribution in and around Barrow Canyon in the northeastern Chukchi Sea and western Beaufort Sea. *Deep Sea Research Part II: Topical Studies in Oceanography*, 152, 170-181.

Mackay, J. R. (1959). Glacier ice-thrust features of the Yukon coast. *Geographical Bulletin*, 13(5), 21.

Mackensen, A. (2008). On the use of benthic foraminiferal $\delta^{13}\text{C}$ in palaeoceanography: constraints from primary proxy relationships. *Geological Society, London, Special Publications*, 303(1), 121-133.

Madsen, H. B. et Knudsen, K. L. (1994). Recent foraminifera in shelf sediments of the Scoresby Sund fjord, East Greenland. *Boreas*, 23(4), 495-504.

Mann, M. E. (2007). Climate over the past two millennia. *Annual Review of Earth and Planetary Sciences*, 35(1), 111-136.

Mann, M. E., Zhang, Z., Rutherford, S., Bradley, R. S., Hughes, M. K., Shindell, D., . . . Ni, F. (2009). Global signatures and dynamical origins of the Little Ice Age and Medieval Climate Anomaly. *science*, 326(5957), 1256-1260.

Mantua, N. J., Hare, S. R., Zhang, Y., Wallace, J. M. et Francis, R. C. (1997). A Pacific interdecadal climate oscillation with impacts on salmon production. *Bulletin of the american Meteorological Society*, 78(6), 1069-1080.

Mathis, J. T., Pickart, R. S., Hansell, D. A., Kadko, D. et Bates, N. R. (2007). Eddy transport of organic carbon and nutrients from the Chukchi Shelf: Impact on the upper halocline of the western Arctic Ocean. *Journal of Geophysical Research: Oceans*, 112(C5).

McCorkle, D. C., Corliss, B. H. et Farnham, C. A. (1997). Vertical distributions and stable isotopic compositions of live (stained) benthic foraminifera from the North Carolina and California continental margins. *Deep Sea Research Part I: Oceanographic Research Papers*, 44(6), 983-1024.

McDougall, K. A., Brouwers, E. M. et Smith, P. (1986). *Micropaleontology and sedimentology of the PB borehole series, Prudhoe Bay, Alaska*. US Government Printing Office Washington, DC.

McLaughlin, F. A. et Carmack, E. C. (2010). Deepening of the nutricline and chlorophyll maximum in the Canada Basin interior, 2003–2009. *Geophysical Research Letters*, 37(24).

Meier, W. N., Fetterer, F., Savoie, M., Mallory, S., Duerr, R. et Stroeve, J. (2017). NOAA/NSIDC Climate Data Record of Passive Microwave Sea Ice Concentration, Version 3. [goddard_merged_seaice_conc]. Boulder, Colorado USA. NSIDC: National Snow and Ice Data Center. Récupéré en janvier 2020 de <https://doi.org/10.7265/N59P2ZTG>.

Meier, W. N. et Stroeve, J. (2022). An Updated Assessment of the Changing Arctic Sea Ice Cover. *Oceanography*, 35(2).

Meunier, A. (1919). Mikroplankton de la mer Flamande. III. Les Péridiniens. *Mémoires du Musée Royal d'Histoire Naturelle de Belgique*, 8, 1-116.

Milankovitch, M. (1941). Canon of insolation and the iceage problem. *Königlich Serbische Akademie Beograd Special Publication*, 132.

Mioduszewski, J., Vavrus, S. et Wang, M. (2018). Diminishing Arctic sea ice promotes stronger surface winds. *Journal of Climate*, 31(19), 8101-8119.

Mol, J., Thomas, H., Myers, P. G., Hu, X. et Mucci, A. (2018). Inorganic carbon fluxes on the Mackenzie Shelf of the Beaufort Sea. *Biogeosciences*, 15(4), 1011-1027.

Morrison, C. (2017). Life history strategies of northern form Dolly Varden (*Salvelinus malma malma*) in the western Canadian Arctic.

Mulligan, R. P. et Perrie, W. (2019). Circulation and structure of the Mackenzie River plume in the coastal Arctic Ocean. *Continental Shelf Research*, 177, 59-68.

Mulligan, R. P., Perrie, W. et Solomon, S. (2010). Dynamics of the Mackenzie River plume on the inner Beaufort shelf during an open water period in summer. *Estuarine, Coastal and Shelf Science*, 89(3), 214-220.

Murray, J. W. (2006). *Ecology and applications of benthic foraminifera*. Cambridge university press.

Nguyen, L., Pilfold, N. W., Derocher, A. E., Stirling, I., Bohart, A. M. et Richardson, E. (2017). Ringed seal (*Pusa hispida*) tooth annuli as an index of reproduction in the Beaufort Sea. *Ecological Indicators*, 77, 286-292.

Nicolle, M., Debret, M., Massei, N., Colin, C., Devernal, A., Divine, D., . . . Linderholm, H. W. (2018). Climate variability in the subarctic area for the last 2 millennia. *Climate of the Past*, 14(1), 101-116.

- Nielsen, D. M., Pieper, P., Barkhordarian, A., Overduin, P., Ilyina, T., Brovkin, V., . . . Dobrynin, M. (2022). Increase in Arctic coastal erosion and its sensitivity to warming in the twenty-first century. *Nature Climate Change*, 12(3), 263-270.
- Notz, D. et Stroeve, J. (2016). Observed Arctic sea-ice loss directly follows anthropogenic CO₂ emission. *Science*, 354(6313), 747-750.
- Obu, J., Lantuit, H., Fritz, M., Pollard, W. H., Sachs, T. et Günther, F. (2016). Relation between planimetric and volumetric measurements of permafrost coast erosion: a case study from Herschel Island, western Canadian Arctic. *Polar Research*, 35(1), 30313.
- Olivier, F., Gaillard, B., Thébault, J., Meziane, T., Tremblay, R., Dumont, D., . . . Chauvaud, L. (2020). Shells of the bivalve *Astarte moerchi* give new evidence of a strong pelagic-benthic coupling shift occurring since the late 1970s in the North Water polynya. *Philosophical Transactions of the Royal Society A*, 378(2181), 20190353.
- Overeem, I., Anderson, R. S., Wobus, C. W., Clow, G. D., Urban, F. E. et Matell, N. (2011). Sea ice loss enhances wave action at the Arctic coast. *Geophysical Research Letters*, 38(17).
- Papik, R., Marschke, M. et Ayles, G. B. (2003). *Inuvialuit traditional ecological knowledge of fisheries in rivers west of the Mackenzie River in the Canadian Arctic*. Canada/Inuvialuit Fisheries Joint Management Committee Technical Report Series.
- Paranjape, M. A. (1987). The seasonal cycles and vertical distribution of tintinnines in Bedford Basin, Nova Scotia, Canada. *Canadian Journal of Zoology*, 65(1), 41-48.
- Pickart, R. S. (2004). Shelfbreak circulation in the Alaskan Beaufort Sea: Mean structure and variability. *Journal of Geophysical Research: Oceans*, 109(C4).
- Pickart, R. S., Spall, M. A. et Mathis, J. T. (2013). Dynamics of upwelling in the Alaskan Beaufort Sea and associated shelf–basin fluxes. *Deep Sea Research Part I: Oceanographic Research Papers*, 76, 35-51.
- Pickart, R. S., Spall, M. A., Moore, G. W., Weingartner, T. J., Woodgate, R. A., Aagaard, K. et Shimada, K. (2011). Upwelling in the Alaskan Beaufort Sea: Atmospheric forcing and local versus non-local response. *Progress in Oceanography*, 88(1-4), 78-100.
- Pierce, R. W. et Turner, J. T. (1993). Global biogeography of marine tintinnids. *Marine Ecology Progress Series*, 94, 11-26.
- Poitevin, P., Thébault, J., Siebert, V., Donnet, S., Archambault, P., Doré, J., . . . Lazure, P. (2019). Growth response of *Arctica islandica* to North Atlantic oceanographic conditions since 1850. *Frontiers in Marine Science*, 6, 483.

- Polyak, L., Korsun, S., Febo, L. A., Stanovoy, V., Khusid, T., Hald, M., . . . Lubinski, D. J. (2002). Benthic foraminiferal assemblages from the southern Kara Sea, a river-influenced Arctic marine environment. *The Journal of Foraminiferal Research*, 32(3), 252-273.
- Polyak, L., Stanovoy, V. et Lubinski, D. J. (2003). Stable isotopes in benthic foraminiferal calcite from a river-influenced Arctic marine environment, Kara and Pechora Seas. *Paleoceanography*, 18(1).
- Porter, T. J., Pisaric, M. F., Kokelj, S. V. et deMontigny, P. (2013). A ring-width-based reconstruction of June–July minimum temperatures since AD 1245 from white spruce stands in the Mackenzie Delta region, northwestern Canada. *Quaternary Research*, 80(2), 167-179.
- Radosavljevic, B., Lantuit, H., Pollard, W., Overduin, P., Couture, N., Sachs, T., . . . Fritz, M. (2016). Erosion and flooding—threats to coastal infrastructure in the Arctic: a case study from Herschel Island, Yukon Territory, Canada. *Estuaries and Coasts*, 39(4), 900-915.
- Rainville, L. et Woodgate, R. A. (2009). Observations of internal wave generation in the seasonally ice-free Arctic. *Geophysical Research Letters*, 36(23).
- Rantanen, M., Karpechko, A. Y., Lipponen, A., Nordling, K., Hyvärinen, O., Ruosteenaja, K., . . . Laaksonen, A. (2022). The Arctic has warmed nearly four times faster than the globe since 1979. *Communications Earth & Environment*, 3(1), 1-10.
- Ravelo, A. C. et Hillaire-Marcel, C. (2007). Chapter eighteen the use of oxygen and carbon isotopes of foraminifera in paleoceanography. *Developments in marine geology*, 1, 735-764.
- Reimnitz, E., McCormick, M., McDougall, K. et Brouwers, E. (1993). Sediment export by ice rafting from a coastal polynya, Arctic Alaska, USA. *Arctic and Alpine Research*, 25(2), 83-98.
- Retamal, L., Bonilla, S. et Vincent, W. F. (2008). Optical gradients and phytoplankton production in the Mackenzie River and the coastal Beaufort Sea. *Polar Biology*, 31(3), 363-379.
- Richerol, T., Rochon, A., Blasco, S., Scott, D. B., Schell, T. M. et Bennett, R. J. (2008). Evolution of paleo sea-surface conditions over the last 600 years in the Mackenzie Trough, Beaufort Sea (Canada). *Marine Micropaleontology*, 68(1-2), 6-20.
- Rogers, G., Roff, J. et Lynn, D. (1981). Tintinnids of Chesterfield Inlet, Northwest Territories. *Canadian Journal of Zoology*, 59(12), 2360-2364.

Royer, D. L. (2006). CO₂-forced climate thresholds during the Phanerozoic. *Geochimica et Cosmochimica Acta*, 70(23), 5665-5675.

Scharffenberg, K. C., MacPhee, S. A. et Loseto, L. L. (2020). Upriver sightings of beluga whales (*Delphinapterus leucas*) follow storm surges and high water in the Mackenzie Delta, Northwest Territories, Canada. *Arctic Science*, 7(3), 679-689.

Scharffenberg, K. C., Whalen, D., MacPhee, S. A., Marcoux, M., Iacozza, J., Davoren, G. et Loseto, L. L. (2019). Oceanographic, ecological, and socio-economic impacts of an unusual summer storm in the Mackenzie Estuary. *Arctic Science*, 6(2), 62-76.

Schell, T. M., Moss, T. J., Scott, D. B. et Rochon, A. (2008). Paleo-sea ice conditions of the Amundsen Gulf, Canadian Arctic Archipelago: Implications from the foraminiferal record of the last 200 years. *Journal of Geophysical Research: Oceans*, 113(C3).

Schulze, L. M. et Pickart, R. S. (2012). Seasonal variation of upwelling in the Alaskan Beaufort Sea: Impact of sea ice cover. *Journal of Geophysical Research: Oceans*, 117(C6).

Scott, D. B., Schell, T., Rochon, A. et Blasco, S. (2008). Modern benthic foraminifera in the surface sediments of the Beaufort Shelf, Slope and Mackenzie Trough, Beaufort Sea, Canada: Taxonomy and summary of surficial distributions. *The Journal of Foraminiferal Research*, 38(3), 228-250.

Scott, D. B., Schell, T., St-Onge, G., Rochon, A. et Blasco, S. (2009). Foraminiferal assemblage changes over the last 15,000 years on the Mackenzie-Beaufort Sea Slope and Amundsen Gulf, Canada: Implications for past sea ice conditions. *Paleoceanography*, 24(2).

Seidenkrantz, M.-S. (2013). Benthic foraminifera as palaeo sea-ice indicators in the subarctic realm—examples from the Labrador Sea–Baffin Bay region. *Quaternary Science Reviews*, 79, 135-144.

Seidenstein, J. L., Cronin, T. M., Gemery, L., Keigwin, L. D., Pearce, C., Jakobsson, M., . . . Driscoll, N. W. (2018). Late Holocene paleoceanography in the Chukchi and Beaufort Seas, Arctic Ocean, based on benthic foraminifera and ostracodes. *arktos*, 4(1), 23.

Semiletov, I., Pipko, I., Gustafsson, Ö., Anderson, L. G., Sergienko, V., Pugach, S., . . . Bröder, L. (2016). Acidification of East Siberian Arctic Shelf waters through addition of freshwater and terrestrial carbon. *Nature Geoscience*, 9(5), 361-365.

Serreze, M. C. et Barry, R. G. (2011). Processes and impacts of Arctic amplification: A research synthesis. *Global and planetary change*, 77(1-2), 85-96.

- Shackleton, N. J. (2000). The 100,000-year ice-age cycle identified and found to lag temperature, carbon dioxide, and orbital eccentricity. *Science*, 289(5486), 1897-1902.
- Souto, S. (1979). Tintinnidos del Atlántico Sudoccidental y Antártida Argentina (Protozoa, Ciliata): Estudio taxonómico, distribucional y ecológico. Universidad de Buenos Aires. Facultad de Ciencias Exactas y Naturales.
- Speetjens, N. J., Tanski, G., Martin, V., Wagner, J., Richter, A., Hugelius, G., . . . Koch, B. P. (2022). Dissolved organic matter characterization in soils and streams in a small coastal low-Arctic catchment. *Biogeosciences*, 19(12), 3073-3097.
- Stepanova, A., Taldenkova, E. et Bauch, H. A. (2003). Recent Ostracoda from the Laptev Sea (Arctic Siberia): species assemblages and some environmental relationships. *Marine Micropaleontology*, 48(1-2), 23-48.
- Stepanova, A., Taldenkova, E., Simstich, J. et Bauch, H. A. (2007). Comparison study of the modern ostracod associations in the Kara and Laptev seas: Ecological aspects. *Marine Micropaleontology*, 63(3-4), 111-142.
- Tanski, G., Bröder, L., Wagner, D., Knoblauch, C., Lantuit, H., Beer, C., . . . Koch, B. P. (2021). Permafrost carbon and CO₂ pathways differ at contrasting coastal erosion sites in the Canadian Arctic. *Frontiers in Earth Science*, 207.
- Tanski, G., Chassiot, L., Carnero-Bravo, V., Falardeau, J., Vonk, J. E., Fritz, M., . . . Irrgang, A. M. (en prép.). Lateral and vertical organic matter dynamics in an Arctic permafrost lagoon.
- Terhaar, J., Lauerwald, R., Regnier, P., Gruber, N. et Bopp, L. (2021). Around one third of current Arctic Ocean primary production sustained by rivers and coastal erosion. *Nature communications*, 12(1), 1-10.
- Thompson, D. W. et Wallace, J. M. (1998). The Arctic Oscillation signature in the wintertime geopotential height and temperature fields. *Geophysical research letters*, 25(9), 1297-1300.
- Tremblay, J. É., Bélanger, S., Barber, D., Aspin, M., Martin, J., Darnis, G., . . . Archambault, P. (2011). Climate forcing multiplies biological productivity in the coastal Arctic Ocean. *Geophysical Research Letters*, 38(18).
- Tripathi, A. K., Roberts, C. D. et Eagle, R. A. (2009). Coupling of CO₂ and ice sheet stability over major climate transitions of the last 20 million years. *science*, 326(5958), 1394-1397.

- Ullrich, A. D., Cowan, E. A., Zellers, S. D., Jaeger, J. M. et Powell, R. D. (2009). Intra-annual variability in benthic foraminiferal abundance in sediments of Disenchantment Bay, an Alaskan glacial fjord. *Arctic, antarctic, and alpine research*, 41(2), 257-271.
- Usher, P. J. (2002). Inuvialuit use of the Beaufort Sea and its resources, 1960-2000. *Arctic*, 18-28.
- Voltski, I., Korsun, S., Pillet, L. et Pawlowski, J. (2015). *Protoelphidium niveum* (Lafrenz, 1963) and the taxonomy of "lower" elphidiids. *Journal of Foraminiferal Research*, 45(3), 250-263.
- Walkusz, W., Williams, W. J., Harwood, L. A., Moore, S. E., Stewart, B. E. et Kwasniewski, S. (2012). Composition, biomass and energetic content of biota in the vicinity of feeding bowhead whales (*Balaena mysticetus*) in the Cape Bathurst upwelling region (south eastern Beaufort Sea). *Deep Sea Research Part I: Oceanographic Research Papers*, 69, 25-35.
- Williams, B. et Carmack, E. C. (2012). Ocean water and sea ice. Dans C. R. Burn (dir.), *Herschel Island Qikiqtaryuk: A Natural and Cultural History of Yukon's Arctic Island* (p. 54-59). Presses de l'Université de Calgary.
- Wollenburg, J. E. et Kuhnt, W. (2000). The response of benthic foraminifers to carbon flux and primary production in the Arctic Ocean. *Marine Micropaleontology*, 40(3), 189-231.
- Wolter, J., Lantuit, H., Herzschuh, U., Stettner, S. et Fritz, M. (2017). Tundra vegetation stability versus lake-basin variability on the Yukon Coastal Plain (NW Canada) during the past three centuries. *The Holocene*, 27(12), 1846-1858.
- Wood, K. R., Bond, N. A., Danielson, S. L., Overland, J. E., Salo, S. A., Stabeno, P. J. et Whitefield, J. (2015). A decade of environmental change in the Pacific Arctic region. *Progress in Oceanography*, 136, 12-31.
- Wood, K. R., Overland, J. E., Salo, S. A., Bond, N. A., Williams, W. J. et Dong, X. (2013). Is there a "new normal" climate in the Beaufort Sea? *Polar Research*, 32(1), 19552.
- Yunda-Guarin, G., Brown, T. A., Michel, L. N., Saint-Beat, B., Amiraux, R., Nozais, C. et Archambault, P. (2020). Reliance of deep-sea benthic macrofauna on ice-derived organic matter highlighted by multiple trophic markers during spring in Baffin Bay, Canadian Arctic. *Elementa: Science of the Anthropocene*, 8(1), 047.

